

AES 2017 Incheon - Korea

The 5th Advanced Electromagnetics Symposium



Proceedings

ISSN 2491-2417

mysymposia.org

AES 2017 Incheon - Korea

The 5th Advanced Electromagnetics Symposium

Please share your comments, photos & videos !

facebook

[https ://www.facebook.com/aes.symposium](https://www.facebook.com/aes.symposium)

twitter

@aes_contact

Edited by

Said Zouhdi | Paris-Sud University, France
Junsuk Rho | POSTECH, Korea

CONTENTS

AES 2017 ORGANIZATION	5
AES 2017 VENUE	6
GUIDELINES FOR PRESENTERS	9
TABLE OF CONTENTS	10

AES 2017 ORGANIZATION



Said Zouhdi, General Chair
Paris–Sud University, France



Junsuk Rho, General Co-Chair
POSTECH, Korea

INTERNATIONAL ADVISORY COMMITTEE

Yahia Antar, Canada
Jean Chazelas, France
Wen-Shan Chen, Taiwan
Christos Christopoulos, UK
Peter de Maagt, Netherlands
Apostolos Georgiadis, Spain
Dave V. Giri, USA
Xun Gong, USA
Lixin Guo, China

Yang Hao, United Kingdom
Nathan Ida, USA
Koichi Ito, Japan
Andrzej Karwowski, Poland
Kwai Man Luk, Hong Kong
Adel Razek, France
Alain Sibille, France
Ari Sihvola, Finland
Paul Smith, Australia

C-K Clive Tzuang, China
J(Yiannis) C. Vardaxoglou, UK
Junhong Wang, China
Yu Zhang, China
Jian Wu, China
Yong-Jun Xie, China

TECHNICAL PROGRAM COMMITTEE

Silvio Ernesto Barbin, Brazil
Muhammad Bawa'aneh, Jordan
Xavier Begaud, France
Qin Chen, China
Christophe Craeye, Belgium
Tie Jun Cui, China
Laurent Daniel, France
Salvador G. Garcia, Spain
Brahim Guizal, France
Tian Sen Jason Horng, Taiwan
Zhirun Hu, UK

Ruey-Bing Hwang, Taiwan
Sungtek Kahng, Korea
Ali Khenchaf, France
Ahmed Kishk, Canada
Ken-ichi Kitayama, Japan
Maciej Krawczyk, Poland
Sebastien Lallechere, France
Allen M. Larar, USA
Jean-Claude Levy, France
Jean-Marc Lopez, France
Andrea Massa, Italy

Ozlem Ozgun, Turkey
Oscar Quevedo-Teruel, Sweden
Blaise Ravelo, France
Josaphat T. S. Sumantyo, Japan
Van Yem Vu, Viet Nam
Konstantin Vytovtov, Russia
Amir I. Zaghloul, USA
Qi-Jun Zhang, Canada
Tao Zhou, China
Arkady Zhukov, Spain

SPECIAL SESSIONS ORGANIZERS

Youchung Chung, Korea
Shanhui Fan, USA
Susan Hagness, USA
Laure Huitema, France

Laurent Santandrea, France
Thomas Schneider, Germany
Konstantin Vytovtov, Russia
Steve Hang Wong, Hong Kong

Zongfu Yu, USA
Linjie Zhou, China

AES 2017 VENUE

AES 2017 will be held at the **Songdo Convensia**, 123 Central-ro, Yeonsu-gu, 21998, **Incheon**, Korea.
 Tel. : +82-32-210-1037
 Fax : +82-32-210-1005
 Website : www.songdoconvensia.com



GETTING TO VENUE

Address

Songdo Convensia, 123 Central-ro, Yeonsu-gu, 21998, **Incheon**, Korea.
 Tel. : +82-32-210-1037
 Fax : +82-32-210-1005
 Website : www.songdoconvensia.com

Seoul (Downtown) -> Songdo Convensia

- By Subway

Subway Station	Information
University of Incheon (Incheon Line)	Take Seoul subway line number 1 and get off at Bupyeong Station Transfer Bupyeong Station to Incheon subway and get off at University of Incheon Station Take a walk around 10-15minutes to Songdo Convensia (next to Sheraton Hotel)
Dongmak Station (Incheon Line)	Take Seoul subway line number 1 and get off at Bupyeong Station Transfer Bupyeong Station to Incheon subway and get off Dongmak Station Through exit 3, take bus 8, 6, 780 to Songdo Convensia Bus Stop

- By Taxi

Fee	Taxi Fare ranges from 60,000 – 90,000 KRW ※ Receipt can be collected from driver if needed
Hours	Available 24hours
About	Ask Taxi Driver for 'Songdo Convensia' (at Songdo of Incheon City nearby Sheraton Hotel)

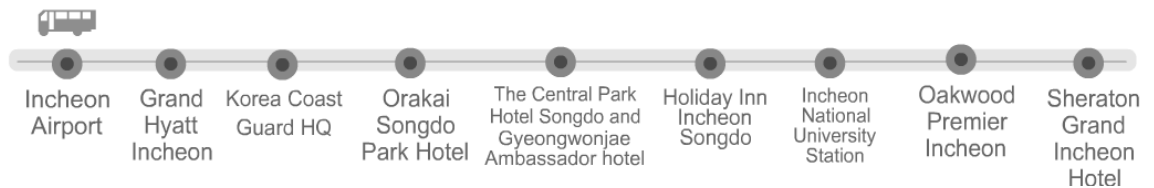
Incheon International Airport (ICN) -> Songdo Convensia

1) By KAL-limousine (~40 min, 7,000 KRW)

- Board the limousine bus (6707B) at the platform 4A



- Get off at **Sheraton Grand Incheon Hotel** (last stop)



Time schedule

Departure Point Incheon Airport (Bus Stop #4A)

Arrival Point Sheraton Grand Incheon Hotel

Please be advised that actual times may vary depending on traffic conditions.

Travel Time : 30min

Departure time					
05:53	06:21	06:58	07:33	08:13	08:58
09:38	10:23	11:13	12:03	12:53	13:43
14:33	15:23	16:14	17:03	17:43	18:22
19:03	19:53	20:42	21:30	22:11	

- For more information, please visit,
https://www.kallimousine.com/eng/guide01_en.html or
<http://www.airport.kr/pa/en/a/3/1/1/index.jsp#none>

2) By Bus (~1 hour, ~3,000 KRW)

- Board a bus line 303 at the platform 13A



- Get off at **Songdo The Sharp First World (East gate) station** (~40 mins)
- Walk 450m (~7 mins on foot)



Time schedule

To Incheon	first	05:00	To CAT	first	05:40
	last	21:30		last	23:00
Interval	15min.		Transit time	210분(MI)	
Type	Local City		Fare	KRW 2,800	

GUIDELINES FOR PRESENTERS

ORAL PRESENTATIONS

Each session room is equipped with a stationary computer connected to a LCD projector. Presenters must load their presentation files in advance onto the session computer. Technician personnel will be available to assist you.

Scheduled time slots for oral presentations are 15 mn for regular, 20 mn for invited presentations, 30 mn for keynote talks and 35 mn for plenary talks, including questions and discussions. Presenters are required to report to their session room and to their session Chair at least 15 minutes prior to the start of their session.

The session chair must be present in the session room at least 15 minutes before the start of the session and must strictly observe the starting time and time limit of each paper.

POSTER PRESENTATIONS

Presenters are requested to stand by their posters during their session. One poster board, A0 size (118.9 x 84.1 cm), in portrait orientation, will be available for each poster (there are no specific templates for posters). Pins or thumbtacks are provided to mount your posters on the board. All presenters are required to mount their papers 30mn before the session and remove them at the end of their sessions. Posters must be prepared using the standard AES poster template (available on the symposium website).

TABLE OF CONTENTS

Integrated photonic devices for information processing

Recent Progress in Slow Light Modulators (pp. 17)

Toshihiko Baba, Y. Terada, Y. Hinakura, K. Hojo, H. Ito,

Integrated Twisted Light Emitter for Orbital Angular Momentum Multiplexing Optical Communications (pp. 18)

Ting Lei,

Advances in quantum dot lasers for silicon photonics (pp. 19)

Yasuhiko Arakawa,

Optical Parametric Oscillators in Silicon: limitations, prospects and applications to Ising machine (pp. 20)

Kambiz Jamshidi, M. Namdari, M. Catuneanu, R. Hamerly, D. Gray, C. Rogers, H. Mabuchi,

Stimulated Brillouin Scattering in Nano-Waveguides as Optical Sensors (pp. 21)

Thomas Schneider, Ali Dorostkar, Linjie Zhou,

2x2 silicon optical switch elements based on coupled ring resonators with tunable coupling coefficient (pp. 23)

Liangjun Lu, Linjie Zhou, Jianping Chen,

Nanophotonic Devices Based on Dielectric-nano-posts-array for Small Footprint Si-Photonics Chips (pp. 25)

Aimin Wu, H. Y. Huang, C. Qiu, Y. X. Zhao, Z. Sheng, F. W. Gan, X. Wang,

Advanced reconfigurable antennas for modern wireless communications

Hybrid Dielectric Resonator Antenna with Pattern Reconfigurability (pp. 28)

Zhe Chen, Hang Wong, J. Xiang,

A 60-GHz Multi-Beam Magneto-Electric Dipole Antenna Array (pp. 30)

Yujian Li, Kaixu Wang,

BST thin film capacitors integrated within a frequency tunable antenna (pp. 32)

Laure Huitema, Aurelian Crunteanu, Areski Ghalem,

Low-Profile Cassegrain-Reflectarray-Fed Transmitarray Antenna (pp. 34)

Shi-Wei Qu, Geng-Bo Wu, Shiwen Yang,

Computational electrodynamics and its emerging applications

Analytic derivations of the effective constitutive parameters and their electrostrictive and magnetostrictive tensors for bi-anisotropic metamaterials (pp. 37)

Neng Wang, C. T. Chan,

Toroidal Modes in the System of Antennas (pp. 38)

Lixin Ge, Hong Xiang, Dezhuan Han,

Topological one-way fiber of second Chern number (pp. 40)

Ling Lu, Zhong Wang,

Plasmonic computing of spatial differentiation (pp. 41)

Tengfeng Zhu, Yihan Zhou, Yijie Lou, Hui Ye, Min Qiu, Zhichao Ruan, Shanhui Fan,

Optical Metasurface Design Optimization Assisted by Artificial Neural Networks (pp. 42)

Jonghwa Shin, Myungjoon Kim, Arthur Baucour, Suwan Jeon,

Electromagnetic Theory, Simulation and Modeling

Theoretical and experimental approaches on galvanometer scanners for high-end biomedical imaging applications (pp. 45)

Virgil-Florin Duma,

Analyzing quantum mechanism of frequency up-conversion (pp. 47)

Jeong Ryeol Choi, Jinmy Song,

Maxwell's equations based models for large-scale simulations of interaction of ultrashort laser pulses with transparent solids (pp. 49)

Vladimir Zhukov, Nadezhda Bulgakova,

Modeling of multi-pulse irradiation of transparent solids based on Maxwell's equations (pp. 50)

Vladimir Zhukov, Nadezhda Bulgakova,

Spiral Bull's Eye Structure for Multi-frequency High-transmission Plasmonic Antenna (pp. 51)

Xiangying Deng, Shunri Oda, Yukio Kawano,

Simulating the linear and nonlinear response of nanostructures under a focused beam with a B-spline modal method (pp. 53)

Patrick Bouchon,

Graphene Electromagnetics from Modelling to Applications (pp. 55)

X. Zhang, X. Huang, T. Leng, K. Pan, Habiba Ouslimani, Zhirun Hu,

Modeling linear and nonlinear optical wave dynamics in nanophotonic devices (pp. 57)

Qiang Lin,

Femtosecond laser induced dynamics of the processes in transparent solids: Insights from Maxwell's-based model (pp. 58)

Nadezhda M. Bulgakova, Vladimir P. Zhukov,

Adjoint Sensitivity of Nonlinear Structures Using the FDTD Method (pp. 60)

Mahmoud Maghrabi, Mohamed Bakr, Shiva Kumar, Atef Elsherbeni, Veysel Demir,

Imaging of photogenerated electron dynamics on a semiconductor surface (pp. 62)

Keiki Fukumoto, Shin-Ya Koshihara,

Absorption and Transmission of Electromagnetic Radiation from a Maxwellian Plasma Slab (pp. 64)

M. Bawa'aneh, Y. C. Ghim, Ahmed M. Al-Khateeb,

Motion and the Fourth Dimension (pp. 65)

Sara Liyuba Vesely, Alessandro Alberto Vesely, Sibilla Renata Dolci, Caterina Alessandra Dolci,

RFID Antennas, Technologies and Applications

Evolution-Strategy Optimized Dual-Band Antenna for UHF-band RFID/IoE Applications (pp. 76)

Muhammad Salman Khattak, Abdul Rehman, Changhyeong Lee, Dajung Han, Hejun Park, Sungtek Kahng, Muhammad Kamran Khattak,

Auto-parts Logistic System Using Long Range UHF RFID Smart Metal Pallet (pp. 80)

Byondi Franck Kimetya, Chang-Hwan Suel, Berhe Hintsa Teklebrhan, You-Chung Chung,

UHF RFID Automobile Plate Tag Antenna Controlling the Radiation Beam Pattern with T-Matching Structure (pp. 84)

Berhe Hintsa Teklebrhan, Byondi Franck Kimetya, Chang Hwan Suel, Youchung Chung,

Small UHF RFID Tag Antenna for Vehicle License Plate (pp. 88)

Berhe Hintsa Teklebrhan, Byondi Franck Kimetya, Chang Hwan Suel, Youchung Chung,

Electromagnetic Theory

Electromagnetic Wave Absorption Properties of Novel Green Composites Coconut Fiber Coir and Charcoal Powder over X-band Frequency for Electromagnetic Wave Absorbing Applications (pp. 93)

Nurul Fatimah Nabila Yah, Hasliza A. Rahim, Yeng Seng Lee, F. H. Wee, H. H. Zainal,

Antenna and Propagation

T-Shaped Slot Antenna Design for Handsets with Metal Back Cover (pp. 97)

Tai Heng Hsieh, Wan Rou Lin, Shu-Kai Tuan, W.-J. Liao,

Performance Optimization of Copper Tube Antenna Design for Outdoor Access Points (pp. 99)

Shu Kai Tuan, Wan Rou Lin, Hao-Ju Hsieh, W.-J. Liao,

Design and Realization of A Patch Array Integrated with System Board of WLAN Point-to-Point Link Device. (pp. 101)

Wan Rou Lin, Tai Heng Hsieh, Hao Ju Hsieh, W.-J. Liao,

Computational Analysis of a Novel Yagi-Uda Antenna for VHF Band (pp. 103)

R. E. Musril, Hasliza A. Rahim, M. Abdulmalek, M. Jusoh,

Dynamic Subject-Specificity On-Body Communications Channel Models for WBAN (pp. 105)

Hasliza A. Rahim, P. J. Soh, M. Abdulmalek, M. Jusoh, G. A. E. Vandenbosch,

Cross dipole EBG based high efficiency dual band antenna for millimeter wave communication systems (pp. 107)

Abhishek Kandwal, Qingfeng Zhang, Xiaolan Tang, L. W. Y Liu, R. Das, Yifan Chen,

Multiple Frequency Microstrip Five-Port Ring Junction Circuit for Six-Port Reflectometer (SPR) (pp. 111)

Siti Aishah Baharuddin, E. M. Cheng, Hasliza Rahim, Kim Yee Lee, Zulkifly Abbas, Nashrul Fazli Mohd Nasir, Yeng Seng Lee,

Voltage Multiplication on Ambient AC Electromagnetic Fields (pp. 116)

Louis W. Y. Liu, Abhishek Kandwal, Qingfeng Zhang,

Investigation on Various Structural Compositions of Textile-Integrated Antenna (pp. 119)

A. A. Sharatol Ahmad Shah, N. H. Abd Rahman, Mohd Tarmizi Ali, M. R. Ahmad, Muhammad Shakir Amin Nordin,

Amalgamation of Rectangular Microstrip Antenna with Light Emitting Diode (LED) (pp. 124)

Suhaila Binti Subahir, Mohd Tarmizi Ali, Hamizan Yon, Siti Norhidayah Kamarudin, A. H. Awang,

Microwave and Millimeter Circuits and Systems

Substrate Integrated Waveguide Circular Cavity Resonators for Planar Diplexer Design (pp. 130)

N. H. Baba, A. H. Awang, M. T. Ali, H. M. Hizan,

Electromagnetic Compatibility

Electromagnetic effects and detection on Integrated Circuits (pp. 135)

David Michel El-Baze, Jean-Baptiste Rigaud, Philippe Maurine,

Shielding Effectiveness Measurement for Conductive Textile-based RF-shielded Environment (pp. 139)

M. A. Humayun, H. A. Rahim, M. AbdulMalek, P. J. Soh, M. S. Zulkefli, C. M. Nor, A. A. Al-Hadi,

Computational Electromagnetics

Wideband Adjoint Sensitivity of Anisotropic Structures Using the FDTD Method (pp. 142)

Mohamed Bakr, Atef Elsherbeni, Veysel Demir,

Optimization Techniques

Coupling Matrix Synthesis Method for Microwave Filters using Genetic Algorithm Optimization (pp. 145)

Abdul Rehman, M. Salman Khattak, ChangHyeong Lee, Dajung Han, Heejun Park, M. Kamran Khattak, Sungtek Kahng,

RF and Wireless Communication

Far-Field Measurement of LTE Base Station-like Exposure in RF-shielded Environment (pp. 150)

M. A. Humayun, H. A. Rahim, M. AbdulMalek, P. J. Soh, M. S. Zulkefli, C. M. Nor, A. A. Al-Hadi,

Adaptive Rate and Power Adaptation Techniques for Packet (pp. 152)

Wan Norsyafizan W. Muhamad, Darmawaty Mohd Ali, Suzi Seroja Sarnin,

Light Harvesting (photovoltaics and solar cells)

Simulation of multilayer waveguide solar cell structure based on nanoparticles (pp. 158)

Hala J. El-Khozondar, Rifa J. El-Khozondar, Mohammed M. Shabat, Daniel M. Schaad,

Electromagnetic and Nanophotonic Materials (metamaterials, plasmonics, etc)

Lattice vibrations and impurity contribution into terahertz electrodynamic response of semi-insulating InP:Fe (pp. 161)

Liudmila Alyabyeva, Elena Zhukova, Mikhail Belkin, Boris Gorshunov,

Linking the properties of surface plasmon polaritons and the quality of laser-induced periodic surface structures (pp. 163)

Thibault J.-Y. Derrien, Yoann Levy, J. Bonse, Laroslav Gnilitzky, Leonardo Orazi, Tomas Mocek, Nadezhda M. Bulgakova,

Directional thermal infrared absorption and emission of zero refractive index dielectric metamaterials (pp. 165)

Byungsoo Kang, Hyeon-Don Kim, Hyun-Sung Park, Kanghee Lee, Sunwoo Han, Jaeman Song, Bong Jae Lee, Bumki Min,

Nanocarbon based lossy photonic crystal microwave absorbers (pp. 167)

G. I. Mark, K. Kertesz, G. Piszter, I. Biro, A. Paddubskaya, P. Kuzhir, L. P. Biro,

Electroactive and Magnetoactive Materials

Dielectric response of Al substituted Ba_{0.8}Pb_{0.2}Fe(12-x)Al_xO₁₉ single crystal hexaferrites in terahertz spectral region (pp. 170)

Liudmila Alyabyeva, Denis Vinnik, Victor Torgashev, Svetlana Gudkova, Elena Zhukova, Anatoly Prokhorov, Dmitry Zherebtsov, Boris Gorshunov,

Bioeffects of EM fields, Biological Media, Medical electromagnetics

Planar microwave resonator for bio-sensing and material characterisation (pp. 173)

Ayodunni Ayodele Oloyo, Zhirun Hu,

Influence of the Metallic Loop-like Accessory on the SAR of Broadband Wearable Planar Monopole Textile Antenna (pp. 175)

Hayati Hasibuan Zainal, Hasliza A. Rahim, Ping Jack Soh, K. N. Abdul Rani, H. Lago, M. S. Zulkefli, N. F. N. Yah,

Measurement Techniques

RCS Evaluation from Small Scatters in Automotive Collision Avoidance Radar Band (pp. 179)

Hao-Ju Hsieh, Tai-Heng Hsieh, Shu-Kai Tuan, W.-J. Liao,

Integrated photonic devices for information processing

Recent Progress in Slow Light Modulators

T. Baba, Y. Terada, Y. Hinakura, K. Hojo and H. Ito

Yokohama National University, Japan

*corresponding author: baba-toshihiko-zm@ynu.ac.jp

Abstract—Photonic crystal slow light waveguides allow Si MZ modulators to enhance the modulator efficiency. We optimized the p-n junction profile in this modulator to balance the phase shift and modulation speed. The device fabricated by CMOS process showed practical performance (32 Gbps, 3 dB extinction ratio, <0.2 pJ/bit energy consumption, 20 nm bandwidth, 5 dB insertion loss) is obtained in a 200-micron device. WDM, QPSK, PAM and sub-bandgap photodiode operations are also demonstrated.

Acknowledgements This work was supported by the NEDO Project.

REFERENCES

1. H. C. Nguyen, Y. Sakai, M. Shinkawa, N. Ishikura and T. Baba, "10 Gb/s operation of photonic crystal silicon optical modulators," *Opt. Express*, vol. 19, no. 14, pp. 13000-13007, 2011.
2. T. Baba, H. C. Nguyen, N. Yazawa, Y. Terada, Hashimoto, T. Watanabe, "Slow-light Mach-Zehnder modulators based on Si photonic crystals," *Sci. Technol. Adv. Mat.*, vol. 15, no. 2, pp. 024602, 2014.
3. Y. Terada, H. Ito, H. C. Nguyen and T. Baba, "Theoretical and experimental investigation of low-voltage and low-loss 25-Gbps Si photonic crystal slow light Mach-Zehnder modulators with interleaved p/n junction," *Front. Phys.*, vol. 2, no. 61, pp. 1-9, 2014.
4. H. Ito, Y. Terada, N. Ishikura and T. Baba, "Hitless tunable WDM transmitter using Si photonic crystal optical modulators," *Opt. Express*, vol. 23, no. 17, pp. 21629-21636, 2015.
5. Y. Terada, K. Miyasaka, H. Ito and T. Baba, "Slow-light effect in a silicon photonic crystal waveguide as a sub-bandgap photodiode," *Opt. Lett.*, vol. 41, no. 2, pp. 289-292, 2016.
6. Y. Hinakura, Y. Terada, T. Tamura and T. Baba, "Wide spectral characteristics of Si photonic crystal Mach-Zehnder modulator fabricated by complementary metal-oxide-semiconductor process," *Photonics*, vol. 3, no. 2, pp. 17(1-11), 2016.
7. K. Hojo, Y. Terada, N. Yazawa, T. Watanabe and T. Baba, "Compact QPSK and PAM modulators with Si photonic crystal slow light phase shifters," *IEEE Photon. Technol. Lett.*, vol. 28, no. 13, pp. 1438-1441, 2016.
8. Y. Terada, T. Tatebe, Y. Hinakura and T. Baba, "Si photonic crystal slow-light modulators with periodic p-n junctions," *J. Lightwave Technol.*, vol. 35, 2017 (available on line).

Integrated Twisted Light Emitter for Orbital Angular Momentum Multiplexing Optical Communications

T. Lei *

Nanophotonics Research Center, Shenzhen University, China

*corresponding author: leiting@szu.edu.cn

Abstract-Twisted light carrying orbital angular momentum (OAM) provides additional multiplexing freedom for the high capacity optical communications. We demonstrate an integrated optical OAM emitter on standard SOI, which generates two coaxial twisted light beams across the entire telecom band from 1450nm to 1650nm. We apply the emitter in OAM communication with 1.2Tbit/s data rate assisted by 30-channels optical frequency combs (OFC). The emitter breaks the current bandwidth bottleneck and it will probably provide a new solution to the on-chip OFC compatible OAM communication.

On-chip twisted light emitter is an essential component for orbital angular momentum (OAM) communications, which could address the growing demand for massive capacity by providing additional degree of freedom to wavelength/frequency division multiplexing (WDM/FDM) [1]. In the past, although the whispering gallery mode enabled OAM emitters had shown advantages of compact size and accurate phase, the inherent narrow bandwidth prevented their compatibility to the WDM/FDM techniques [2, 3]. We demonstrate an ultra-broadband multiplexed OAM emitter, where a new concept of joint path-resonance phase control is proposed and verified. The multiplexed on-chip OAM emitter has a micron sized radius and nanometer sized features, which enable its 200nm bandwidth covering C+L+S bands. The demonstrated twisted light emission efficiency is up to 35%, and the mode purity is better than 95%. We apply the emitter in OAM communication with 1.2Tbit/s data rate assisted by 30-channels optical frequency combs. The OAM multiplexed emitter will probably pave the way for large capacity chip-to-chip optical interconnects. More importantly, the proposed joint path resonance phase control will further inspire fundamental thinking for manipulating and mapping phase structures in generalized photonics devices with the broadband property.

REFERENCES

1. Wang J., Yang J. Y., Fazal I. M., Ahmed N., Yan Y., & Huang H., et al. "Terabit free-space data transmission employing orbital angular momentum multiplexing." *Nature Photonics*, Vol 6, No 7, 488-496, 2012
2. Cai, X., and Yu, S., "Integrated compact optical vortex beam emitters." *Science*, Vol 338, No 6105, 363-366, 2012
3. Miao P., Zhang Z., Sun J., Walasik W., Longhi S., Litchinitser N. M., Feng L., "Orbital angular momentum microlaser." *Science*, Vol 353, No 6298, 464-467, 2016

Advances in quantum dot lasers for silicon photonics

Yasuhiko Arakawa, Bongyong Jang, Jinkwan Kwoen, Satoshi Iwamoto

The University of Tokyo, Japan

*corresponding author: arakawa@iis.u-tokyo.ac.jp

Abstract- We discuss a hybrid InAs/GaAs quantum dot (QD) laser, evanescently coupled to a silicon waveguides, by using wafer bonding. The direct epitaxial growth of InAs/GaAs QD lasers on silicon (100) on-axis substrates is also demonstrated.

Optical Parametric Oscillators in Silicon: limitations, prospects and applications to Ising machine

K. Jamshidi¹, M. Namdari¹, M. Catuneanu¹, R. Hamerly², D. Gray³, C. Rogers³, and H. Mabuchi³

¹Integrated Photonic Devices Group, Technische Universität Dresden, Helmholtzstraße 16, 01069, Dresden, Germany

² National Institute of Informatics, Hitotsubashi 2-1-2, Chiyoda-ku, Tokyo 101-8402, Japan

³ Edward L. Ginzton Laboratory, Stanford University, Stanford, CA 94305, USA

Abstract- Circulation of the pump in a silicon ring resonator makes it possible for integrated photonics to have compact-sized devices like: optical parametric amplifiers, optically bistable devices, and optical parametric oscillators. Optical parametric oscillators are basic building blocks for the realization of an Ising machine.

Silicon photonics, with its high light confinement factor and a reasonably large nonlinear coefficient, is a promising area of research for Kerr-related nonlinear signal processing. But silicon suffers from two-photon absorption (TPA) and the free-carrier absorption (FCA) which is a result of TPA [1]. The free carriers can be controlled with reversed biased electrical field [2]. Other than that, dispersion engineering is possible in silicon waveguides, subject to constraints of the fabrication process. By enhancement of the fields inside a ring resonator, optical parametric amplification-related lengths could be reduced, thus the effective pump power is considerably reduced as the power circulating in the ring structure increases. It is interesting that it is possible to realize four-wave mixing (FWM) in silicon ring resonators [3]. Using the ring resonator structures, we could develop a CMOS-compatible nonlinear signal processing platform for optical bistability, optical parametric amplifiers and oscillators. Finally we will discuss the possible use of optical parametric oscillators for the realization of an Ising machine [4-5].

REFERENCES

1. Lin, Q. et al, "Dispersion of silicon nonlinearities in the near infrared region", *Appl. Phys. Lett.* Vol. 91, No. 2, 021111 (2007)
2. R. Hamerly, et al., "Optical bistability, self-pulsing, and soliton formation in silicon micro-rings with active carrier removal," in *Proc. of SPIE*, San Francisco, US, January 2017, 100980D.
3. M Jazayerifar, et al, "Feasibility study of optical parametric amplification using CMOS compatible ring resonators." in *Proc. of SPIE*, San Francisco, US, January 2017, 101060A-1.
4. Takata, K. et al. "A 16-bit coherent Ising machine for one-dimensional ring and cubic graph problems" *Sci. Rep.* Vol. 6, 34089; (2016).
5. Marandi, A., Wang, Z., Takata, K., Byer, R. L., and Yamamoto, Y., "Network of time-multiplexed optical parametric oscillators as a coherent Ising machine," *Nature Photonics*, Vo. 8, No. 12, 937-942, (2014).

Stimulated Brillouin Scattering in Nano-Waveguides as Optical Sensors

T. Schneider^{1*}, A. Dorokstar¹, and L. Zhou²

¹Institut für Hochfrequenztechnik, TU-Braunschweig, Schleinitzstrasse 22,
38106 Braunschweig, Germany

²State Key Lab of Advanced Optical Communication Systems, Shanghai Jiao Tong University,
800 Dongchuan Rd, Shanghai 200240, China

*corresponding author: thomas.schneider@ihf.tu-bs.de

Abstract—Stimulated Brillouin scattering (SBS) is an interaction between a pump-wave and a counter-propagating Stokes wave. This interaction will be mediated by an acoustical wave. Usually, SBS in very long waveguides like optical fibers is used to measure the temperature or strain distribution over long distances. However, the coherent interaction of radiation pressure and electrostriction in nano-waveguides leads to strong, radial guided acoustic modes in very short waveguide segments. These waveguides might be used as integrated small-scale sensors.

In optical fibers the strength of the SBS is dictated by intrinsic, material dependent nonlinearities and the effect of the waveguide geometry has only little effect. However, recently it has been shown that this paradigm breaks down at the nano-scale [1]. The coherent combination of radiation pressure and electrostrictive forces can enhance both, the forward and backward SBS by orders of magnitude. This makes the photon-phonon coupling highly tailorable by the design of the optical waveguides. The backward SBS can be 4 orders of magnitude and the forward SBS even 5 orders of magnitude higher than in conventional silica fibers [1].

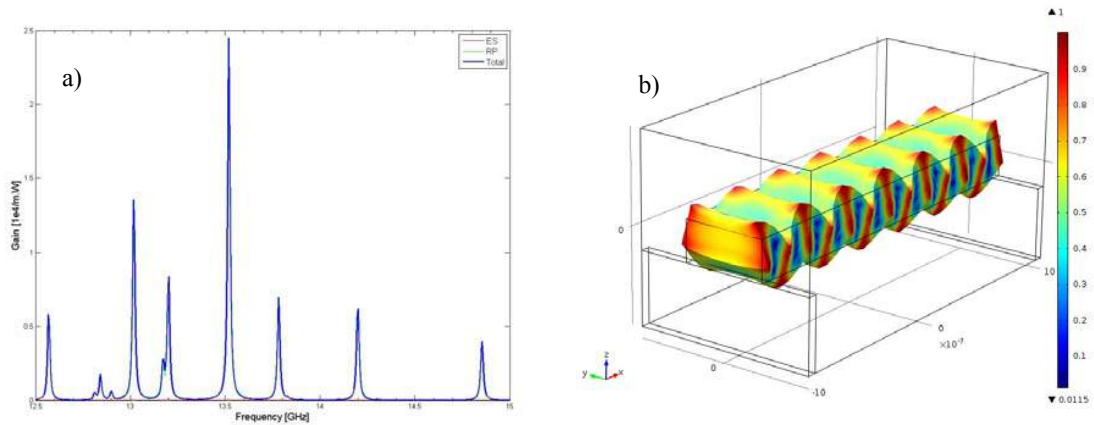


Figure 1 (a): Brillouin gain in dependence on frequency shift for a suspended nano-waveguide with a length of $1\mu\text{m}$, width 450nm , height 220nm and a pump power of 100mW (ES electrostriction, RP radiation pressure). The suspended waveguide can be seen like a bridge laid between two piles (see the black drawing in the right figure). Each pile has a length of 100nm , height of 390nm and a width of $1\mu\text{m}$. **(b):** Acoustic mode for the resonance at a frequency shift of around 13.5GHz .

The SBS interaction in the nano-waveguide leads to strong, radial guided acoustic modes. Figure 1 (a) shows the simulated SBS gain in dependence on the frequency shift between the pump and the Stokes wave in a nano-waveguide with a length of 1 μm . Several acoustic modes at different frequency shifts with a quite high gain can be seen. In Fig.1 (b) the behavior of one of these acoustical modes is shown exemplarily. The acoustic wave can interact with the environment which may lead to a change of the SBS properties. This change might be used to measure or sense distinct properties of the environment. The acoustic wave along the waveguide will be influenced by the material around the waveguide, resulting in a change of the SBS. If just one nano-particle is placed on the waveguide, this should change as well the SBS properties. Additionally, by design the sensing properties of the nano-waveguides might be adapted to the envisioned sensing application. Another interesting field is the cross-talk between two parallel waveguides. This cross-talk might be influenced by the material between the two waveguides. Two parallel waveguides or waveguide arrays might as well be useful, to bring liquids in close contact with the acoustic waves. This makes the SBS in integrated nano-waveguides a very promising candidate for a variety of sensing applications at the nano-scale.

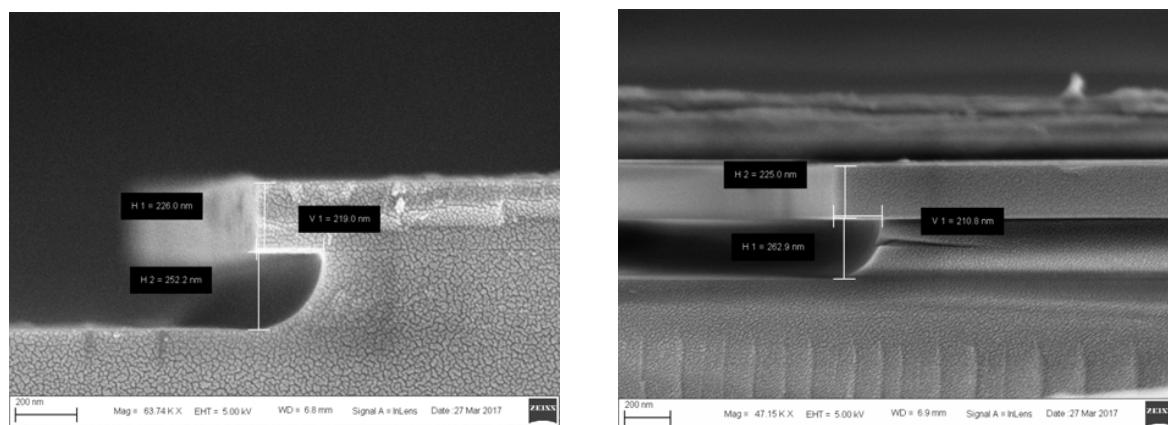


Figure 2: Etched waveguides with a lateral etch of 219 nm (**left**) and around 211 nm (**right**).

First etched waveguides for a test of the SBS were fabricated and tested. Figure 2 shows sample pictures of the etched waveguides. The lateral etch rate can be well controlled. The waveguides in the figures are with a width of 2 μm quite broad. Suspended waveguides with a width of 500 nm were fabricated as well, but since they were not cut through, pictures of their cross-section are not available yet.

We will present first experimental results of the SBS in nano-waveguides and discuss their applicability to sensing applications.

REFERENCES

1. Rakich, P. T., Reinke, C., Camacho, R., Davids, P., Wang, Z., "Giant Enhancement of Stimulated Brillouin Scattering in the Subwavelength limit," *Phys. Rev. X*, Vol. 2, 011008, 2012.

2×2 silicon optical switch elements based on coupled ring resonators with tunable coupling coefficient

Liangjun Lu*, Linjie Zhou, and Jianping Chen

State Key Laboratory of Advanced Optical Communication Systems and Networks, Department of Electronic Engineering, Shanghai Jiao Tong University, Shanghai 200240, China

*corresponding author: luliangjun@sjtu.edu.cn

Abstract—We present a silicon 2×2 switch element based on coupled ring resonators. The input and output coupling is enabled by tunable MZI couplers with both thermo-optic and electro-optic phase shifters. Experimental results show that the switch has a low crosstalk of -45 dB at the bar state and -26 dB at the cross state.

High performance 1×2 or 2×2 switch elements are fundamental components in optical communication networks and other optical signal processing systems. Silicon-based optical switches are a viable solution for large-scale switch fabrics due to its compatibility with CMOS processes and the capability for dense integration [1]. In our previous work, we demonstrated a 2×2 switch based on the dual-ring assisted Mach-Zehnder interferometer (DR-MZI) [2], and later realized larger port-count (4×4 and 16×16) switches with the DR-MZI as the elemental building blocks [3]. Here, we present a 2×2 switch element based on coupled ring resonators with tunable coupling coefficient, which is promising for optical switch fabric application.

Figure 1(a) shows the schematic of the proposed 2×2 switch, which consists of two coupled ring resonators and two bus waveguides. Tunable couplers based on MZIs are used to tune the coupling coefficient between the bus waveguides and the ring resonators. Here we define the amplitude transmission coefficient between the top (bottom) bus waveguide and the top (bottom) ring as $\tau_1(\tau_3)$. When $\tau_1=\tau_3=1$ (MZIs are at bar state), light from the input port passes through the MZI and directly comes out of the bar port without coupling to the rings. Thus, the switch is at the bar state. It works as a single waveguide, and shows a flat spectral response as illustrated in Fig. 1(b). When $\tau_1, \tau_3 < 1$, a portion of the light will couple to the rings on resonance. By properly choosing τ_1 and τ_3 , the switch can be configured as a second-order optical add-drop filter with a high extinction ratio as shown by the solid lines in Fig. 1(b). As we set the operation wavelength at the resonance wavelength, light from the input port is switched to the cross port and the switch is flipped to the cross state.

The 2×2 switch is based on silicon ridge waveguides with waveguide height and width of 220 nm and 500 nm, respectively. The coupling length and gap of the two rings are 2 μm and 200 nm, respectively. Multimode interferometers (MMIs) are used as 3-dB couplers in the MZIs. The excess loss of MMI is about ~ 0.22 dB [4]. TiN microheaters and p-i-n diodes are integrated in the phase shifters of both MZIs. Therefore, the switch can be actuated by both thermo-optic (TO) and electro-optic (EO) methods. The device was fabricated using CMOS-compatible processes in IME, Singapore.

Figure 1(c) shows the measured transmission spectra of the device under TO tuning. Light with transverse-electric (TE) polarization is used in the measurements. Grating couplers with coupling loss of ~ 5.5 dB/facet are used for light coupling in and out of the chip. Although we introduce a tiny length difference between the two MZI arms to ensure π phase difference at the initial state, both of the MZIs are not at the bar

state due to the fabrication errors. The TO power for phase error correction is 5.96 mW and 7.15 mW for the top and bottom MZIs, respectively. It can be seen that the bar port has a flat spectral response and the crosstalk is lower than -45 dB. To flip the switch state to the cross state, the TO tuning power is tuned to 26.4 mW and 20.2 mW, respectively. At the cross state, light is routed to the cross port with an on-chip insertion loss of ~2.5 dB. The free spectral range (FSR) of the device is 0.45 nm and the crosstalk is ~-28 dB. The 3-dB optical bandwidth is ~8.3 GHz, which can be increased with a larger coupling coefficient κ_2 . We also flip the switching state by EO tuning, as shown in Fig. 1(d). The EO switching power is 1.96 mW and 1.4 mW, respectively. It shows a similar response with the TO tuning except for a higher insertion loss of ~4.5 dB caused by free carrier absorption. The measured crosstalk is ~-26 dB.

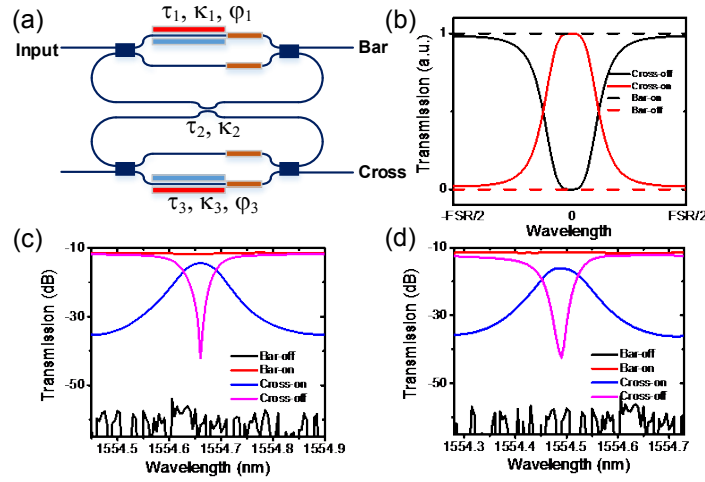


Fig. 1 (a) Schematic view of the 2×2 optical switch. (b) Calculated transmission spectra of the switch. (c) and (d) Measured transmission spectra of the device under (c) TO and (d) EO tuning, respectively.

In conclusion, a 2×2 silicon optical switch based on coupling-tuned ring resonators has been experimentally demonstrated. The measured insertion loss of the switch is 2.5 dB and 4.5 dB for TO and EO tuning, respectively. The crosstalk is below -26 dB. Our 2×2 switch can function as a good building block for large-scale integrated optical switch fabrics.

Acknowledgements This work was supported in part by the National Natural Science Foundation of China (NSFC) (61422508, 61535006, 61661130155). We acknowledge IME Singapore for device fabrication.

REFERENCES

1. Chen, L., and Chen, Y.-K., "Compact, low-loss and low-power 8×8 broadband silicon optical switch," *Opt. Express*, Vol. 20, No. 17, 18977-18985, 2012.
2. Lu, L., Zhou, L., Li, X., and Chen, J., "Low-power 2×2 silicon electro-optic switches based on double-ring assisted Mach-Zehnder interferometers," *Opt. Lett.* Vol. 39, No. 6, 1633-1636, 2014.
3. Lu, L., Zhou, L., Li, Z., Li, D., Zhao, S., Li, X., and Chen, J., "2×2 silicon optical switches based on double-ring assisted Mach-Zehnder interferometers," *IEEE Photon. Technol. Lett.* Vol. 27, No. 23, 2457-2460, 2015.
4. Lu, L., Zhao, S., Zhou, L., Li, D., Li, Z., Wang, M., Li, X., and Chen, J., "16×16 non-blocking silicon optical switch based on electro-optic Mach-Zehnder interferometers," *Opt. express*, Vol. 24, No. 9, 9295-9307, 2016.

Nanophotonic Devices Based on Dielectric-nano-posts-array for Small Footprint Si-Photonics Chips

A.M. Wu^{*1}, H.Y.Huang^{1,2}, C.Qiu¹, Y.X. Zhao^{1,2}, Z. Sheng¹, F.W. Gan¹, and X.Wang¹

¹State Key Laboratory of Functional Materials for Informatics, Shanghai Institute of Microsystem and Information Technology, CAS, Shanghai, China

*Corresponding author: wuaimin@mail.sim.ac.cn

Abstract-Nanophotonic devices based on dielectric-nano-posts-array are promising candidates in subwavelength scale applications. Here, we demonstrate an ultrathin nano-posts-chain that can route and manipulate light, realizing splitting and sharp bending while exhibiting broadband, incident-angle-tolerant, and robust against disorder. The nano-posts-chain is further designed and turns into a novel silicon nano-antenna array, which can direct light vertically emitting to the third dimension. These devices provide small footprint components for Si-photonics chips.

Recent photonic integrated circuits meet higher demand for light confinement and manipulation at subwavelength scale [1]. Compared with the candidates such as Plasmon [2, 3] and all-dielectric periodic nanoparticle chains [4, 5], ultrathin dielectric nano-posts-chain is competitive because it is broadband, incident-angle tolerant and robust against fabrication disorder. We experimentally demonstrated a subwavelength sharp bend consisting of a thin line of silicon nano-posts. This effect is attributed to the excitation and tailoring of the scattering of the high permittivity nano-posts at the peculiar resonant state. The thickness of the nano-posts array is only 1/3 of the operational wavelength (1.55 μm), which makes the device extremely compact. Furthermore, the nano-posts array can also be used for guiding light with appropriate design. Fig.1 (a) shows the incident-angle tolerance that the chain could receive light beam with incident angle up to 75°. Figure 1(b-e) demonstrate excellent robustness against position-disorder and size-disorder. These results indicate that the array can be used for bend and splitter below the diffraction limit by tailoring the position of the nano-posts, which is experimentally demonstrated in Fig.1 (f, g). These low loss all-dielectric structures are compatible with complementary metal-oxide semiconductor (CMOS) technologies, offering an effective solution for in-plane beam steering and routing for on-chip photonics.

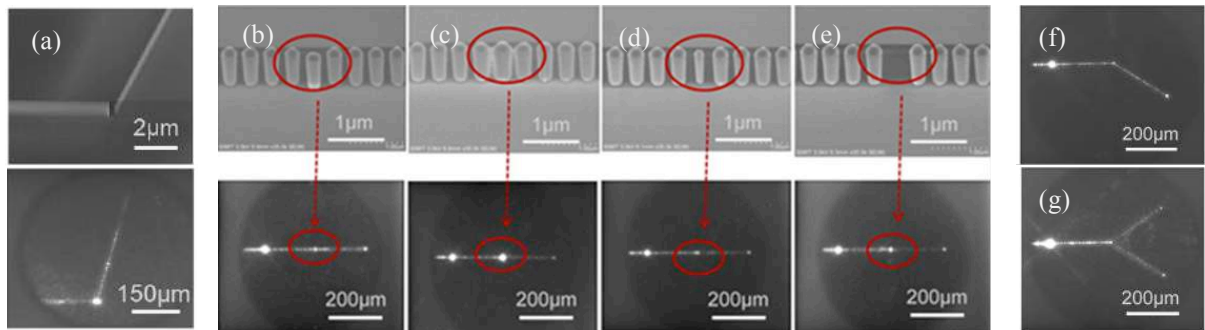


Fig.1 (a) Ray trace of the 75° incident light beam. (b) Ray trace when position-disorder is introduced with a deviation of 160 nm from the chain. (c) - (e) Ray traces when size-disorder is introduced with a radius of 240nm,

100 nm and 0, respectively. (f) The ray trace of light bending. (b) The ray trace of light splitting.

To connect different layers of the 3D integrated chips by optical approach is another demand for optical interconnection. We demonstrate a novel silicon nano-antenna array (SNA), that direct light emission vertically. The width of the SNA is only one wavelength, which is the most compact silicon optical antenna built to date. The SNA consists of two parallel chains of silicon nano-posts, and a pair of intentionally designed defects is used to replace two interval posts in the end for each chain, as shown in Figure 2. Light beam is equally guided into the two chains, generating out-of-plane far-field optical radiation on top of the defects area. Numerical simulations show that the upward radiation has a well-confined shape and the efficiency reaches as high as 46%, and the optical field distribution and the optical spot size are confirmed when SNOM probes and placed on top of the defects to collect the light.

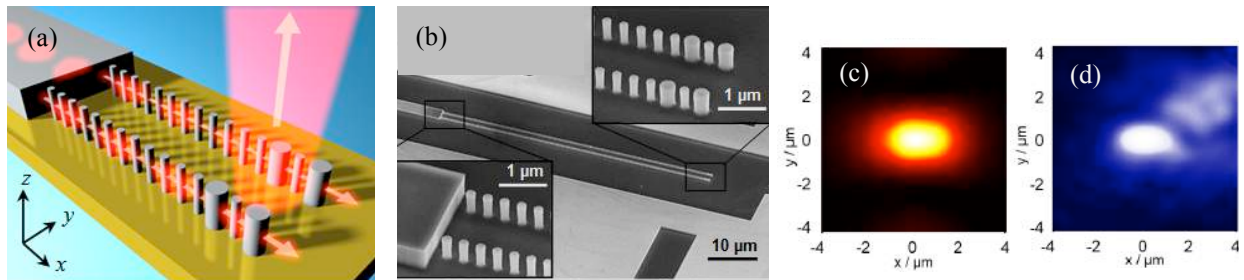


Fig.2 (a) Schematic illustration of the SNA. Each SNA consists of a line of rods with a pair of defect rods at the end. The distance between the rows is 1.6 μm. (b) SEM images of the fabricated structures. (c) – (d) The simulated (c) and detected (d) intensity profiles at 5 μm above the defect area.

As a summary, nano-photonics devices based on thin silicon nano-posts array are proposed and experimentally demonstrated to fulfill the demand for miniaturization of the optical interconnection on-chip and off-chip.

ACKNOWLEDGEMENT

This work was supported by International Collaboration Program of Chinese Ministry of Science and Technology (Grants 2016YFE0130000), and Science and Technology Commission of Shanghai Municipality (Grant 16ZR1442600).

REFERENCES

1. Li, M., Li, W., Huang, H., Wang, J., Li, Y., Wu, A., Sheng, Z., Wang, X., Zou, S., & Gan, F. All-Angle quasi-self-collimation effect in a rod-type silicon photonic crystal. *IEEE Photonics J*7, 1-8 (2015).
2. Kumar, G., Li, S., Jadidi, M. M., Murphy, T. E. Terahertz surface plasmon waveguide based on a one-dimensional array of silicon pillars. *New J Phys*15, 085031 (2013).
3. Fung, K. H., Tang, R. C. & Chan, C. T. Analytical properties of the plasmon decay profile in a periodic metal-nanoparticle chain. *Opt Lett*36, 2206-2208 (2011).
4. Savelev, R. S., Slobozhanyuk, A. P., Miroshnichenko, A. E., Kivshar, Y. S. & Belov, P. A. Subwavelength waveguides composed of dielectric nanoparticles. *Phys Rev B*89, 035435 (2014).
5. Zhang, L., Zhan, Q., Zhang, J., Cui, Y. Diffraction inhibition in two-dimensional photonic crystals. *Opt Lett*36, 651-653 (2011).

Advanced reconfigurable antennas for modern wireless communications

Hybrid Dielectric Resonator Antenna with Pattern Reconfigurability

Z. Chen¹, H. Wong^{1*}, and J. Xiang²

¹ State Key Lab of MMWs (HK), City University of Hong Kong, Hong Kong

² Shenzhen Key Lab of MWWC, Shenzhen Research Institute, City University of Hong Kong, China

*corresponding author: hang.wong@cityu.edu.hk

Abstract—a hybrid dielectric resonator antenna (HDRA) to realize radiation pattern reconfigurable design is proposed. The inner part of the HDRA is fabricated by solid material with no need for altering, while the outer part is filled with liquid material which can be rebuilt conveniently. Therefore, by flowing control of liquid in the outer zone, radiation pattern reconfigurable design is realized.

INTRODUCTION

The application of reconfigurable technology for antenna design has drawn much attention these years due to its attractive characteristic [1]. Generally, reconfigurable antennas fall into three categories: frequency reconfigurability [2], polarization selection [3], and radiation pattern beamforming control [4]. To obtain above-mentioned reconfigurable electrical characteristic, the most traditional technology is electrical switching control such as the application of PIN-diode. However, the presence of PIN-diode may lead to narrow bandwidth and high loss.

Consequently, a radiation pattern reconfigurable HDRA without PIN-diode is proposed. For the HDRA, the inner part is fabricated by K9 glass which need no altering, while the outer part is filled with liquid dielectric called ethyl acetate. Therefore, the pattern reconfigurability is achieved by the injection and discharging of the outer part of liquid dielectric. The proposed HDRA demonstrates how to manipulate $TM_{01\delta}$ and $HEM_{11\delta}$ modes of the cylindrical DRA (CDRA) to devote conical beam and broadside radiation pattern in two states. What's more, the proposed HDRA has a wide effective working band (VSWR<2 for both two states) of 35.5 % and high radiation efficiency.

ANTENNA DESIGN

As mentioned above, the two states of the pattern reconfigurable HDRA is manipulated by $TM_{01\delta}$ and $HEM_{11\delta}$ modes of the CDRA. The electric field distributions and the corresponding feed mechanisms of the $TM_{01\delta}$ and $HEM_{11\delta}$ modes in the CDRA are shown in Fig. 1 with different radiation patterns. For the $TM_{01\delta}$ mode, it achieves a conical beam, while for the $HEM_{11\delta}$ mode, it obtains a broadside pattern.

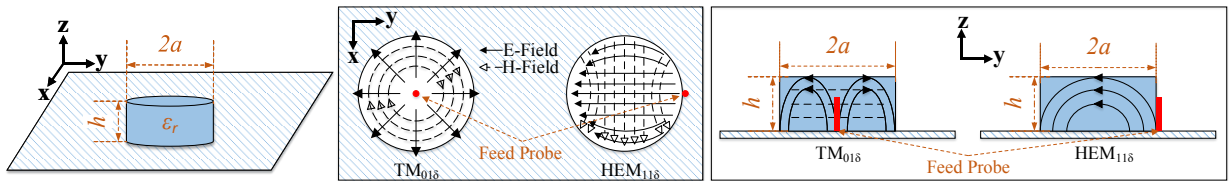


Fig.1 The E- and H-field distributions and corresponding feed mechanisms of the $TM_{01\delta}$ and $HEM_{11\delta}$ modes in the CDRA

According to this basic principle, the pattern reconfigurable HDRA is designed as in Fig. 2. In STATE 1, the liquid and solid material working together as a bigger CDRA with a conical beam. In STATE 2, the solid material working alone as a smaller CDRA with a broadside pattern. Therefore, the resonant frequencies of the $TM_{01\delta}$ and $HEM_{11\delta}$ modes of cylindrical DRA is calculated by the formula in [5].

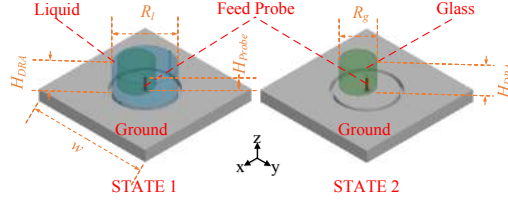


Fig. 2 Two working states of the HDRA

For the $TM_{01\delta}$ mode,

$$k_0 a = \frac{\sqrt{3.83^2 + \left(\frac{\pi a}{2h}\right)^2}}{\sqrt{\epsilon_r + 2}} \quad (1)$$

For the $HEM_{11\delta}$ mode,

$$k_0 a = \frac{6.324}{\sqrt{\epsilon_r + 2}} \left[0.27 + 0.36 \frac{a}{2h} + 0.02 \left(\frac{a}{2h} \right)^2 \right] \quad (2)$$

Finally, the resonant frequencies of these two modes can be calculated,

$$k_0 a = \frac{f_{GHz} \cdot h_{cm} \cdot \frac{a}{h}}{4.7713} \quad (3)$$

In these formulas, h is the height of cylindrical DRA, a is the radius, and ϵ_r is the dielectric constant.

CONCLUSION

A novel radiation pattern reconfigurable HDRA is investigated in this paper. According to the basic principle of $TM_{01\delta}$ and $HEM_{11\delta}$ modes in the CDRA, the HDRA fabricated by solid and liquid material is designed. More importantly, it has a wide effective working band of 35.5 % and high radiation efficiency.

Acknowledgements, this project was supported in part by the Research Grants Council of the Hong Kong SAR, China (Project No. CityU 11216915) and the National Science and Technology Major Project under Grant 2015ZX03001006.

REFERENCES

1. C. G. Christodoulou, Y. Tawk, S. A. Lane and S. R. Erwin, "Reconfigurable Antennas for Wireless and Space Applications," *Proc. IEEE*, vol. 100, no. 7, pp. 2250-2261, July 2012.
2. D. Peroulis, K. Sarabandi and L. P. B. Katehi, "Design of reconfigurable slot antennas," *IEEE Trans. Antennas Propagat.*, vol. 53, no. 2, pp. 645-654, Feb. 2005.
3. W. Lin; H. Wong, "Multi-polarization Reconfigurable Circular Patch Antenna with L-shaped Probes," *IEEE Antennas Wireless Propag. Lett.*, vol. PP, no. 99, pp. 1-1.
4. S. L. S. Yang and Kwai-Man Luk, "Design of a wide-band L-probe patch antenna for pattern reconfiguration or diversity applications," *IEEE Trans. Antennas Propagat.*, vol. 54, no. 2, pp. 433-438, Feb. 2006.
5. A. Petosa, *Dielectric Resonator Antenna Handbook*. Norwood, MA, USA: Artech House, 2007.

A 60-GHz Multi-Beam Magneto-Electric Dipole Antenna Array

Yujian Li¹, and Kaixu Wang^{2,3}

¹ Institute of Lightwave Technology, Beijing Jiaotong University, Beijing, China

² State Key Laboratory of Millimeter Waves, City University of Hong Kong, Hong Kong, China

³ the CityU Shenzhen Research Institute, City University of Hong Kong, Hong Kong, China

*corresponding author: liyujian@bjtu.edu.cn

Abstract—A 4×4 magneto-electric (ME) dipole antenna array that can generate sixteen beams scanning in two dimensions is proposed in V-band. By utilizing a passive beamforming network with a novel topology, the entire array configuration can be integrated into multi-layered planar substrates. A bandwidth of 16.4%, stable radiation patterns and gain up to 14.7 dBi are obtained.

There is an increasing demand for passive multi-beam antenna arrays with a relatively large size in recent years due to their low fabrication cost and low power consumption at millimeter-wave frequencies [1]. However, the conventional passive multi-beam arrays that have been widely adopted in lower microwave bands usually have complex three-dimensional topologies [2]. Therefore, they are not easy to fabricate precisely for millimeter-wave applications.

In order to overcome the challenge, a modified array topology is proposed for designing millimeter-wave multi-beam antenna arrays with a relatively large size as shown in Fig. 1. Two sets of sub-beamforming-networks are arranged into a series of planar substrates. Two sets of vertical interconnections are used for connecting the sub-beamforming-networks in different layers. With the help of the proposed topology, the multi-beam array with a planar configuration can be implemented conveniently at millimeter-wave frequencies.

By applying the topology aforementioned, a 4×4 aperture-coupled magneto-electric (ME) dipole antenna array with sixteen radiation beams is designed as presented in Fig. 2. The whole array is composed of five printed circuit board (PCB) substrates. Eight four-way substrate integrated waveguide (SIW) Butler matrixes are employed as the sub-beamforming-networks in this design. Two types of aperture-coupled ME-dipole antennas are located in the top PCB substrate. Sixteen simulated 3-dB radiation beams radiated from the array are illustrated in Fig. 3. More details of the design can be found in [3].

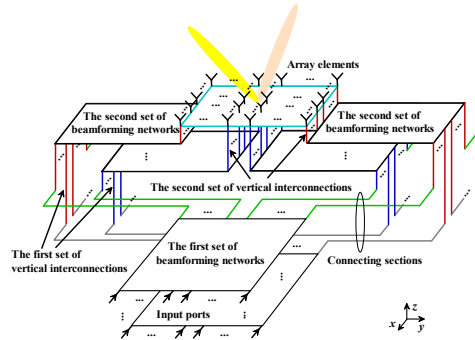


Fig. 1. Topology of the proposed two-dimensional multi-beam antenna array.

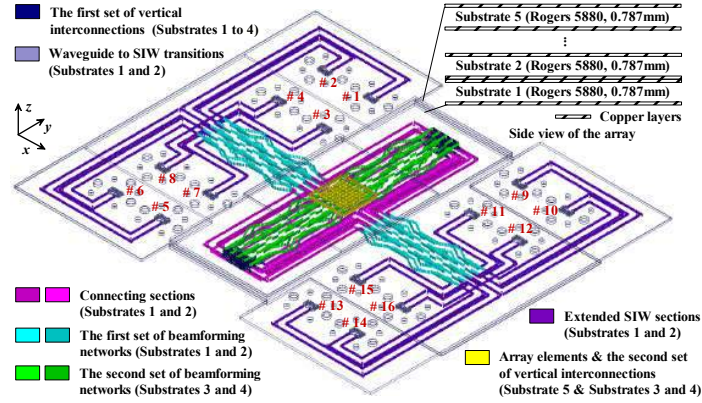


Fig. 2. Geometry of the 4×4 ME-dipole antenna array.

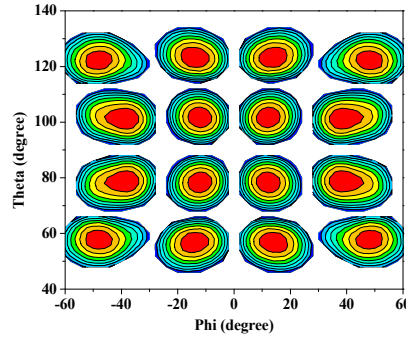


Fig. 3. Simulated radiation beams generated by the proposed antenna array.

Acknowledgements

This work was supported in part by the National Natural Science Foundation of China under Grant No. 61671052, and the Research Grants Council of the Hong Kong, SAR, China (Project No. CityU 11216915).

REFERENCES

1. C. Tseng, C. Chen, and T. Chu, "A low-cost 60-GHz switched-beam patch antenna array with butler matrix network," *IEEE Antennas Wireless Propag. Lett.*, vol. 7, pp. 432–435, 2008.
2. G. C. Sole and M. S. Smith, "Multiple beam forming for planar antenna arrays using a three-dimensional rotman lens," *Microwaves, Antennas and Propagation, IEE Proceedings H*, vol.134, no.4, pp.375-385, Aug. 1987.
3. Y. J. Li, J. H. Wang, and K. M. Luk, "Millimeter-Wave Multi-Beam Aperture-Coupled Magneto-Electric Dipole Array with Planar Substrate Integrated Beamforming Network for 5G Applications," *IEEE Trans. on Antennas and Propagation*, Accepted for publication.

BST thin film capacitors integrated within a frequency tunable antenna.

L. Huitema¹, A. Ghalem¹, and A. Crunteanu¹

¹Xlim Laboratory UMR 7252 CNRS/University of Limoges, 87060, Limoges, France

*corresponding author: laure.huitema@unlim.fr

Abstract- Ferroelectric (FE) thin film varactors can be a convenient technology for tuning miniature antennas. In this paper we present the design of a compact, agile, slot antenna integrating barium strontium titanate ($\text{Ba}_{(1-x)}\text{Sr}_x\text{TiO}_3$, BST) thin film capacitors. Capacitance values were measured at different temperatures and bias voltages ranging from 0V to 20V showing a capacitance variation of more than 90% up to 5 GHz. Their integration within a compact antenna design allows tuning its operating frequency on a large frequency band, with efficiencies higher than 50%.

The miniaturization of electronic devices implies a stringent reduction of the radiating element dimensions, which becomes one of the most important challenges for antenna designers [1]. However, small, compact antennas are limited by fundamental physical limits, generally in terms of radiation performances (efficiency) and bandwidth (quality factor) [2]. Moreover, the performances of small antennas are directly linked to the package of the transceiver module and their embedding environment. The current state-of-the-art is based on frequency reconfigurable antennas for mobile terminals, integrating different agile devices for fine-tuning their operation frequencies [3]. Existing reconfiguration solutions are based on varactor diodes, Micro-Electro-Mechanical systems (MEMS), PIN diodes, field effect transistors (FET) or the introduction of tunable ferroelectric materials. Among these, PIN diodes present only two possible states (On/Off) and, like the FETs devices, have high power consumption. The MEMS-based solutions have a relatively low tuning speed and require complex integration while varactor diodes (although widely referenced), have a very low power handling capability (restricting their use only for reception antenna devices).

In this context, the integration of agile capacitors based on ferroelectric materials within compact antenna systems could be an attractive solution. Indeed, the high agility of ferroelectric materials with an applied DC bias and their reasonable loss tangent values can be employed to develop tunable systems [4] and the integration of ferroelectric tunable capacitors and compact antennas do not raise complex technological issues.

In this paper, we present the dielectric properties and the tunable performances of barium strontium titanate (BST) thin films integrated in capacitors as reconfigurable components within a miniature antenna. We will characterize the dielectric properties of the as-deposited, bare ferroelectric thin film using a resonant cavity method and we will compare these results with those extracted from the measurements and the electromagnetic simulations of the fabricated BST-capacitors. The BST-based capacitance has been optimized to present the optimal agility with the minimal losses. Finally, we will describe the design and the performances of a miniature agile antenna incorporating these BST-based devices. The BST material is a ferroelectric type material with the main property of changing its dielectric permittivity when applying an external electric field. The capacitor device was fabricated starting from an MgO(100) substrate on which a 100-nm thick Ir(100) bottom electrode has been deposited by radiofrequency magnetron reactive sputtering at 600°C. The BST film was afterward

deposited by PLD (KrF excimer laser at 248 nm wavelength, 10 Hz repetition rate and fluence of 4.5 J/cm²) from a stoichiometric Ba₂/3Sr₁/3TiO₃ target at 700°C in oxygen atmosphere (ambient pressure of 0.3 mbar). This specific composition has been chosen to obtain a paraelectric behaviour of the BST thin film near room temperature and thus for attaining a linear variation of the final device capacitance without the onset of a ferroelectric-type hysteresis cycle [5]. Following their deposition, the BST films were structured in square patterns (100 x 100 µm²) using a photolithography step and wet etching. A 200-nm thick Au electrode with 10-nm thick Ti adhesion layer (total area of 30 x 30 µm²) was finally evaporated and patterned by a lift-off process on top of the BST patterns. We prepared MIM devices integrated BST films with different thicknesses (200 nm, 450 nm and 1450 nm, respectively) and a SEM image is presented on Fig. 1.

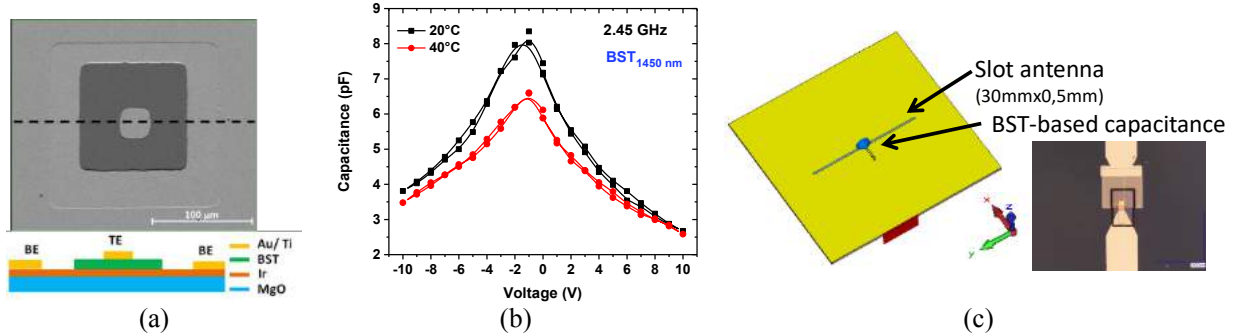


Fig. 1. SEM image of a MIM device with the associated cross section TE: top electrode, BE: bottom electrode (a), Capacitance variation for a -10 V - +10 V dc bias cycle for the 1450-nm thick BST at 20°C and 40°C. (b) and the integration inside a slot antenna (c)

Obtained capacitances show very high tunability of around 90%, defined as following:

$$T(\%) = \left(\frac{C(0V) - C(10V)}{C(0V)} \right) * 100$$

A typical capacitance-voltage cycle of the tunable capacitance is presented on Fig. 1. Losses have been minimized by avoiding electrostrictive effects around the frequency of interest for the antenna between 2 GHz and 3 GHz. Indeed, the equivalent resistance of such a device is equal to 1.13Ω in the worst case, i.e. when applying a dc bias of 10V.

The BST-based antenna structure is a basic slot antenna. In this case, the BST capacitance is directly loading the slot as shown on Fig. 1. The antenna is integrating BST capacitors with structured electrodes in order to have optimized capacitance values and obtained the higher antenna tunability. In this framework, the simulated |S₁₁| parameters are presented on Fig. 1. A frequency band of 400 MHz (going from 2.37 GHz to 2.77 GHz) is covered, corresponding to 17% of bandwidth, which allows this antenna to work on both the ISM and the LTE bands. Its total efficiency is remaining higher than 50% on the whole working frequencies.

This work was partially supported by the “Agence National de la Recherche” (ANR)-France and the National Authority for Scientific Research (ANCS)-Romania, under the project MAESTRO. We thank C. Constantinescu, P. Marchet, F. Dumas-Bouchiat and C. Champeaux from the SPCTS Laboratory (France) for the preparation of the ferroelectric layers.

REFERENCES

1. M.R. Yuce et al., "Easy-to-swallow antenna and propagation", *IEEE Microwave Magazine*, vol.14, no.4, 2013.
2. R.C Hansen, "Fundamental limitations in antennas", *Proceedings of the IEEE*, vol.69, no.2, pp. 170- 182, 1981.
3. L. Huitema, *Progress in compact antennas*, Intech, 2014.
4. N. K. Pervez, P. J. Hansen, and R. A. York, "High tunability barium strontium titanate thin film for RF circuit applications", *Applied Physics Letters*, vol. 85, no. 19, pp. 4451-4453, 2004.
5. M. Tyunina et al. "The paraelectric state in thin-film (Ba,Sr)TiO₃" *J. Appl. Phys.*, vol 101, 084119, 2007.

Low-Profile Cassegrain-Reflectarray-Fed Transmitarray Antenna

Shi-Wei Qu*, Geng-Bo Wu, and Shiwen Yang

School of Electronic Engineering, University of Electronic Science and Technology of China, China
shiweiqu@uestc.edu.cn

Abstract—In this paper, a novel low-profile Cassegrain-reflectarray-fed transmitarray antenna is introduced. A flat Cassegrain reflectarray with compact ring focus feed is employed as the source to illuminate the upper transmitarray. The numerical results of a $6\lambda \times 6\lambda$ reflectarray-fed transmitarray antenna with a small focus-to-diameter ratio (F/D) of 0.3 demonstrate that this transmitarray antenna has achieved a gain of 22.6dB at 12GHz, corresponding to an aperture efficiency of about 40%.

Microstrip reflectarrays and transmitarrays are rapidly becoming attractive alternatives to traditional parabolic reflectors, dielectric lens and phased arrays for wireless communications due to their various advantages such as low cost, low mass and ease of fabrication [1]-[2]. Space feeding is employed in both reflectarrays and transmitarrays to avoid complexity and losses of the feeding networks used in conventional constrained fed phased arrays. Nevertheless, the space feeding arrangement of reflectarrays and transmitarrays encounters the problem of large distance between the feed point and the reflectarray or transmitarray aperture, which is not desired in many applications where low-profile high gain antennas are required.

In this work, a novel low-profile planar high-gain antenna configuration, which combines two kinds of conventional planar reflectarray and transmitarray antenna, is introduced. The basic cross-section of a Cassegrain-reflectarray-fed transmitarray antenna is sketched in Fig. 1. In this hybrid configuration, a flat Cassegrain reflectarray antenna with compact ring focus feed is employed as the source to illuminate the transmitarray. Electromagnetic waves propagate from the standard circular waveguide are guided by the dielectric connecting portion and reflected by the sub-reflector to impinge on the reflectarray aperture. The dimensions of the reflectarray elements are adjusted properly to compensate spatial delay from the sub-reflector and form a desired amplitude distribution on the upper transmitarray aperture. Then the dimensions of the transmitarray elements are adjusted to compensate the phase delay from the lower reflectarray and form a collimated beam.

To demonstrate the proposed reflectarray-fed transmitarray antenna configuration, a $6\lambda \times 6\lambda$ reflectarray-fed transmitarray antenna operating at 12GHz with a small focus-to-diameter ratio (F/D) of 0.3 is designed. The lower reflectarray is made up of a 1.5mm thick dielectric substrate having a relative permittivity 2.2 with a ground plane on the backside and various size square patch elements on the upper side. The unit-cell dimensions are fixed at 12.5×12.5 mm ($0.5\lambda_0 \times 0.5\lambda_0$, where λ_0 is the free-space wavelength at 12GHz). Due to the large incident angles of the coning waves for reflectarray elements, the incidence angle effects are considered in the reflectarray design. The four-layer double square rings element [2] is employed here for transmitarray design and the unit-cell dimensions of the transmitarray elements is identical to that of the reflectarray elements. The simulated radiation patterns of the whole reflectarray-fed transmitarray antenna at 12GHz are shown in Fig. 2. The simulated realized gain is 22.6dB, corresponding to an aperture efficiency of about 40%. It is noted that the aperture efficiency of this transmitarray antenna is larger than that of the reflectarray designed by D. M. Pozar *et*

al. with a F/D of around 0.3 and an aperture efficiency of about 30% [3], which validates that the introduced hybrid configuration can achieve a low-profile design with high gain performance.

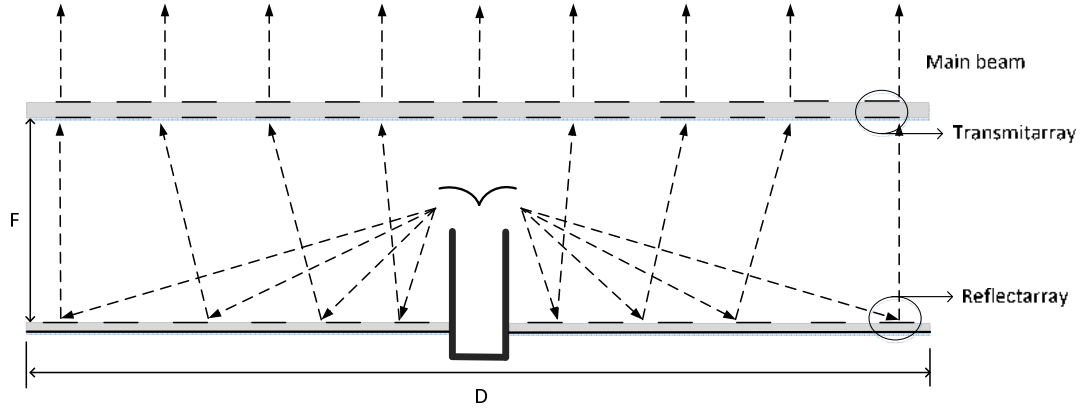


Fig. 1. Cross-section view of the Cassegrain-reflectorarray-fed transmitarray.

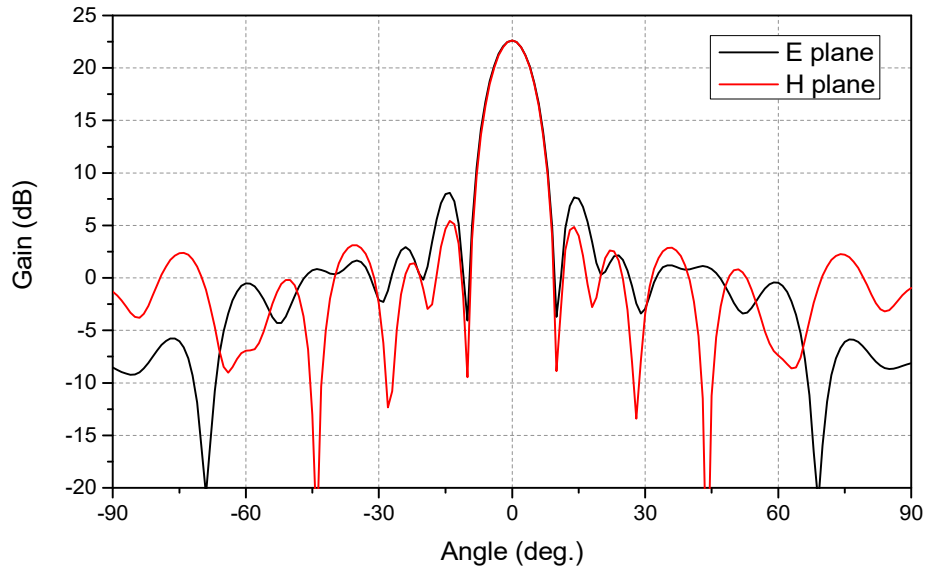


Fig. 2. Simulated radiation patterns of the Cassegrain-reflectorarray-fed transmitarray.

Acknowledgements

This work was supported by the Natural Science Foundation of China (NSFC) Project under 61622104.

REFERENCES

1. J. Huang and J. A. Encinar, *Reflectorarray Antennas*. New York, NY, USA: IEEE, 2008.
2. C. G. M. Ryan, *et al.*, "A wideband transmitarray using dual-resonant double square rings," *IEEE Trans. Antennas Propag.*, vol. 58, no. 5, pp. 1486–1493, May 2010.
3. D. M. Pozar, S. D. Targonski, and H. D. Syrigos, "Design of millimeter wave microstrip reflectarrays," *IEEE Trans. Antennas Propag.*, vol. 45, no. 2, pp. 287–296, Feb. 1997.

Computational electrodynamics and its emerging applications

Analytic derivations of the effective constitutive parameters and their electrostrictive and magnetostrictive tensors for bi-anisotropic metamaterials

Neng Wang and C. T. Chan*

Department of Physics and Institute for Advanced Study, The Hong Kong University of Science and Technology, Hong Kong, China.

*Corresponding author: phchan@ust.hk

Abstract—based on multiple scattering theory, we derived for the first time the analytic formulas of effective constitutive parameters as well as their electrostrictive and magnetostrictive tensors for bi-anisotropic metamaterials in the long wavelength limit. The former can be regarded as an extension of the traditional Maxwell-Garnet formula to chiral metamaterials and the latter are very useful for calculating the optical force distribution inside the metamaterials.

The metamaterials considered in this study are composed of parallel identical isotropic chiral inclusions arranged in a square or hexagonal lattice whose electromagnetic properties can be described by the effective permittivity, permeability and chirality tensors with diagonal matrix form. The effective constitutive parameters as well as their electrostrictive and magnetostrictive tensors can be obtained from the secular equations using multiple scattering formalism.

A typical result is shown in Fig. 1, where we compared the results obtained from the derived analytic formulas and the numerical calculations for both square and hexagonal lattice structures. We can see that the formulas can give the correct results independent of the arrangement of the chiral inclusions, and the formulas work with no restriction on the magnitude of the chirality of the inclusions.

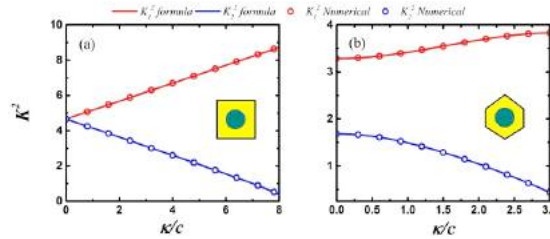


Figure 1: Comparison between the slopes of the band in the limit of $k \rightarrow 0, \omega \rightarrow 0$ obtained from the formulas and the numerical calculations.

Acknowledgements: This work is supported by RGC Hong Kong.

REFERENCES

1. Y. Wu and Z. Q. Zhang, ‘Dispersion relations and their symmetry properties of electromagnetic and elastic metamaterials in two dimensions’, *Phys. Rev. B* Vol 79, 195111, 2009.
2. W. Sun, S. B. Wang, J. Ng, L. Zhou and C. T. Chan, ‘Analytic derivation of electrostrictive tensors and their application to optical force density calculations’, *Phys. Rev. B* Vol 91, 235439, 2015.

Toroidal Modes in the System of Antennas

Lixin Ge, Hong Xiang, and Dezhuan Han

¹Department of Applied Physics, Chongqing University, China

*corresponding author: dzhan@cqu.edu.cn

Abstract - A class of resonant modes with intrinsic toroidal moment is identified in the discrete dipole systems such as the system of dipole antennas in the THz and microwave regime and plasmonic nanoparticles at optical frequencies. An eigenmode analysis are developed and this method can give a complete description for this system. In these systems, the toroidal multipoles will interfere with the conventional multipoles in the far field, leading to the non-radiating “anapoles” and unidirectional scattering.

Summary: It is well known that a closed loop of magnetic dipoles can give rise to the rather elusive toroidal moment. However, artificial structures required to generate the necessary magnetic moments in metamaterials are typically optically large, complex to make, and easily compromised by the kinetic inductance at high frequencies. Instead of using magnetic dipoles, we propose a minimal model based on just three aligned discrete electric dipoles in which the occurrence of resonant toroidal modes is guaranteed by symmetry. The advantage of this model is its simplicity and the same model supports toroidal moments from the microwave regime up to optical frequencies as exemplified by a three-antenna array and a system consisting of three nanosized plasmonic particles. Both the microwave and high-frequency configurations exhibit non-radiating “anapoles.” Experiments in the microwave regime confirm the theoretical predictions. It is also found that the toroidal dipole moment can play a significant role in the unidirectional backward scattering.

We firstly derive the equation of linear response for the system of wire antennas. Consider a cylindrical antenna with a length L and radius ρ_0 , lying in the region $z \in [-L/2, L/2]$. The current oscillating along the antenna is assumed to be: $\mathbf{J}(z) = \hat{e}_z J(z) \pi \rho_0^2 \delta(x) \delta(y)$, where the current is treated as a line current for a distant observer. $J(z)$ should be zero at the end of the antenna. As a result, $J(z)$ can be expanded by the Fourier harmonics: $J(z) = \sum_m J_m \cos(zm\pi/L)$, where m is an odd positive integer. To expand by a complete basis, the harmonics $J_n \sin(2zn\pi/L)$ with odd symmetry should be also incorporated. However, numerical calculations show that the contributions from these harmonics are extremely small under the normal incidence of plane waves. The amplitude of m -th harmonics, J_m , is given by:

$$J_m = \frac{2}{L} \int_{-L/2}^{L/2} J(z) \cos(zm\pi/L) dz. \quad (1)$$

In the cylindrical coordinates (ρ, ϕ, z) , the vector potential \mathbf{A} induced by the m -th current harmonics can be written as $\mathbf{A} = \mathbf{A}_m(\rho, \phi, z) = \hat{e}_z A_{z,m}(\rho, \phi, z)$, which is independent on the azimuth angle ϕ . The z component of the electric field $E_{z,m}$ can be found through A .

The radiated electric field of the antenna will react on itself. We assume that it is the electric field E_z on the boundary of the antenna that acts on the current source itself. The electric field at $\rho = \rho_0$ can be expanded by the Fourier series again:

$$E_{z,m}(\rho_0) = \sum_n E_{z,nm} \cos(zn\pi/L), \quad (3)$$

which implies that the source, i.e., the m -th current harmonics J_m , can induce many field harmonics indexed by n . The Fourier coefficients are given by:

$$E_{z,nm} = -\frac{iZ_0\rho_0^2}{4k_0} \frac{2}{L} \int_{-L/2}^{L/2} \left(\int_{-L/2}^{L/2} J_m \cos(z'm\pi/L) f^A(\rho_0, z, z') dz' \right) \cos(zn\pi/L) dz. \quad (4)$$

The current and electric field can be related by the Ohm's law. The electric field consists of two parts: the external one and the one induced by the current itself, namely:

$$J_n \cos(zn\pi/L) = \sigma \left(\sum_m E_{z,nm} \cos(zn\pi/L) + E_n^{\text{ext}} \cos(zn\pi/L) \right). \quad (5)$$

The above equation can be written in a compact form by introducing a Green function:

$$\sigma^{-1} J_n - \sum_m G_{nm}(\rho_0, L, L) J_m = E_n^{\text{ext}}. \quad (6)$$

The above equation can be further generalized to the system of multiple antennas:

$$\sigma^{-1} J_m^{(i)} - \sum_n \sum_j G_{mn}(r_{ij}, L_i, L_j) J_n^{(j)} = E_{i,m}^{\text{ext}}, \quad (7)$$

where $r_{ij}=|\mathbf{r}_i-\mathbf{r}_j|$ is the center-to-center distance between the antennas A_i and A_j as $i \neq j$, and we choose $r_{ii}=0$ as $i=j$ (the “on-site energy”).

Acknowledgements. National Natural Science Foundation of China (Grant No. 11574037).

REFERENCES

1. Kaelberer, T., Fedotov, V. A., Papasimakis, N., Tsai, D. P. and Zheludev, N. I. “Toroidal dipolar response in a metamaterial,” *Science*, Vol. **330**, 1510-1512, 2010.
2. Papasimakis, N., Fedotov, V. A., Savinov, V., Raybould, T. A. & Zheludev, N. I. “Electromagnetic toroidal excitations in matter and free space,” *Nat. Mater.*, Vol. **15**, 263-271, 2016.
3. Xiang, H., Ge, L., Liu, L., Jiang, T., Zhang Z. Q., Chan C. T., and Han, D. Z. “A minimal discrete model for toroidal moments and its experimental realization,” *Phys. Rev. B*, 95, 045403, 2017.
4. Ge, L., Liu, L., Dai, S., Chai, J., Song Q., Xiang H., and Han, D. Z., “Unidirectional scattering induced by the toroidal dipole moment in the system of plasmonic nanoparticles,” arXiv:1612.03637v1.

Topological one-way fiber of second Chern number

Ling Lu¹, Zhong Wang²

¹Institute of Physics, Chinese Academy of Sciences, Beijing, China

²Institute for Advanced Study, Tsinghua University, Beijing 100084, China
linglu@iphy.ac.cn

Abstract— We propose topological one-way fibers enabled by the recently discovered Weyl points in a double-gyroid (DG) photonic crystal. By annihilating two Weyl points by supercell modulation in a magnetic DG, we obtain the photonic analogue of the 3D quantum Hall phase with a non-zero first Chern number (C1). When the modulation becomes helices, one-way fiber modes develop along the winding axis, with the number of modes determined by the spatial frequency of the helix. These single-polarization single-mode and multi-mode one-way fibers, having nearly identical group and phase velocities, are topologically-protected by the second Chern number (C2) in the 4D parameter space of the 3D wavevectors plus the winding angle of the helices. They are readily realizable at microwave frequencies with magnetic materials. This work suggests a unique way to utilize higher-dimensional topological physics without resorting to artificial dimensions.

1. INTRODUCTION

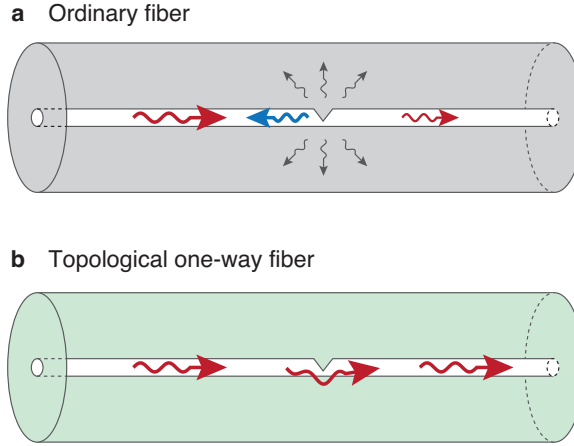


Figure 1: Ordinary fiber versus topological one-way fiber. a) The optical mode in an ordinary fiber is confined in the core, where both forward and backward modes exist. The imperfection induces scattering losses into back and radiation channels. (b) The optical mode in a topological one-way fiber is confined by the 3D topological bandgap which spatially separates the forward and backward modes. The one-way mode in the core is immune to scattering losses of any kinds.

Plasmonic computing of spatial differentiation

Tengfeng Zhu¹, Yihan Zhou¹, Yijie Lou¹, Hui Ye², Min Qiu², Zhichao Ruan^{1*}, Shanhui Fan³

¹ State Key Laboratory of Modern Optical Instrumentation, and Department of Physics, Zhejiang University, Hangzhou 310027, China

² State Key Laboratory of Modern Optical Instrumentation and College of Optical Engineering, Zhejiang University, Hangzhou 310027, China

³ Department of Electrical Engineering, and Ginzton Laboratory, Stanford University, California 94305, USA
zhichao@zju.edu.cn

Abstract— In this talk, we show that the interference effects associated with surface plasmon excitations at a single metal-dielectric interface can perform spatial differentiation. And we experimentally demonstrate edge detection of an image without any Fourier lens. This work points to a simple yet powerful mechanism for optical analog computing at the nanoscale.

Optical analog computing offers high-throughput low-power-consumption operation for specialized computational tasks. Traditionally, optical analog computing in the spatial domain uses a bulky system of lenses and filters. Recent developments in metamaterials enable the miniaturization of such computing elements down to a sub-wavelength scale. However, the required metamaterial consists of a complex array of meta-atoms, and direct demonstration of image processing is challenging. Here, we show that the interference effects associated with surface plasmon excitations at a single metal-dielectric interface can perform spatial differentiation. And we experimentally demonstrate edge detection of an image without any Fourier lens. This work points to a simple yet powerful mechanism for optical analog computing at the nanoscale.

ACKNOWLEDGMENT

This work was supported by the Thousand Youth Talents Plan, Fundamental Research Funds for the Central Universities (2014QNA3007), and the National Natural Science Foundation of China (NSFC 61675179).

REFERENCES

1. Ruan, Z., Wu, H., Qiu, M., and Fan, S. “Spatial control of surface plasmon polariton excitation at planar metal surface,” *Opt. Lett.* Vol. 39, 3587–3590, 2014.
2. Ruan, Z. “Spatial mode control of surface plasmon polariton excitation with gain medium: from spatial differentiator to integrator,” *Opt. Lett.* Vol. 40, 601–604, 2015.
3. Zhu, T., Zhou, Y., Lou, Y., Ye, H., Qiu, M., Ruan, Z., and Fan, S., “Plasmonic computing of spatial differentiation,” 2017.

Optical Metasurface Design Optimization Assisted by Artificial Neural Networks

J. Shin^{1*}, M. Kim¹, A. Baucour², and S. Jeon¹,

¹Korea Advanced Institute of Science and Technology, Republic of Korea

²Université de Technologie de Troyes, France

*corresponding author: qubit@kaist.ac.kr

Abstract—Artificial neural networks (ANNs) can predict the optical properties of metasurfaces based on their structural parameters. Once trained, ANN-based predictions require orders-of-magnitude smaller computational resources than full numerical simulations. It is shown that ANN can be incorporated into conventional numerical optimization routines to reduce the optimization time significantly. Examples of waveplate and color filter metasurfaces are presented.

Finding the optimal design for a given application is one of the central objectives in any engineering field. Except for very simple cases such as problems with high symmetries or problems with a known figure of merit function, the solution process typically involves numerical optimization steps. Various optimization methods have been utilized in designing optical metasurfaces: some of them are gradient-based methods while population-based methods such as particle swarm optimization and genetic algorithms are also popular. Regardless of the methods, finding the global optimum or a good local optimum requires numerous evaluations of the merit function. The total computation time is therefore proportional to the amount of time it takes to evaluate the figure of merit of a particular design and the total number of evaluations, and it can range from several minutes for simple 2D problems with just one or two design parameters to many years for large 3D problems with many design parameters.

Considering that the brain of animals, including humans, have limited memory, computation throughput, and energy budget compared to a single modern CPU, it is awe-inspiring that they can perform complex maneuvers such as flying and running with instant corrections. It is hard to imagine that they are performing finite element calculations of fully vectorial fluid dynamics on the fly—it is more reasonable to assume that they developed efficient internal circuitry that can provide quick approximate answers for difficult problems. Artificial neural networks have been studied as a possible way to mimic such functions. While it takes some time to educate these networks with known examples, they can instantaneously deliver answers with a good accuracy once trained. Fig. 1 demonstrate an example of optical metasurface color filters. Using only 40 neurons, the color coordinates (X, Y, Z values) can be very accurately predicted as a function of structural parameters.

However, training the networks requires data and computational resources. First, there should be training datasets from which the network can learn. Building these datasets, experimentally or numerically, require considerable time, which may diminish the benefit of using neural networks for fast optimization. Second, training the networks from the datasets typically involves iterative methods that also can take some time. For the metasurface designs we considered, the time consumed for the second step was negligible compared to the first step. Hence, if one can develop a new hybrid optimization routine that can minimize the time used for the dataset generation while not affecting the ability of the algorithm to avoid local minima, one may be able to reduce the

total optimization time significantly.

We developed a hybrid optimization method that gradually replaces full simulations with neural network predictions as the optimization progresses. This method does not require separate preparation steps to build the datasets and to train the neural network a priori. Initially, the method has a similar speed as conventional optimization methods as full simulations are required to evaluate the figure of merit. However, as the optimization progresses and datasets are accumulated, one can gradually utilize the predictions of simultaneously evolving neural networks to reduce the computation time by orders of magnitudes. Fig. 2 presents an example: the optimization time is reduced by more than 50 times.

In summary, we showed that artificial neural networks can be useful in design optimization problems. By using them to complement the full numerical simulations, orders of magnitude enhancement of the performance can be expected compared to the conventional optimization methods.

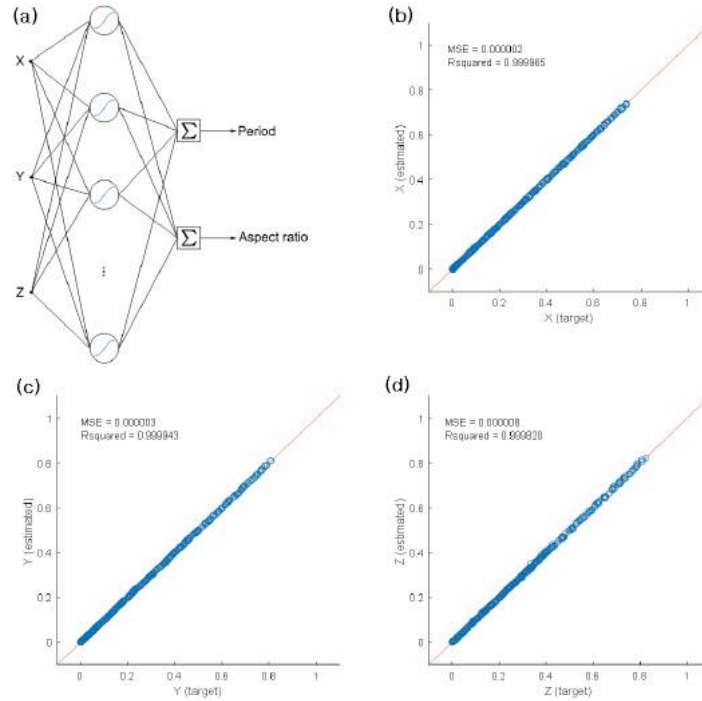


Figure 1 Artificial neural network and its predictions. (a) The network (b-d) Predicted and actual values of the color coordinates of a color filter metasurface.

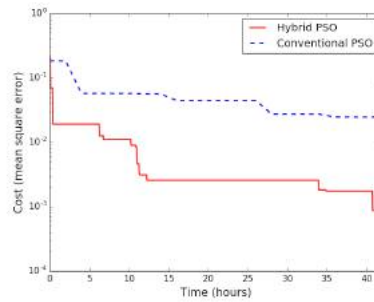


Figure 2 Comparison of the optimization speed of the proposed hybrid method and the conventional method.

Electromagnetic Theory, Simulation and Modeling

Theoretical and experimental approaches on galvanometer scanners for high-end biomedical imaging applications

V.-F. Duma^{1,2}

¹3OM Optomechatronics Group, Aurel Vlaicu University of Arad, Romania

²Doctoral School, Polytechnics University of Timisoara, Romania

*corresponding author: duma.virgil@osamember.org

Abstract-Galvanometer-based scanners have been studied and optimized, especially for high-end applications like biomedical imaging, with a focus on Optical Coherence Tomography (OCT). Based on experimental investigations, a mathematical model have been developed, in order to maximize the duty cycle of these scanners for different input signals and to collate individual OCT images for larger fields-of-view. The optimal scanning functions that can provide the maximum possible duty cycle of such scanners have been demonstrated theoretically.

Optical Coherence Tomography (OCT) is an established, yet dynamic imaging technique that has unique non-destructive cross-section capabilities, with millimeter penetration depths and micrometer resolutions [1, 2]. Most of its variants use electromagnetic lateral scanning of the samples, usually with dual axis galvanometer scanners (GSs). With regard to other laser scanners, GSs have superior positioning precisions, good scan frequencies and angular amplitudes, at reasonable costs per scan axis [3].

The major issue of GSs is related to their working principle, i.e., an oscillatory mirror which has stop-and-turn portions that, due to mechanical inertia, introduce a non-linearity in purely triangular input signals. We demonstrated that such symmetrical signals are the best with regard to other two most common input signals of GSs – sinusoidal and sawtooth [4]. Thus, triangular scanning provides the smallest distortions with regard to the other two – for example in OCT imaging, but also in other techniques, such as confocal microscopy. This is due to the smallest time interval of the non-linear stop-and turn portions for triangular scanning.

This also gives the highest duty cycle/time efficiency η of the scanner – aspect that is essential in numerous applications, including industrial (e.g., in laser manufacturing), not only in imaging. However, η depends on several parameters: theoretical duty cycle (of the input signal) – especially for sawtooth scanning, scan frequency f_s and amplitude θ_a – as we have shown and studied experimentally in [4], and then modeled mathematically in [5], for both triangular and sawtooth scanning. The latter model was also validated with OCT imaging, using the high-resolution Gabor Domain Optical Coherence Microscopy (GD-OCM) [5]. These latter results serve as an optimized algorithm for generating collated OCT images from individual ones [5], as it is necessary for example in scanning the entire human retina [6].

To increase η further more the solution is to design input signals with non-linear portions for GSs. While it has been considered that such portions should be sinusoidal [3], we demonstrated analytically that the optimal triangular-type signals should be linear plus parabolic – in order to maximize η [7]. This result has been obtained for open-loop GSs, but we also demonstrated that the transfer function of close-loop GSs is – for the scan frequencies specific to biomedical imaging, at least – similar to the one of open-loop devices. This direction of research targets improved control structures of GSs, in order to obtain higher speeds and/or better stability to

disturbances. GSs researches also prove useful when approaching other scanner with oscillatory mirrors, included constructed as Micro-Electro-Mechanical Systems (MEMS). A recent research has obtained in this respect the first time, in vivo, non-invasive images with an in-house MEMS-based handheld OCT probe [8] – for GD-OCM -, in contrast to previous researches [9].

Other works in our groups include 1D GS-based handheld probes for OCT which are simple, light weight (up to 0.3 kg [10] – in comparison to 0.5 kg in state-of-the art and no less than 1.5 kg for commercial probes), and low cost [11]. These probes have been applied so far especially for dental medicine [10], but also for ENT (ear-nose-throat) researches [12]. Future work includes the use of 1D and 2D GS-based OCT probes in a range of applications, including in industry, for materials studies [13].

Acknowledgements: This study was supported by the Romanian Authority for Scientific Research, CNDI-UEFISCDI project PN-III-P2-2.1-PTE-2016-0181 (<http://3om-group-optomechatronics.ro/>) and by the European Union through the European Regional Development Fund under the Competitiveness Operational Program (BioCell-NanoART = Novel Bio-inspired Cellular Nano-architectures, POC-A1-A1.1.4-E nr. 30/2016).

REFERENCES

1. Huang, D., et al., and Fujimoto, J.G. "Optical coherence tomography," *Science* 254, 1178-1181, 1991.
2. Drexler, W., Liu, M., Kumar, A., Kamali, T., Unterhuber, A. and Leitgeb, R. A., "Optical coherence tomography today: speed, contrast, and multimodality," *J. Biomed. Opt.*, Vol. 19, 071412, 2014.
3. J. Montagu, *Scanners-galvanometric and resonant*, Encyclopedia of Opt. Eng., Taylor & Francis, 2465-2487, 2003.
4. Duma, V.-F., Lee, K.-S., Meemon, P. and Rolland J. P., "Experimental investigations of the scanning functions of galvanometer-based scanners with applications in OCT," *Appl. Opt.*, Vol. 50, No. 29, 5735-5749, 2011.
5. Duma, V.-F., Tankam, P., Huang, J., Won, J. J. and Rolland, J. P., "Optimization of galvanometer scanning for Optical Coherence Tomography," *Appl. Opt.*, Vol. 54, No. 17, 5495-5507, 2015.
6. Braaf, B., Vermeer, K. A., Vienola, K. V., and de Boer, J. F., "Angiography of the retina and the choroid with phase-resolved OCT using interval-optimized backstitched B-scans," *Opt. Express*, Vol. 20, 20516–20534, 2012.
7. Duma, V.-F., "Optimal scanning function of a galvanometer scanner for an increased duty cycle," *Opt. Eng.*, Vol. 49, No. 10, 103001, 2010.
8. Cogliati, A., et al., Duma, V.-F., and Rolland, J. P., "MEMS-based handheld scanning probe with pre-shaped input signals for distortion-free images in Gabor-Domain Optical Coherence Microscopy," *Opt. Express*, Vol. 24, No. 12, 13365-13374, 2016.
9. Lu, C. D., et al., and Fujimoto, J. G., "Handheld ultrahigh speed swept source optical coherence tomography instrument using a MEMS scanning mirror," *Biomed. Opt. Express* 5, 293–311, 2014.
10. Demian, D., Duma, V.-F., et al., and Podoleanu, A. Gh., "Design and testing of prototype handheld scanning probes for optical coherence tomography," *J. Eng. in Medicine*, Vol. 228, No. 8, 743-753, 2014.
11. Duma, V.-F., et al., and Podoleanu, A. Gh., "Handheld scanning probes for optical coherence tomography," *Romanian Reports in Physics*, Vol. 67, No. 4, 1346-1358, 2015.
12. Cernat, R., et al., "Dual instrument for in vivo and ex vivo OCT imaging in an ENT department," *Biomed. Opt. Express*, Vol. 3, 3346–3356, 2012.
13. Hutiu, Gh., Duma, V.-F., Demian, D., Bradu, A., and Podoleanu, A. Gh., "Surface imaging of metallic material fractures using optical coherence tomography," *Appl. Opt.*, Vol. 53, 5912–5916 (2014).

Analyzing quantum mechanism of frequency up-conversion

Jeong Ryeol Choi* and Jinny Song

Department of Radiologic Technology, Daegu Health College, Buk-gu, Daegu 41453, Republic of Korea

*corresponding author: choiardor@hanmail.net

Abstract—Quantum mechanism of frequency up-conversion has been investigated. The mathematical representation of quantized electromagnetic waves associated with frequency switching in time-varying media is obtained by using the invariant operator method. The time behavior of wave packets during the conversion of frequency has been analyzed.

Frequency up-conversion is a technology for obtaining high frequency electromagnetic waves from lower frequency waves that can be easily producible from existing instruments. There are many important applications of frequency up-conversion, such as developing highly sensitive single photon detectors [1], millimeter-wave generation techniques [2], and Terahertz imaging [3]. For this reason, frequency up-conversion for fields in time-varying media has attained a considerable interest in quantum optics and other research areas. This technique is necessary in the field of electromagnetic engineering [4], including diagnosis of a plasma state in thermonuclear fusion power generation [5]. The quantization of electromagnetic waves associated with frequency switching in time-varying media can be achieved by utilizing invariant operator theory [6].

Among diverse electromagnetic materials, plasma, which reveals many unique properties, is a typical example of time-varying media. The analysis of electromagnetic-wave propagation in such media requires rigorous mathematical manipulations. Artificial frequency conversion for electromagnetic signal in nonstationary and inhomogeneous plasma is realizable [7,8]. The technique of frequency up-conversion in plasma can be used on diagnosis of plasma states in a tokamak during nuclear fusion.

In this work, we analyze quantum mechanism of frequency up-conversion for electromagnetic waves propagating in time-varying media. We consider abrupt exponential growth of frequency and some of other types of frequency increase. The change of quantum wave packets during the conversion of frequency will be studied in detail. The Lewis-Riesenfeld invariant method will be used for mathematical treatment of electromagnetic waves in time-varying media in this analysis.

Acknowledgements, This research was supported by the Basic Science Research Program through the National Research Foundation of Korea (NRF) funded by the Ministry of Education (Grant No.: NRF-2016R1D1A1A09919503).

REFERENCES

1. Ma, L., O. Slattery, and X. Tang, "Single photon frequency up-conversion and its applications," *Phys. Rep.*, Vol. 521, No. 2, 69–94, 1986.
2. Mohamed, N., S. M. Idrus, A. B. Mohammad, H. Harun, R. Mohamad, and S. Yaakob, "Frequency up-conversion technique for radio over fiber (RoF) remote antenna unit configuration," *The Open Electrical & Electronic Engineering Journal*, Vol. 6, 7-13, 2012.
3. Fu, Z. L., L. L. Gu, X. G. Guo, Z. Y. Tan, W. J. Wan, T. Zhou, D. X. Shao, R. Zhang, and J. C. Cao,

- “Frequency up-conversion photon-type Terahertz imager,” *Sci. Rep.*, Vol. 6, 25383, 2016.
4. Malkin, I. A., V. I. Man'ko, and D. A. Trifonov, “Coherent states and transition probabilities in a time-dependent electromagnetic field,” *Phys. Rev. D*, Vol. 2, No. 8, 1371–1385, 1970.
 5. Kalluri, D. K. *Electromagnetics of Time Varying Complex Media*, 2nd Ed. CRC Press, Boca Raton, 2010.
 6. Lewis, H. R. Jr. and W. B. Riesenfeld, “An exact quantum theory of the time-dependent harmonic oscillator and of a charged particle in a time-dependent electromagnetic field,” *J. Math. Phys.*, Vol. 10, No. 8, 1458–1473, 1969.
 7. Wilks, S. C., J. M. Dawson, and W. B. Mori, “Frequency up-conversion of electromagnetic radiation with use of an overdense plasma,” *Phys. Rev. Lett.* 61, No. 3, 337–340, 1988.
 8. F. Meng, M. D. Thomson, and H. G. Roskos, “Relativistic Doppler frequency upconversion of terahertz pulses reflecting from a photoinduced plasma front in silicon,” *Phys. Rev. B*, Vol. 90, No. 15, 155207, 2014.

Maxwell's equations based models for large-scale simulations of interaction of ultrashort laser pulses with transparent solids

V.P. Zhukov^{1,2}, N.M. Bulgakova^{3,4}

¹ *Institute of Computational Technologies SB RAS, 6 Lavrentyev Ave., 630090 Novosibirsk, Russia*

² *Novosibirsk State Technical University, 20 Karl Marx ave., 630073, Novosibirsk, Russia*

³ *HiLASE Centre, Institute of Physics ASCR, Za Radnici 828, 25241 Dolni Břežany, Czech Republic*

⁴ *Institute of Thermophysics SB RAS, 1 Lavrentyev Ave., 630090 Novosibirsk, Russia*

zhukov@ict.nsc.ru

Irradiation of bulk transparent solids by femtosecond laser pulses is widely used in scientific research and technological applications. To study theoretically the complicated phenomenon of laser beam propagation in absorbing media, the models based on nonlinear Maxwell's equations (NLME) or the nonlinear Schrödinger equation (NLSE) are usually used. To describe ionization of the medium and its optical response to laser irradiation, the models are either supplemented with kinetic equations or involve more sophisticated approaches based on hydrodynamics-type equations for free-electron plasma. The validity of the NLSE, which is obtained by simplification of Maxwell's equations under the assumption of slowly varying envelop propagating unidirectionally, is limited to the cases of relatively low beam focusing angles and ionization levels when free-electron plasma is not yet able to scatter light to large angles. The NLME-based models are free from these limitations; however, their direct application for large scale simulations is limited by available computer resources.

In this report, we present different aspects of application of the NLME-based models to the large-scale simulations of the processes in transparent dielectrics irradiated by ultrashort laser pulses in the regimes of volumetric modification. The problems of proper descriptions of photo- and impact ionization rates, absorbed laser energy, electron collision cross-sections, which are still debated, are discussed. Ways to accelerate simulations, numerical schemes, and boundary conditions are addressed. For the case of fused silica as an example, the results of simulations for single- and multiple-pulse irradiation as well as for bi-chromatic laser pulse action will be analyzed in detail.

This work is supported by the Russian Foundation for Basic Research (RFBR project No. 15-01-02432).

Modeling of multi-pulse irradiation of transparent solids based on Maxwell's equations

V.P. Zhukov^{1,2}, N.M. Bulgakova^{3,4}

¹ *Institute of Computational Technologies SB RAS, 6 Lavrentyev Ave., 630090 Novosibirsk, Russia*

² *Novosibirsk State Technical University, 20 Karl Marx ave., 630073, Novosibirsk, Russia*

³ *HiLASE Centre, Institute of Physics ASCR, Za Radnici 828, 25241 Dolní Břežany, Czech Republic*

⁴ *Institute of Thermophysics SB RAS, 1 Lavrentyev Ave., 630090 Novosibirsk, Russia*

zhukov@ict.nsc.ru

Ultrashort laser writing of photonic structures inside optical glasses is a rapidly developing technique for a number of technological applications. To advance this technique, numerical simulations of multi-pulse irradiation is of high demand to better understand and control imprinting of desired structures into glass matrix. Multi-pulse action on the same volume of a glass material triggers a complicated sequence of the processes with creation of memory effects which relate to pulse-to-pulse accumulation of defect states, heat, and stress. Comprehensive modelling of such regimes requires development of sophisticated models which would allow to account for accumulation processes.

In this report, the model based on nonlinear Maxwell's equations supplemented by the hydrodynamics equations for the laser-generated free electrons oscillating in the laser field is applied for a case of multi-pulse irradiation regimes. The results of simulations of propagation of femtosecond laser pulses in fused silica are presented for several pulse energies. It is assumed that the pulse repetition rate is relatively low, of the order or smaller than 1 kHz. This implies that heat dissipation occurs between pulses and the accumulation effect can be attributed to defect states (E'-centers in fused silica). The defect accumulation process can influence on the subsequent pulse absorption dynamics in two ways, by facilitating ionization and by changing the refractive index in the laser-affected zone. The simulations have shown that, depending on the irradiation conditions, the maximum free electron density does not increase or even decreases from pulse to pulse if the refractive index change is not taken into account while the growth of the refractive index can lead to a higher local absorption of the laser energy.

This work is supported by the Russian Foundation for Basic Research (RFBR project No. 15-01-02432).

Spiral Bull's Eye Structure for Multi-frequency High-transmission Plasmonic Antenna

X. Deng¹, S. Oda¹, and Y. Kawano^{1*}

¹Quantum Nanoelectronics Research Center, Department of Physical Electronics, Tokyo Institute of Technology
2-12-1, Ookayama, Meguro-ku, Tokyo 152-8552, Japan

*corresponding author: kawano@pe.titech.ac.jp

Abstract-We built a simulation model and conducted simulation for axial symmetric bull's eye antenna. The structure was proven to have potential in large transmission enhancement and high electric field concentration together with multi-frequency selection. These advantageous features enabled frequency-selective plasmonic antennas and their applications to various investigations.

Plasmons, which is charge oscillations at the interface between a metal and a dielectric, forms an essential part of the nanophotonics field and demonstrated that electromagnetic fields can be confined over dimensions smaller than the wavelength.[1] It can be used to enhance sources and detectors for various applications. However, surface plasmon polaritons (SPP) on a flat interface between a metal and a dielectric cannot be excited directly by incident light source since $\beta > k$, where β is the SPP propagation constant and k is the wave vector of light on the dielectric side. This mismatch can be overcome by several methods, the most commonly used one among those is by patterning the metal surface with grating of grooves or holes with lattice constant a . Then the excitation of SPP strongly depends on the lattice constant of grooves, as expressed by Eq. (1) and Eq. (2)[2]:

$$\beta = k \sin \theta \pm v g \quad (1)$$

$$g = \frac{2\pi}{a} \quad (2)$$

In our previous work, we have present 6 plasmonic antenna structures.[3] The spiral bull's eye antenna can excites SPP with the concentric grooves on its surface and achieve high transmission enhancement together with tunable frequency selection. The groove edges are defined as Eq. (3):

$$r = a \frac{150\pi \times 10^{-6}}{2\pi + \varphi}, 0 < \varphi < \pi, \quad a = 5, 7, 9, 11, 13 \dots \quad (3)$$

It is an extreme case of the split-joint bull's eye structure, and can provide more continuous transmission spectra. A simulation model was built according to the above function, and an FDTD simulation was conducted, as indicated in figure 1 (a), (b). The transmission enhancement coefficient presented in figure 1 (c)-(e) was calculated from the simulation result, showing that the structure is capable of multi-frequency transmission. Those features are expected to make the bull's eye structure a useful tool for multiple frequency applications in sub-wavelength regions, such as security, medicine, food quality inspection, electronics and astro-observation.[4-6]

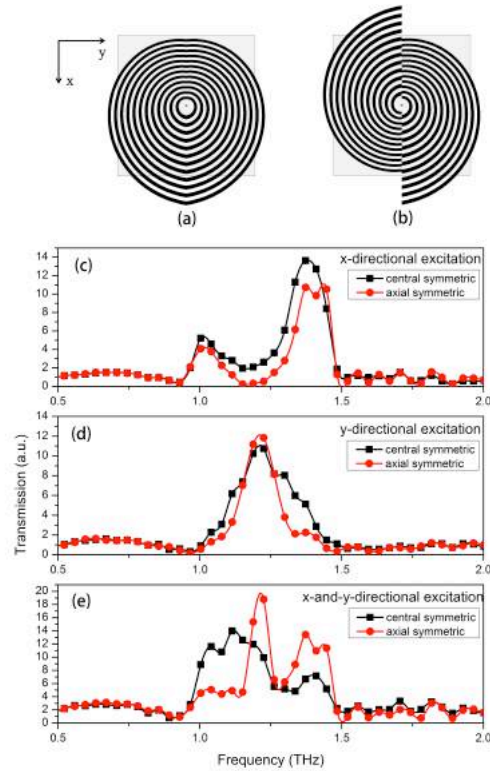


Fig. 1. The structure of (a) the axial symmetric SBE antenna and (b) the central symmetric SBE antenna. The transmission spectra of the SBE antenna when the incident pulse excites surface plasmon along (c) x-axis, (d) y-axis, and (e) both x-axis and y-axis.

Acknowledgements, This work was partly supported by Collaborative Research Based on Industrial Demand and the Center of Innovation Program from the Japan Science and Technology Agency, JSPS KAKENHI Grant Numbers JP26286005, JP16H00798, JP16H00906, JP15K21722, JP16J09937 from Japan Society for the Promotion of Science, and Support for Tokyotech Advanced Researchers (STAR).

REFERENCES

1. R. Stanley, "Plasmonics in the mid-infrared," *Nature Photonics*, Vol. 6, 409–411, 2012.
2. S. Maier, "Plasmonics: Fundamentals and Applications," Springer, pp. 39-47, 2007.
3. X. Deng, S. Oda, and Y. Kawano, "Frequency Selective, High Transmission Spiral Terahertz Plasmonic Antennas," *Journal of Modeling and Simulation of Antennas and Propagation*, Vol. 2, 1–6, 2016.
4. S. Nakajima, H. Hoshina, M. Yamashita, C. Otani, and N. Miyoshi, "Terahertz Imaging Diagnostics of Cancer Tissues with a Chemometrics Technique", *Appl. phys. let.* Vol. 90, No. 4, 041102, Jan. 2007.
5. S. Ariyoshi, C. Otani, A. Dobroiu, H. Sato, K. Kawase, H. M. Shimizu, T. Taino and H. Matsuo, "Terahertz Imaging with a Direct Detector Based on Superconducting Tunnel Junctions" *Appl. Phys. Lett.* Vol. 88, No. 20, pp. 203503, May 2006.
6. C. Kulesa, "Terahertz Spectroscopy for Astronomy: From Comets to Cosmology", *IEEE T. on Terahertz Science and Technology*, Vol. 1, No. 1, pp. 232-240 Sept. 2011.

Simulating the linear and nonlinear response of nanostructures under a focused beam with a B-spline modal method

P. Bouchon¹

¹ONERA, the French Aerospace Lab., Palaiseau 91761 France

*corresponding author: Patrick.bouchon@onera.fr

Abstract- The linear and non linear responses of nanostructures are investigated with the B-spline modal method. The study is depicted for both plane waves and focused beam illumination. The simulation of a focused beam can be used to simulate the real conditions of experiments.

Focusing the light onto nanostructures thanks to spherical lenses is a first step to enhance the field, and is widely used in applications, in particular for enhancing non-linear effects like the second harmonic generation.

Nonetheless, the electromagnetic response of such nanostructures, which have subwavelength patterns, to a focused beam can not be described by the simple ray tracing formalism. Here, we present a method to compute the response to a focused beam, based on the B-spline modal method, which is known to be fast thanks to a non-uniform mesh and sparse matrices. The eigenmodes are computed in each layer for both polarizations in conical mounting, and are then combined for the computation of scattering matrices. The simulation of a gaussian focused beam is obtained thanks to a truncated decomposition on plane waves computed on a single period, which limits the computation burden.

Eventually, we develop a formalism to compute the second harmonic field under the undepleted pump approximation. The nonlinear polarization induced by a fundamental plane wave or a focused beam generates a source term at the doubled frequency. The latter is divided into a finite number of sub-sources and the second harmonic field is subsequently computed by integration of these sub-sources contributions.

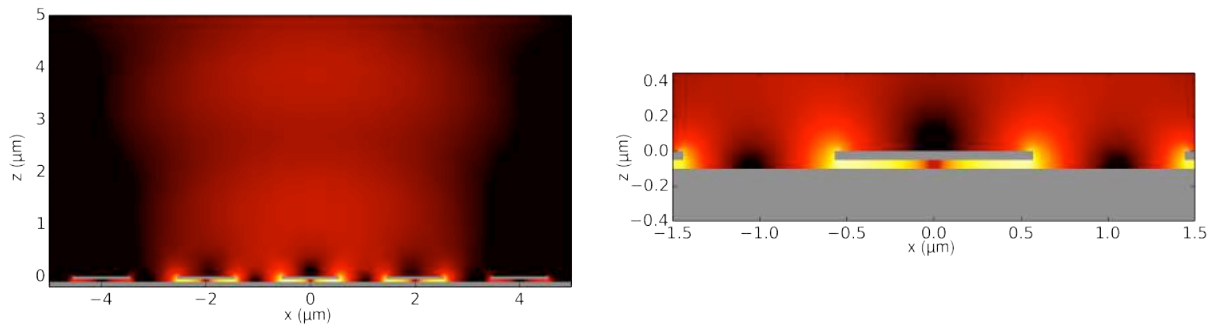


Figure 1: Metal-insulator-metal resonators array under a focused beam at the resonance wavelength. The beam is impinging on mainly three resonators of the array.

REFERENCES

1. Bouchon, P., F. Pardo, R. Haïdar, and J.L. Pelouard, “Fast modal method for subwavelength gratings based on B-spline formulation,” *Journal of the Optical Society of America A*, Vol. 27, No. 4, 696–702, 2010.

2. Chevalier P., P. Bouchon, F. Pardo, and R. Haïdar, "Electromagnetic modelization of spherical focusing on a one-dimensional grating thanks to a conical B-spline modal method," *Journal of the Optical Society of America A*, Vol. 31, No. 8, 1692–1697, 2014.
3. Héron S., F. Pardo, P. Bouchon, J.L. Pelouard, and R. Haïdar, "Modal method for second harmonic generation in nanostructures," *Journal of the Optical Society of America B*, Vol. 32, No. 2, 275–280, 2015.

Graphene Electromagnetics from Modelling to Applications

X. Zhang¹, X. Huang¹, T. Leng¹, K. Pan¹, Habiba Ouslimani² and Z. Hu^{1*}

¹School of Electrical and Electronic Engineering, University of Manchester, Manchester, United Kingdom

² Université Paris Ouest Nanterre La Défense, IUT 50, rue de Sèvres, Ville d'Avray, France

z.hu@manchester.ac.uk

Abstract-Graphene electromagnetic simulation, device design, fabrication and analysis from RF to microwave are presented. Both exfoliated and Chemical Vapor Deposited (CVD) graphene are studied and used to fabricate transmission lines and resonators. Raman spectroscopy has been adopted to confirm the layer number of graphene. In addition, printed graphene nano-flakes ink enabled RF/microwave devices such as radar absorber have been studied numerically and verified experimentally.

Graphene is a two-dimensional (2D) planar layer of carbon atoms packed in a honeycomb lattice. It has been drawing a great attention from both research institutes and industry due to its potential applications since it was firstly peeled from graphite in 2004. Due to the unique chemical, thermal, mechanical, electronic and optical properties of graphene, many studies on its application for RF, microwave/millimeter-wave and THz devices and circuits have been reported [1-6]. However, work on the application of graphene in the RF/microwave components is still in its infancy.

In this contribution, monolayer graphene as well as printed graphene devices are numerically studied, designed, fabricated and characterized.

Acknowledgements, This work was partially funded by the Engineering and Physical Sciences Research Council (EPSRC), UK under EPN/010345/1.

REFERENCES

1. J. S. Moon, H. C. Seo, M. Antcliff, D. Le, C. McGuire, A. Schmitz, L. O. Nyakiti, D. K. Gaskill, P. M. Campbell, K. M. Lee, and P. Asbeck, "Graphene FETs for zero-bias linear resistive FET mixers," *IEEE Electron Device Lett.*, vol. 34, no.3, pp. 465-468, Mar. 2013.
2. Leng, T.; Huang, X.; Chang, K.; Chen, J.; Abdalla, M.A.; Hu, Z., "Graphene Nanoflakes Printed Flexible Meandered Line Dipole Antenna on Paper Substrate for Low Cost RFID and Sensing Applications," *IEEE Antennas and Wireless Propagation Letters*, , no.99, pp.1-1 .
3. X. Huang, T. Leng, X. Zhang, J. Chen, K. Chang, A. Geim, K. Novoselov and Z. Hu, "Binder-free highly conductive graphene laminate for low cost printed radio frequency applications", *Appl. Phys. Lett.*, vol. 106, no. 20, p. 203105, 2015.
4. X. Huang, T. Leng, M. Zhu, X. Zhang, J. Chen, K. Chang, M. Aqeeli, A. Geim, K. Novoselov and Z. Hu, "Highly Flexible and Conductive Printed Graphene for Wireless Wearable Communications Applications", *Sci. Rep.*, vol. 5, p. 18298, 2015.

5. Xianjun Huang, Ting Leng, Kuo Hsin Chang, Jia Cing Chen, Kostya S Novoselov and Zhirun Hu, 'Graphene Radio Frequency and Microwave Passive Components for Low Cost Wearable Electronics', *2D Mater.* 3(2016)025021.
6. Xianjun Huang, Kewen Pan and Zhirun Hu, 'Experimental Demonstration of Printed Graphene Nano-flakes Enabled Flexible and Conformable Wideband Radar Absorbers', *Sci. Rep.* 6, 38197, 2016.

Modeling linear and nonlinear optical wave dynamics in nanophotonic devices

Qiang Lin¹

¹Department of Electrical and Computer Engineering, University of Rochester, Rochester, NY 14627, USA
qiang.lin@rochester.edu

Abstract— In this talk, we will discuss our recent progress in modeling linear and nonlinear optical wave dynamics in micro/nanophotonic waveguides and resonators, and compare them with experimental characterization. We will discuss some open challenges in current numerical modeling techniques.

Micro/Nanophotonic devices offer excellent platforms for studying a variety of linear and nonlinear optical phenomena and for realizing novel functionalities that are otherwise difficult to achieve. On one hand, optical functionalities rely crucially on specific device properties (geometry, dispersion, optical, mechanical, electrical, etc.) which requires intensive numeric modeling. On the other hand, understanding intriguing physical phenomena in the devices requires intuitive physical modeling to reveal the essential underlying physical mechanism.

In this talk, we will discuss in detail our recent effort in device modeling to achieve multi-octave spanning dispersion engineering [1], to introduce a novel mechanism, namely multi-color cavity soliton generation, for ultra-broadband phase-locked Kerr frequency comb generation [2], in understanding complex nonlinear optical dynamics in high-quality microresonators [3], and in exploring the fundamental thermo-optic noises of microresonators in the nonlinear regime [4]. We will compare our theoretical modeling with some experimental characterizations. We will also discuss some open challenges in current numerical modeling techniques for micro/nanophotonic device design.

This work is supported in part by NSF under grants numbers ECCS-1509749 and ECCS-1610674 and by the DARPA SCOUT program through grant number W31P4Q-15-1-0007 from AMRDEC.

REFERENCES

1. H. Liang, Y. He, R. Luo, and Q. Lin, Opt. Express **24**, 29444 (2016).
2. R. Luo, H. Liang, and Q. Lin, Opt. Express **24**, 16777 (2016).
3. H. Liang, W. C. Jiang, X. B. Sun, X.-C. Zhang, and Q. Lin, Proc. CLEO/QELS 2017, STu1E.4 (2016).
4. X. Sun, R. Luo, X.-C. Zhang, and Q. Lin, Phys. Rev. A **95**, 023822 (2017).

Femtosecond laser induced dynamics of the processes in transparent solids: Insights from Maxwell's-based model

N. M. Bulgakova^{1*} and V. P. Zhukov^{2,3}

¹HiLASE Centre, Institute of Physics ASCR, Za Radnici 828, 25241 Dolní Břežany, Czech Republic

²Institute of Computational Technologies SB RAS, 6 Lavrentyev Ave., 630090 Novosibirsk, Russia

³Novosibirsk State Technical University, 20 Karl Marx ave., 630073, Novosibirsk, Russia

*corresponding author: bulgakova@fzu.cz

Abstract—Based on Maxwell's equations supplemented by the hydrodynamics-type equations for laser-generated free-electron plasma, the processes inside transparent materials induced by ultrashort laser pulses have been studied for the regimes of irradiation typical for direct laser writing of photonic structures. Simulations have been performed for fused silica irradiated by laser beams with linear and radial polarization. Effects of spatiotemporal features of laser beams and pump-probe irradiation on laser energy deposition are also analyzed. Post-irradiation evolution of material is discussed.

Interaction of ultrashort laser pulses with transparent materials is a powerful technique of modification of material properties for various scientific and technological applications. The physics behind the laser-induced modification phenomenon is rich and still far from complete understanding. There are no experimental diagnostics with enough resolution to directly follow the complexity of laser-triggered processes inside transparent materials at femtosecond timescales and nanometer spatial scales. Only indirect techniques are available that give valuable but incomplete information that must be analyzed and properly understood. In such circumstances, theory and computer simulations based on full Maxwell's equations [1-6] are important means for advancing laser writing techniques via determining and controlling the spatiotemporal dynamics of material restructuring into a desired final structure.

We present an overview of our modeling results on interaction of ultrashort laser pulses with fused silica glass in the regimes of volumetric modification by linearly and radially polarized laser beams. It has been found that, for Gaussian pulses focused inside glass at numerical aperture < 0.3 , the maxima of laser intensity, free electron density, and absorbed laser energy density do not considerably change with the beam energy (intensity clamping effect). At pulse energies of $200 \text{ nJ} - 2 \text{ }\mu\text{J}$, the free electron density in the laser-excited region remains subcritical while the locally absorbed energy density does not exceed $\sim 4000 \text{ J/cm}^3$. Increasing pulse energy results mainly in increased laser-excited volume. The effect of increasing the numerical aperture on the laser energy deposition is studied. Double-pulse irradiation has been modeled to gain insight into experimentally observed “exciton-seeded multiphoton ionization” [7]. For such regimes, formation of a defect-states shield has been uncovered (Fig. 1), which has to be characteristic of multipulse irradiation of glass materials. Asymmetry of light absorption for the cylindrically-symmetric linearly-polarized beams has been revealed.

For radially polarized laser pulses, an intriguing dynamics of the laser beam collapsing toward the axis has been observed, which results in generation of overcritical electron densities and overcoming the intensity clamping effect. The resulting tube-like shape of the deposited energy should lead to implosion of material that can be used for improving the direct writing of high-refractive index optical structures inside glasses.

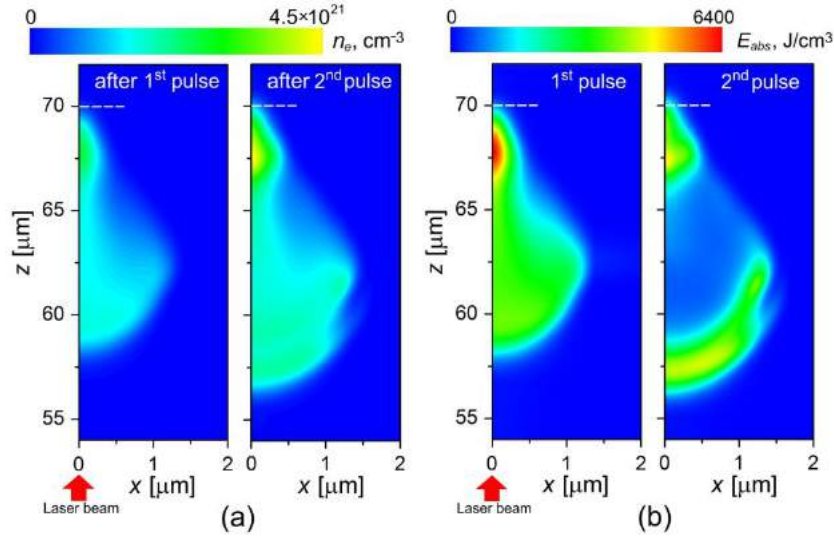


Figure 1. Simulation results on laser beam focusing inside fused silica in double pulse irradiation regime with equal energies of two pulses. (a) Free electron density distributions immediately after pump and probe laser pulse action. (b) Corresponding distributions of the adsorbed laser energy. Irradiation parameters: pulse duration of 150 fs; energy of 200 nJ in each pulse; NA = 0.4; time separation between pulses of 1-3 ps. Geometrical focus is located at 70 μm beneath sample surface.

Acknowledgements. N.M.B. acknowledges the support from the European Regional Development Fund and the state budget of the Czech Republic (project BIATRI: Grant No. CZ.02.1.01/0.0/0.0/15_003/0000445) and from the Ministry of Education, Youth and Sports of the Czech Republic (Programs NPU I Project No. LO1602, and Large Research Infrastructure Project No. LM2015086). The work of V.P.Z. was supported by the Russian Foundation for Basic Research (Project No. 15-01-02432).

REFERENCES

1. Popov, K. I., C. McElcheran, K. Briggs, S. Mack, and L. Ramunno, "Morphology of femtosecond laser modification of bulk dielectrics," *Opt. Express*, Vol. 19, No. 1, 271-282, 2011.
2. Schmitz H. and V. Mezentsev, "Full-vectorial modeling of femtosecond pulses for laser inscription of photonic structures," *J. Opt. Soc. Am. B*, Vol. 29, No. 6, 1208-1217, 2012.
3. Bulgakova, N.M., V. P. Zhukov, Yu. P. Meshcheryakov, "Theoretical treatments of ultrashort pulse laser processing of transparent materials: Towards understanding the volume nanograting formation and "quill" writing effect," *Appl. Phys. B*, Vol. 113, No. 3, 437-449, 2013.
4. Buschlinger, R., S. Nolte and U. Peschel, "Self-organized pattern formation in laser-induced multiphoton ionization," *Phys. Rev. B*, Vol. 89, No. 18, 184306, 2014.
5. Bulgakova, N. M., V. P. Zhukov, S. V. Sonina and Y.P. Meshcheryakov, "Modification of transparent materials with ultrashort laser pulses: What is energetically and mechanically meaningful?" *J. Appl. Phys.*, Vol. 118, No. 23, 233108, 2015.
6. Rudenko, A., J.-P. Colombier and T. E. Itina, "From random inhomogeneities to periodic nanostructures induced in bulk silica by ultrashort laser," *Phys. Rev. B*, Vol. 93, No. 7, 1064-1076, 2016.
7. Grojo, D., M. Gertsvolf, S. Lei, T. Barillot, D. M. Rayner and P. B. Corkum, "Exciton-seeded multiphoton ionization in bulk SiO_2 ," *Phys. Rev. B*, Vol. 81, No. 21, 212301, 2010.

Adjoint Sensitivity of Nonlinear Structures Using the FDTD Method

M. M. T. Maghrabi¹, M.H. Bakr^{1*}, S. Kumar¹, A. Elsherbeni², and V. Demir³

¹ McMaster University, Hamilton, Ontario, Canada

² Colorado School of Mines, Golden, Colorado, USA

³ Northern Illinois University, Dekalb, Illinois, USA

*mbakr@mcmaster.ca

Abstract—We present a novel finite-difference time-domain (FDTD)-based algorithm for adjoint sensitivity analysis of nonlinear electromagnetic (EM) structures. Using only one extra FDTD simulation, our approach estimates the sensitivities of the desired objective function or response with respect to all design parameters of the problem. The validity and efficiency of the proposed approach is illustrated here through a one-dimensional (1D) EM example.

Adjoint sensitivity analysis (ASA) approach is an alternative to the computationally expensive classical finite-differences approaches. It estimates the sensitivities of a general objective function or response with respect to all design parameters using at most one extra system simulation [1]. This ASA approach was developed for EM structures with nonlinear materials using the transmission line matrix (TLM) method [2]. It was also developed using the FDTD method [3]. Recently, a simpler FDTD-based ASA approach, derived from Maxwell's equations rather than the wave equation, has been reported [4]. However, all existing FDTD-based approaches are limited for estimating the sensitivities of EM problems with only linear materials.

In this paper, we extend the ASA approach presented in [4] to general EM problems with nonlinear materials. Using the FDTD method, the electromagnetic simulation can be formed as [4]:

$$\begin{bmatrix} \boldsymbol{\varepsilon} & \mathbf{0} \\ \mathbf{0} & -\boldsymbol{\mu} \end{bmatrix} \begin{bmatrix} \dot{\mathbf{E}} \\ \dot{\mathbf{H}} \end{bmatrix} + \begin{bmatrix} \boldsymbol{\sigma}_e & \mathbf{0} \\ \mathbf{0} & -\boldsymbol{\sigma}_m \end{bmatrix} \begin{bmatrix} \mathbf{E} \\ \mathbf{H} \end{bmatrix} + \mathbf{K}_c \begin{bmatrix} \mathbf{E} \\ \mathbf{H} \end{bmatrix} = \begin{bmatrix} -\mathbf{J}_e \\ \mathbf{J}_m \end{bmatrix}, \quad (1)$$

where \mathbf{E} and \mathbf{H} are the vectors representing the electric and magnetic fields over the whole computational domain, respectively, and “ $\dot{}$ ” denotes the first-order time derivative. \mathbf{J}_e and \mathbf{J}_m represent the electric and magnetic current density sources existing in the entire domain. The block diagonal matrices $\boldsymbol{\varepsilon}$, $\boldsymbol{\mu}$, $\boldsymbol{\sigma}_e$, $\boldsymbol{\sigma}_m$ represent the constitutive parameters of the materials at all spatial cells of the computational domain. Unlike the linear case, these constitutive parameters are nonlinear functions of the corresponding electric or magnetic field. For example, the nonlinearity dependence of permittivity can be represented as: $\varepsilon = C_0 + C_1 E + C_2 E^2$, where E is the local electric field. It can be shown that the adjoint simulation corresponding to (1) is given by:

$$\begin{bmatrix} \boldsymbol{\varepsilon} & \mathbf{0} \\ \mathbf{0} & -\boldsymbol{\mu} \end{bmatrix} \begin{bmatrix} \dot{\boldsymbol{\lambda}}_E \\ \dot{\boldsymbol{\lambda}}_H \end{bmatrix} + \begin{bmatrix} \boldsymbol{\sigma}_e + \frac{\partial \psi}{\partial \mathbf{E}} \mathbf{E} & \mathbf{0} \\ \mathbf{0} & -\boldsymbol{\sigma}_m - \frac{\partial \psi}{\partial \mathbf{H}} \mathbf{H} \end{bmatrix} \begin{bmatrix} \boldsymbol{\lambda}_E \\ \boldsymbol{\lambda}_H \end{bmatrix} + \mathbf{K}_c \begin{bmatrix} \boldsymbol{\lambda}_E \\ \boldsymbol{\lambda}_H \end{bmatrix} = \begin{bmatrix} -\frac{\partial \psi(T_m - t)}{\partial \mathbf{E}} \\ \frac{\partial \psi(T_m - t)}{\partial \mathbf{H}} \end{bmatrix}, \quad (2)$$

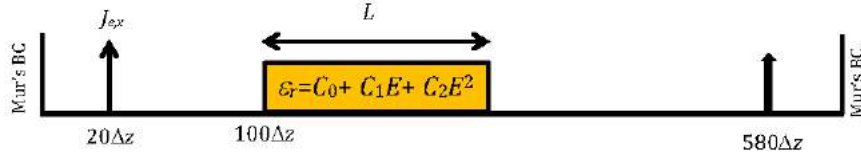


Fig. 1. The domain of the considered nonlinear dielectric slab example.

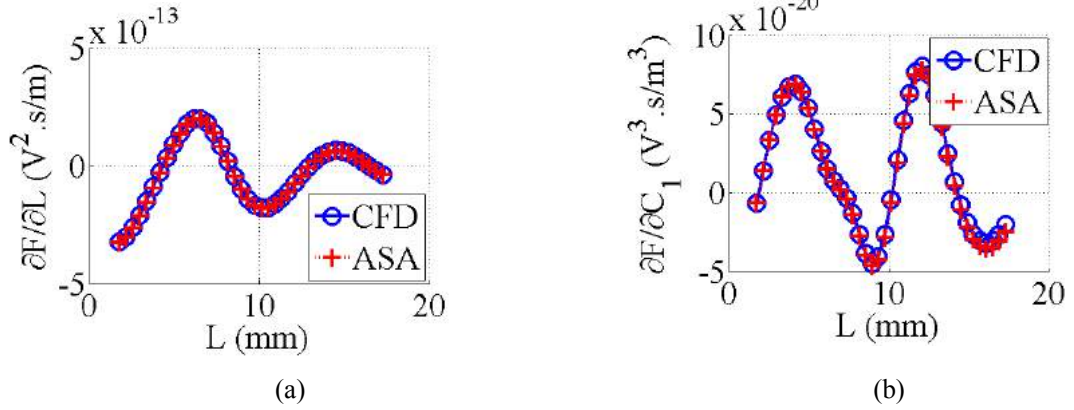


Fig. 2. The sensitivity of the objective function with respect to (a) the dielectric length L , and (b) the parameter C_1 , for a sweep of the parameter L , as compared with the more expensive central finite difference approach.

where the excitation in the right hand side of (2) is determined using the considered response or objective function. Once the temporal original and adjoint fields are determined using (1) and (2), the sensitivities of the response under consideration with respect to all design parameters are estimated.

To illustrate our algorithm, we consider the 1D nonlinear dielectric slab shown in Fig. 1. The dielectric constant at every cell in the slab is given by $\epsilon = 3 + 50E + 100E^2$. The slab is lossy with a constant electric conductivity $\sigma_e = 0.04$. The computational domain has a length of $600\Delta z$, where the utilized discretization is $\Delta z = 0.5$ mm. We allow for maximum simulation time $T_m = 12,000\Delta t$, where $\Delta t = \Delta z/c$, where c is the velocity of light. The domain is excited with a Gaussian-modulated electric current density source at $z = 20\Delta z$, whose center frequency and bandwidth are 10 GHz and 8 GHz, respectively. Mur's boundary conditions are used to terminate the computational domain. The objective function is the average energy measured at $z = 580\Delta z$. Fig. 2 shows the sensitivities of the objective function with respect to the dielectric length L and the parameter C_1 , for a sweep of the parameter L . Good match is achieved with central finite differences (CFD) for all parameters.

REFERENCES

1. M. H. Bakr and N. K. Nikolova, "An Adjoint variable method for time domain TLM with fixed structured grids," *IEEE Trans. Microwave Theory Tech.*, vol. 52, pp. 554-559, 2004.
2. M. H. Bakr, O. S. Ahmed, M. H. El Sherif, and T. Nomura, "Time domain adjoint sensitivity analysis of electromagnetic problems with nonlinear media," *Optics Express*, vol. 22, no. 9, pp. 10831-10843, 2014.
3. M. A. Swillam, M. H. Bakr, N. K. Nikolova, and X. Li, "Adjoint sensitivity analysis of dielectric discontinuities using FDTD," *Journal of Electromagnetics*, vol. 27, pp. 123-140, 2007.
4. M. H. Bakr, A. Elsherbeini, and V. Demir, "An FDTD-based adjoint sensitivity approach," *Proceedings of the IEEE Antenna and Propagation Symposium (APS 2016)*, Puerto Rico, June 2016.

Imaging of photogenerated electron dynamics on a semiconductor surface

Keiki Fukumoto¹, and Shin-ya Koshihara²

¹High Energy Accelerator Research Organization (KEK), Japan

²Tokyo Institute of Technology, Japan

keiki@post.kek.jp

Abstract— We have developed and optimized a system for time-resolved photoemission electron microscopy (TR-PEEM) conducted with femtosecond laser pulses to visualize the electron dynamics with time, space and energy resolutions. In this contribution, we introduce the details of the equipment and present recent results obtained by application of the system on to nano-structures, such as surface defects, Si quantum dots, and graphene.

We developed a system for time-resolved photoemission electron microscopy with femtosecond laser pulses (TR-PEEM) to visualize the dynamics of photo-excited states of matters. By using a repetition rate variable laser system and by the development of the energy tuning system in the UV range, the photogenerated electron dynamics on semiconductor surfaces was successfully observed with time, space, and energy resolutions of 100 fs, 50 nm, and 40 meV, respectively. To date, the estimation of the drift velocity and the mobility by directly imaging the propagation of electron bunches on a semiconductor surface [1], and the different relaxation and recombination times in randomly distributed surface defects on a semiconductor surface [2, 3] have been observed. By combination with other microscopic techniques, we have observed the relation between electron dynamics and nano-scale structures such as graphene [4] and semiconductor quantum dots [5].

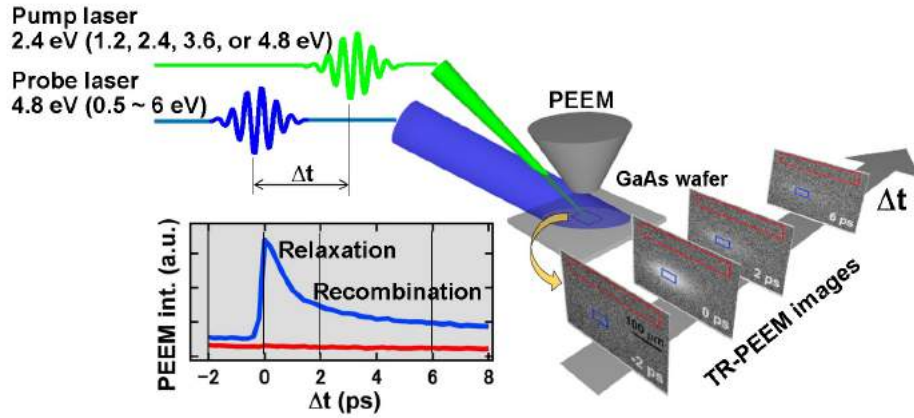


Figure 1: Demonstration of the observation of photogenerated electron dynamics with time and space resolutions by TR-PEEM. The sample was a GaAs wafer. The blue and red curves in the graph show the temporal evolution of the PEEM intensity in the blue (pumped) and red (unpumped) regions in a series of TR-PEEM images.

Figure 1 shows a demonstration of spatio-temporal resolved experiments for the photogenerated electron dynamics on a GaAs surface. The pump laser pulses with the energy of 2.4 eV excite electrons into the conduction band. Spatial distribution of photogenerated electrons are imaged by the probe pulses with 4.8 eV as locally different photoemission intensity. A series of TR-PEEM images with different pump and probe delay times (Δt) are shown in the figure. Time evolution of the photoemission intensity in the blue (pumped) and red (unpumped) regions in the TR-PEEM images are plotted in the graph.

By developing the energy tuning system in the UV range, local ionization energy (or workfunction) was allowed to be observed. Figure 2 is an estimation of the workfunction on a SiO_2/Si

surface. PEEM images were obtained with different photon energy of the excitation source from 4 to 5.2 eV with approximately 40 meV step. The photoemission intensity from each PEEM image is plotted in the figure. The estimated workfunction of approximately 5 eV was in consistent with the reported values.

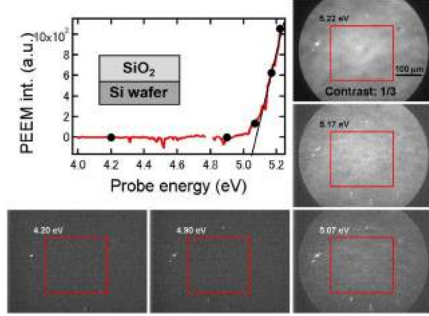


Figure 2: Estimation of workfunction on a SiO₂/Si surface.

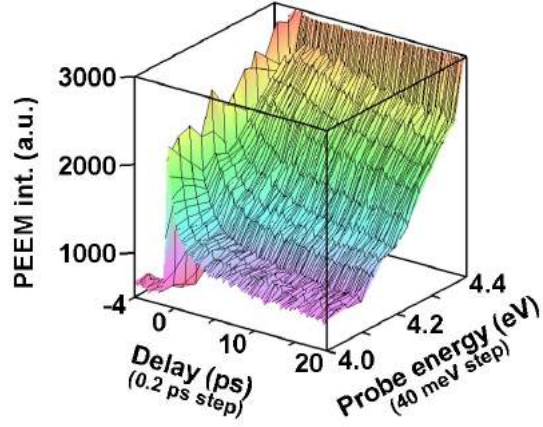


Figure 3: time, space, and energy resolved experiments on a GaAs surface. PEEM intensity is plotted with Δt and probe energy.

In Figure 3, the temporal evolutions of photogenerated electron density (lifetimes) with different probe energies are presented, where the probe energy was scanned from 4.0 to 4.4 eV with 40 meV step and the pump energy was 2.4 eV. In the case with the probe energy of 4.0 eV, the faster decay in a few ps originate from energy relaxation of photogenerated electrons and the slower decay on the order of 10 ps of recombination have been observed. By increasing the probe energy up to the ionization energy (4.4 eV), the signal from photogenerated electrons increased. We found that by optimization of the probe energy at around the workfunction, photoemission was induced only from the photogenerated electrons, but not from the electrons trapped on the impurity states which did not contribute the electron dynamics. This results the suppression of the sample charging and increasing the signal to noise ratio.

ACKNOWLEDGMENT

We gratefully acknowledge support from “Revolution of the opto-electronic materials design by direct probing of the electron dynamics with nanometer and femtosecond spatio-temporal resolution”, ACCEL Feasibility Studies, KAKENHI (15K17677) and the CREST project by Japan Science and Technology Agency (JST)

REFERENCES

1. Fukumoto, K, *et al.*, “Direct imaging of electron recombination and transport on a semiconductor surface by femtosecond time-resolved photoemission electron microscopy,” *Appl. Phys. Lett.*, Vol. 104, 053117–053121, 2014.
2. Fukumoto, K, *et al.*, “Femtosecond time-resolved photoemission electron microscopy for spatiotemporal imaging of photogenerated carrier dynamics in semiconductors,” *Rev. Sci. Instrum.*, Vol. 85, 083705–083710, 2014.
3. Fukumoto, K, *et al.*, “Direct imaging of electron recombination and transport on a semiconductor surface by femtosecond time-resolved photoemission electron microscopy,” *Appl. Phys. Exp.*, Vol. 8, 101201–101204, 2015.
4. Invited talk on the 4th Advanced Electromagnetics Symposium (2016)
5. *preparation for submission*

Absorption and Transmission of Electromagnetic Radiation from a Maxwellian Plasma Slab

M. S. Bawa'aneh^{1*}, YC. Ghim², and Ahmed M. Al-Khateeb¹

¹Department of Physics, Yarmouk University, Irbid, Jordan

²Department of Nuclear Engineering, KAIST, Daejeon, Republic of Korea

*corresponding author: msbawaaneh@yu.edu.jo

Abstract- The problem of reflection and transmission of electromagnetic radiation from plasma has attracted many researchers for decades because of its wide range of applications in telecommunications, stealth technology and industry. In this work, we investigate the problem of reflection and transmission from Maxwellian plasma, where the dielectric function of the plasma is obtained by calculating the Fried - Conte plasma dispersion function numerically for a given set of plasma parameters.

Two configurations for a Maxwellian plasma slab will be considered; the first configuration will be a plasma slab surrounded by vacuum and the second one will be a plasma slab sandwiched between vacuum on the left and a semi-infinite conductor on the right. In both cases we have three slabs with the plasma being the middle slab with thickness d sandwiched between two semi-infinite media. Reflection (R) and transmission (Tr) coefficients from the two configurations will be obtained numerically and compared together.

For a plasma slab in vacuum, reflectance and transmittance vs wavelength curves show peaks of a periodic (standing wave) pattern with minima occurring at frequency values where the wavelength matches with the width of the plasma slab according to the equation $d = m(\lambda/2)$, d is the width of the plasma slab and m is a positive integer. For a plasma slab sandwiched between vacuum and a semi-infinite conductor, the periodic pattern still exists and the metallic wall on the right of the plasma slab reflects the most part of the wave and reflectance is very close to one; a very small part of the wave is transmitted to the metal that should be absorbed within a small depth inside the metal.

Acknowledgement, YCG was supported by the KUSTAR-KAIST Institute throughout this work.

Motion and the Fourth Dimension

S. L. Vesely¹, A. A. Vesely², S. R. Dolci³ C. A. Dolci⁴

¹ITB-CNR, Milan, Italy

²Via L. Anelli, 13 Milan, Italy

³Via Sant'Orsola, 11 Milan, Italy

⁴Politecnico di Milano, Italy

*corresponding author, E-mail: sara.vesely@cnr.it

Abstract

From an engineering point of view no substantial difference between analytical and numerical approaches is usually admitted. Accordingly, the primary goal of computer solutions of field problems consists in getting numerical answers, and in producing accurate numbers easily. Still, unlike Newtonian trajectories, which describe curves as functions of time in a space, that is deemed to be Euclidean, the electromagnetic field is a function of space and time, taken as variables on a par with each other. Electromagnetic field solvers for advanced applications attempt to reduce dimensions by taking care of the relationship among space-time variables, and will possibly end up by requiring reasoning in a Cartesian geometry of four dimensions or more at the outset. Moreover, the question if and how those four independent variables could give rise to pictorial representations of the field has not been addressed, despite the impact such representations of the field would have on the general understanding of electromagnetism. The recent advances in rendering suggest that the analytical approach could be revised, and that perhaps geometrically rooted visual elements and graphic displays should be favored in electromagnetism over purely numerical answers. After recalling dynamical and optical approaches to the fourth dimension for the purpose of graphical rendition and modeling, we focus on the type of reduction from four to three dimensions attainable through projective transformations.

1. Introduction

Modern physical field theories no longer require adherence to a visual spatial display of phenomena. They take for granted the conceptual framework of the special relativity theory, and regard the geometric representation as accomplished within algebra. Moreover, they consider symmetries to better express the deep features of the physical world, and deal with space-time symmetries of electromagnetic fields by linking them to conservation laws as well as to interactions with matter through Noether's theorems. As a result, notwithstanding the fact that computational electromagnetics faces real-world problems at the cutting edge of technology, solving Maxwell's equations keeps some cumbersome traits both graphically and conceptually. The laws link together the variations of four elusive field quantities (E, B, D, H), which are functions of

four independent continuous parameters (x, y, z, t) . Time domain solvers interpret the parameters as geometric space and time, (\mathbf{r}, t) , by analogy with mechanics. Full wave simulators and planar tools alike, suppose t to vary so as to ensure that fields can be represented point by point at each fixed time. For example, in applications to plasmonics it is told that traditional 3D methods have the advantage over a 4D method of allowing profiting from the Fourier transform. Each geometric point corresponds to a determinate value of each field at the time given, like force fields in statics. However, if fields' variation with t must be taken care of, the meaning given to the fields under static assumptions can be no longer preserved, and the uneasiness of intuitive geometric notions is fully exacerbated by the unfathomable relationship between a space with the same cardinality as \mathbb{R}^4 and the so called physical space.

Computational electromagnetics covers two main areas. On the one hand, it substitutes for closed form solutions to Maxwell's equations, taking care of robustness and stability, and compares simulations with specific instance measurements, in order to better either the instance or the computation. On the other hand, computer-aided modeling contributes warranting theoretically predicted effects, and interpreting experimentally both acquired and simulated patterns.[1, 2]

As to computational geometry, by now, it doesn't lend itself to any alternative approaches, as it tends to be a reshaping of algorithmic computation methods. Although geometric algorithms, involving complex objects at the software level, which must be organized as data structures, have evolved, it is known that theorems are scarcely relevant for the computational geometric description of shapes. Therefore, special symmetries, such as rotational, cylindrical, periodic, or with respect to one or several planes are put to use in reducing computation time. Mathematical visualization of functions on a computer screen, an application of computational geometry, is considered akin to analytic geometry. When the latter was adapted to the number system, it was stated that the intuitive linear continuum of geometry is order-isomorphic to real numbers. However, since Dedekind freed the theory of numbers from the influences of geometry, which is quite upstream of computer graphics, analytic geometry became a way of illustrating the properties of numbers, and can fail on the terrain of geometric

constructions, as a fallout of the discrete origin of numeral systems.[3] The increasing mismatches between geometric input at the graphic level and computational geometry seems to justify the belief that optical circuitry, a merging of electronics with optics, may substitute for continuous media.

We think that, if there is a more effective way to geometrically model electromagnetism, that geometry has to first be elaborated “by hand”. Resuming the differences between different types of synthetic geometries can suggest new algorithms and break new ground in computational geometry. In this article we shall pick up a couple of aspects that are faced when trying to visually represent functions of four parameters.

2. The birth of the 4th dimension in mechanics

Traditionally, mechanics is not concerned with models of space. A Euclidean three-dimensional space E^3 is assumed, with material objects having the possibility to move through it. Time t is taken as a one-dimensional thread, so as to suit the concept of cause and effect. Newtonian kinematics is a description of the states of motion relative to a reference frame, rather than a representation of E^3 itself. For example, in point mass mechanics relative motion is represented by $\mathbf{v} = \frac{d\mathbf{r}(t)}{dt}$. In E^3 , the function $\mathbf{r}(t) = x(t)\mathbf{i} + y(t)\mathbf{j} + z(t)\mathbf{k}$ with arbitrarily prescribed initial conditions $\mathbf{r}(0) = \mathbf{r}_0$, $\mathbf{v}(0) = \mathbf{v}_0$ describes a trajectory. The branch of dynamics leaves aside both \mathbf{r} and \mathbf{v} , and accounts for the evolution of motion subjected to forces like $\mathbf{F} = m\frac{d\mathbf{v}}{dt}$.

Shortly after the groundbreaking work of d’Alembert, Lagrange took up the problem of exploiting the laws of force. He identified the geometric branch of analytical mechanics —kinematics— as analytic geometry. To describe the configurations of a given dynamical system, he availed himself of so called free coordinates q , which are independent generalized coordinates. Unlike Newtonian mechanics, the velocities \dot{q} contemplated by Lagrange are related to the q through the principle of virtual work: the system can perform *all* the displacements $\dot{q}\delta t$ compatible with the imposed constraints. A state of motion and the circumstances under which it takes place are further characterized by a Lagrangian function $L(q, \dot{q}) = T - V$, where $V(q)$ is the potential, and T is the kinetic energy of the system. The Lagrangian allowing to obtain the Euler-Lagrange equations of motion of the system is derived by making the action integral with fixed end points $S = \int L dq$ stationary. For an unconstrained point mass $E = \frac{1}{2}m\dot{q}^2 + V(q)$ is the total energy, and thus its speed is $\dot{q} = \sqrt{\frac{2}{m}(E - V)}$. Minimizing the Lagrangian one can recover Newtonian trajectories. Let’s emphasize again that the terms $\dot{q}\delta t$ are neither directly linked to the trajectory of the moving point mass, say to a translation/rotation in E^3 , like Newton’s $\mathbf{v}dt$, nor are linked to translational/rotational symmetry, but rather are linked to the Lagrangian and to the variational procedure for

obtaining the equations of motion. On a locally Euclidean Riemann manifold M , the Euler-Lagrange equations of a point mass can be so parametrized that the tangent vectors to affine geodesics are parallel transported. Yet, differentiability of the manifold already presupposes some added dynamical structure, e.g., that the dynamical space of states is canonically diffeomorphic to the tangent bundle. When dealing with systems of N point masses, the configuration space is likewise a Riemann manifold Q . However, the equivalence among configurations is even more clearly unrelated to geometrical properties. The manifold depends on $q \leq 3N$ free coordinates, and is supposed to be isometrically embeddable in E^q . Again, for physical reasons the velocity coordinates may be assumed to be tangent to the configuration space at every point, i.e. they belong to the tangent bundle TQ .

To be sure, in Lagrange’s time our space was supposed to be at most 3D, and the compatible configurations were not framed according to symmetry, but rather according to data. Nevertheless, kinematics is where the concept of 4th dimension originates from. Anticipating events, in 1754 D’Alembert mentioned t as a variable amenable to a geometric interpretation on a par with \mathbf{r} . [4] A short account of how kinematics was promoted to a 4D geometry is given by S. in 1885. By analogy with Flatland, a fictional two-dimensional world where 3D objects can only be experienced as sections, the fourth dimension is conceived as a film of the sections of a higher dimensional space passing across the space we live in. [5] The problem of how to experience the fourth dimension was posed insistently, especially in connection with electric phenomena, about the end of 1800. Even if nowadays equivalent configurations are dubbed symmetries without further ado, symmetry principles entered physics much later, in concomitance with spectral transitions and selection rules in quantum mechanics. Going back to classical physics, Maxwell linked his theory to Faraday’s experiments, to the effect that after him correspondence to real-world electromagnetic problems was retained, and nowadays many partial solutions from static fields to optics match experiments. Yet, correspondence with spatial representations was lost. As a matter of fact, the solutions to Maxwell’s equations are fields rather than trajectories in E^3 . In the Lagrangian specification, the mathematical quantity $(\mathbf{E}, \mathbf{B}, \mathbf{D}, \mathbf{H})$ isn’t even nearly posed in concurrence with the ideas of space and time. Rather, the field is handled as a system with an infinite number of degrees of freedom, with the aim of tracing electromagnetism back to analytical mechanics. The infinitely dimensional space of kinematics states is an abstract collection of points, defined by configuration coordinates $(\nabla \mathbf{E}, \dot{\mathbf{E}})$, and velocity coordinates $(\nabla \mathbf{B}, \dot{\mathbf{B}})$, say. Usually, the free field Lagrangian is taken to correspond to the wave equation for the vector potential $A^\mu = (\varphi, \mathbf{A})$, and Ibragimov has shown that if writing down the Lagrangian in a vacuum directly in terms of the fields \mathbf{E} and \mathbf{B} Maxwell’s equations in the standard differential formulation appear to be overdetermined. [6, 7]

2.1. Interplay between dimensions and symmetries

In the wake of probability theories, physics doesn't put too much weight in evidence. It takes sensory and perceptual qualities to be deceptive, preferring to leave the links to the external world in their Pandora's box of ambiguities. Instead, it centers on symmetry as a constraint to reasonableness.[8, 9] The cornerstone is that, if a theory is mathematically consistent, with correct premises and deductive reasoning, the conclusions shall be correct and numerically substantiated. The option taken, to keep the fundamental laws of motion in coordinate free form, so as to preserve their validity independently of the number of dimensions, obviates the representation problem. The description is in a manifold Q , locally homeomorphic with \mathbb{R}^q , and possessing a differentiable atlas. It is cast upon a spacetime background only when it comes to interpreting the mathematical formalism of the fields in terms of physical entities. For example, in the standard model of particle physics, supplemental dimensions are packed in the so called internal space, possessing a curvature radius much smaller than 10^{17} cm . It is assumed that the internal space cannot be discovered by experiment, because of the high energy needed to penetrate it. Since the symmetry in abstract space is tied to the known types of interaction, one sometimes wonders what happens to the inherent properties of a system, described by n free coordinates, if it is embedded in an m -dimensional space with $m \neq n$.

3. Virtual camera and the space to take pictures of

The gap between calculative and perceptive approaches was not always as pronounced as it is nowadays. For instance, when Einstein left the hypothesis of stationary aether with the aim of generalizing mechanics so as to cover the electrodynamics of moving bodies, he was among the physicists contending that the validity of a geometry is a problem of physics. If he had been more concerned about electromagnetism, he would have had the opportunity of pondering on the geometric representation of $(\mathbf{E}, \mathbf{B}, \mathbf{D}, \mathbf{H})$. He rather chose to improve upon the problem of inferring the geometry of the physical space from mechanical motion, a fascinating problem Newton had left open.[10] As everybody knows, the metric content of geometry had just been challenged by allowing for length contraction and time dilation, two features on whose assumption Lorentz had derived the transformations bearing his name. Einstein incorporated both of them in his relativity theory by prescribing that length measurements be accompanied by time recording. His operative length measuring procedure specifies that the coordinate positions of the two ends of a ruler rapidly moving past an observer must be recorded simultaneously by the observer, i.e. each coordinate position in the rest frame is equipped with its synchronized clock. The simultaneity thus measured is relative to the reference frame: adopting it, the lengths of rapidly moving objects appear to be shorter in a rest

frame. Concomitantly, the time coordinates of clocks synchronized in that rest frame yield different readings for the moving one, which entails time dilation. On account of the fact that the ruler-clock systems serve the purpose of replacing Galilean inertial frames with the ones underlying the Lorentz transformations, relativity theory assumes reciprocity of the observations, spoiling contraction and dilation of objective meaning.

Einstein's approach to the *geometry in motion* was cut short by Minkowski, who restored the invariant concept of length in an unobservable 4D space he called world. He justified having recourse to spacetime by explaining that, to keep track of Einstein's relativity of simultaneous events, an infinity of 3D spaces is needed. Setting the fundamental tensor equal to $g_{\mu\nu} = \text{diag}(1, 1, 1, -1)$, and the light speed equal to $c = 1$, Minkowski's spacetime events have coordinates $(x, y, z, it) \rightarrow (x^1, x^2, x^3, x^4)$, and Lorentz' transformations become a group of isometries. To satisfy the requirement of Lorentz covariance, the electromagnetic field in a vacuum is represented in gaussian units by the components of the following covariant 4-tensor:

$$F_{\mu\nu} = \begin{bmatrix} 0 & H_3 & -H_2 & -iE_1 \\ -H_3 & 0 & H_1 & -iE_2 \\ H_2 & -H_1 & 0 & -iE_3 \\ iE_1 & iE_2 & iE_3 & 0 \end{bmatrix}. [11]$$

Maybe Minkowski did build for himself a picture of his world, and saw how it conformed with the set of 3D hyperbolic spaces Helmholtz had dealt with. As might be expected, the business of recasting all physical quantities in four-dimensional terms, and of fitting them into suitable conservation principles, didn't get many physicists to share his vision. Anyway, physicists realized that there is no seamlessly $3\text{D} \rightarrow 4\text{D}$ extension in analogy with Flatland. In fact, Einstein's definition of relative simultaneity has an impact on the slicing of 3D space at constant time for each observer.[12] Albeit time has an equal status as space variables, it is no longer shared among all inertial observers in relative motion with respect to one another. To sketch the particularities of Lorentz transformations of the spacetime with respect to Galilean transformations, Minkowski resorted to two-dimensional (r, t) diagrams, which are mappings onto a Euclidean plane. His interpretation of spacetime is generally accepted.

3.1. Computer graphics rendering of Minkowski's world

Einstein's theory is about measurements performed on the fly with ruler and clock, and is almost entirely concerned with "fully symmetrically shaped" point events. But by 1959 the importance of the relativistic aberration on the visual appearance of rapidly moving extended bodies also emerged. A thought experiment on their visual appearance can be performed with a virtual camera. According to Weisskopf,[13] the outlook on the shape-deformations in snapshot images came together with other insights on illumination and color changes, which in our opinion can-

not be adequately supported by purely geometric considerations. Shape aberration occurs in ray optics approximation because, as an object moves past the observer, the light emitted from parts located further away from him reaches his eyes after that emitted from closer parts. But, according to the mentioned virtual camera experiment, when a picture is taken by adjusting resolution and sharpening, light collected during the shot interval arrives from the different parts according to the position they had when it was emitted. Thus, more distant parts appear displaced with respect to nearer ones. The Lorentz contraction is canceled, and the overall effect results in a rotation of the trailing side toward the observer.

Recently, in computer science many rendering algorithms have been developed for video games and movie making, that avail of a rendering pipeline with configurable real-time graphics. Due to them, the opportunity is given in physics to avail of computer-based visualization methods for instructional purposes, and the camera metaphor has been resurrected as a complement of ruler-clock systems in coping with the special theory of relativity.[14] Until now the graphical representations offered for scientific purposes are directed toward a faithful presentation of extant theories. Computer graphics applications to special relativity visualize the relationship between physical quantities that match Lorentz transformations in Minkowski world. In his 4D geometry conception, every physical body is described by a world-tube, whose different 3D sections are interpreted as contractions by different inertial observers. However, virtual camera or ray tracing solve the problem of getting rid of two dimensions in a way different from Minkowski's diagrams.

By and large, conveying illustrative explanations of complex mathematical equations might be quite apart from computational electromagnetics purposes. Nevertheless, computer graphics is a bridge between computational electromagnetics and the wish to extract new information from measurements on real field patterns. As a diversion, one may wonder whether real cameras can be used under relativistic conditions, which presumably imply motion blur, or whether super-snapshot can keep the subject within the depth of field, thereby reducing the number of spatial dimensions.

3.2. Computer, mind, and visual experience

Computer graphics is believed to have a visual nature. The eyes explore the simulated patterns, and make rendering convey the information generated by computers through them to the brain. In humans, the vision system is the sensory channel with the highest capacity for distributed parallel processing.[15] Although we envisage the issue of spatial representations of received electromagnetic signals only for the purpose of interpreting phenomena, visual communication addresses many other exciting goals.[16]

The presupposition that computers might help understanding the functioning of human brain, which stems from Leibniz' belief in an alphabet of human thoughts, initially

spurred research on mimicking tasks such as learning, and machine vision. However, the computer metaphor of mind couldn't be substantiated, as human perception in particular turned out to be a highly integrated performance too difficult to detail. Computer vision chose to pursue further very special, and stylized tasks, such as pattern recognition, tracking and motion estimation, while visual processing evolved into a mainly physiological and psychological scientific discipline that analyzes visual cues to color, depth, and motion, for the purpose of extracting visual information.[17] By now, that information is believed to be disassembled and recreated internally within a virtual visual space only after elaboration by the striated cortex. [18] Thus, psychophysics has been getting involved in the study of synthesization of stimuli at the level of the target neurons. Neither it nor computer vision match with the task to render for conscious perception the extension open to the visual experience.

The program of reconstructing and interpreting images received under differing lighting conditions, in selected frequency ranges over the whole electromagnetic spectrum, is less ambitious than the computer-mind metaphor, but can be put to test at the semantic level. After all, the sensed space is part of the available information on the external world, that needs to be extracted to consciously perceive it.

4. Emergence of the 4th dimension in optics

Since Maxwell, the theory of light has been subsumed under electromagnetism, and exactly the task of incorporating the latter theory into mechanics required to explicitly address the fourth dimension, interpreted as time variable. By way of comparison, let's now have a look at the emergence of the fourth dimension in connection with optical images. As regards binocular perception under nearly physiological conditions, besides visual arts, Helmholtz' experiments,[19] and more recently the ones of Luneburg,[20] seem to indicate that hyperbolic geometry approximates it more closely than the Euclidean one. This means that the space perceived exhibits traits deductible from the relevant postulates, and in no way grants full being to any form of hyperbolic space H^3 .

The process of working out in mathematics non-Euclidean geometries, to which the above Bolay-Lobachevskii geometry belongs, can be traced back to the replacement of Euclid's parallel postulate by: "The parallels to a given line through a given point not on it belong to a coplanar pencil of lines that neither meet it, nor diverge from it in a specified direction." [21] Parallel postulates conform to plane geometry, and are of no concern in space. They matter when modeling starts out with conformal maps of the hyperbolic plane, or when a hyperbolic geometry is induced onto surfaces of the ambient Euclidean three-dimensional space E^3 , that are locally identified by differential equations (isometric embedding.) By these methods, the space H^3 itself requires embedding into a Cartesian space of higher dimension, and has no visual realization. It involves generalizing the definitions of the elements point, straight line and plane

in keeping with its intrinsic geometric properties, that is, independently on the embedding space.

Now let's turn to projective modelling. Besides being used to model fields in physical theories, for example in statics, projective geometry provides *global models* to non-Euclidean spaces. The approach to non-Euclidean geometries through projective models differs radically from the methods resorting to differential geometry. An algebraically defined non degenerate quadric surface is prescribed. That quadric is called projective metric, because it allows to define a distance function in both classes of constant curvature spaces, hyperbolic and elliptic. Now, in the context of synthetic projective modelling the quadric, written as a homogeneous quadratic polynomial $F(x, y, z, t) = 0$, specifies a non-projective relation between the geometric elements of each non-Euclidean projective space. Thus, rather than embedding the non-Euclidean space in an ambient space, the constructible model consists of the projective space endowed with a metric relationship drawn in it. Obviously, one must be careful not to confuse the drawn metric with the geometric figures belonging to projective geometry. To give an intuitive example, by looking toward a concave mirror under restricted head's motion, according to Helmholtz and others, a projective model of H^3 is perceived, in which the distance between points depends on the curvature (of the mirror), and the observed image is projective. If the head's motion is not restricted, and in addition the person concerned is walking, the perceived space is projective without any further qualification, since there is no way to specify a projective metric. More formally, although the projective space itself lives in the abstract, mathematical world, projective constructions can be carried out in a way akin to visual perception, and would allow useful representations in optics.

Mathematically, projective transformations of space are very general linear transformations. Thus projective geometry is eligible for rendering electromagnetic images in a broad sense: it supplies buildable spatial models and, at the same time, it is a logico-deductive system allowing to interpret geometric constructions at an abstract syntactic level. That projective geometry itself is dealt with in a tricky manner is unfortunate. The projective space is seldom introduced for its own sake. In algebraic geometry, the points of a 3-space \mathbb{P}^3 on \mathbb{R} are represented by the classes of all ordered quadruples of real numbers $x = (x_1, x_2, x_3, x_4)$, where two quadruples represent the same point if and only if they are proportional.[22] Clearly, until the above pointwise representation is needed, the projective space will not really become visualizable. In the remainder of this paper we'll show why projective constructions are indeed buildable in the space we are accustomed to.

5. Geometric transformations and projective space

Besides the kinematics approach to spacetime in terms of four Cartesian coordinates, that was exposed thus far,

there is a geometric approach, which consists in generating the space from a given group of congruences. In physics, geometric transformations were introduced in order to pursue the study of free mobility of rigid bodies. It was expected that groups of motions retrieve the physical space with no additional dimensions. This line of inquiry, summarized up in the elaboration of an ontology of space, dictated the difference in approach between physicists and mathematicians.[23] Physicists, like Helmholtz and Mach, delved into the nature of our understanding of the external world, and inquired about the functional relationship between physical object world and visual space, eventually asking how the theorems of geometry apply to the geometry of perception. In mathematics no such relationship was ever supposed. As already stressed, synthetic projective geometry is supported by graphic constructions on its own, without making any commitment either to the physical object world, or to perceptual space. As the mathematical inquiry evolved, the group-theoretic classification of geometric transformations associated to motion was linked to the book *Traité des substitutions* by C. Jordan, and was brought to the fore by F. Klein and S. Lie about the end of 1800s. Thus, besides re-establishing geometry on motion, the geometric invariant approach became the manifesto of the algebraization of geometry. Nowadays projective transformations can be subsumed under Cremona's birational transformations, and understood in terms of algebraic geometry, indeed. Reciprocally, the opportunity was taken in algebra to undertake a comprehensive study of rational curves, by projecting them in a manifold of higher dimension, so as to resolve knots, obtaining simpler curves. Projective n -dimensional spaces in \mathbb{R}^{n+1} were first introduced that way. Conversely, the central projection onto a plane from a point outside it is the best known way to achieve dimensional reduction in algebraic geometry. This discipline satisfies a quest for universal language in contemporary mathematics, that goes quite beyond the study of kinematics by means of geometric transformations.

Unlike projective transformations, the projective space belongs to synthetic geometry; that is, to build figures a tool and some construction rules are deployed. Moreover, tools, construction rules and axioms differ from their Euclidean analogues. Therefore, one cannot expect to execute some or all Euclidean shapes, but rather projective figures to bear peculiar characteristics. Those differences were not taken in due consideration during the course of axiomatic formalization of mathematics, because geometric constructions were not part of it. Indeed, the purpose of formalization was to obtain a conceptual unification. According to Hilbert: "One must be able to say at all times – instead of points, straight lines, and planes – tables, chairs, and beer mugs."

As a fallout of the dissociation of transformations and space from one another, with contextual drop out of the projective constructions, some difficulties arise when trying to pursue projective geometric tasks algebraically:

- although the projective geometric space is linear, space transformations don't need to correspond to linear coordinate substitutions;
- enumeration of the rigid motions, i.e. excluding operations such as similarities and deformations, depends on the dimension of space. In particular, reflection is either included or excluded.

Since theorems are primarily intermingled with constructions, when addressing the display of space at the graphic level, one should be careful to avoid obliterating from the very beginning its distinctive features. We wish to notice in passing that, since projective geometric elements do not terminate, each spatial construction is a model of the whole projective space. Alternatively, an abstract geometric space can be defined so as to embrace the whole set of possible constructions. For example, one can think of all constructible Platonic solids as pertaining to a unique, void Euclidean space. Again, for reasons which we further elaborate below, Cartesian coordinates don't provide the most appropriate mathematical background.

5.1. Enantiomorphic forms and mirror symmetry

Let's recall that, in addition to the rigid motions, i.e. translation and rotation, there is a spatial symmetry group, reflection, which is often included among isometries, but seldom as a displacement. It seems to require an additional dimension – the 4th – in order to be interpreted as a set of continuous displacements. In *Der Baryzentrische Calcul* Möbius, discussed superposing of three-dimensional shapes, and interpreted their half-revolutions in a 4D space as a reflection operation. According to this argument, the topological property of orientability of incongruent objects seems to depend at least partially on the space of embedding. If the space is connected, mirror symmetry depends on its dimension and/or on its intrinsic orientability. Since the mathematical description of mirror symmetry shows such puzzling characteristics, recently it has been invoked in the description of physical interactions at the boundary between geometry and dynamics. Yet, even if the result of one reflection on a handed body differs from that of any rigid continuous motion, when dealing with it in optics there seems to be no reason to add one dimension to the space readily seen.

Differently from Euclidean geometry, the projective one deals with mirror images as if they performed a continuous motion, and in addition allows to display them in space based on its own constructions. In our opinion the above geometric continuity allows to do without point by point reconstructions of images. Below we elucidate the peculiar traits involved in projective transformations and constructions by appealing to the common move of taking off a pullover by turning it inside out, which is executed in our space. We mention that the way of carrying out a mirror symmetry motion is also analogous to the algebraic

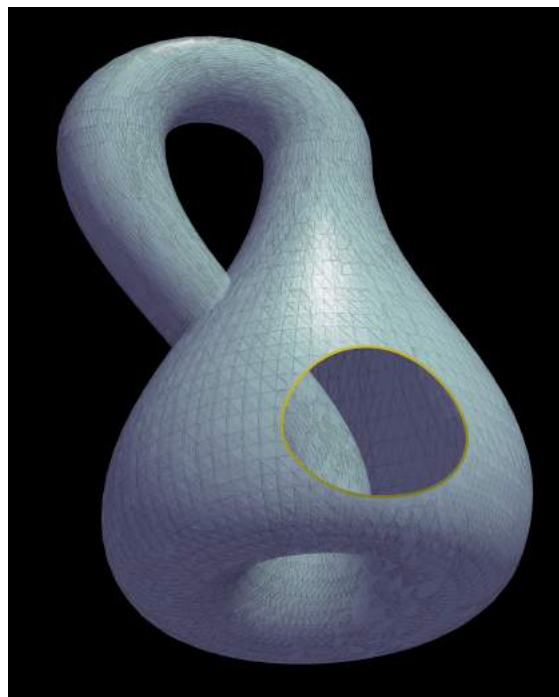


Figure 1: Klein's bottle in 3D

surface named Klein bottle (Fig. 1), which shows a self-intersection, when immersed in a 3D space.

6. Mirror reflection

Usually, it is stressed that, except for plane mirrors, a scaled point by point image is formed of any flat, symmetric, small object normal to the optical axis. Thus, in the paraxial approximation, reflection by a convex or concave mirror would imply geometric similarity and some distortion. By contrast with the geometrical optics description, the projective description regards the space as rigid, and thus we are going to consider mirror reflection a rigid motion. We take into account that a concave mirror is a linear receiver, that the real image forms in the same space as the object, and moreover, that the path of the object crosses that of the image at the center of curvature of the mirror. The journey of the object starts from the latter location, where it appears to touch its reflected and upside down image. In 4D this situation is explained by saying that, with respect to the object, the image has performed a double rotation about two independent planes: one through the plane of the mirror, and one through that including its path. When the object proceeds, and crosses the focal plane, the image clearly turns upside down (in truth, downside up), undergoing the transformation *real image* \rightarrow *virtual image*. This flip can be regarded as the result of a continuous motion, during which the image itself travels through an abysmal path behind the observer, compared to the observer-mirror distance. Finally, the object comes to rest when facing the



Figure 2: Taking off a pullover by inversion

vertex of the mirror because material objects don't interpenetrate. There, it touches again its image. If it could proceed further, the impossible transformation $object \rightarrow virtual\ image$ would take place as the second rotation. Whereas in practice piercing a mirror is no seamless, linear transformation, reflection through it is exactly the motion implied according to the geometric description.

Turning now to the ways of slipping off a pullover, there isn't a single way to do it. The one folding the arms across the chest comes closest to the envisaged reflection object-virtual image. Besides turning upside down, the pullover turns inside out exactly like a glove. A right glove turns into a left one, that remains similar and equal except for becoming the incongruent counterpart of itself (in relational sense). The small thickness of cloths may not concern us here, for the ethereal image's hull is hardly thicker. In order to tackle the deficiency of handedness of the pullover, which is a symmetric piece of clothing indeed, its exterior right and left sides were labeled with a red and a green thread respectively. The colors were exchanged on the reverse side. In Fig. 2 one of the authors wears the garment and shows how it turns.

A crossing, is requisite also for moving continuously from the outside to the inside of a mathematical object such as the well known Klein bottle, shown in Fig. 1, above.

We underline that we had to swap the colors of the threads in order to demonstrate how that motion is related to mirror symmetry. In the next section, we'll meet the same problem with numerical labels of hyperbolas: their order swaps. Vice-versa, if we don't discriminate self-intersecting motions, or two-branched curves, then enantiomorphic objects become indistinguishable. In the next section we are going to see that projective geometry doesn't do that discrimination; that is, it treats reflection motion like any other rotation. The discrimination emerges at the level of constructions.

6.1. Projective constructions of conics

To explain how reflection is related to projective geometry transformations, we need three premises:

- Poncelet's continuity principle allows to derive a figure from another by continuous changes. It doesn't go as far as Hilbert's statement on beer mugs above. However, it extends the definitions of basic projective elements beyond Euclid.[24]
- The axiom that any two lines belonging to a plane are incident with at least one point, gets rid of Euclid's parallel axiom (insofar as the plane is concerned). It introduces no points at infinity, essentially because there is no such class of elements. Disregarding infinity makes it possible to consider the motion of a reflected ethereal image continuous when the object crosses/turns into its image, as well as when it passes through the focal point of a mirror.
- The fundamental theorem of projective transformations, which we explain in the next section, can be used both to characterize transformations and for construction purposes. In fact, Helmholtz' expectation that groups of motions retrieve the space with no additional dimensions is ultimately only justified within the old purely synthetic methods.

Due to the point-plane duality, before starting discussion, we caution against thinking of synthetic projective geometry as a plane geometry. It is a geometry of space: Poncelet's point-plane duality in Gergonne's form mandates that any theorem has a dual counterpart, formally obtainable by replacing each occurrence of the term point by the term plane, and vice-versa. The term line is self-dual. The basic projective relationship, incidence, does not imply hierarchical inclusion. Again, according to group theoretic classifications, projection of space onto a plane isn't

even a projective transformation, as it is degenerate. Thus, drawing a flat section of a projective figure, or its projection on a plane, is a graphical operation in the absence of better choice. We stick at the point-plane duality, so that our conics are really cuts through quadrics, and our lines are mostly planes. The aim of Coxeter in writing his book *The real projective plane* is to give an idea of projective constructions on a sheet of paper, by comparing them with Euclid's.[25] He reformulates the set of axioms, and especially the duality principle for a projective plane geometry. In chap. 7 he introduces the "notion that the points on the conic form a range, resembling in many ways the points on a line." In clear text, he warns that according to projective geometry both lines and conics are linear, closed curves, none of which is expected to satisfy a quadratic equation. In projective geometry there are more than one way to arrive at conics, of course (cf. Coxeter, loc. cit., p. 75), none of which is based on their center or eccentricity, which cannot be determined by projective constructions.[26]

The task of constructing a conic with straightedge only can readily turn into a lapse into Euclidean geometry. In such case, besides the methods using a straightedge only, geometry in the classical sense avails of the focus-directrix, mechanical, and algebraic methods. In the figures 3, 4, 5 below we show some point conics constructed according to the fundamental theorem of projective transformations. The method of construction as well as the theorem are due to Steiner. Let the pencil of rays S be perspective to C . That means that the locus of points where (bijectively) corresponding rays of S and C intersect is a straight line, which we call u . Again, let C be perspective to S' , and call u' its perspective representation. $S \Leftrightarrow S'$ is a projective non-perspective correspondence. In fact, the fundamental theorem of projective transformations states that given two ranges (first species figures, such as lines of points, and pencils of rays) g_1 and g_n , their relationship can be determined by arbitrarily assigning three elements in g_1 and their corresponding elements in g_n . That relationship is known as harmonic cross ratio. Any finite chain of ranges g_2, g_3, \dots in perspective relationship with each other may be interposed during construction. However, the projective relationship between g_1 and g_n allows disregarding intervening ranges. That means that, if g_1 and g_n are not directly perspective, the linear transformation $g_1 \rightarrow g_n$ is described by a conic, in Euclidean parlance. Yet, projective geometry doesn't acknowledge perspective as a subclass, of linear projective transformations $g_1 \rightarrow g_n$, and thus neither distinguishes transformations described by a straight line from those described by a conic. Again, the fundamental theorem prevents from defining a metric, and interpreting the cross ratio as a double ratio of magnitudes.[27] In Fig. 3, besides being a transformation, $S \Leftrightarrow S'$ allows construction of a conic locus in the sense previously mentioned. By Steiner's method, five elements, either lines or points, such as the ones we used C, S, u, S', u' , are enough to determine graphically a unique conic.

Twenty eight ordered points have been chosen on u' , and

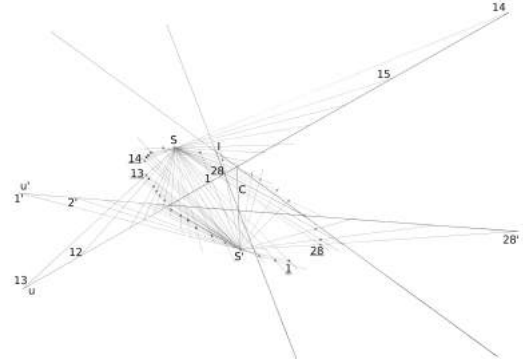


Figure 3: Point ellipse

their corresponding points by C have been constructed on u . The intersections of corresponding rays give rise to points labeled with the same name on an ellipse. Graphically, the ellipse is a range. It can be seen either as a fixed relation in the transformation $(S', u') \rightarrow (S, u)$, [28] or as a projective (linear) correspondence between S' and S . The constructed ellipse shows a hole between points 1 and 28, due to the fact that range u' extends beyond the sheet of paper. For the same reason, due to u there is another hole between points 13 and 14. Except for the fact that, by producing u or u' points could be added at will, in particular between 13 and 14, the increasing order of the points on this ellipse is clockwise. This is usually not explicitly mentioned when the ellipse is already drawn, because the construction method itself is exposed just for the purpose of demonstrating the theorems.

Now, in order to point out a constructive aspect, let's distinguish between ellipse and hyperbola, which projective theorems never do, and visualize how the order of points swaps. The rarely shown hyperbola-relation is drawn in Figs. 4 and 5. The construction goes as in Fig.3, except that I is taken as the "prospective center" instead of C . Thus, when choosing I instead of C in a picture illustrating a projective theorem, to be precise we should draw a hyperbola.

Holes are visible between 36-1 and 18-19 Fig.4, and between 32-1 and 5-6 Fig.5. Since hyperbola points are ordered clockwise on the left branch, but counterclockwise on branch $S \dots 31$ on the right (Fig.4), and conversely on Fig.5, one can imagine that the part of the hyperbola-considered-range laying in the projective plane outside the paper sheet, is bound to cross itself somewhere. Dual constructions are shown in figs. 6 and 7. A line conic is generated when taking two projective non-perspective pencils of points on distinct linear supports u, u' , and joining pairs of corresponding points on them by means of rays. Both, u and u' are perspective to u'' , and S, S' are used to establish the perspectivities. In our drawings the lines are terminated even if we ought not to do so. Our point ellipse cuts u and u' , while our line ellipse doesn't. Just as a diversion, we notice that usually the theorems involving

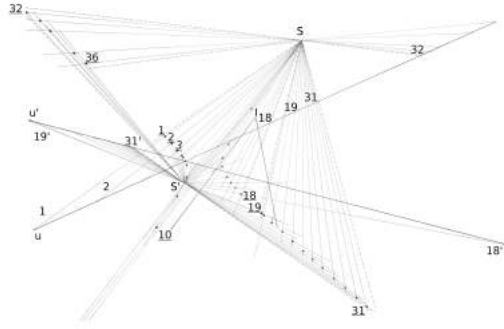


Figure 4: Point hyperbola

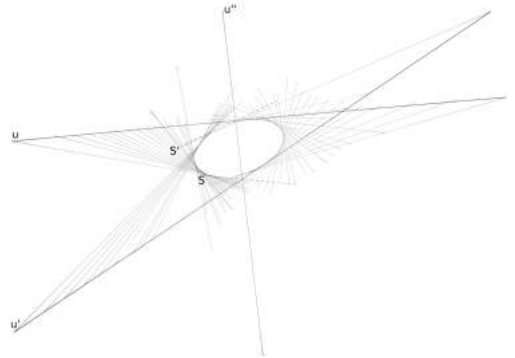


Figure 6: Line ellipse

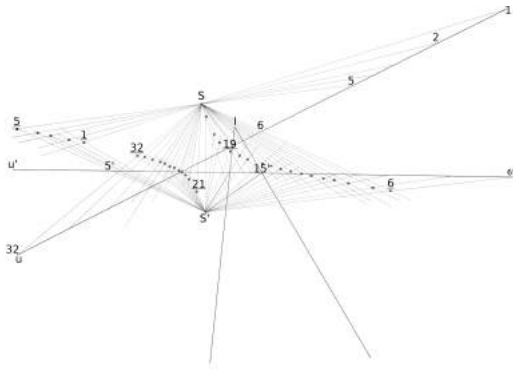


Figure 5: Point hyperbola

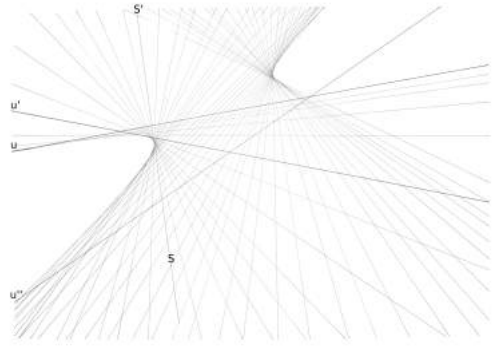


Figure 7: Line hyperbola

7. Conclusions

the construction of conics suppose the conic to be already drawn where it should, for example Woods.[29] In particular this is done when demonstrating the very important theorems of Pascal and Brianchon. Pascal has: “if a hexagon is inscribed in a point conic, the three pairs of opposite sides meet in three collinear points.”, whereas Brianchon states: “if a hexagon is circumscribed about a line conic, the three diagonals are concurrent” (Coxeter, p.88). Both theorems are valid for self-intersecting polygons with cyclic vertices/sides. Thus, while conics and pairs of straight lines are projectively equivalent for the purpose of demonstrating Pascal’s or Steiner’s theorems, as already stressed, they are not such if the specific relation is needed for graphical purposes. The possibility of self intersection matters in general, because it doesn’t preserve orientation on the conics, and is a big problem in point by point transformations. Both traits, the holes between nearby points and the swap in the orientation, are clear indications that analytical geometry is not too adequate to represent projective space in 3D.

In our excursus on the motion in four dimensions, we hit at a link between projective constructions and projective transformations that is distinctive for synthetic projective geometry. In our opinion, computational electromagnetics is not restricted to the choice of a good multipurpose solver, but also requires a better comprehension of the reasons why the electromagnetic field depends from the outset on four independent variables. Our intention is not so much to emphasize the number four, as to mark the loss of contact with representations based on simple geometric rules and theorems, which accompanied the rise of electromagnetism. Old-fashioned geometric insights, constructive approaches, and new modeling aspects were abandoned at once to make way for general formalism. However, real coordinate spaces modeled with Cartesian coordinates neither leave room for any visual interpretation, nor tell how to accomplish faithful dimensional reductions.

Traditionally, the extra dimension is interpreted as time in mechanics, whereas in optics the mechanical and geometric traditions clashed. Light rays were assimilated to particle trajectories, and the expression “geometrical optics” wasn’t analyzed further for the purpose of highlighting ways to vi-

sualize the extension for conscious perception. Nowadays if geometry is resurrected for rendering purposes, projective geometry could prove to be a good candidate. However, the representation problem should be tackled where it was left, and connected directly to the actual mathematical and technical developments. We discussed the projective modelling of the hyperbolic space, and the implications it has on the fourth dimension. The hyperbolic space, which seems to be the one perceived, also played a role in Minkowski's world. It can be modeled, provided one understands what the characteristic features of this space are in synthetic geometry. Finally, when rethinking the approaches to rendering, account should be taken, that the interpretation of images depends on past experience, and is subject to upgrade. Geometrical constructions should somehow keep pace with it.

References

- [1] L. Grant, Book reviews: Computer simulation, rhetoric, and the scientific imagination: How virtual evidence shapes science in the making and in the news, by A. K. Roundtree, *Bus. Prof. Comm. Q* 77(4): 499–501, 2014.
- [2] H. Obermaier, K. I. Joy, Future challenges for ensemble visualization, *IEEE Comput. Graph.* 34(3): 8–11, 2014.
- [3] R. Dedekind, *Stetigkeit und irrationale Zahlen*, (1892) Edition Opera Platonis, New York, 2013.
- [4] R. C. Archibald, Time as a fourth dimension, *Bull. Amer. Math. Soc.* 20(8): 409–412, 1914.
- [5] S. Four-dimensional space, *Nature* 31: 481, 1885.
- [6] N. H. Ibragimov, Symmetries, Lagrangian and conservation laws for the Maxwell equations, *Acta Appl. Math.* 105: 157–187, 2009.
- [7] J. B. Pitts, T first class constraint generates not a gauge transformation, but a bad physical change: The case of electromagnetism, *Ann. Phys. - New York* 351: 382–406, 2014.
- [8] N. J. Teh, Galileo's gauge: Understanding the empirical significance of gauge symmetry, *Phil. Sci. Archive* 83: 93–118, 2016.
- [9] D. van Dantzig, On the relation between geometry and physics and the concept of space-time, *Helv. Phys. Acta* 29 (supp 4): 48–53, 1956.
- [10] E. Macagno, *Leonardian fluid mechanics*, IIHR Monograph N. 112, Iowa City, 1991.
- [11] H. Minkowski, Die Grundgleichungen für die elektromagnetischen Vorgänge in bewegten Körpern, *Nachr. Ges. Wiss. Göttingen, Math.-Phys. Kl.* 12: 472–524, 1908.
- [12] E. A. Milne, *Relativity, gravitation and world structure*, Clarendon Press, Oxford, pp.107, 1935.
- [13] V. F. Weiskopf, The visual appearance of rapidly moving objects, *Phys. Today* 13(9): 24–27, 1960.
- [14] D. Weiskopf, A survey of visualization methods for special relativity, *Scientific Visualization: Advanced Concepts*, Vol. 1, Dagstuhl Follow-Ups, Dagstuhl, Germany pp.289–302, 2010.
- [15] F. S. Montalvo, Human vision and computer graphics, *Proc. of the 6th annual conference on Computer graphics and interactive techniques SIGGRAPH '79*, Chicago, USA, pp. 121–125, 1979.
- [16] C. Chen, Information visualization, *Wiley Interdiscip. Rev. Comput. Stat.* 2(4): 387 – 403, 2010.
- [17] M. R. M. Jenkin, L. R. Harris, *Seeing Spatial Form*, Oxford University Press, pp. 35, 2006.
- [18] R. Jerath, M. W. Crawford, V. A. Barnes, Functional representation of vision within the mind: A visual consciousness model based in 3D default space, *J. of Medical Hypotheses and Ideas* 9: 45–56, 2015.
- [19] V. Blåsjö, Hyperbolic Space for Tourists, *J. of Humanistic Mathematics* 3(2): 88–95, 2013.
- [20] A. A. Blank, The Luneburg theory of binocular visual space, *J. Opt. Soc. Am.* 43(9): 717–727, 1953.
- [21] J. Gray, Non-Euclidean geometry: a re-interpretation, *Historia Math.* 6: 236–258, 1979.
- [22] H. Busemann, P. J. Kelly, *Projective Geometry and Projective Metrics*, Academic Press Inc., New York, pp. 238–240, 1953.
- [23] A. P. Cox, C. K. Nebelecky, R. Rudnicki, W. A. Tagliferri, J. L. Crassidis, B. Smith, The Space Object Ontology, *19th Proc. FUSION Heidelberg (D)*, pp. 146–153, 2016.
- [24] J. L. Coolidge, The Rise and Fall of Projective Geometry, *Am. Math. Mon.* 41(4): 217–228, 1934.
- [25] H. S. M. Coxeter, *The Real Projective Plane*, McGraw-Hill Book Company Inc., New York, 1949.
- [26] E. B. Wilson, The synthetic treatment of conics at the present time, *Bull. Amer. Math. Soc.* 9(5): 248–254, 1903.
- [27] E. B. Wilson, Projective and metric geometry, *Ann. Math. 2nd Series* 5(3): 145–150, 1904.
- [28] M. Konstantatou, A. McRobie, Reciprocal constructions using conic sections and Poncelet duality, *Proc. of the IASS*, Tokyo, Japan, Oct. 2016.
- [29] B. M. Woods, The construction of conics under given conditions, *Am. Math. Mon.* 21(6): 173–180, 1914.

RFID Antennas, Technologies and Applications

Evolution-Strategy Optimized Dual-Band Antenna for UHF-band RFID/IoE Applications

Muhammad Salman Khattak, Abdul Rehman , Changhyeong Lee,
Dajung Han, Hejun Park, Sungtek Kahng, Muhammad Kamran Khattak

Incheon National University

E-mail: s-kahng@inu.ac.kr, salmankhattak43@gmail.com

Abstract

This paper presents an optimization-based design method for a multi-band antenna. From various optimization techniques, evolution strategy is adopted to find the proper initial geometry for creating the resonance at two frequencies (433 MHz and 900 MHz) with a limited physical size. The antenna structure is finalized by adjusting the geometrical parameters to meet the specifications of the UHF-band RFID/IoE services. The design method is validated by fabricating the antenna and testing its frequency responses which turn out compliant with the simulated results

1. Introduction

The field of RFID drew much attention from almost all walks of life, say, logistic industry, construction, safety, security, etc[1], and sparked system integration professionals, and RF engineers to devote their time to developing adequate components and systems. While the growth of the RFID became sluggish due to the advent of unprecedented political and economic issues compared to the early days, D2D, M2M, and IoT have been put forward as the new keyword of technology planning. People are dreaming of an ideal world that one device can talk to another device, and the things of the IoT can autonomously network with one another without human commands.

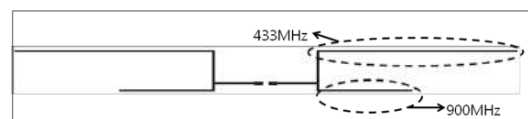
Though the D2D, M2M, and IoT look different from the RFID in terms of high-end users and the detailed items of the respective standards, all of them can share almost the same technology. In particular, the hardware development skills and techniques of the RFID can apply to IoE (Internet of Everything) representing the d2D, M2M, and IoT. The design techniques of the RFID modules and systems that were aimed at surveillance, logistics and security can be employed to health-care service, remote health-monitoring, power saving for smart buildings, and so on[2].

Multi-function is still required for a wireless device, and IoE and RFID are no exception in this notion. As an example, multi-band RFID and Zigbee platforms are highly welcome to cope with the increasing expense to take care of multiple frequencies. Especially, when frequencies for the wireless service are low as the UHF and the physical size of the device becomes large with longer wavelengths, right design methods should be considered to prevent the device from being bigger. In this paper, a dual UHF-band RFID/IoE antenna is designed. An optimization technique named

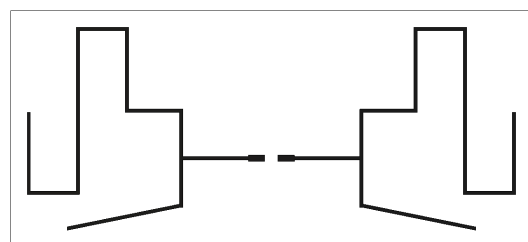
‘Evolution Strategy’ is adopted to determine the geometry of a compact antenna which does not necessitate the switch for two different resonant paths. The initial antenna resonates at 433 MHz and 900 MHz, and is tuned to have better isolation between the aforementioned two bands with good impedance match. This finalized antenna is manufactured and its performance is measured to verify the validity of the design method. Consequently, the simulated results agree with the experimental ones, showing acceptable antenna gain and far-field patterns along with the return loss below -10dB at both 433 MHz and 900 MHz. The paper is organized as follows. Sections 2 and 3 explain the basic part of the antenna design and the application of the evolution strategy optimization. In section 4, the simulated radiated field patterns of the antenna are confirmed by the measurement and comparison is made, and the agreement between them is shown. Last but not least, the conclusive remarks are given in section 5

2. Basic part of antenna design

When it comes to the wireless link between two distant points, radiated electromagnetic fields from an antenna will be taken into account. The antenna radiates an electromagnetic power at the resonance condition of the structure. For wire and planar antennas, the dominant resonance frequency is equated with the half-wavelength.



(a)



(b)

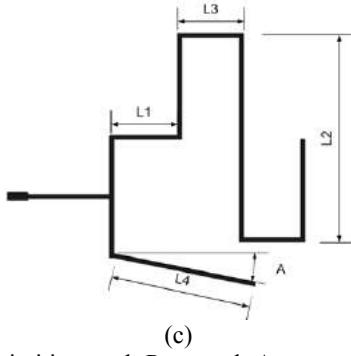


Figure 1: Primitive and Proposed Antennas (a) Primitive geometry (b) Modified geometry (c) Allocating the geometrical parameters

A single-band antenna works with a single resonance frequency, and it is inferred that the dual-band antenna will be made by the two individual geometries for two different resonance modes. The combination of the two individual structures will end up with an increased physical volume where a switch circuit is embedded. Instead of two separate radiating elements, two resonant paths are laid out together in one device as in Fig. 1(a), following the half-wavelength concept. This doesn't guarantee the desired performance as is, since a number of things are yet to be tackled for impedance matching. Fig. 1(a) is long, and its length can be decreased by modifying the straight branches like Fig. 1(b). The modified antenna is given the geometrical parameters as in Fig. 1(c) as the half of the symmetric shape, and will be optimized in the following section. The initial quantities for the parameters are assumed as

Table 1: Initial values of parameters.

Variables	values [mm]
L1	15.5
L2	26
L3	14
L4	0.2
A	0.2 rad

Basically, the length variables L1, L2, L3, and L4 stem from the half-wavelength condition. The inclination angle of L4 is set at random.

3. Evolution strategy

There are a variety of optimization methods. All told, they are categorized into a group of deterministic schemes and another of stochastic techniques. When the search region of the root can be clearly decided by guessing the behavior of the function or having the function as an explicit form, the deterministic optimization like the gradient method can be adopted. However, the EM problems of 3D structures cannot be explicitly expressed as simple mathematical formulae, and the stochastic schemes are proper to use. Evolution strategy is chosen to find the optimal geometry by following the rule that the initial population is firstly entered into the evaluation function and if the evaluation function doesn't meet the objectives, the initial population changes to become the parents.

If the parents do not satisfy the objective, they are varied to the children, and this process is reiterated until the solution is found. It can be summarized into the following chart.

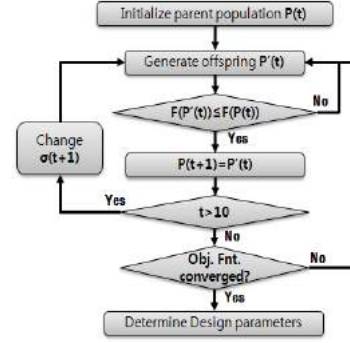


Fig. 2: Flowchart of the evolution strategy

The evaluation is made by linking the evolution strategy algorithm to a commercial EM simulator of the SEMCAD through the Visual Basic. Along with this, it is critically important how to define the objective function. The return loss is set as the objective function, and $r_{freq,1}$, $r_{freq,2}$, and r_{dB} are the weights for the two sub-objectives.

$$r_{freq,1} = 0.7, r_{freq,2} = 0.3, \text{ and } r_{dB} = 10$$

$$f_1 = 433 \text{ MHz}, f_2 = 900 \text{ MHz}$$

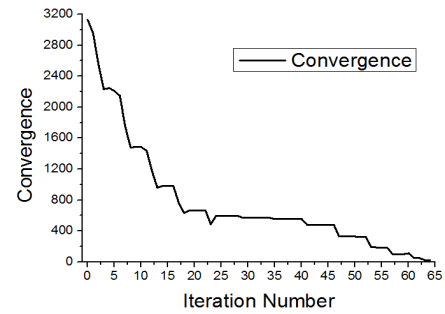
$$dB_{1,2} = -12 \text{ at the two resonance frequencies} \\ = 0 \text{ at the other frequency} \quad (1)$$

$$F_{freq} = \sum_i r_{freq,i} (f_i - freq)^2$$

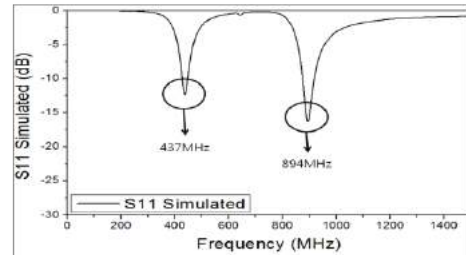
$$F_{dB} = \sum_i r_{dB} (S_{11} - dB_i)^2$$

$$Obj = F_{freq} + F_{dB}$$

In a total, 64 iterations have been conducted for the optimization and result in the forthcoming convergence profile and S_{11} as the return loss.



(a)



(b)

Fig. 3: The characteristics of the adopted optimization (a)Convergence behavior (b)Return loss of the optimized antenna

The evolution strategy programmed here shows the convergence as in Fig. 3(a) and the process converges rather slow. This convergence can be accelerated by employing the elitism from the GA approach[3] as well as better initial guesses[4]. As the result of the optimization scheme, the low return loss can be obtained at 433 MHz and 900 MHz. This is possible with the following optimal geometrical parameters

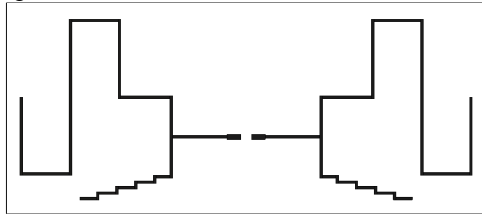
Table 2: Optimal values of parameters.

Variables	values [mm]
L1	18.11
L2	29.10
L3	17.59
L4	36.64
A	0.44 rad

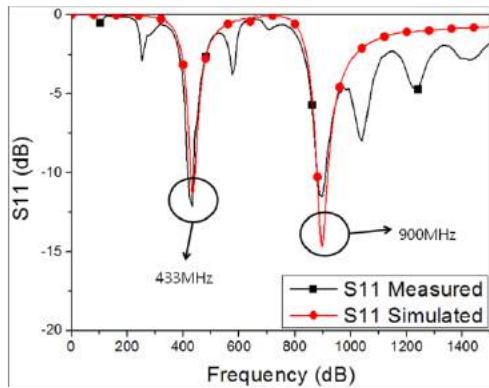
Final L4 is greater than initial L4, which is accompanied by the impedance match for highly isolated resonance frequencies. This parameter will be changed to a staircase shape to prevent the entire metal pattern from exceeding the quarter-wavelength of the 433 MHz in next phase where the optimized antenna is fabricated.

4. Fabrication and performance

As is mentioned in the previous section, the path of the higher frequency resonance denoted as L4 is modified in need of curbing the size growth.



(a)

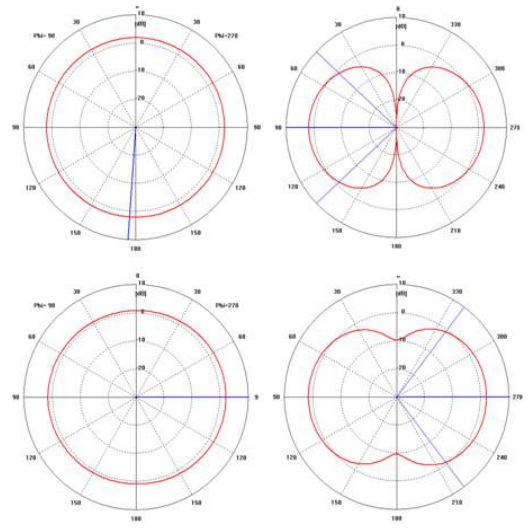


(b)

Fig. 4: The finalized antenna and its return loss in cases of the simulation and measurement (a)Final structure (b)Return loss of the simulated and fabricated antenna

Fig. 4(a) presents the staircase path for the resonance at 900 MHz unlike the straight line of Fig. 1(c). This finalized antenna is fabricated with FR4-substrate, and has the return loss as shown in Fig. 4(b). Between the simulated and measured S_{11} , they agree well with each other.

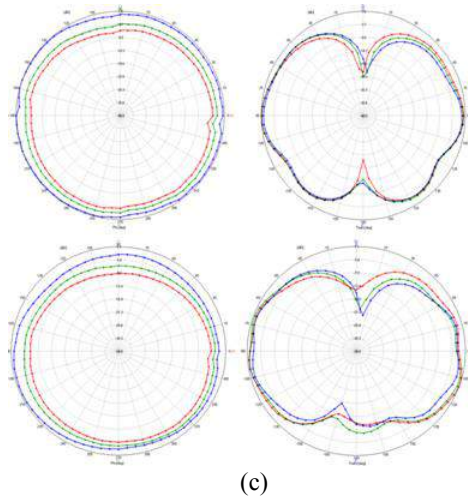
Until now, the return loss has been observed. It is worth investigating the radiated field patterns of the proposed antenna.



(a)



(b)



(c)

Fig. 5: The far-field patterns of the proposed antenna and its return loss in cases of the simulation and measurement (a)Simulation(H-plane and E-plane: from left to right, 433MHz and 900 MHz: from top to bottom) (b)Test set-up (c)Measurement(H-plane and E-plane: from left to right, 433MHz and 900 MHz: from top to bottom)

The simulated far-field patterns using the SEMCAD X[5] tell us that the omni-directional property is achieved for both 433 MHz and 900 MHz as presented in Fig. 5(a), which is required for RFID/IoE applications. The peak gain and antenna efficiency are greater than 1 dBi and 90 %, respectively for the two resonance modes in the simulation. The simulation of the design is checked by the comparison with the measurement. Fig. 5(b) is the photography of the beam-pattern test facility. Through this test, the measured far-field characteristics are obtained as in Fig. 5(c). The measured beam-patterns are very similar to the simulated ones. The antenna peak-gain becomes larger than 1 dBi, but the efficiency goes down to more than 60 %. When this antenna design method is applied to the real situation, multiple tests should be carried out to find the true cause of any degradation from the simulation and it should be mitigated.

Acknowledgements

This work was supported by ICT R&D program of MSIP/IITP.[2014-044-047-001, Dev. of radio services Antenna for the future Using Hybrid propagation medium]. And thanks to SPEAG for providing free license of SEMCAD X used in this study.

References

- [1] K. Finkenzeller, *RFID Handbook: Fundamentals and applications in Contactless Smart Cards and Identification 2nd Ed.*, John Wiley & Sons, 2003.
- [2] Nikitin, Pavel V., Rao, K. V. S., "Helical antenna for

handheld UHF RFID reader," *2010 IEEE International Conference on RFID*, pp. 166-173, 2010.

- [3] S. Kahng, "GA-optimized decoupling capacitors damping the rectangular power-bus' cavity-mode resonances," *IEEE MWCL*, vol. 16, no. 6, pp.375-377, 2006..
- [4] Jorge Nocedal, Stephen Wright, *Numerical Optimization*, Springer, 2006
- [5] SEMCAD X by SPEAG, www.speag.com

Auto-parts Logistic System Using Long Range UHF RFID Smart Metal Pallet

Byondi Franck Kimetya, Chang-Hwan Suel, Berhe Teklebrhan Hintsu,
Youchung Chung*

Information and Communication Eng. Dept. Daegu University, Gyeongsan, South Korea,
E-mail: *youchung@daegu.ac.kr

Abstract

This paper presents a passive RFID (Radio Frequency Identification) 920 MHz long read range UHF band tag to attach to metal pallet for car product logistic. The goal is to improve pallet or cart management system. When cart or pallet which contain car product are exported abroad, in importing countries, pallets and iron carts are considered as imported goods and pay customs duties. When the cart or pallet is returned back, the tariffs paid are returned by the exporting companies. So it's good to get back the carts or pallets exported. However, the recovery rates of carts and pallets that go abroad without specific labeling are quite low. Therefore, by increasing the recovery rate of carts and pallets through UHF band tag labeling, it is possible to reduce the damage including the tariff paid by the company to help profit creation.

1. Introduction

RFID(Radio-frequency identification) is the wireless non-contact use of radio-frequency electromagnetic fields to transfer data for the purposes of automatically identifying and tracking tags attached to assets. The three primary frequency ranges used in RFID are LF(Low Frequency) working at 125-134kHz frequency range for passive tags, used typically for animal identification, the reading range reaches up 10cm; HF(High Frequency) working at 13.56MHz for passive tags, used typically for Near Field Communication (NFC), smart cards, tickets, the reading range reaches 30cm. UHF(Ultra-High Frequency) working at 433 MHz for active tags and at 840-960MHz for passive tags, used in all types of applications. The reading range depends on tag and can reach up to 100+ meters for 433 MHz [1-9]. Although the first paper on modulated backscatter (basic principle of passive RFID) was published in 1948 [7] it took considerable amount of time before the technology advanced to current level [8]. Now RFID finds many applications in various areas listed above.

In special RFID applications such as metallic components, the general label tags attached on conducting material cannot operate well, because of the degradation of tag antennas. The metal environment where the general label tag is placed causes an electromagnetic interference, and no matched antenna impedance and the tag impedance. Like the

passive tag attached on a livestock box [10] has a long read range when attached only on paper box but when attached on metal the read range is less than 1m. Proper antenna design for RFID tag applications is becoming essential for the maximization of RFID system performance [2]. The tags introduced by reference [11-12] have been commercialized and are currently used in many applications, such as automotive containers, large metal containers, postal roll cages, and metal drums. But the read range is only 7meters and 4 meters when attached on metal container. This paper presents a long range RFID Tag antenna to attach on metal for car product pallet management.

2. RFID Metal Pallet Management System

The paper presents a passive RFID 920 MHz UHF band tag to attach to metal cart or pallet for car product logistic. The goal is to improve pallet or cart management system figure 1. When cart or pallet which contain car product are exported abroad from Korea, in importing countries, pallets and iron carts are considered as imported goods and pay customs duties. When the cart or pallet is returned back, the tariffs paid are returned by the exporting companies of Korea. So it's a must to get back the carts and pallets exported.

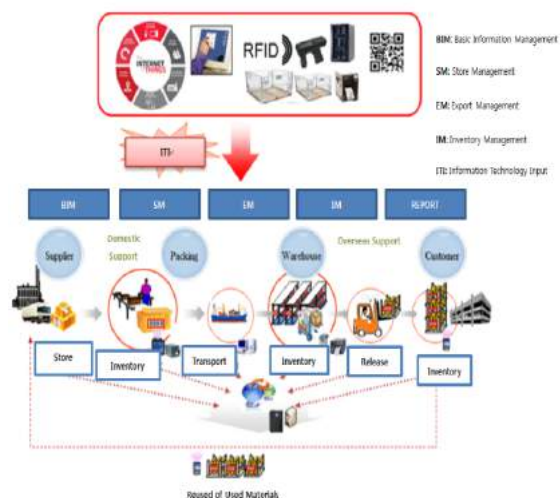


Figure 1: Smart RFID Pallet Management System

However, the recovery rates of carts and pallets that go abroad without specific labeling are quite low. Therefore, by increasing the recovery rate of carts and pallets through UHF band tag labeling, it is possible to reduce the damage including the tariff paid by the company to help profit creation.

The car products are packaged into the smart labeled pallet figure 2. The tag attached has each cart or pallet's specific information. The reader reads the tag's information and saves it in the Data base system. When Carts or pallets are shipped abroad, they are unpacked and are resent back to Korea; in case of pallet missing, the traceability is guaranteed. This system contributes to the improvement of company profit.

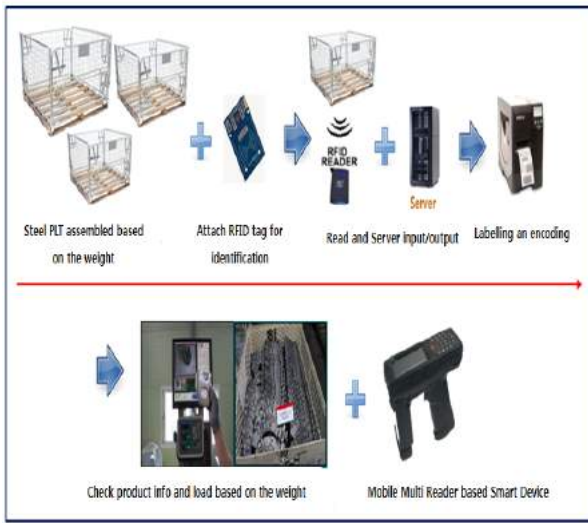


Figure 2: Labelling the Smart RFID Cart

The developed long range UHF Bottom Metal Tag Antenna (BMTA) solve the problems of the existing general label tags which lose their characteristics such as reading range when they are attached on the metal. The antenna has copper metal on the bottom of Styrofoam 9 mm thick, and the patch type antenna is on IS680 board 1mm thick, IS680 board is placed on the top of Styrofoam which makes 10mm height. We used a UHF Alien Gen2 RFID chip with chip impedance $Z_c = 11.7 - j132 \text{ Ohm}$ at 920 MHz. The antenna was designed using electromagnetic simulation tool CST which allowed us to calculate antenna gain, impedance, and proper matching to the RFID chip. The Tag was attached on the antenna using "ELCOAT electroconductives silver paste".

The BMTA size is (140 x 60 x 10 mm³), and when it's attached on metal environment such pallet or cart the reading range is about 7m; the interesting thing is that this antenna can be read also at the back side on about 8m distance, which is a characteristic similar to dipole antenna.

To make it be read just in one face and at a longer distance than 7m, it's better to increase the bottom metal size and shape for reflecting signal to the front face. The BMTA were equipped with a plastic cover for it protection.

3. UHF BMTA design and simulation result

The long reading range UHF RFID BMTA for metal pallet or cart of auto parts was designed using MWS (Micro Wave Studio) of CST (Computer Simulation Technology). Considering the dielectric constant of Styrofoam ($\epsilon=1.01$) between the tag antenna and metal cart, the dielectric constant of the ABS plastic cover $\epsilon=1.3$, the dielectric constant of the board $\epsilon=3.2$ [30mil (0.75mm) thick] on which the tag antenna were designed. The parameters, dielectric constant, and conductivity are entered into CST program. The tag antenna has the T-matching structure and is attached at the bottom part of the pallet. The design was done that the antenna impedance has conjugate matching with the RFID chip impedance [1]. The simulated reflection coefficient $|S_{11}|$ and the measured value of $|S_{11}|$ were compared. The Agilent Technologies ENA series Network Analyzer was used to measure the tag antenna impedance value at 920 MHz. We measured the tag Antenna Reading Range (TARR) pattern at 0, 15, 30, 45, 60, 75, 90 degree. The designed antenna can operate on 915MHz and 920 MHz frequency.

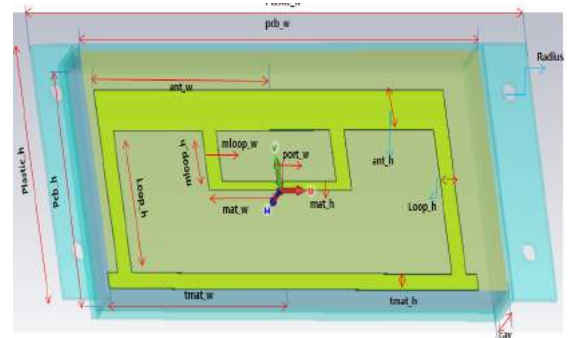


Figure 3: BMTA parameter and plastic cover in CST

Table 1: BMTA antenna parameters:

BMTA				
ant_w	ant_h	tmat_h	tmat_w	loop_h
61.3	10	4	65	36
loop_w	mat_h	mat_w	mloop_h	mloop_w
5	2.2	19	15	5

Figure 3 shows the BMTA CST parameter. The parameters values are shown in table 1 all in mm. Tag antenna was designed using CST Microwave studio, during simulation we used air instead of Styrofoam because it has almost same dielectric constant ($\epsilon=1.01$). An ABS plastic cover was considered during simulation too. After simulation we got the reflection coefficient $|S_{11}|$. Higgs 3 chip was inserted at the antenna interruption. The design was done to

have conjugate matching with Gen 3 chip impedance. Gen 3 chip has good sensitivity among recent chip.

BMTA has copper metal on the bottom and has dipole antenna characteristic. The antenna compared to the general antenna, is designed to have long reading range when attached on the metal product. We did parameter sweeping simulation based on the change of the BMTA ant_w values in mm 60.7, 61, 61.3, 61.6, 61.9. The optimized reflection coefficient value was at ant_w=61.3.

Figure 4 shows the BMTA reflections coefficient $|S_{11}|$ value of simulation and real value measured using Agilent technologies E5071B ENA series Network Analyzer. Through many tries, the simulation value at 920 MHz was -15.5dB and -13dB at 915 MHz while the measured gain was about -9.7 dB at 920 MHz. At -3 dB the band width is 225MHz. The antenna was actually fabricated, covered with a plastic cover and the reading range was measured. As the measurement method, two types of antennas were used: Linear Polarization Antenna (LPA) and Circular Polarization Antenna (CPA) of Alien Company. The recognition distance was measured when the RFID tag antenna was tilted vertically or horizontally. The results are shown in table 2.

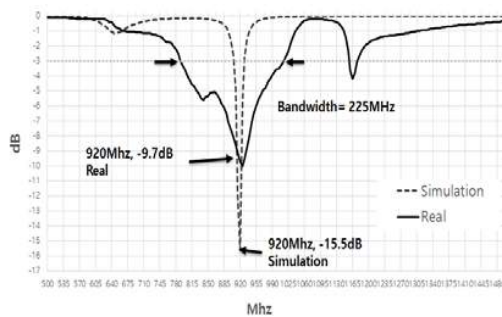


Figure 4: BMTA measured and simulated $|S_{11}|$

Table 2: BMTA measured read range

Tag antenna Position	LP Antenna		CP Antenna	
	Horizontal	Vertical	Horizontal	Vertical
BMTA	-	7.5	7	7.2

When using LP antenna, The Reading range is longer than CP antenna. LP antenna was set vertically so the tag is only detected for vertical position of the RFID tag antenna. When using CP antenna, in whatever position the RFID tag antenna is detected. There is a light deference of reading range for horizontal and vertical position of the RFID tag antenna. The BMTA can increase it read range if the bottom metal is wider to allow more reflection to the front of tag antenna.

Figure 5 shows BMTA Gain Pattern. The beam pattern of BMTA has directivity. Due to the copper metal on the back of Styrofoam, at 920MHz the antenna has 6.93dBi main lobe gain, the direction of the main lobe 179 degree (blue line), the 3dB angle in the main direction is 91.7 degree (sky blue line), and the side lobe level is -2.5dB. The interesting point on this BMTA is that seeing the gain pattern the antenna can be detected even on its back side at a reading range distance over than 5m. This antenna has almost dipole antenna characteristics.

Figure 6 shows the fabricated BMTA RFID tag antenna front and back views. The antenna was fabricated using LPKF milling machine with +/-10mill accuracy. The RFID antenna is attached on a board with the dielectric constant of the $\epsilon=3.2$ [30mil (0.75mm) thick]. Between the copper metal and board there is Styrofoam which has the permittivity ($\epsilon=1.01$) almost equal with air. The tag was attached on antenna using silver paste. The antenna was covered with the plastic cover and then we measured the reading range with Alien program using Alien's ALR 9900 reader and reader antenna (gain 6 dBi).

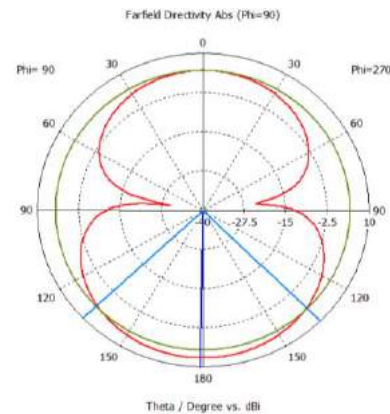


Figure 5: BMTA gain pattern

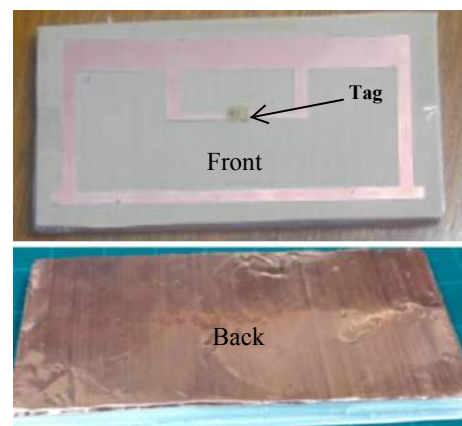


Figure 6: Front and back views of fabricated BMTA

Figure 7 shows the fabricated BMTA RFID tag antenna's Read Range according to Theta (θ) and Phi (Φ) angle direction. BMTA theta (θ) angle direction reading range at 0° is 7.5m using LP antenna. At 120° we have 7.2m and 7.5m for 180° because of the dipole antenna characteristic. The Phi (Φ) angle direction reading Range at 0° is 7.5m; the minimum reading range at 120° is 7.1m and 7.5m for 180° . BMTA has a long reading range when antenna is 180° and 0° facing the reader antenna 0° .

Pallet is made with metal; we designed the antenna considering the metal environment. Figure 8 shows the size of the pallet 1550 x 860 x 800mm and the antenna covered with ABS plastic material. The covered antenna is attached at bottom-left side which is specified as widest area. The designed antenna height is 70mm and length is 177mm.

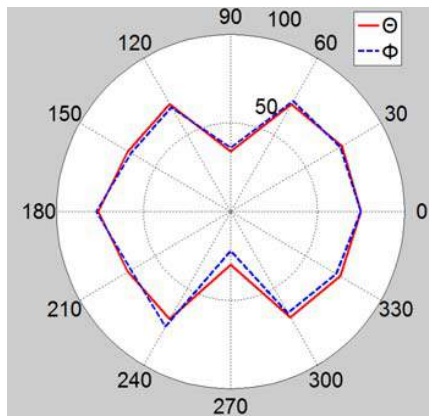


Figure 7: Measured BMTA Reading range pattern

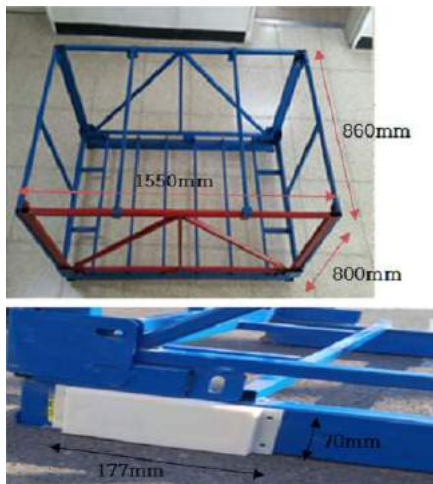


Figure 8: Antenna attached on cart, Cart size

4. Conclusions

This paper presents a long read range 915, 920 MHz RFID UHF band tag which can be detected even when

attach on metal pallet for car product logistic. The goal is to provide a real-time pallet logistic management system using the smart RFID pallet. This will help to increase company gain. Developing a program to store, release, and count, identifier tag antenna attached on car product pallet is very important. The read range was measured in open air using alien's company RFID reader and LP, CP antenna. LP antenna has a long range than CP antenna. BMTA ($140 \times 60 \times 10 \text{ mm}^3$) has 7.5m with LP and 7m with CP antenna as reading range. The Alien Company's reader and antenna were used for the experiment. A good tuning and accurate fabrication can increase the reading range up to 20m

References

- [1] K. Finkenzeller. RFID Handbook, 2nd Edition, John Wiley & Sons, England, 2003.
- [2] 손해원, 최원규, 표철식, "UHF RFID 태그기술, 한국전자과학회 전자과학기술, 16(2), pp. 55-63, 2005 년.
- [3] atlasrfidstore, "basics of rfid system atlasrfidstore"; <http://rfid.atlasrfidstore.com/hs-fs/hub/300870/file-252314647-pdf/Content/basics-of-an-rfid-system-atlasrfidstore.pdf>.
- [4] Asad ullah Noor, Hans Johansson, " Design of Microstrip Patch Antennas at 5.8 GHz", Kapsch TrafficComm AB, onkoping, Sweden, 2012.
- [5] <http://www.antenna-theory.com/>
- [6] Per-Simon Kildal. FOUNDATIONS of ANTENNAS A Unified Approach for Line-Of-Sight And Multipath. March 2009.
- [7] H. Stockman, "Communication by means of reflected power," Proc. IRE, pp. 1196-1204, Oct. 1948.
- [8] K. Finkenzeller, RFID Handbook: Radio-Frequency Identification Fundamentals and Applications, 2nd ed: Wiley, 2004.
- [9] R. Bansal. "Coming soon to a Wal-Mart near you," IEEE Antennas Propag. Mag., vol. 45, pp. 105-106, Dec. 2003.
- [10] F. Kimetya B., Sungfeel C., Juwon K., Jihyun J., Youchung C., "Smart School-Food Materials Inspection and Logistic System Using Intelligent HF/ UHF RFID Smart Box", 한국통신학회 하계종합학술발표회, pp. 434-435, 2015 년.
- [11] K. V. S. Rao, Sander F. Lam, Pavel V. Nikitin, "UHF RFID Tag for Metal Containers", Proceedings of Asia-Paci. Microwave Conf., pp. 179 - 182, 2010
- [12] IT67 Enterprise Lateral Transmitting (L T) Tag, Intermec, www.intermec.com/products/rfid.

UHF RFID Automobile Plate Tag Antenna Controlling the Radiation Beam Pattern with T-Matching Structure

Berhe Teklebrhan Hints*, Frank Byondi, Chang Hwan Suel, Youchung Chung

Information and Communication Eng. Dept. Daegu University, Kyungsan, Korea

*corresponding author, E-mail: youchung@daegu.ac.kr

Abstract

This paper presents Designing of RFID Tag Antenna in the UHF range, which is applicable in the vehicular license plate and attached to the vehicle bumper. The main goal is, first to increase the reading distance range, second to improved identification ratio by controlling the radiation beam pattern. Since every vehicle have a license plate, the available plate structure is used to design the antenna. The shape of the antenna is rectangular and has a dimension of 520mm X 110mm, which is a typical size of the standard plate used in Korea. The fabricated tag antenna that the license plate and the vehicular bumper were fixed by bolt and nut. For vehicle tracking and identification, Radio Frequency Identification (RFID) readers are deployed on the road side. For efficient identification, long distance passive UHF RFID license plate with patch antenna is proposed to provide not only line of sight identification but also left and right beams. Unlike the general UHF tag antennas, in this paper the patch antenna is designed to attach to metal part of the car, license plate holder. Beam patterns can be controlled by the patch antenna parameter values. For maximum transmission power T-matching method is used to match the input impedance of tag antenna with the RFID chip. A commercial simulator, CST is used to analyze the proposed antenna performance. Simulation result demonstrates that the proposed UHF RFID tag antenna has beam radiation pattern as required at 920MHz. In addition, the estimated read range of the proposed plate meets the requirement of RFID system.

Index Terms - License plate, Radiation pattern, Read range, UHF RFID Tag, Current Density.

I. Introduction

RFID (Radio Frequency Identification) is a technology that recognizes tags attached to things by radio and collects information stored in the tag chip, it is used in the fields of pharmaceutical, automobile, iron and steel, logistics, alcoholic beverage industry. It has been widely used and applied to the transparency of the distribution process through traceability of. And it is used in various fields such as transportation, education and

culture, environment, medicine, etc. RFID systems of various frequency bands are used [1].

ISO (International Organization for Standard) and IEC (International Electro-technical Commission) which determine international standards relating to RFID wireless interface for each frequency band prescribe as follows. The band below 135 kHz is defined by ISO 18000 - 2, 13.56 MHz is defined by ISO 18000 - 3 for HF band, ISO 18000 - 7 for 433 MHz band, ISO 18000 - 6 for 840 - 960 MHz UHF band, 2.45 GHz band is specified by ISO 18000-4. In Korea, according to the regulations changed in 2009, UHF band is used at 4 W in the 917 - 920.8 MHz band and 200 mW EIRP (Effective Isotropic Radiated Power) in the 920.8 - 923.5 MHz band. The HF (High Frequency) band utilizes the coupling of the magnetic near field, whereas the UHF band (840 to 960 MHz) uses the electromagnetic wave in the far field then, backscattering method information is conveyed and used for various applications. [1, 2].

One of the fields of application is in transportation management system. In recent years, RFID-based license plate has received much attention for the use in vehicle identification. Automatic management of RFID system is more time and cost effective compared to manual management by human. Many researches of RFID system for automotive applications have been conducted and researches on RFID tag position which is to be attached to vehicle have been also considered and studied for the long readable range and the identification ratio improvement [3] ~ [7]. But the performance of RFID tag antenna are affected depending on the vehicle object such as conductor of car body, bumper and window glass, which makes the impedance to change. The impedance change affects the tag antenna performance such as reading range and identification ratio. Therefore, the tag antenna design needs to consider absolutely the surrounding environment where the tag antenna is installed, as well as the car object to be attached.

In [8] a very small RFID Antenna is designed for a seal bolt shape but still the reading distance is limited to 3.5m. E-plate antenna design to serve as RFID tag was reported in [9] ~ [11] but this method used active RFID system where the constraint is cost of tag. Because an antenna, application specific integrated circuit (ASIC) and battery are included in an active RFID tag embedded in the e-plate. The

proposed tag antenna in [12] is installed as a tag inside a car's side-view mirror for optimum reading. In this paper the RFID system is applied to license plate. Automobile plate with a Patch antenna is proposed. The antenna gain can increase because the license plate is conductor (made of copper) and is operated as antenna. Thus, the reading distance range can become more longer than conventional commercial tag antenna. Furthermore, it has the advantage of improved identification ratio by controlling the radiation beam pattern in a way that the vehicular license plate tag antenna can easily detected by the readers installed on the road side or toll gates as the vehicle passes through it.

II. Design of Tag Antenna

Fig. 2 shows the design structure of the proposed Automobile plate with a Patch antenna considered the vehicle bumper of plastic. It is composed of copper metal plate as license plate and plate holder, bolts and nuts, and a part of vehicle bumper. The bumper is made of plastic with dielectric constant, $\epsilon_r=3.5$ and loss tangent=0.015. When general UHF tag antennas attached to a metal, the reading distance will drastically decreased because the impedance of the tag antenna is changed. In this paper the patch antenna is designed to attach to metal part of the car, license plate holder. Even though the kinds of Korea license plate size are various, the considered standard plate size in design is 520 mm X 110 mm X 1 mm used practically as shown in Fig. 1(a).

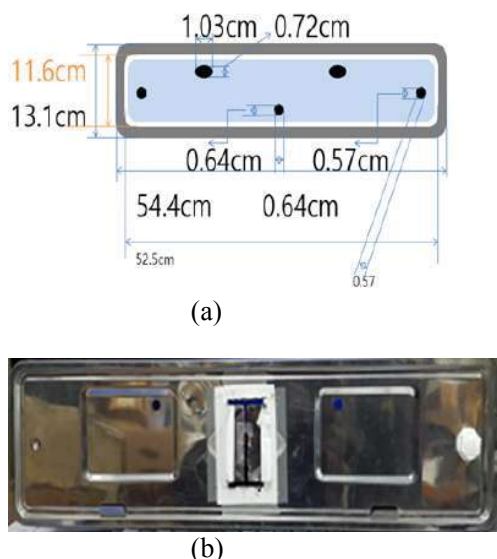


Fig.1 (a) Official standard plate size of Koea: 520mm*110mm (b) License plate holder

The proposed antenna was simulated using CST simulation software here a discrete port has been

used to represent RFID tag terminal. There is a gap of 2 mm between the two edges of discrete port. The simulated results of proposed antenna are expected to give acceptable performances at a center frequency of 920 MHz band for UHF RFID application.

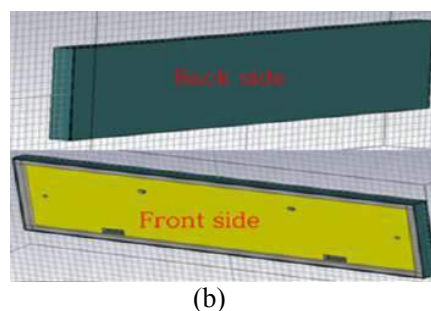
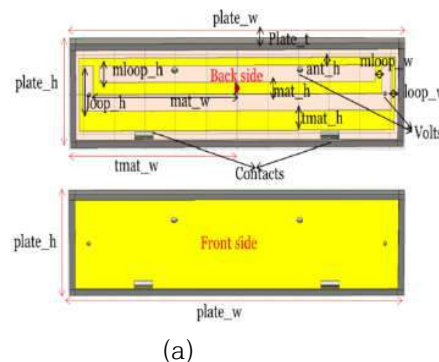
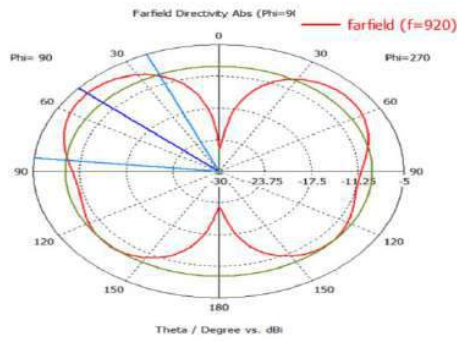


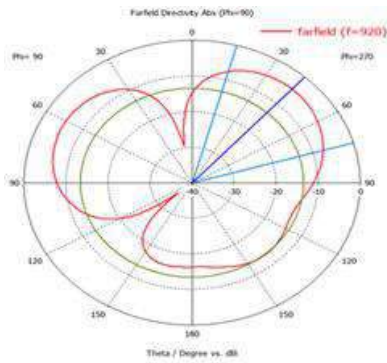
Fig.2. Design structure of the proposed antenna, front and back side of License Plate tag antenna, (a) without bumper (b) with bumper

III. Simulation Results and Performance

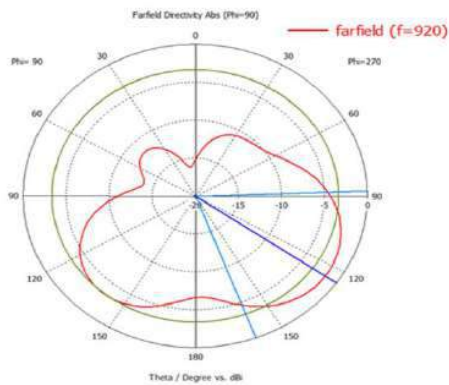
For demonstration, the proposed tag antenna is designed to operate at 920MHz. The geometric parameters defined in Fig. 2 have been designed and optimized by parameter sweeping. The resulting optimized values are: plate_w=525mm, tmat_h=25mm, ant_h=10mm, tmat_w=257.5mm, plate_h=116mm, mat_w=235mm, mat_h=15mm, loop_w=5mm, mloop_w=10mm. The signal radiating towards the bumper cannot be identified by the reader, only signal radiating towards the front side of the car is readable by the reader. So we need a strong signal radiating towards front. The 0 degree in Fig. 3 means the back direction that tag antenna and reader antenna stand opposite to each other. On the other hand, the 180 degrees indicate the front direction with respect to the above back direction. Since the readers are deployed along the road side, from Fig. 3 we can see that there is strong signal radiating towards right and left direction. This is achieved by controlling the parameter values of the patch antenna.



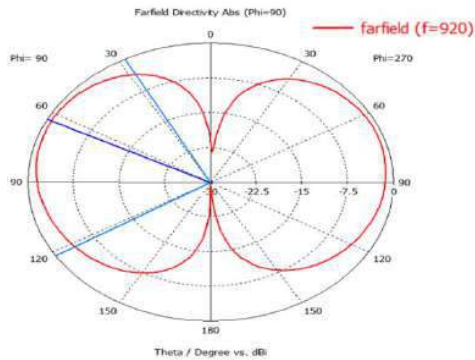
(a) at $mat_h=15$, $tmatch_h=25$, $mloop_w=10$



(b) at $mat_h=2.2$, $tmatch_h=2$, $mat_w=235$.



(c) at $mat_h=15$, $tmatch_h=25$, $mloop_w=10$



(d) at $mat_w=235$, $tmatch_h=4$, $mloop_w=5$

Fig.3. Polar radiation pattern of antenna at 920 MHz.

The above radiation pattern will meet the requirement of the deployment of RFID readers in the management of vehicles such as in the Intelligent Transportation Systems (ITS). For example, if the reader can be placed on a lamppost on the roadside, the beam emanating from the tag antenna will allow the license plate and reader communicate with each other very well. The 3D radiation pattern in Fig. 4 shows that there is strong signal radiating from the plate towards left and right side of the road, where readers are deployed. There is no doubt that volts and nuts and the vehicle's body for the license plate to be mounted will have influence on the performance of the antenna, so all these conditions are included in our numerical simulation.

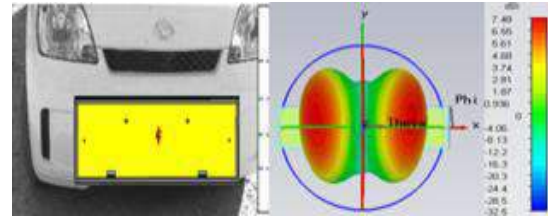
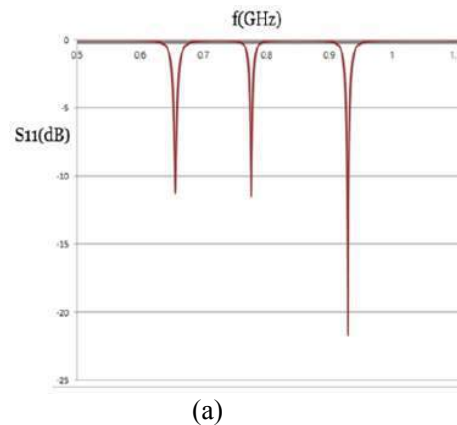


Fig.4. The three-dimensional radiation pattern of the tag antenna at 920MHz.

Fig. 5(a) shows the surface current distribution on the tag antenna at 920MHz. The current is flowing almost in the entire patch. The computed return loss of the proposed tag antenna is shown in Fig. 5(b).The results of simulation show that the proposed tag antenna has a reflection coefficient of 23.5dB at 920MHz.



(a)

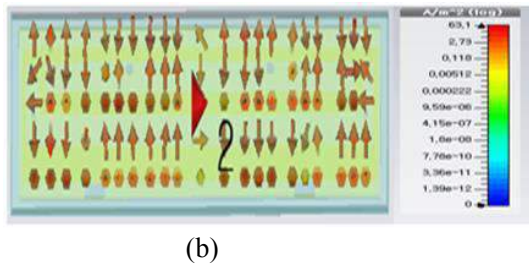


Fig 5. (a) Simulated return loss, (b) Current density at $f=920\text{MHz}$.

VI. Conclusion

A passive automobile plate with a patch antenna is designed, and demonstrated by positioning the patch antenna on the back side of plate holder (i.e towards the bumper of the vehicle). Plate dimensions are according to Korean standard license. RFID metal tag has approximately 20db in 910 MHz frequency and the impedance is 50Ω with T-matching. Performance analysis of the proposed license plate indicates that the proposed plate can meet the requirements for on-road vehicle identification when the RFID readers are deployed on the roadside lampposts.

References

- [1] Finkenzeller, RFID handbook, 2nd edition, John Wiley & Sons, England, 2011.
- [2] Y. C. Chung "A study on animal information management system using an insertion type UHF RFID tag", Journal of KICS, Networks, vol. 36, no. 12, pp. 1680- 1685, Dec. 2011.
- [3] Wenjing Zhao, Xunguang Ju1 and Shuangjiang Wu, "RFID-Based E-Plate with Slot-Dipole Antenna Design and Roadside Interrogator Deployment", The Open Electrical & Electronic Engineering Journal, pp. 27-33, 2014.
- [4] Dae-Hwan Park and Kyeong-Sik Min, "Design for a Tag Antenna Using License Plate Attached Vehicle Bumper", The Korean Institute of Electromagnetic and Science, 20(6), pp. 535-543, June. 2009.
- [5] Dae-Hwan Park and Kyeong-Sik Min, "Design for license plate RFID tag antenna with dual resonance to improve identification ratio", IEEE Proceedings of the Fourth European Conference on Antennas and Propagation, pp. 1-4, 2010.
- [6] Kyeong-Sik Min and Jin-Woo Kim " Experimental Performance Evaluation according to the Sticked Backside Plate of Dipole Antenna for RFID Tag", The Korean Institute of Electromagnetic and Science, 18(3), pp. 273-281, March. 2007.
- [7] K. Penttila, M. Keskilammi, L. Sydanheimo, and M. Kivikoski, "Radar cross section analysis for passive RFID system", IEEE Microwave and Wireless components letters, 153(1) February. 2006.
- [8] Kisis Kim*, Changhwan Seol, Jihye Kim, Myeongeun Lee, Youchung Chung, "A Study on Detecting Illegal Automobile Detection System Using an UHF RFID tag Antenna for Seal-Bolt Shape", KICS. 2016, pp. 169-170
- [9] Evizal, Tharek Abd Rahman, Sharul Kamal Abdul Rahim, "RFID Vehicle Plate Number (e-Plate) for Tracking and Management System", IEEE International Conference on Parallel and Distributed Systems, pp. 611-616. 2013.
- [10] Evizal, Tharek Abd Rahman, Sharul Kamal Abdul Rahim, "RFID Tag Antenna Design For Vehicle Plate Number (e-Plate)", TELKOMNIKA Telecommunication, Computing, Electronics and Control, Vol 11, No 2. 2014
- [11] Z. Wenjing, et al., "Active E-Plate with Slot Antenna," in Wireless Communications, Networking and Mobile Computing, 2008. WiCOM '08. 4th International Conference on, 2008, pp. 1-3.
- [12] K. Min-Seong, et al., "Directivity Design of RFID Tag Antenna Using Side-view Mirror for Vehicle," in Microwave Conference, 2008. APMC 2008. Asia-Pacific, 2008, pp. 1-4.

Small UHF RFID Tag Antenna for Vehicle License Plate

Berhe Teklebrhan Hintsa*, Frank Byondi, Chang Hwan Suel, Youchung Chung

Information and Communication Eng. Dept. Daegu University, Kyungsan, Korea
E-mail: youchung@daegu.ac.kr

Abstract

This paper presents designing of passive UHF RFID Tag Antenna which is applicable in the vehicular license plate and attached to the vehicle bumper. The main goal is, to increase the reading distance range of the vehicular plate by readers installed on the road side. Since every vehicle have a license plate, the available plate structure is used to design the antenna. The tag antenna have a rectangular shape with a dimension of 140mm X 60mm X 10mm and it is attached to the license plate holder with dimension of 520mm X 110mm, which is a typical size of the standard plate used in Korea. The fabricated tag antenna, which the license plate and vehicular bumper are fixed by bolt and nut. The front face of the tag antenna is designed towards the bumper side. The back side of the antenna is towards the front direction of the car and a Styrofoam of 10mm thickness, license plate holder and the plate number are placed in sequential order. Therefore, for maximum reading distance, magnitude of back lobe must be much greater than the front lobe. Accordingly, Magnitude of the back lobe is 6.29dBi with lobe direction of 179degree. Unlike the general UHF tag antennas, in this paper the tag antenna is designed to attach to metal part of the car, license plate holder. Far field directivity is controlled by the tag antenna parameter values. For maximum transmission power T-matching method is used to match the input impedance of tag antenna with the RFID chip. A commercial simulator, CST is used to analyze the proposed antenna performance. Simulation result demonstrates that the proposed UHF RFID tag antenna have reflection coefficient and beam radiation pattern as required at 920MHz. In addition measurement result shows that the reading range of the proposed Tag Antenna is 11.6m without bumper and 10.3m with bumper.

Index Terms - License plate, UHF RFID Tag, UHF RFID Tag

1. Introduction

RFID (Radio Frequency Identification) is a technology that recognizes tags attached to things by radio and collects information stored in the tag chip, it is used in the fields of pharmaceutical, automobile, iron and steel, logistics, alcoholic beverage industry. It has been widely used and applied to the transparency of the distribution process

through traceability of. And it is used in various fields such as transportation, education and culture, environment, medicine, etc. RFID systems of various frequency bands are used [1].

ISO (International Organization for Standard) and IEC (International Electro-technical Commission) which determine international standards relating to RFID wireless interface for each frequency band prescribe as follows. The band below 135 kHz is defined by ISO 18000 - 2, 13.56 MHz is defined by ISO 18000 - 3 for HF band, ISO 18000 - 7 for 433 MHz band, ISO 18000 - 6 for 840 - 960 MHz UHF band, 2.45 The GHz band is specified by ISO 18000-4. In Korea, according to the regulations changed in 2009, UHF band is used at 4 W in the 917 - 920.8 MHz band and 200 mW EIRP (Effective Isotropic Radiated Power) in the 920.8 - 923.5 MHz band. The HF (High Frequency) band utilizes the coupling of the magnetic near field, whereas the UHF band (840 to 960 MHz) uses the electromagnetic wave in the far field then, backscattering method information is conveyed and used for various applications. [1, 2].

One of the fields of application is in transportation management system. In recent years, RFID-based license plate has received much attention for the use in vehicle identification. Automatic management of RFID system is more time and cost effective compared to manual management by human. Many researches of RFID system for automotive applications have been conducted and researches on RFID tag position which is to be attached to vehicle have been also considered and studied for the long readable range and the identification ratio improvement [3] ~ [7]. But the performance of RFID tag antenna are affected depending on the vehicle object such as conductor of car body, bumper and window glass, which makes the impedance to change. The impedance change affects the tag antenna performance such as reading range and identification ratio. Therefore, the tag antenna design needs to consider absolutely the surrounding environment where the tag antenna is installed, as well as the car object to be attached.

In [8] a very small RFID Antenna is designed for a seal bolt shape but still the reading distance is limited to 3.5m. E-plate antenna design to serve as RFID tag was reported in [9] ~ [11] but this method used active RFID system where the constraint is cost of tag. Because an antenna, application specific integrated circuit (ASIC) and battery are included in an active RFID tag embedded in the e-plate. The

proposed tag antenna in [12] is installed as a tag inside a car's side-view mirror for optimum reading. In this paper the RFID Automobile plate applied to license plate is proposed. The antenna gain can increase because the license plate is conductor (made of copper) and is operated as antenna. Thus, the reading distance range can become more longer than conventional commercial tag antenna. Furthermore, it has the advantage of improved identification ratio by controlling the radiation beam pattern in a way that the vehicular license plate tag antenna can easily detected by the readers installed on the road side or tool gates as the vehicle passes through it.

2. Design of Tag Antenna

Fig. 2 shows the design structure of the proposed Automobile plate considered the vehicle bumper of plastic. It is composed of copper metal plate as license plate and plate holder, volts and nuts, and a part of vehicle bumper. The bumper is made of plastic with dielectric constant, $\epsilon_r=3.5$ and loss tangent=0.015. When general UHF tag antennas attached to a metal, the reading distance will drastically decreased because the impedance of the tag antenna is changed. In this paper the antenna is designed to attach to metal part of the car, license plate holder. Even though the kinds of Korea license plate size are various, the considered standard plate size in design is 520 mm X 110 mm X 1 mm used practically as shown in Fig. 1(a).

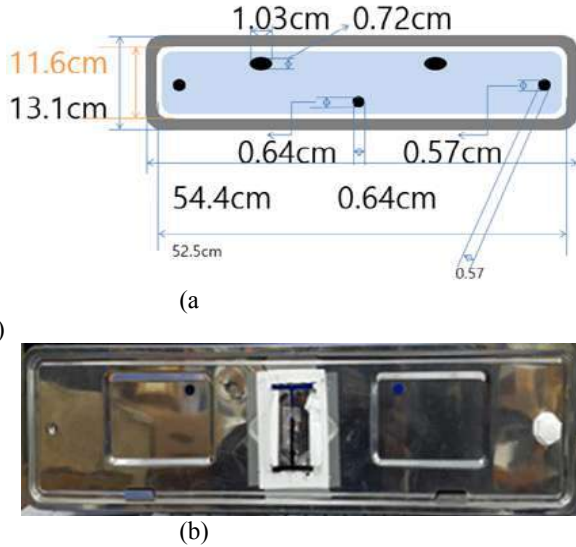


Fig.1: (a) Official standard plate size of Korea: 520mm*110mm (b) License plate holder

The proposed antenna was simulated using CST simulation software, here a discrete port has been used to represent RFID tag terminal. There is a gap of 2 mm between the two edges of discrete port. The simulated results of proposed antenna are expected to give acceptable performances at a center frequency of 920 MHz band for UHF RFID application.

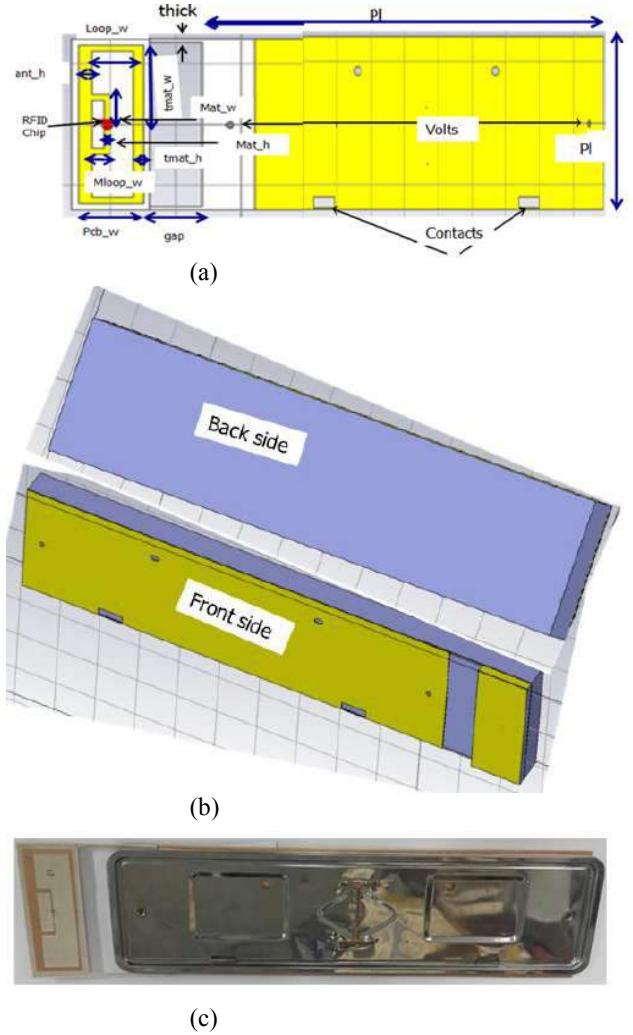


Fig.2: (a) design structure of the proposed License Plate tag antenna (b) front and back side of with bumper (c) fabricated tag antenna

3. Simulation Results and Performance

For demonstration, the proposed tag antenna is designed to operate at 920MHz. The geometric parameters defined in Fig. 2 have been designed and optimized by parameter sweeping method. The resulting optimized values are: $ph=116$, $pl=525$, $t_{mat_h}=4\text{mm}$, $ant_h=10\text{mm}$, $t_{mat_w}=65\text{mm}$, $mat_w=25\text{mm}$, $mat_h=2.2\text{mm}$, $loop_w=5\text{mm}$, $mloop_w=5\text{mm}$, $gap=40\text{mm}$, $thick=5\text{mm}$. The signal radiating towards the bumper cannot be identified by the reader, only signal radiating towards the front side of the car is readable by the reader. So we need a strong signal radiating towards front. The 0 degree in Fig. 3 means the back direction that tag antenna and reader antenna stand opposite to each other. On the other hand, the 180 degrees indicate the front direction with respect to the above back direction. Since the readers are deployed along the road side, from Fig. 3 we can see that there is strong

signal radiating towards the front direction. This is achieved by controlling the parameter values of the tag antenna.

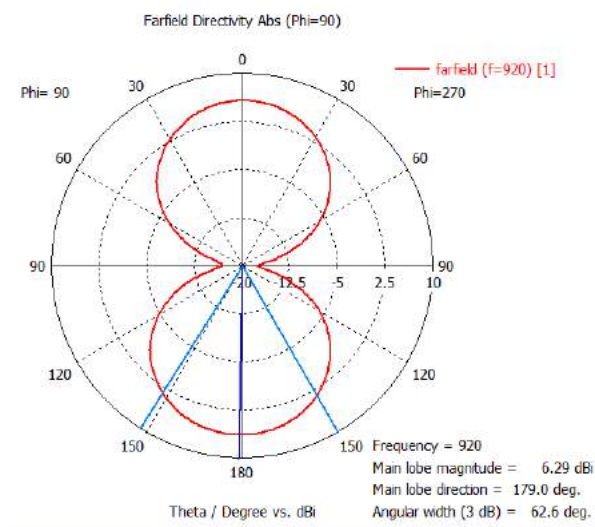


Fig.3: Polar radiation pattern of antenna at 920 MHz

The above radiation pattern will meet the requirement of the deployment of RFID readers in the management of vehicles such as in the Intelligent Transportation Systems (ITS). For example, if the reader can be placed on a lamppost on the roadside, the beam emanating from the tag antenna will allow the license plate and reader communicate with each other very well. The 3D radiation pattern in Fig. 4 shows that there is strong signal radiating from the plate towards the front and back side of the road, where readers are deployed. But still the signal strength towards the front direction is stronger, which is our desired signal level. There is no doubt that volts and nuts and the vehicle's body for the license plate to be mounted will have influence on the performance of the antenna, so all these conditions are included in our numerical simulation.

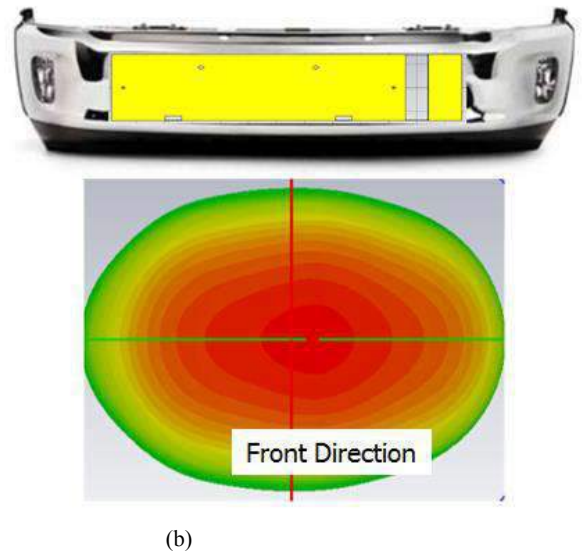
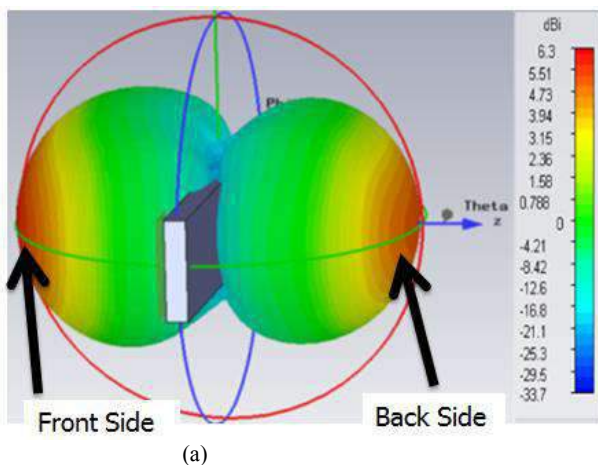


Fig.4: 3D radiation pattern of the tag antenna at 920MHz, (a) front and back side (b) front side only.

Fig. 5 shows the simulation and measured result of reflection coefficient of the proposed plate antenna. Results of simulation and measurement show that the proposed tag antenna has a reflection coefficient of 29dB and 17dB respectively at 920MHz.

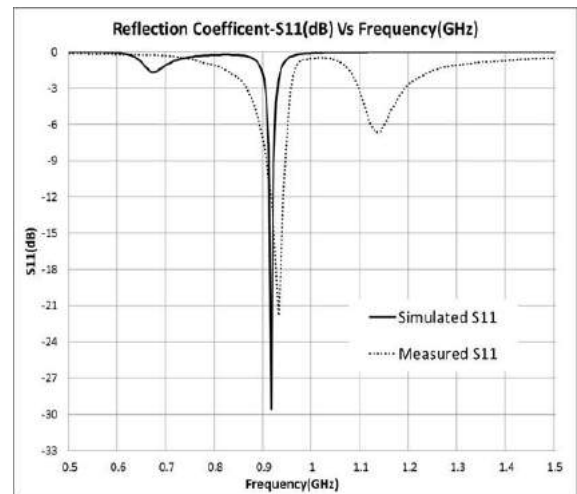


Fig 5: Simulated and measure return loss at f=920MHz

4. Conclusions

A passive automobile plate antenna is designed, and demonstrated by positioning the tag antenna on the side of plate holder. Plate dimensions are according to Korean standard license. RFID tag has approximately 29db in 910 MHz frequency and the impedance is 50Ω with T-matching. Performance analysis of the proposed license plate indicates that the proposed plate met the requirements for on-road vehicle identification when the RFID readers are deployed on the roadside lampposts.

References

- [1] Finkenzeller, RFID handbook, 2nd edition, John Wiley & Sons, England, 2011.
- [2] Y. C. Chung "A study on animal information management system using an insertion type UHF RFID tag", Journal of KICS, Networks, vol. 36, no. 12, pp. 1680- 1685, Dec. 2011.
- [3] Wenjing Zhao, Xunguang Ju1 and Shuangjiang Wu, "RFID-Based E-Plate with Slot-Dipole Antenna Design and Roadside Interrogator Deployment", The Open Electrical & Electronic Engineering Journal, pp. 27-33, 2014.
- [4] Dae-Hwan Park and Kyeong-Sik Min,"Design for a Tag Antenna Using License Plate Attached Vehicle Bumper", The Korean Institute of Electromagnetic and Science, 20(6), pp. 535-543, June. 2009.
- [5] Dae-Hwan Park and Kyeong-Sik Min, "Design for license plate RFID tag antenna with dual resonance to improve identification ratio", IEEE Proceedings of the Fourth European Conference on Antennas and Propagation, pp. 1-4, 2010.
- [6] Kyeong-Sik Min and Jin-Woo Kim " Experimental Performance Evaluation according to the Sticked Backside Plate of Dipole Antenna for RFID Tag", The Korean Institute of Electromagnetic and Science, 18(3), pp. 273-281, March. 2007.
- [7] K. Penttila, M. Keskilammi, L. Sydanheimo, and M. Kivikoski, "Radar cross section analysis for passive RFID system", IEEE Microwave and Wireless components letters, 153(1) February. 2006.
- [8] Kisis Kim*, Changhwan Seol, Jihye Kim, Myeongeun Lee, Youchung Chung, "A Study on Detecting Illegal Automobile Detection System Using an UHF RFID tag Antenna for Seal-Bolt Shape", KICS. 2016, pp. 169-170
- [9] Evizal, Tharek Abd Rahman, Sharul Kamal Abdul Rahim, "RFID Vehicle Plate Number (e-Plate) for Tracking and Management System", IEEE International Conference on Parallel and Distributed Systems, pp. 611-616. 2013.
- [10] Evizal, Tharek Abd Rahman, Sharul Kamal Abdul Rahim, "RFID Tag Antenna Design For Vehicle Plate Number (e-Plate)", TELKOMNIKA Telecommunication, Computing, Electronics and Control, Vol 11, No 2. 2014
- [11] Z. Wenjing, et al., "Active E-Plate with Slot Antenna," in Wireless Communications, Networking and Mobile Computing, 2008. WiCOM '08. 4th International Conference on, 2008, pp. 1-3.
- [12] K. Min-Seong, et al., "Directivity Design of RFID Tag Antenna Using Side-view Mirror for Vehicle," in Microwave Conference, 2008. APMC 2008. Asia-Pacific, 2008, pp. 1-4.

Electromagnetic Theory

Electromagnetic Wave Absorption Properties of Novel Green Composites Coconut Fiber Coir and Charcoal Powder over X-band Frequency for Electromagnetic Wave Absorbing Applications

N. F. N. Yah^{1*}, H. A. Rahim¹, Y. S. Lee², F. H. Wee¹, and H. H. Zainal¹

¹Bioelectromagnetic Research Group (BioEM), School of Computer and Communication Engineering, Universiti Malaysia Perlis (UniMAP), Kampus Pauh Putra, 02600, Arau, Perlis, Malaysia

²Department of Electronic Engineering Technology, Fakulti Teknologi Kejuruteraan, Universiti Malaysia Perlis (UniMAP), Perlis, Malaysia

*corresponding author: fatihahnabila@studentmail.unimap.edu.my

Abstract

This paper presents the electromagnetic wave (EW) absorption properties, complex permittivity and permeability, of novel green composites coconut fiber coir and charcoal powder materials. The samples were fabricated using raw agricultural waste coconut fiber coir, charcoal powder, epoxy resin and hardener with varied composition. The dielectric properties of the materials were characterized using two-port waveguide measurement method over the X-band frequency (8.2 – 12.4GHz). The result shows the composite material is a promising organic material for electromagnetic absorber applications.

1. Introduction

As an electromagnetic wave travelling in free space penetrates into a material, the wave will be reflected, transmitted or absorbed [1]. The design of electromagnetic wave absorber is enhanced with material having electric or magnetic dipoles. Absorption properties of a material is usually analyzed and determined by two material parameters; permittivity and permeability [1], [2]. Permittivity and permeability relate to a material's ability to transmit an electric field and magnetic field respectively. Based on these parameters, materials are classified as either dielectric or magnetic. Complex permittivity ($\epsilon^* = \epsilon' - j\epsilon''$) and complex permeability ($\mu^* = \mu' - j\mu''$) describe the interactions of electromagnetic wave through a material. The real parts of complex permittivity and permeability (ϵ' , μ') are associated with electric and magnetic energy storage, whereas the imaginary parts (ϵ'' , μ'') represent the dielectric and magnetic loss or energy dissipated within a material. Furthermore, the ratio of imaginary parts (energy loss) to the real parts (energy stored) is the loss tangent of the complex permittivity and permeability. Thus, for an electromagnetic wave absorber, high imaginary parts of complex permittivity and permeability will enable greater absorption.

Recently many researchers show interest in EM wave absorbing material due to widespread use in military and

civil applications, such as anechoic chambers, EM shielding, and radiation proof material [3]. Various kinds of research and work have been done into finding the ideal EM wave absorber with a lightweight, thin layer, good absorption and wider broadband. EM wave absorbers are mostly made of polymer and absorbing material composite such as carbon nanotubes, ferrite and ultrafine metal powder. However, there has been growing expectation by consumers and industry to use sustainable materials or green technologies. Due to this, organic materials such as agricultural wastes have gained a lot of interest among researchers. Different types of microwave absorbers from varied agricultural wastes have been studied such as rice husk [4], sugar cane bagasse [5], corn stove [6], dried banana leave [7], oil palm ash [8] and many others.

To the best of authors' knowledge, no work has been done for the electromagnetic wave absorption properties of composite coconut fiber coir. Coconut fiber coir is a coconut by-product mostly from coconut milk processing field that is physically abundant and cheap [9]. Therefore, in this work, the performance of green organic coconut fiber coir as a microwave absorber was investigated.

This paper is organized into four parts. In part two the preparation and measurement of the sample are explained. Next the paper discusses and analyzes the result obtained from the measurement. Lastly the potential of coconut fiber coir as microwave absorber briefly discuss in conclusion.

2. Methodology

The first step of the measurement is to collect the material which is coconut fiber coir for the sample preparation. The material was grinded into powder form using grinding machine. Then, it was mixed different percentage of charcoal and also the epoxy resin as bonding agent and later mixed with epoxy hardener as hardening agent. The composition of the coconut fiber coir with charcoal, resin and hardener are 50wt%, 40wt% and 10wt% respectively as represent in Table 1.

Table 1 : Compositions of each sample

Sample	Coconut Fiber Coir	Charcoal	Epoxy Resin	Epoxy Hardener
0wt% charcoal	5.0g	0.0g	4.0g	1.0g
5wt% charcoal	4.5g	0.5g	4.0g	1.0g
10wt% charcoal	4.0g	1.0g	4.0g	1.0g
15wt% charcoal	3.5g	1.5g	4.0g	1.0g
100wt% charcoal	0.0g	5.0g	4.0g	1.0g

The samples were fabricated in a rectangular mould with the same dimension as the WR-90 waveguide adapter that operates in the specific frequency range of x-band (8.2GHz – 12.4GHz). Five samples of coconut fiber coir / charcoal composite with different weight percentage (0wt%, 5wt%, 10wt%, 15wt%, and 100wt%) of charcoal powder were fabricated.

The characterization of coconut fiber coir was conducted through extensive measurements using high performance measurement equipment which is two-port Agilent Network Analyzer model PNA and software Agilent Technologies 85071E. The complex permittivity and permeability of the samples were measured over the X-band frequency using two-port waveguide measurement method with Agilent Network Analyzer [10]. Two-port waveguide transmission line was applied for this project for its high accuracy.

3. Result and Discussion

Fig. 1 - 4 shows the complex permittivity and permeability obtained from the measurement.

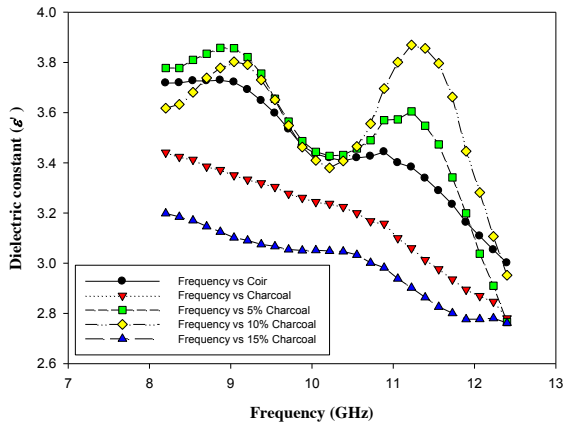


Figure 1 : Dielectric constant of 5 different samples

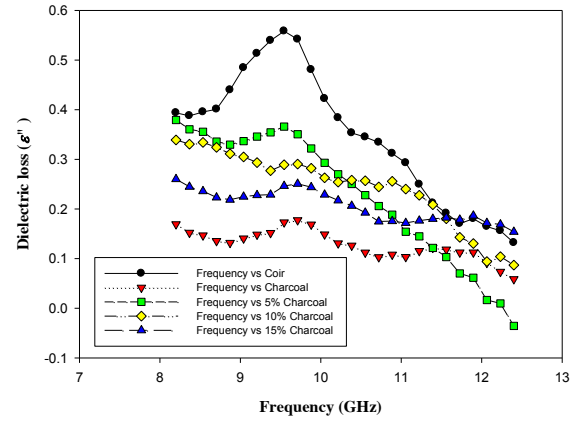


Figure 2 : Dielectric loss of 5 different samples

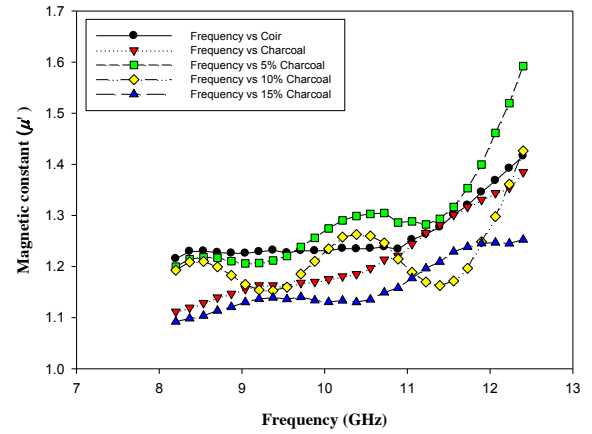


Figure 3 : Magnetic constant of 5 different samples

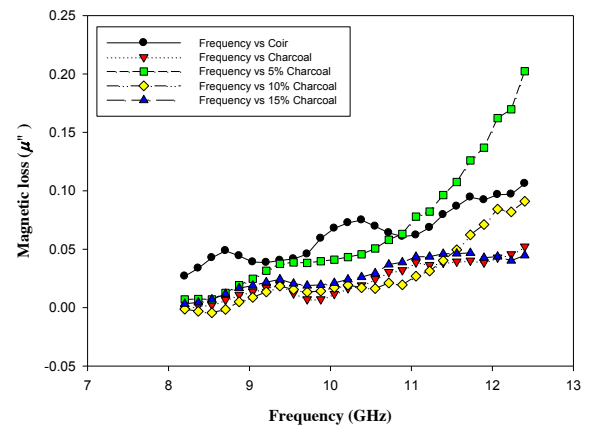


Figure 4 : Magnetic loss of 5 different samples

From Fig. 1, it can be observed that the performance of the samples varies when the frequency increases from 8.2GHz to 12.4 GHz. However, the result shows that the sample

with 5wt% and 10wt% of charcoal exhibits higher value of dielectric constant compared to the other composition. In addition, the graph in Fig. 4 also shows that the magnetic loss factor, μ'' of the samples increases with the increases of frequency. Higher loss factor enable greater electromagnetic wave absorption. Thus, with an optimal percentage of charcoal powder, the best performance for coconut fiber coir composite microwave absorber could be achieved.

4. Conclusions

As conclusion, the coconut fiber coir and charcoal composite with different percentage of charcoal were investigated to determine their complex permittivity and complex permeability. The performance of the samples varies when the frequency increases. The result from the measurement shows that coconut fiber coir has promising properties to be developed into a suitable material for microwave absorber.

Acknowledgements

The authors would like to thank School of Computer and Communication, Universiti Malaysia Perlis for the support and facilities.

References

- [1] F. M. Idris, M. Hashim, Z. Abbas, I. Ismail, R. Nazlan, and I. R. Ibrahim, "Recent developments of smart electromagnetic absorbers based polymer-composites at gigahertz frequencies," *J. Magn. Magn. Mater.*, vol. 405, pp. 197–208, 2016.
- [2] S. T. Liu, K. K. Yan, Y. H. Zhang, S. Di Jin, Y. Ye, and X. G. Chen, "Magnesiothermic reduction of rice husk ash for electromagnetic wave adsorption," *J. Magn. Magn. Mater.*, vol. 394, pp. 266–273, 2015.
- [3] Y. Ding, Q. Liao, S. Liu, H. Guo, Y. Sun, and G. Zhang, "Reduced Graphene Oxide Functionalized with Cobalt Ferrite Nanocomposites for Enhanced Efficient and Lightweight Electromagnetic Wave Absorption," *Nat. Publ. Gr.*, no. April, pp. 1–9, 2016.
- [4] L. Y. Seng, F. H. Wee, H. A. Rahim, M. AbdulMalek, Y. K. You, Z. Liyana, and A. A. M. Ezanuddin, "Design of multiple-layer microwave absorbing structure based on rice husk and carbon nanotubes," *Appl. Phys. A*, vol. 123, no. 1, p. 73, 2017.
- [5] Z. Liyana, F. Malek, H. Nornikman, N. A. Mohd Affendi, L. Mohamed, N. Saudin, and A. A. Ali, "Investigation of sugar cane bagasse as alternative material for pyramidal microwave absorber design," *IEEE Symp. Wirel. Technol. Appl. ISWTA*, pp. 66–70, 2012.
- [6] B. Smythe, S. Casserly, and D. Arakaki, "Organic-based microwave frequency absorbers using corn stover," *IEEE Antennas Propag. Soc. AP-S Int. Symp.*, pp. 920–921, 2014.
- [7] R. Kaur, G. D. Aul, and V. Chawla, "Improved Reflection Loss Performance of Dried Banana Leaves Pyramidal Microwave Absorbers by Coal for Application in Anechoic Chambers," vol. 43, no. July, pp. 157–164, 2015.
- [8] I. R. M. Noordin, H. Abdullah Idris, M. N. Taib, J. Md Sharif, A. D. Rosli, A. Zanal, and A. T. Abdullah, "Investigation of oil palm ash microwave absorber for broadband application," *Proc. - 2012 IEEE 8th Int. Colloq. Signal Process. Its Appl. CSPA 2012*, pp. 232–235, 2012.
- [9] B. S. Yew and F. H. Wee, "A GRICULTURAL WASTE BASED -COCO PEAT MICROWAVE," *Int. J. Eng. Sci. Emerg. Technol.*, vol. 7, no. 2, pp. 547–554, 2014.
- [10] "Agilent Basics of Measuring the Dielectric Properties of Materials," 5989–2589EN, 2013.

Antenna and Propagation

T-Shaped Slot Antenna Design for Handsets with Metal Back Cover

T.-H. Hsieh^{1*}, W.-R. Lin¹, S.-K. Tuan¹, and W.-J. Liao¹

¹National Taiwan University of Science and Technology, Taiwan

Email: M10407622@mail.ntust.edu.tw

Abstract—Broadband LTE antenna design is challenging for handsets with metal body enclosures. In this work, a T-shape open-ended slot antenna embedded in the metal back cover is proposed. Two feeds are placed on different slot locations. The low-band feed excites the one-end open slot to cover the 698 to 960 MHz band. The other feed excites the two-end open slot arm to operate in both 1710 to 2690 and 3400 to 3600 MHz bands.

Introduction: In recent years, metal body handsets have been embraced by smartphone manufacturers for flagship products due to customers' preference. Nevertheless, the metal housing can be quite a challenge for antenna designers. Various types of antennas have been attempted on handheld devices to meet the ever growing bandwidth need. In order to reduce antenna sizes and increase the operating bandwidth, the coupling feed [1] and the lumped component technique [2] have been devised. The slot antenna, which is compatible with the metal body, can meet many antenna operation needs [3]. Nevertheless, slot antennas may require customized feed networks since they tend to be narrow banded. Also, if the LTE-Advanced antenna is designed with active components, the design of the feed network would be even more challenging [4].

In this paper, an LTE antenna design that can be placed on the top edge of a metal handset is developed. The form factor is rather compact while the LTE/WWAN band coverage is comprehensive. Simulations and measurements are conducted to validate its superior performances.

Antenna Design: The geometry of the proposed T-shape open slot antenna is shown in Fig. 1. It is placed on the metal back cover of a 5-inch smart phone. Close-up views of the slot region are shown to the right of Fig. 1. The antenna locates near the top edge of the $150 \times 75 \text{ mm}^2$ back cover. Slot openings are placed on the metal rim to reduce visual intrusion. The bended slot on the corner has both ends open. The straight slot, which has an opening on the rim, contains a thin metal strip in the middle. The slot width is 3mm. The length of the two slot arms are 49 and 26 mm, respectively. The fabricated prototype uses a 0.8 mm-thick FR4 substrate to emulate the handset back cover. FR4 strips of 7 mm-wide and 0.8 mm-thick are attached to the back cover to form the metal rim of the handset.

The low-band coupled feed contains a 50Ω microstrip line embedded with a matching network for the low band, which is a L-matching circuit formed by chip inductor L1 of 22 nH, L2 of 5.1 nH and a chip capacitor C1 of 1.2 pF. The matching network achieves two resonances in the low band, which merge into a wide operation band that extends from 698 to 960 MHz. On the other hand, the high band feed is placed directly across the two-end open slot.

Results: Simulated and measured reflection coefficient spectra as well as total radiation efficiency are compared in Fig. 2. Resonance locations of the prototype match well to simulated ones while measured matching nulls are deeper in general. A comprehensive LTE band coverage can be achieved according to the 3:1 VSWR criterion. As to the radiation efficiencies, the numbers are above 40% in the low band and are in general greater than 70% in LTE mid and high bands.

Conclusion: A multi-band and T-shaped open slot antenna is developed for handheld devices with metal back covers. The slot antenna is placed at the device edge. Comprehensive LTE/WWAN operation, which includes the 698 to 960, 1710 to 2690, and 3400 to 3600 MHz bands, is achieved. This design yields two broad operation bands using two feeds. This feeding scheme makes antenna tuning much easier in each band. Measured matching and radiation results demonstrate that the T-shaped open slot antenna design is applicable to uses on metal body smart phones without compromises on performance.

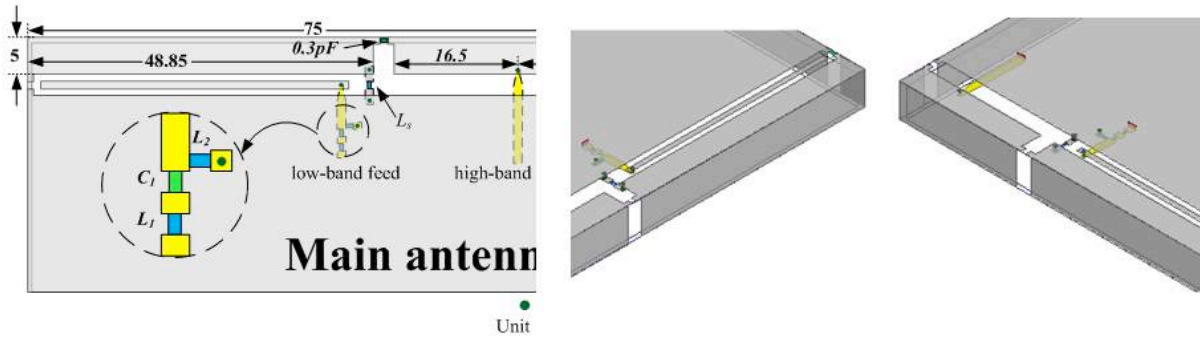


Figure 1: Geometry and closed-up view of the proposed T-shaped slot antenna design

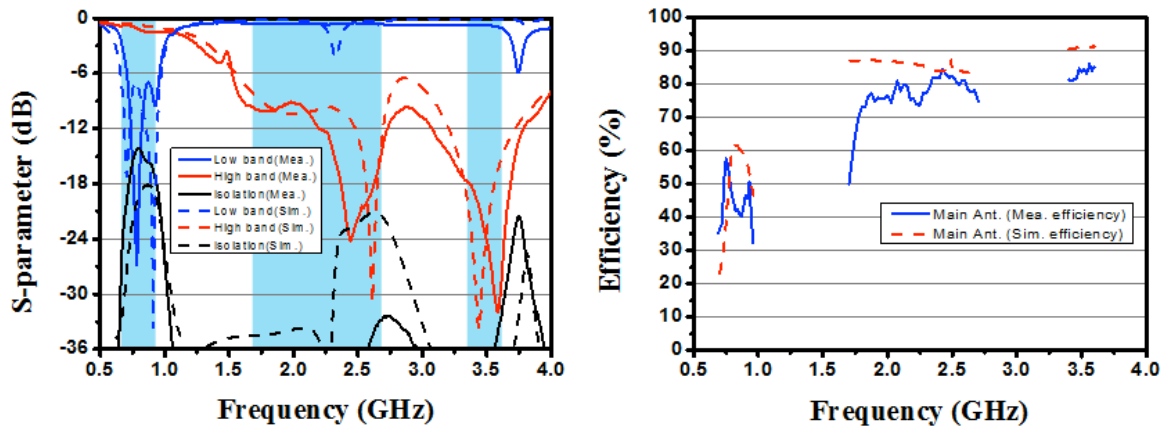


Figure 2: Simulated and measured reflection coefficient and radiation efficiency of the proposed design.

REFERENCES

1. C.-T. Lee and K.-L. Wong, "Planar monopole with a coupling feed and an inductive shorting strip for LTE/GSM/UMTS operation in the mobile phone," *IEEE Trans. Antennas Propag.*, Vol. 58, No. 57, pp. 2479–2483, 2010.
2. K. -L. Wong and C.-Y. Tsai, "Small-size stacked inverted-F antenna with two hybrid shorting strips for the LTE/WWAN tablet device," *IEEE Trans. Antennas Propag.*, Vol. 62, No. 8, pp. 3962–3969, 2014.
3. C.-K. Chang, W.-J. Liao and C.-C. Tsai, "Metal body-integrated open-end slot-antenna designs for handset LTE uses," *IEEE Trans. Antennas Propag.*, Vol. 64, No. 57, pp. 5436–5440, 2016.
4. T.-W. Kang, and S.-H. Yeh, " Multi-band LTE-advanced antenna design for mobile phone", in *Proc. Asia-Pacific Conference on Antennas and Propagation (APCAP)*, pp. 191–192, 2016.

Performance Optimization of Copper Tube Antenna Design for Outdoor Access Points

S.-K. Tuan^{1*}, W.-R. Lin¹, H.-J. Hsieh¹, and W.-J. Liao¹

¹National Taiwan University of Science and Technology, Taiwan

*Email: M10407601@mail.ntust.edu.tw

Abstract- This work aims to optimize the copper tube antenna design, which contains radiating elements connected in series. It provides an omnidirectional coverage for outdoor access point uses. In-depth analyses are performed by establishing a numerical model. Various parametric studies are conducted to explore measures for improving the performance. An eight-element design is optimized to yield a 6 to 7 dBi gain on the azimuthal plane. The antenna operation frequency ranges from 5.15 to 5.85 GHz.

Introduction- For conventional mobile wireless communication protocols, the outdoor access point is an indispensable part since it relays mobile users to the backhaul network. Because the user locations are not fixed, the access point usually desires an omnidirectional coverage on the azimuthal plane. Various attempts have been made to devise cost-effective high-performance omnidirectional antenna. In [1], a broadband dual-polarized planar antenna for base station is developed for base stations. A compact design is provided in [2] using inverted-F antennas and a compact feeding network. A printed dipole array that provides coverage on the azimuthal plane is proposed in [3]. Its bandwidth is enhanced by using impedance matching feed circuit. However, all above design use the parallel type feeding network, which incurs substantial loss for large scale designs. On the other hand, the serial connected radiating elements may provide an attractive frame work if the array size is not fixed. The copper tube antenna as shown in Fig. 1 is a well-known example. It has several half-wavelength long coaxial segments, which are connected in a staggered fashion by reversing the inner and outer conductors. Such a connection scheme constitutes a 180° phase inverter and hence radiates a small fraction of the power passing through the coaxial feed line. Though, it seems one can enhance the antenna gain by increasing the number of element, this can only be done by controlling the amounts of radiation from those phase inverters. Therefore, in this work, we study the radiation mechanism by first establishing a realistic model, then fine tuning the performance by looking into current distributions.

Antenna Structure- The design shown in Fig. 1 consists two sections. The leading section contains the connector and the impedance matching line. The radiating section in the back comprises eight copper tube segments. It is aimed to be used in the 5 GHz hyperLAN band for outdoor WLAN access points. A simulation model is made according to the fabricated antenna. The length of the antenna is 247 mm. Each half-wavelength copper tube is 19 mm long. The leading impedance transform section is 75 mm long, which is equivalent to 1.5 guided wavelengths. The impedance can be adjusted by changing the inner to outer radius ratio. The half-wavelength copper tube segment is 19 mm long. The thickness of the Teflon spacer between segments is 1 mm. The radius of the inner conductor is 1 mm, the radius of the short copper tube is 2.5 mm. The copper tube thickness is 0.5 mm.

Results- As can be seen from Fig. 2(a), the real part of the impedance without the transformer is 34 to 127 Ω . On the other hand, the resistance is 26 to 83 Ω . Fig. 2(b) shows the reflection coefficient spectrum. The simulated -10 dB band is from 5.16 to 6.3 GHz, while the measured bandwidth is from 5.35 to 5.55 GHz. It

demonstrates that by fine tuning the design parameter via simulation, the impedance matching performance can be greatly improved. Fig. 3 shows simulated and measured radiation pattern. In the elevation plane (XZ plane), the gain maximum is 6.29 dBi and the measured maximum is 6 dBi. An omnidirectional pattern is observed in the horizontal plane (XY plane). After the design optimization, the gain on the azimuthal plane is improved by more than 3 dB.

Conclusion- In this paper, we demonstrate that design optimization can be preceded by simulation for the omnidirectional copper tube antenna. Both the matching bandwidth and gain performances are substantially improved. This approach can be forwarded to configure longer design for achieving higher gains.

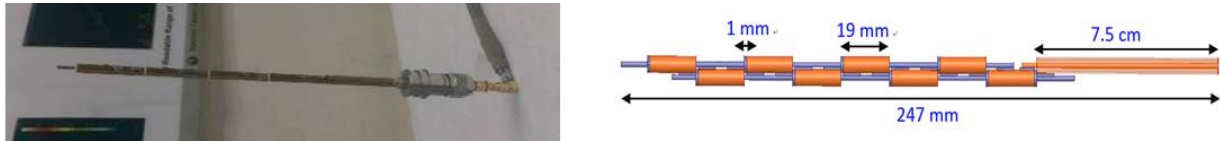


Figure1. Proposed copper tube antenna structure

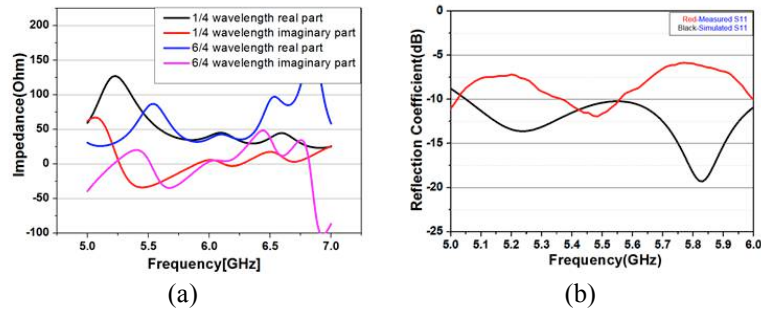


Figure 2. Matching performance. (a) simulated impedance, (b) simulated and measured reflection coefficient.

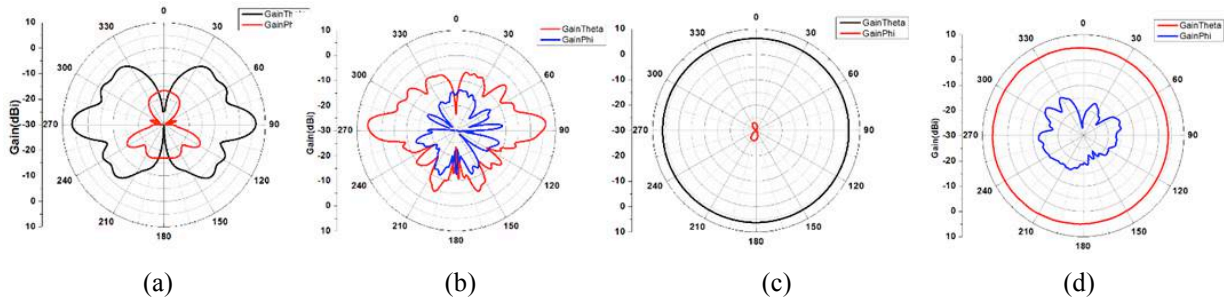


Figure 3. Radiation patterns of the copper tube antenna. (a) simulated XZ plane, (b) simulated XY pattern, (c) measured XZ pattern, (d) measured XY pattern.

REFERENCES

1. Xu, H.-J., X.-W. Zhu and Z.-Q. Kuai, "Broadband dual-polarized antenna and array for mobile for mobile communication base station," in *APMC*, Nanjing, China, December 2015, 1-3.
2. Liu P., J. Zhang, S. Lu and J. Lin, "Design and achievement of miniaturization in Wi-Fi base station antenna," in *APCAP*, Harbin, China, July 2014, 208-211.
3. Yu, C., W. Hong, X. Zhu and Z. Kuai, "A new printed dipole array omnidirectional antenna with bandwidth enhancement," in *ISSSE*, Nanjing, China, September 2010, 1-3.

Design and Realization of A Patch Array Integrated with System Board of WLAN Point-to-Point Link Device.

W.-R. Lin^{1*}, T.-H. Hsieh¹, H.-R. Hsieh¹ and W.-J. Liao¹

¹National Taiwan University of Science and Technology, Taiwan

*Email: M10407614@mail.ntust.edu.tw

Abstract—This paper presents a low-cost, low-profile, two-element patch array design, that utilizes the system board of a WLAN device as the patch ground plane. Due to imperfections on the circuit board, realizations of air transmission line and resonant cavity are challenging. By developing a detailed numerical model, effects of connector pins and apertures on the board can be assessed. Measurement results suggest that matching, pattern, and cross polarization performances can be maintained using the system board.

Introduction: As the wireless technology prevails, mobile communication gadgets are becoming people's everyday necessity. Since consumer electronics are sensitive to the cost issue, various measures have been devised to reduce product fabrication cost. The antenna component is of no exception. In this work, we attempt to use the system board of a point-to-point link device as the ground plane of a two-element patch array. Because the system board dimensions are about two times larger than the half wavelength patch at 2.4 GHz, substantial fabrication cost can be saved if the patch array can do without an additional ground slab.

For a point-to-point wireless communication device, a directive high gain antenna is an indispensable part [1]. The patch antenna is a common used approach. It contains either a square or a circular patch on one side and a ground plane, which is larger than the patch, on the other side. The patch and the ground forms a resonant cavity and the patch sizes in general the resonant frequency. Therefore, one can employ a dielectric substrate to reduce the patch sizes [2]. The trade-off of such a measure is the drop in radiation efficiency. Note, the patch antenna's polarization characteristic is quite versatile. According to the feeding scheme, a patch can be configured into linear, circular, and even two orthogonal polarizations [3]. Fig. 1 shows the system board inside the product enclosure. The close-up view shows that on top of surface-mount components, the board also contains connector pins and various apertures including slits, slots, and holes. Though these structures are relatively small in terms of wavelength, the patch characteristics may be disturbed.

Antenna Design: According to system board dimensions, ground plane sizes of the two-patch array are set as $70 \times 220 \text{ mm}^2$. Since a point-to-point device can employ the MIMO technology to enhance the throughput, the diversity antenna measure can be applied. For this end, the patch array is configured with two perpendicular polarizations. As shown in Fig. 2, air transmission lines are branched from the feeding pins, and are attached to patch edges. Note, the left of the top line is longer than the right one by a half-wavelength to align excitation phases, and the bottom line begins with a 60Ω wide sections before branching to two 120Ω lines. The $51.7 \times 56 \text{ mm}^2$ patches as well as the air transmission lines are fabricated with a 0.5 mm thick aluminum sheet. The metal layer is hanged above the system board by 4 mm. The patch and line locations are chosen to avoid apparent apertures on the board.

Results: Matching and radiation measurements are performed for the proposed array antenna. In order to

provide a baseline reference, measurements are also conducted for the patch layer placed on a solid ground made of intact copper sheet. Fig. 3 compares the results shows reflection coefficient spectra. Though the performance characteristics are similar for the two design. The one with solid ground yields higher radiation efficiencies and the peak gain difference between the two ports is smaller.

Conclusion: Results of this work demonstrates that the system board can be used as the patch antenna ground plane to save cost. However, structures on the board more or less affect the antenna performances. Acceptable results can be achieved by avoid critical radiating and transmission line structures from apparent defect locations.



Figure 1. The system board of a WLAN point-to-point link device and close-up view of board structures.

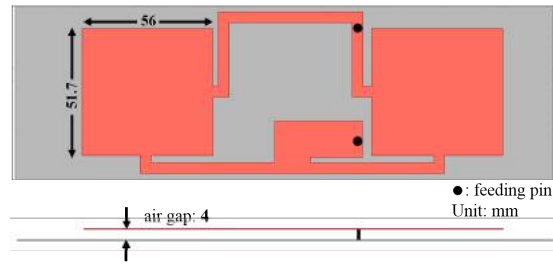
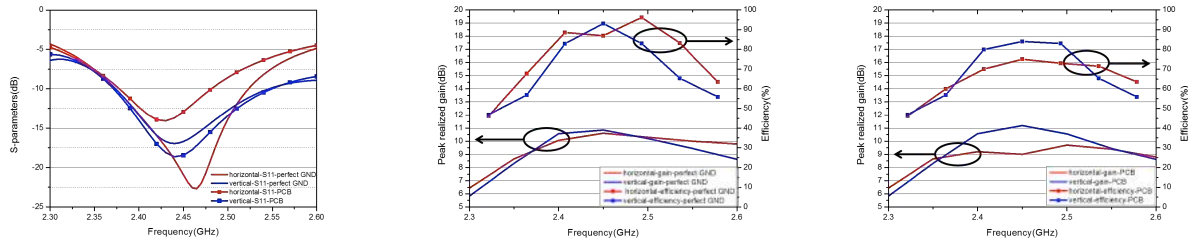


Figure 2. Top view and side view of the proposed patch antenna array.



(a) Reflection coefficients, (b) efficiency and gain on solid metal sheet, (c) efficiency and gain on PCB

Figure 3 Comparison of measured matching and radiation performances.

REFERENCES

1. Wu C., H. Wang, X. Jiang, S. Quan and X. Liu, "High-gain dual-polarization higher order mode substrate integrated cavity antenna array," in *proc. International Symposium on Antennas, Propagation and EM Theory (ISAPE)*, pp. 129–131, 2016.
2. Haris Hadžić, Wally Verzotti, Zoran Blažević and Maja Škiljo, "2.4 GHz micro-strip patch antenna array with suppressed sidelobes," in *proc. International Conference on Software, Telecommunications and Computer Networks (SoftCOM)*, pp. 96–100, 2015.
3. C-T Chiang and W-J Liao, "A broadband dual-polarization patch array," in *proc. Asia-Pacific Conference on Antennas and Propagation (APCAP)*, pp. 89–90, 2016.

Computational Analysis of a Novel Yagi-Uda Antenna for VHF Band

R. E. Musril¹, H. A. Rahim^{1*}, M. Abdulmalek², and M. Jusoh¹

¹Bioelectromagnetics Research Group (BioEM),

²Advanced Communication Engineering (ACE),

School of Computer and Communication Engineering, Universiti Malaysia Perlis (UniMAP),

Kampus Pauh Putra, Perlis, Malaysia

³Department of Engineering and Information Science, University of Wollongong in Dubai, Block 15,
Dubai Knowledge Village, Dubai, UAE

⁴ESAT-TELEMIC Research Div., Katholieke Universiteit Leuven, Kasteelpark Arenberg 10, 3001
Leuven, Belgium

*corresponding author: haslizarahim@unimap.edu.my

Abstract- This paper presents computational analysis of a novel Yagi-Uda antenna for Very High Frequency (VHF) band. The analysis is performed using CST Microwave Studio Suite software. The structure of this directional antenna integrates three main parts which are directors, reflectors and feeder point of 50Ω. The gain of the antenna increases up to 2 % when added with 7 elements of reflector than with one element of reflector and enhanced significantly by 23.6% compared to the conventional Yagi-Uda antenna.

Very high frequency (VHF) band is widely used in a long range communication system, enabling communication across the cities and the rural regions. An amateurish radio that utilizes the VHF band is used to extend the communication range of the base stations in remote areas and provide 100% coverage of the amateur radio system in Peninsular Malaysia. The aim of the amateur radio is to offer secondary coverage during the harsh environment especially emergency, disaster and distress rural areas. Thus, it is important in designing the Yagi-Uda antenna for local communities in rural areas so as to channel the information in a wide range area through the amateurish radio VHF band. Yagi-Uda has been utilized by amateur radio group. However, such antenna is deprived of a wide coverage in rural areas, thereby, leading to poor communication links in that most needed areas. Thus, in this work, a new Yagi-Uda antenna is designed to achieve an enhanced gain with good impedance bandwidth at resonant frequency of 144 MHz.

The proposal antenna is designed using electromagnetic solver, CST Microwave Studio Suite software. A directional simple 7 elements Yagi with 3.7 m boom length for the lower 144 MHz is modeled and designed. The dimensions of the optimized antenna structure are presented in Table 1.

Table.1. Design specification of Yagi-Uda antenna.

Specification	Value	Specification	Value
Length of Reflector (R)	0.482λ	Spacing b/n Reflector and Driven Element	0.238λ
Length of Driven Element(DE)	0.48λ	Spacing b/n Driven Element and Director 1	0.124λ
Width of Feed Element (FE)	0.009λ	Spacing b/n Director 1 and Director 2	0.287λ
Length of Director 1 (D1)	0.457λ	Spacing b/n Director 2 and Director 3	0.335λ
Length of Director 2 (D2)	0.446λ	Spacing b/n Director 3 and Director 4	0.431λ
Length of Director 3 (D3)	0.437λ	Spacing b/n Director 4 and Director 5	0.335λ
Length of Director 4 (D4)	0.430λ	Diameter of elements	0.0014λ
Length of Director 5 (D5)	0.443λ		

The additional of reflector design with 7 elements improves the gain significantly by 23.6% more than the conventional Yagi-Uda. This can be explained by two principles in which the far-field pattern of a Yagi-Uda array may be "tuned" or adjusted for a particular frequency. In this work, the priority focuses more on changing the reflector design and it will change the level of back lobe and control the impedance. The 10-dB impedance bandwidth resonates at 144.46 MHz and remains unchanged regardless the number of elements of reflector. The maximum gain of 14.03 dB is achieved for this proposed design at 144 MHz.

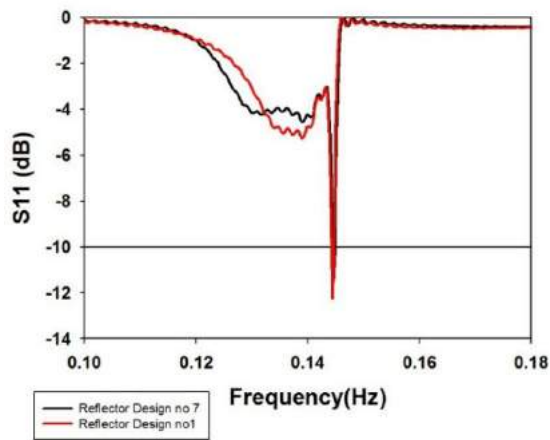


Figure 1: Reflection coefficient, S_{11} of proposed Yagi-Uda antenna.

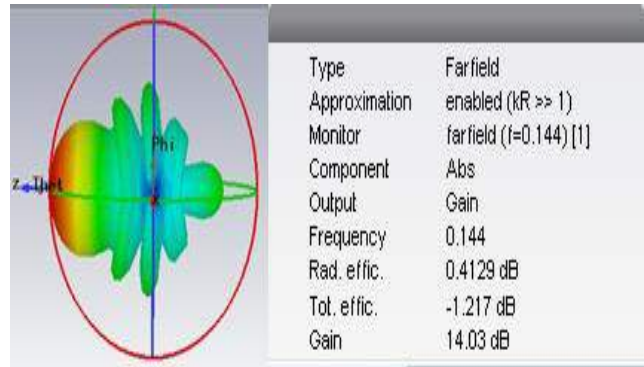


Figure 2: Gain and 3D radiation pattern of proposed Yagi-Uda with 7 elements of reflector.

REFERENCES

1. A. Jharesh, K.Ch.Sri Kavya and S. K .Kotamraju, "Design and Simulation of Cylindrical and Sheet Corner Reflector Yagi Uda Antennas for Amateur Radio Application." ARPN Journal of Engineering and Applied Sciences, vol.10,No.10,June 2015.
2. J. Laviada. 2013. Antenna Manufacturing at VHF Frequencies Applied to Weather-Satellite Data Reception. IEEE Antennas and Propagation Magazine. 55(3).

Dynamic Subject-Specific On-Body Communication Channel

Models for WBAN

H. A. Rahim^{1*}, P. J. Soh², M. Abdulmalek³, M. Jusoh¹ and G. A. E. Vandenbosch⁴

¹Bioelectromagnetics Research Group (BioEM),

²Advanced Communication Engineering (ACE),

School of Computer and Communication Engineering, Universiti Malaysia Perlis (UniMAP),

Kampus Pauh Putra, Perlis, Malaysia

³Department of Engineering and Information Science, University of Wollongong in Dubai, Block 15,

Dubai Knowledge Village, Dubai, UAE

⁴ESAT-TELEMIC Research Div., Katholieke Universiteit Leuven, Kasteelpark Arenberg 10, 3001

Leuven, Belgium

*corresponding author: haslizarahim@unimap.edu.my

Abstract- This paper presents a small-scale fading channel derivation of the dynamic and subject-specific on-body communications channel characteristics at 2.45 GHz. A slotted planar inverted F-antenna (PIFA) fixed on the right upper arm is used as the transmitting antenna in this investigation. Results showed that the lognormal distribution provides the best fit to model the small-scale fading for on-body communication channel in a dynamic and subject-specific environment compared to Normal, Nakagami- m , Weibull and Rician distributions.

The reducing size of wearable hardware, embedded software, and digital signal processing has made it possible to be integrated onto the human body. Wireless Body Area Network (WBAN) has been expanding in a wide range of fields, such as medical monitoring and sensing, emergency response, military, sports, and in the multimedia field. Several sensors, which are made from textile/conventional materials, are integrated into such clothing to enable the monitoring of vital signs such as, electrocardiography (ECG), blood pressure, respiratory rate, and temperature. This form of smart clothing has offered greater flexibility and comfort to the individuals in consistently monitoring their health regardless of location.

Very few publications have addressed the subject-specific effects on the on-body path loss characteristics [1-3]. Researchers in [1] numerically investigated the effects of different body sizes and heights in stationary narrowband 2.4 GHz WBAN channels using the Finite Difference in Time Domain (FDTD) technique. It was found that the on-body radio channel characteristic was indeed influenced by the size and height of the human body. Next, a numerical and experimental investigation of a subject-specific on-body propagation channel for narrowband WBAN (2.4 GHz) under LOS and NLOS conditions was presented in [2]. A more recent study [3] proposed two linear models to estimate the subject-specific effects for LOS and NLOS scenarios based on parallel FDTD (PFDTD) technique in static condition. For all three investigations for the NLOS case, only one on-body link has been considered, i.e., on the waist. However, to the best of our knowledge, there has been no report on the subject-specific effects on the dynamic on-body communication channel characteristics at 2.45 GHz in open literature.

A narrowband on-body measurement campaign was performed in an RF shielded room lined with microwave absorbing sheets. A 2-port PNA (Keysight PNA E8362B) was used to determine the S_{21} of the eight

links with transmitting (Tx)-receiving (Rx) antennas placed on the body. Six subjects were considered, three male and three female with body weights that ranged from 35 to 110 kg.

The best model among the chosen fading models was selected by using the Akaike Information Criterion (AIC) [4] to evaluate the goodness of fit of these statistical models. To rank the models and to proof that one model is better than the other, the relative values of AIC_c were used. The expression for the relative values of AIC_c is:

$$\Delta i = AIC_i - \min(AIC) \quad (1)$$

where AIC_c is the AIC value for model index i .

Table 1 shows the AIC_c favored model for each scenario. The lognormal distribution provided the best fit for the path loss when the users were in motion. The results demonstrated that the lognormal distribution fitted to overweight subjects achieved the highest percentage value, 73%, of all on-body channels analyzed over the three scenarios. This modeled path loss agreed well with the on-body dynamic fading channel model reported in [5].

Table 1: AIC_c favored model for each scenario.

	Lognormal	Normal	Nakagami- <i>m</i>	Weibull	Rician
UW	5/8	1/8	1/8	0/8	1/8
N	5/8	1/8	1/8	0/8	1/8
OW	6/8	1/8	0/8	0/8	1/8
Overall (%)	73	10	7	0	10

REFERENCES

1. Ali, K., Brizzi, A., Lee, S., Hao, Y., Alomainy, A., & Yang, G. (2011). Numerical analysis of on-body channel for statistically-generated body shapes. In 2011 Loughborough Antennas and Propagation Conference (pp. 1–4). Loughborough, UK.
2. Zhao, Y., & Hao, Y. (2011). A subject-specificity analysis of radio channels in wireless body area networks. *Engineering Journal*, 15(3), 39–47.
3. Ali, K., Brizzi, A., Lee, S., Yang, G., Alomainy, A., & Hao, Y. (2015). Quantitative analysis of the subject-specific on-body propagation channel based on statistically created models. *IEEE Antennas and Propagation Letters*, 14, 398–401.
4. Abbasi, Q. H., Sani, A., Alomainy, A., & Hao, Y. (2011). Experimental characterization and statistical analysis of the pseudo-dynamic ultrawideband on-Body radio channel. *IEEE Antennas and Wireless Propagation Letters*, 10, 748–751.
5. Alomainy, A., Hao, Y., Owadally, A., Parini, C. G., Nechayev, Y., Constantinou, C. C., & Hall, P. S. (2007). Statistical analysis and performance evaluation for on-body radio propagation with microstrip patch antennas. *IEEE Transactions on Antennas and Propagation*, 55(1), 245–248.

Cross dipole EBG based high efficiency dual band antenna for millimeter wave communication systems

Abhishek Kandwal¹, Qingfeng Zhang^{1*}, X. Tang¹, L WY Liu¹, R. Das^{1,2}, Y. Chen^{1,3}

¹ Southern University of Science and Technology, Shenzhen, China

² Indian Institute of Technology, Bombay, India

³ The University of Waikato, Hamilton, New Zealand

*corresponding author, E-mail: zhangqf@sustc.edu.cn

Abstract

This paper proposes a cross dipole EBG based dual band antenna design for millimeter wave communication systems. The antenna is resonating in two different frequency bands that are K-band and V-band. Design consists of a slotted rectangular patch with cross dipole shaped elements surrounding it on a very thin substrate of 300 micrometers. The antenna is giving a dual band performance with a gain of around 10 dB and reduced side lobe levels of about -22 dB. The losses due to atmospheric attenuation and absorption coefficients have also been discussed in this paper. The radiation pattern shows a single radiating beam at the lower frequency and a dual beam at the higher frequency with a high efficiency of 97 percent. The frequency of operation and small size of the proposed antenna makes it a very good candidate for mm-wave communication applications.

Index Terms — Dual band, EBG, Millimeter wave, communication, Dual beam.

1. Introduction

Demands of modern communication and sensor systems for more bandwidth, higher resolution and compactness lead to operating frequency up to the millimeter wave or sub-mm wave regime. Recent research in the field of metamaterials have led to the development of promising new microwave and millimeter-wave devices which are crucial in designing high bit rate communication systems. Several industrial and academic research laboratories and world class clusters have developed considerable programs to design new types of electromagnetic components and devices based on metamaterials. Microwave and millimeter-wave links, as the frequency increases, require directive antennas to avoid the critical issue of loss budget: this happens in the case of point-to-point and point-to-multipoint applications, such as in the Local Multipoint Distribution System. Reconfigurable antennas have a unique advantage in modern wireless communication system, because it can be applied to multiple systems and has a multifunctional role. Earlier, frequency reconfigurable EBG structure is designed and used for a microstrip antenna to shift the resonance frequency of the antenna. Moreover, a novel reconfigurable

EBG structure is proposed to switch its own resonance frequency. The above researches prove the significance of reconfigurable EBG structure [1]-[4]. The superstrate technology is regarded as a promising solution to achieve a high antenna gain. Patches and array of patches are generally used to feed this kind of structures; however the losses can be significantly important in the millimeter range due to the feeding network. To avoid this drawback, a radiating slot antenna fed by a rectangular waveguide is associated to a superstrate medium in order to improve the inherent antenna gain of the structure [5].

Various techniques to improve antenna performances such as bandwidth and efficiency have been reported in the literature. Another approach to improve the bandwidth and efficiency of the conventional patch antenna is to minimize the substrate dielectric constant. It is also known that the antenna gain can be considerably increased by covering the antenna with a high permittivity superstrate. The fundamental effects of the substrate-superstrate structure on printed-circuit antennas are explored, demonstrating that the antenna radiation efficiency can be optimized to approximately maximum by selecting the proper materials and dimensions of the substrate and superstrate. In addition, metamaterial/EBG (electromagnetic band gap) based antennas with increased antenna gain have also been reported [6]-[7].

Most of the papers published above have shown good impedance bandwidth with good gain but obtaining a dual band with these characteristics is difficult to obtain. In this paper, a dual band antenna has been proposed with a cross dipole based electromagnetic band gap structure. The proposed structure has not provided a dual band but also resulted in the enhancement of overall gain of the antenna thereby reducing the losses such as side lobe level to a very good extent. Further the radiation pattern at higher frequency is providing dual beam. The atmospheric attenuation and absorption coefficients at the resonating frequencies have also been discussed.

2. Antenna Parameters

2.1. The geometry of the proposed cross dipole antenna is shown in fig. 1. Fig. 1(a) shows the patch antenna without cross dipole structure. Figure 1(b) shows the proposed cross dipole EBG antenna structure with a slotted rectangular

patch. The dimension of the central patch is (3 mm x 3mm) and is fed at some distance from the center. A slot has been introduced in this central patch with a dimension of (1 mm x 1 mm). A layer of similar electromagnetic band elements is surrounding the central patch. A single cross-dipole unit element has been shown in the fig. 1. The central patch is fed at a distance of 0.5 mm from the center of the patch in order to get good impedance matching. The substrate used is FR4 with dielectric constant of 4.3 and thickness of 300 micrometer (0.3 mm). The dimension of the substrate and the structure is (15.8 mm x 15.8 mm).

Attenuation and absorption coefficients have been discussed below briefly [8]:

Attenuation: $\alpha(\text{dB/MHz}) \times L(\text{cm}) \times f(\text{MHz})$

At 40 GHz, H₂O molecules interfere with radiation.

$A = 0.02 \text{ dB/Km}$ at around 40 GHz,

$A = 0.03 \text{ dB/Km}$ at around 22 GHz

Water vapor absorption coefficient:

$\text{KH}_2\text{O}(f) = k(f, 22) + kr(f) \text{ dB/Km}$,

where 1st term is absorption coefficient at 22 GHz and 2nd term is residual term accounts for absorption of all high frequency H₂O lines.

Oxygen absorption below 45 GHz can be neglected due to a very low or no contribution.

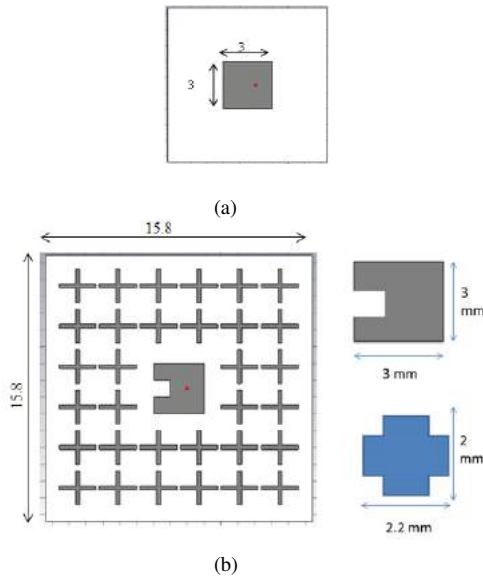


Fig. 1. Geometry (a) Without cross-dipole (b) With cross-dipoles

3. Results and Discussion

The proposed cross dipole antenna has been simulated using a 3D simulation software CST studio suite. The parameters of the antenna have been optimized to obtain good properties and desired results. Fig. 2 shows the variation of S-parameters with frequency. It can be clearly seen from this graph that the patch is giving a dual band but the resulting return loss and the impedance bandwidth is not

good enough. So a cross dipole EBG layer has been introduced along with patch surrounding it. A periodic layer of plus shaped cross dipole elements has been included. It is observed from the graphs that how the cross dipole layer has enhanced the antenna properties such as return loss, bandwidth, etc. The impedance bandwidth has been enhanced from few MHz to about 4.0 GHz. The return loss has also been improved a lot especially at higher resonating frequency.

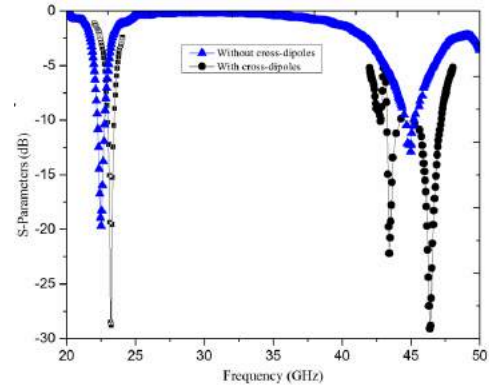
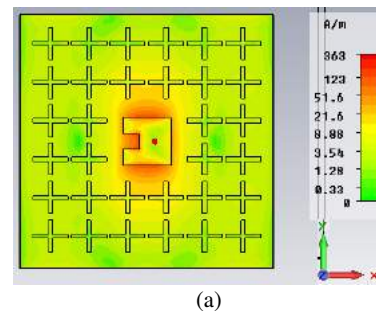


Fig. 2. S-parameters variation with frequency

Fig. 3(a) and 3(b) shows the surface current distribution graph for the proposed antenna structure at lower and higher resonant frequency. We can see the high current density areas at the desired patches on the structure.

Fig. 4 shows the gain plots at the resonant frequencies. Fig. 4(a) shows the pattern without cross dipole layer and 4(b) shows the pattern with cross dipole layer. From these graphs it can be seen that the peak antenna gain without EBG layer is just around 5 dB. But when the EBG layer is introduced in the structure the antenna gain has increased up to 10 dB for 3 dB angular width. The side lobe level has also been improved a lot. It has been reduced to -22 dB.

Fig. 5 shows the 3D radiation patterns at the resonant frequencies. It is observed from the pattern that a single is appearing at the lower frequency whereas a dual beam can be seen at the higher frequency.



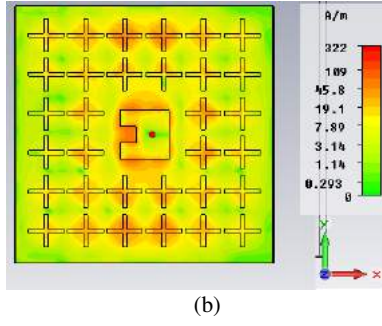
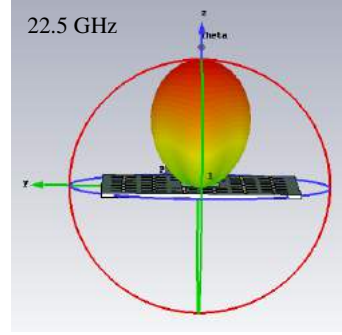
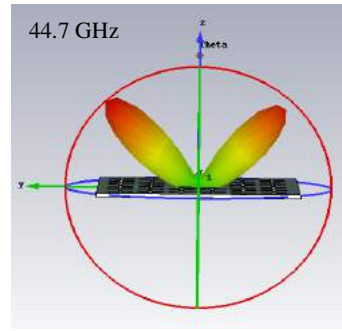


Fig. 3. Surface current distribution (a) lower freq (b) upper freq

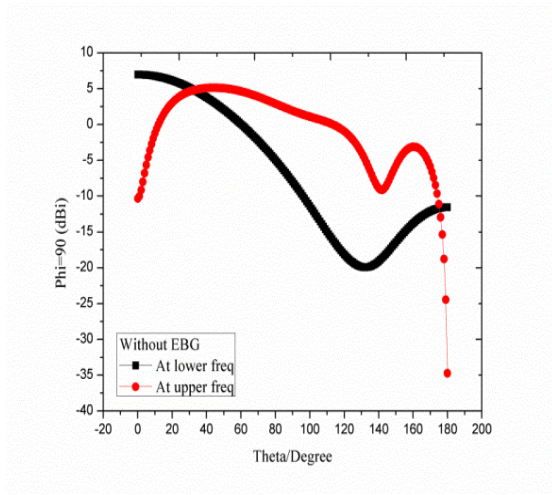


(a)

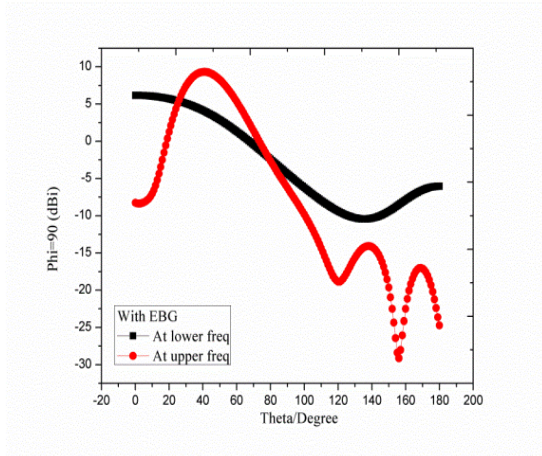


(b)

Fig. 4. 3D radiation pattern at (a) low and (b) high frequency



(a)



(b)

Fig. 4. Gain (a) without cross dipoles (b) with cross dipoles

4. Conclusions

A dual band cross dipole EBG based antenna design has been proposed in this paper. The antenna with an EBG surface has finally resulted in the enhancement of antenna characteristics. Antenna parameters such as impedance bandwidth, antenna gain, and side lobe levels have been improved to a good extent. Dual band and dual beam properties of this antenna makes it a suitable for applications such as terrestrial millimeter wave communication, automotive radars and high data rate communications.

Acknowledgements

This work is supported by National Natural Science Foundation of China (61401191), Guangdong Natural Science Funds for Distinguished Young Scholar (2015A030306032, S2013050014223), Shenzhen Science and Technology Innovation Committee funds (KQJSCX20160226193445650, JCYJ20150331101823678, KQCX2015033110182368, JCYJ20160301113918121, JSGG20160427105120572), and Shenzhen Development and Reform Commission Funds (Grant [2015]944).

References

- [1] C. M. Tran, H. Hafdallah Ouslimani, L. Zhou, A. C. Priou, H. Teillet, J.-Y. Daden and A. Ourir, "High impedance surfaces based antennas for high data rate communications at 40 GHz," *Progress in Electromagnetics Research C*, 13, 217-229, 2010.
- [2] F. Yang and Y. Rahmat-Samii, "Microstrip antennas integrated with electromagnetic band-gap (EBG) structures: A low mutual coupling design for array applications," *IEEE Transactions on Antennas and Propagation*, Vol. 51, 10, 2936-2946, Oct. 2003.
- [3] J. Liang and H. Y. Yang, "Microstrip patch antennas on tunable electromagnetic band-gap substrates," *IEEE Transactions on Antennas and Propagation*, Vol. 57, No. 6, 1612-1617, 2009.
- [4] J. D. Kern, J. A. Bossard, and D. H. Werner, "Design of reconfigurable electromagnetic bandgap surfaces as artificial magnetic conducting ground planes and absorbers," *IEEE Antennas and Propagation Society Int. Symposium*, 2006.
- [5] L. Bernard, R. Loison, R. Gillard and T. Lucidarme, "High directivity multiple superstrate antennas with improved bandwidth," *IEEE Int. Symp. Antennas Propagat.*, 2002.
- [6] L. Leger, T. Monediere and B. Jecko, "Enhancement of gain and radiation bandwidth for a planar 1-D EBG antenna," *IEEE Microwave and Wireless Comp Letter*, 15, 573-575, 2005.
- [7] W. Choi, C. Pyo, Y. H. Cho, J. Choi and J. Chae, "High Gain and Broadband Microstrip Patch Antenna Using a Superstrate Layer," *IEEE Antennas and Propagation Society International Symposium Digest*, Columbus, Vol. 2, 22-25, 292-295, 2003.
- [8] F. T. Ulaby, et al, "Microwave remote sensing: Active and Passive," Vol. 1, Addison-Wesley Publishing Co., Reading, MA, 1981.

Multiple Frequency Microstrip Five-Port Ring Junction Circuit for Six-Port Reflectometer (SPR)

S.A. Baharuddin^{1*}, E. M. Cheng¹, H. A. Rahim@Samsuddin², K.Y. Lee³, Z. Abbas⁴, N. F. Mohd Nasir¹, and Y. S. Lee⁵

¹School of Mechatronic Engineering, Universiti Malaysia Perlis (UniMAP), Pauh Putra Campus, 02600, Arau, Perlis, Malaysia.

²Bioelectromagnetic (BioEM) Research Group, School of Computer and Communication Engineering, Universiti Malaysia Perlis (UniMAP), Pauh Putra Campus, 02600, Arau, Perlis, Malaysia.

³Department of Electrical and Electronic Engineering, Lee Kong Chian Faculty of Engineering and Science, Universiti Tunku Abdul Rahman, 43000, Bandar Sg. Long, Selangor, Malaysia.

⁴Faculty of Science, Universiti Putra Malaysia, 43300, Serdang, Selangor, Malaysia.

⁵Bioelectromagnetic (BioEM) Research Group, Department of Electronic Engineering Technology, Faculty of Engineering Technology, Universiti Malaysia Perlis, Sg. Chuchuh, 02100, Padang Besar, Perlis, Malaysia.

*corresponding author: sitiashah1108@gmail.com

Abstract

The interest of the portable microwave instrument system has grown rapidly in recent years. Thus, Six-Port Reflectometer (SPR) is proposed. SPR provides a simple and inexpensive solution to industrial need of network analyzer. This paper presents the design of the multiple frequencies microstrip Five-Port ring junction which has operating frequencies of 0.37 GHz, 1.40 GHz, 2.10 GHz, 3.10 GHz and 3.80 GHz. The simulation result exhibit optimum specifications and less mismatch error.

Keywords: Five-Port ring junction, multiple frequency, Six-Port Reflectometer, microstrip.

1. Introduction

Nowadays, the microwave reflection technique is widely used in various applications such as in food [1-3] and agricultural [3-5] industries. Vector Network Analyzer (VNA) is a well-known solution to characterize the materials at microwave frequencies through S-parameters measurement [6]. However, VNA is notably bulky and expensive. Hence, the SPR which provides an alternative low cost solution to the commercial network analyzer was introduced by Engen in 1977[7]. The SPR is a simple and passive device for reflection measurement of material under test (MUT).

In this work, five-port ring junction circuit is designed and used for SPR to provide multiple operating frequencies. The ring junction circuit was proposed as in [8] due to its simple configuration, however the ring junction circuit in [8] can operate at 2 GHz, thus multiple frequencies of ring junction circuit is designed.

2. Design and simulation of Five-Port ring junction circuit

The Five-Port ring junction structure which consists of T-junction, arc and straight microstrip line layout was designed and simulated by using AWR Microwave Office (MWO) software [8] to determine the dimensions of the microstrip ring junction at frequencies of 0.37 GHz, 1.40 GHz, 2.10 GHz, 3.10 GHz and 3.80 GHz using Rogers RO3003 Ceramic-Filled PTFE composite with permittivity, ϵ_r and thickness, h , which are 3.0 mm and 1.524 mm, respectively.

The optimized dimensions must be determined to meet requirements of SPR as shown in Table 1. The determined dimensions must be practicable in design. The ring junction circuit was designed to perform according to Hansson and Riblet theory [9] where the reflection coefficient in magnitude ($|\Gamma|$) value of each port S_{11} , S_{22} , S_{33} , S_{44} and S_{55} should approach 0. The transmission coefficients in magnitude ($|\Gamma|$) represented by S-parameter, S_{12} , S_{13} , S_{14} , S_{15} , S_{21} , S_{23} , S_{24} , S_{25} , S_{31} , S_{32} , S_{34} , S_{35} , S_{41} , S_{42} , S_{43} , S_{45} , S_{51} , S_{52} , S_{53} and S_{54} should approximate to 0.5. Meanwhile, the phase difference (ϕ) of the transmission coefficients should be equal to 120° or -120° diversion phase [9]. Fig. 1 and Fig. 2 illustrate the schematic circuit diagram and configuration of Five-Port ring junction, respectively.

Table 1: Values of Length, Radius and Width of Five-Port Ring Junction

Details	Values (μm)
Length l (l1)	5860
Radius l (r1)	83000
Width l (w1)	4410

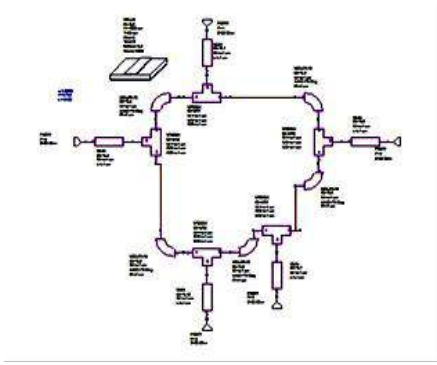


Figure 1: Schematic circuit diagram of Five-Port ring junction

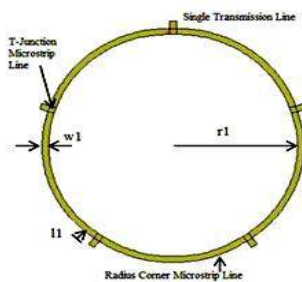


Figure 2: Configuration of Five-Port ring junction

3. Discussion

Five frequencies were found which comply with the requirement, i.e. 0.37 GHz, 1.4 GHz, 2.1 GHz, 3.1 GHz and 3.8 GHz where the S-parameter of each frequency is in accordance to theoretical values [9]. The S-parameter in magnitude, $|\Gamma|$ and phase, ϕ ($^\circ$) with their absolute error were tabulated in Table 2 and Table 11, respectively.

The absolute errors between simulated and theoretical S-Parameter in $|\Gamma|$ for reflection coefficients and transmission coefficients at frequencies of 0.37 GHz, 1.4 GHz, 2.1 GHz, 3.1 GHz and 3.8 GHz are less than 0.0197 (1.97%) and 0.0200 (2%), respectively.

Meanwhile, the absolute errors between simulated and theoretical S-Parameters in ϕ are less than 2.0° (0.56%). Therefore, it can be found that the simulated S-Parameter in $|\Gamma|$ and ϕ at 0.37 GHz, 1.4 GHz, 2.1 GHz, 3.1 GHz and 3.8 GHz have good agreement between theoretical values by Riblet and Hansson [9].

Table 2: $|\Gamma|$ of S-Parameter at 0.37 GHz.

Frequency (GHz)	S-Parameter	From Literature [9]	MWO Simulation	Error
0.37	S ₁₁	0.0000	0.0028	0.0028
	S ₂₂	0.0000	0.0028	0.0028
	S ₃₃	0.0000	0.0028	0.0028
	S ₄₄	0.0000	0.0028	0.0028
	S ₅₅	0.0000	0.0028	0.0028
	S ₂₁	0.5000	0.5000	0.0000
	S ₃₂	0.5000	0.5000	0.0000

	S ₄₃	0.5000	0.5000	0.0000
	S ₅₄	0.5000	0.5000	0.0000
	S ₁₅	0.5000	0.5000	0.0000
	S ₁₂	0.5000	0.5000	0.0000
	S ₂₃	0.5000	0.5000	0.0000
	S ₃₄	0.5000	0.5000	0.0000
	S ₄₅	0.5000	0.5000	0.0000
	S ₅₁	0.5000	0.5000	0.0000
	S ₃₁	0.5000	0.4984	0.0016
	S ₄₂	0.5000	0.4984	0.0016
	S ₅₃	0.5000	0.4984	0.0016
	S ₁₄	0.5000	0.4984	0.0016
	S ₂₅	0.5000	0.4984	0.0016
	S ₁₃	0.5000	0.4984	0.0016
	S ₂₄	0.5000	0.4984	0.0016
	S ₃₅	0.5000	0.4984	0.0016
	S ₄₁	0.5000	0.4984	0.0016
	S ₅₂	0.5000	0.4984	0.0016

Table 3: $|\Gamma|$ of S-Parameter at 1.4 GHz.

Frequency (GHz)	S-Parameter	From literature [9]	MWO Simulation	Error
1.4	S ₁₁	0.0000	0.0123	0.0123
	S ₂₂	0.0000	0.0123	0.0123
	S ₃₃	0.0000	0.0123	0.0123
	S ₄₄	0.0000	0.0123	0.0123
	S ₅₅	0.0000	0.0123	0.0123
	S ₂₁	0.5000	0.4994	0.0006
	S ₃₂	0.5000	0.4994	0.0006
	S ₄₃	0.5000	0.4994	0.0006
	S ₅₄	0.5000	0.4994	0.0006
	S ₁₅	0.5000	0.4994	0.0006
	S ₁₂	0.5000	0.4994	0.0006
	S ₂₃	0.5000	0.4994	0.0006
	S ₃₄	0.5000	0.4994	0.0006
	S ₄₅	0.5000	0.4994	0.0006
	S ₅₁	0.5000	0.4994	0.0006
	S ₃₁	0.5000	0.4926	0.0074
	S ₄₂	0.5000	0.4926	0.0074
	S ₅₃	0.5000	0.4926	0.0074
	S ₁₄	0.5000	0.4926	0.0074
	S ₂₅	0.5000	0.4926	0.0074
	S ₁₃	0.5000	0.4926	0.0074
	S ₂₄	0.5000	0.4926	0.0074
	S ₃₅	0.5000	0.4926	0.0074
	S ₄₁	0.5000	0.4926	0.0074
	S ₅₂	0.5000	0.4926	0.0074

Table 4: $|\Gamma|$ of S-Parameter at 2.1 GHz.

Frequency (GHz)	S-Parameter	From literature [9]	MWO Simulation	Error
2.1	S ₁₁	0.0000	0.0119	0.0119
	S ₂₂	0.0000	0.0119	0.0119
	S ₃₃	0.0000	0.0119	0.0119
	S ₄₄	0.0000	0.0119	0.0119
	S ₅₅	0.0000	0.0119	0.0119
	S ₂₁	0.5000	0.4942	0.0058
	S ₃₂	0.5000	0.4942	0.0058
	S ₄₃	0.5000	0.4942	0.0058

S ₅₄	0.5000	0.4942	0.0058
S ₁₅	0.5000	0.4942	0.0058
S ₁₂	0.5000	0.4942	0.0058
S ₂₃	0.5000	0.4942	0.0058
S ₃₄	0.5000	0.4942	0.0058
S ₄₅	0.5000	0.4942	0.0058
S ₅₁	0.5000	0.4942	0.0058
S ₃₁	0.5000	0.4889	0.0111
S ₄₂	0.5000	0.4889	0.0111
S ₅₃	0.5000	0.4889	0.0111
S ₁₄	0.5000	0.4889	0.0111
S ₂₅	0.5000	0.4889	0.0111
S ₁₃	0.5000	0.4889	0.0111
S ₂₄	0.5000	0.4889	0.0111
S ₃₅	0.5000	0.4889	0.0111
S ₄₁	0.5000	0.4889	0.0111
S ₅₂	0.5000	0.4889	0.0111

Table 5: $|\Gamma|$ of S-Parameter at 3.1 GHz.

Frequency (GHz)	S-Parameter	From literature [9]	MWO Simulation	Error
3.1	S ₁₁	0.0000	0.0047	0.0047
	S ₂₂	0.0000	0.0047	0.0047
	S ₃₃	0.0000	0.0047	0.0047
	S ₄₄	0.0000	0.0047	0.0047
	S ₅₅	0.0000	0.0047	0.0047
	S ₂₁	0.5000	0.4998	0.0002
	S ₃₂	0.5000	0.4998	0.0002
	S ₄₃	0.5000	0.4998	0.0002
	S ₅₄	0.5000	0.4998	0.0002
	S ₁₅	0.5000	0.4998	0.0002
	S ₁₂	0.5000	0.4998	0.0002
	S ₂₃	0.5000	0.4998	0.0002
	S ₃₄	0.5000	0.4998	0.0002
	S ₄₅	0.5000	0.4998	0.0002
	S ₅₁	0.5000	0.4998	0.0002
	S ₃₁	0.5000	0.4800	0.0200
	S ₄₂	0.5000	0.4800	0.0200
	S ₅₃	0.5000	0.4800	0.0200
	S ₁₄	0.5000	0.4800	0.0200
	S ₂₅	0.5000	0.4800	0.0200
	S ₁₃	0.5000	0.4800	0.0200
	S ₂₄	0.5000	0.4800	0.0200
	S ₃₅	0.5000	0.4800	0.0200
	S ₄₁	0.5000	0.4800	0.0200
	S ₅₂	0.5000	0.4800	0.0200

Table 6: $|\Gamma|$ of S-Parameter at 3.8 GHz.

Frequency (GHz)	S-Parameter	From literature [9]	MWO Simulation	Error
3.8	S ₁₁	0.0000	0.0197	0.0197
	S ₂₂	0.0000	0.0197	0.0197
	S ₃₃	0.0000	0.0197	0.0197
	S ₄₄	0.0000	0.0197	0.0197
	S ₅₅	0.0000	0.0197	0.0197
	S ₂₁	0.5000	0.4909	0.0091
	S ₃₂	0.5000	0.4909	0.0091
	S ₄₃	0.5000	0.4909	0.0091
	S ₅₄	0.5000	0.4909	0.0091

S ₁₅	0.5000	0.4909	0.0091
S ₁₂	0.5000	0.4909	0.0091
S ₂₃	0.5000	0.4909	0.0091
S ₃₄	0.5000	0.4909	0.0091
S ₄₅	0.5000	0.4909	0.0091
S ₅₁	0.5000	0.4909	0.0091
S ₃₁	0.5000	0.4859	0.0141
S ₄₂	0.5000	0.4859	0.0141
S ₅₃	0.5000	0.4859	0.0141
S ₁₄	0.5000	0.4859	0.0141
S ₂₅	0.5000	0.4859	0.0141
S ₁₃	0.5000	0.4859	0.0141
S ₂₄	0.5000	0.4859	0.0141
S ₃₅	0.5000	0.4859	0.0141
S ₄₁	0.5000	0.4859	0.0141
S ₅₂	0.5000	0.4859	0.0141

Table 7: Phase Difference (ϕ) of S-Parameter at 0.37 GHz.

Frequency (GHz)	S-Parameter	From literature [9]	MWO Simulation	Error (°)
0.37	S ₂₁	120	119.8	0.2
	S ₃₁			
	S ₃₂	120	119.8	0.2
	S ₄₂			
	S ₄₃	120	119.8	0.2
	S ₅₃			
	S ₅₄	120	119.8	0.2
	S ₁₄			
	S ₁₅	120	119.8	0.2
	S ₂₅			
	S ₂₃	120	119.8	0.2
	S ₁₃			
	S ₃₄	120	119.8	0.2
	S ₂₄			
	S ₄₅	120	119.8	0.2
	S ₃₅			
	S ₅₁	120	119.8	0.2
	S ₄₁			
	S ₁₂	120	119.8	0.2
	S ₅₂			

Table 8: Phase Difference (ϕ) of S-Parameter at 1.4 GHz.

Frequency (GHz)	S-Parameter	From literature [9]	MWO Simulation	Error (°)
1.4	S ₂₁	120	119.5	0.5
	S ₃₁			
	S ₃₂	120	119.5	0.5
	S ₄₂			
	S ₄₃	120	119.5	0.5
	S ₅₃			
	S ₅₄	120	119.5	0.5
	S ₁₄			
	S ₁₅	120	119.5	0.5

	S ₂₅	120	119.5	0.5
	S ₂₃			
	S ₁₃			
	S ₃₄	120	119.5	0.5
	S ₂₄			
	S ₄₅	120	119.5	0.5
	S ₃₅			
	S ₅₁	120	119.5	0.5
	S ₄₁			
	S ₁₂	120	119.5	0.5
	S ₅₂			

Table 9: Phase Difference (ϕ) of S-Parameter at 2.1 GHz.

Frequency (GHz)	S-Parameter	From literature [9]	MWO Simulation	Error (°)
2.1	S ₂₁	120	120	0.0
	S ₃₁			
	S ₃₂	120	120	0.0
	S ₄₂			
	S ₄₃	120	120	0.0
	S ₅₃			
	S ₅₄	120	120	0.0
	S ₁₄			
	S ₁₅	120	120	0.0
	S ₂₅			
	S ₂₃	120	120	0.0
	S ₁₃			
	S ₃₄	120	120	0.0
	S ₂₄			
	S ₄₅	120	120	0.0
	S ₃₅			
	S ₅₁	120	120	0.0
	S ₄₁			
	S ₁₂	120	120	0.0
	S ₅₂			

Table 10: Phase Difference (ϕ) of S-Parameter at 3.1 GHz.

Frequency (GHz)	S-Parameter	From literature [9]	MWO Simulation	Error (°)
3.1	S ₂₁	120	-120.2	0.2
	S ₃₁			
	S ₃₂	120	-120.2	0.2
	S ₄₂			
	S ₄₃	120	-120.2	0.2
	S ₅₃			
	S ₅₄	120	-120.2	0.2
	S ₁₄			
	S ₁₅	120	-120.2	0.2
	S ₂₅			
	S ₂₃	120	-120.2	0.2
	S ₁₃			
	S ₃₄	120	-120.2	0.2
	S ₂₄			
	S ₄₅	120	-120.2	0.2
	S ₃₅			
	S ₅₁	120	-120.2	0.2
	S ₄₁			
	S ₁₂	120	-120.2	0.2
	S ₅₂			

Table 11: Phase Difference (ϕ) of S-Parameter at 3.8 GHz.

Frequency (GHz)	S-Parameter	From literature [9]	MWO Simulation	Error (°)
3.8	S ₂₁	120	118	2.0
	S ₃₁			
	S ₃₂	120	118	2.0
	S ₄₂			
	S ₄₃	120	118	2.0
	S ₅₃			
	S ₅₄	120	118	2.0
	S ₁₄			
	S ₁₅	120	118	2.0
	S ₂₅			
	S ₂₃	120	118	2.0
	S ₁₃			
	S ₃₄	120	118	2.0
	S ₂₄			
	S ₄₅	120	118	2.0
	S ₃₅			
	S ₅₁	120	118	2.0
	S ₄₁			
	S ₁₂	120	118	2.0
	S ₅₂			

4. Conclusions

The simulated results for S-parameter in both $|Γ|$ and $φ$ for 0.37 GHz, 1.40 GHz, 2.10 GHz, 3.10 GHz and 3.80 GHz have good agreement with theoretical and simulated values. Hence, it is verified that the proposed microstrip Five-Port ring junction circuit complies with the requirements and principles of SPR at multiple operating frequencies. Overall, the size of the ring junction is 18 cm wide which is small enough to develop a portable SPR. For further work, this microstrip Five-Port ring junction circuit can be fabricated and verified by using network analyzer.

Acknowledgements

The author would like to thank Universiti Malaysia Perlis and Ministry of Higher Education for the financial support. This research is supported by Research Acculturation Grant Scheme (RAGS) 2013 (No. 9018-00059), School of Mechatronic Engineering, Universiti Malaysia Perlis. In addition, the author would like to deliver deeply gratitude to Universiti Putra Malaysia upon their technical assistance in this work.

References

- [1] E. M. Cheng et al., "Development of Microstrip Patch Antenna Sensing System for Salinity and Sugar Detection in Water," *Int. J. Mech. Mechatronics Eng.*, vol. 14, no. 5, pp. 31–36, 2014.
- [2] E. M. Cheng et al., "Development of Low Cost Microwave Detection System for Salinity and Sugar Detection," *Int. J. Mech. & Mechatronics Eng.*, vol. 14, no. 5, pp. 59–71, 2014.
- [3] E. M. Cheng et al., "Reflection And Dielectric Measurement For Salinity of Water using Microstrip Loop Antenna and Dielectric Probe," *Int. J. GEOMATE*, vol. 11, no. 24, pp. 2335–2340, 2016.
- [4] E. M. Cheng et al., "Finite Difference Analysis of an Open-Ended, Coaxial Sensor Made of Semi- Rigid Coaxial Cable for Determination of Moisture in Tenera Oil Palm Fruit," *ACES J.*, vol. 31, no. 10, pp. 1181–1192, 2016.
- [5] E. M. Cheng et al., "Analysis on Monopole Antenna for Moisture Determination in Oil Palm Fruit Using Finite Difference Method," *J Electr Eng Technol*, vol. 11, no. 6, pp. 1754–1762, 2016.
- [6] Staszek, K., S. Gruszczynski, and K. Wincza, "Theoretical Limits and Accuracy Improvement of Reflection-Coefficient Measurements in Six-Port Reflectometers," *IEEE Transcation Microw. Theory Tech.*, vol. 61, no. 8, pp. 2966–2974, 2013.
- [7] Engen, G., "The Six-Port Reflectometer: An Alternative Network Analyzer," *IEEE Transcation Microw. Theory Tech.*, vol. 25, no. 1, pp. 1075–1079, 1977.
- [8] Aishah, S., M.Fareq, E. M. Cheng, K. Y. Lee, N. F. M. Nasir, and et.al, "Study on Moisture Content in Animal Fats Using Six- Port Reflectometer (SPR)," *2nd Int. Conf. Biomed. Eng.*, March, pp. 30–31, 2015.
- [9] Hansson, E.R, and P. Riblet, "An Ideal Six-Port Network Consisting of a Matched Reciprocal Lossless Five-Port and a Perfect Directional Coupler," *IEEE Transcation Microw. Theory Tech.*, vol. 31, no. 3, pp. 284–288, 1983.

Voltage Multiplication on Ambient AC Electromagnetic Fields

Louis WY Liu^{1*}, Abhishek Kandwal¹, Qingfeng Zhang¹

¹ Southern University of Science and Technology, Shenzhen, China

*corresponding author, E-mail: liaowu@sustc.edu.cn

Abstract

In this work, wireless power has been harvested directly on a trapped surface wave using a transducer with a voltage multiplication functionality. A suspended layer of lossy dielectric was found to be able to support propagation of trapped surface waves. The said transducer can generate a DV voltage directly from the time-varying electromagnetic field on the surface of a suspended layer of high-loss dielectric, with the voltage inversely proportional to square root of the distance from the transmitter.

Index Terms — Wireless Power Transfer, Zenneck Wave, Trapped Surface Wave, Voltage Multiplier, Displacement Current

1. Introduction

Marconi was the first researcher proving the feasibility of trans-oceanic delivery of wireless power way beyond the line-of-sight distance to the horizon. In an attempt to lend credence to Marconi's work, Zenneck and Sommerfeld have later theorized that the interface between the ground and air could be used as a waveguide to propagate a version of surface waves known as Zenneck waves. Their theories have successfully proven that the field amplitude varies inversely as square root of the distance between the transmitter and the receiver but they failed to gain acceptance from the scientific community because of three reasons: 1) their theories allow the phase velocity to exceed the speed of light; 2) many researchers were not able to prove the existence of the poles of Sommerfeld's integrand expressing the electric field around a vertically mounted dipole; and 3) their theories fail to explain why the ground waves in Marconi's experiment has followed the curvature of the earth instead of traveling in a straight direction. As a result of these controversies, the topic of surface waves has completely lost favor for decades until several researchers came forwards to introduce a more promising concept of trapped surface waves [1-5]. Trapped surface wave is a class of evanescent electromagnetic waves propagating inside a volume of dielectric by internal reflection in much the same manner as light rays traveling in an optical fiber.

Trapped surface wave is by far the most promising electromagnetic energy which can potentially improve the

transmission efficiency of a wireless power. It also has a lot of unexplored applications. During the time of an earthquake disaster, for instance, it is not always possible for everyone trapped in a severely damaged building to make emergency phone calls because the battery lives of their cell phones can at most last for two days. In this case, a technology capable of delivering wireless power to the survivors buried underneath the rubles can make a huge difference. The result of our investigation concludes that space waves alone will not accomplish this job. Trapped surface waves are one of the few options that can help.

2. High-loss Dielectric Layer for Wireless Power Transfer

Trapped surface waves are known to exist in a stratified dielectric structure on which a dipole is vertically or horizontally mounted [1-7]. In this work, a suspended layer of dielectric with an elevated loss tangent was found to be able to support propagation of trapped surface waves. A suspended layer of high-loss dielectric can be treated as a special form of 4-layered stratified ground with layer 0 being air, layer 1 being the suspended layer of lossy dielectric, layer 2 being air again and layer 3 being a perfect conductor. For a trapped surface waves to exist, the permittivity of layer 1, $\epsilon_0\epsilon_r + j\sigma_1/\omega$, has to satisfy the pole equation in Equation (2):

$$\begin{aligned} 0 = & k_1^2 \sqrt{k_0^2 - \lambda^2} \\ & (\sqrt{k_1^2 - \lambda^2} k_0^2 - k_1^2 \sqrt{k_0^2 - \lambda^2} \tan(\sqrt{k_1^2 - \lambda^2} l_1) \tan(\sqrt{k_0^2 - \lambda^2} l_2)) \\ & - i k_0^2 \sqrt{k_1^2 - \lambda^2} \\ & (\sqrt{k_1^2 - \lambda^2} k_0^2 \tan(\sqrt{k_1^2 - \lambda^2} l_1) + \sqrt{k_0^2 - \lambda^2} k_1^2 \tan(\sqrt{k_0^2 - \lambda^2} l_2)) \end{aligned} \quad (1)$$

, where

$$k_0 = \omega \sqrt{\mu_0 \epsilon_0}$$

$$k_1 = \omega \sqrt{\mu(\epsilon_0\epsilon_r + j\sigma_1/\omega)}$$

, and ω is the angular frequencies in radian. Equation (1) has no trivial root unless the loss tangent of layer 1 is sufficiently large. In other words, trapped surface waves can propagate in a high-loss dielectric material instead of low-loss dielectric material.

3. Transducer for Harvesting Energy from Ambient Electromagnetic Fields

The most basic Avremenko diode configuration has successfully been used to deliver a DC voltage from a displacement current from a single-wire transmission line known as Goubau line [8,9]. However, the original Avremenko diode configuration was not intended for any application involving wireless power transfer. To harvest energy from a wireless power, we need a transducer much more powerful than the original version of Avremenko diode configuration. This transducer comprises a similar open-circuited Goubau line connected in series with a circuit having a voltage multiplication functionality. Since the ground plane is virtually non-existence, this Goubau line can be left open-circuited to form a dipole with a characteristic impedance comparable to the characteristic impedance of free space. Together with a circuit with voltage multiplication functionality, this transducer can be employed to rectify a trapped surface wave into a scaled DC voltage (see Fig. 1). With this circuit, the time-varying electromagnetic fields in vicinity of the open-ended Goubau line can be converted in a DC voltage at the load. With an assumption that all the capacitors C and diodes D are identical, and that the inductance L_p is negligible, the output voltage can be derived in terms of capacitance C and AC voltage across diode D , V_D . The final expression can be approximated into the following form:

$$V_{out} = \frac{2nKT}{q} \ln\left(\frac{I_s}{2Cf}\right) + 6V_D - \frac{nKT}{q} \ln(4\pi V_D) + \frac{nKT}{q} \left(\left(\frac{q}{nKT} - 1\right) - \frac{1}{2} \left(\frac{q}{nKT} - 1\right)^2 \right) \quad (2)$$

where n is the ideality factor of the diode, I_s is the reverse saturation current, f is the operating frequency, KT/q is approximately 25 mV at room temperature.

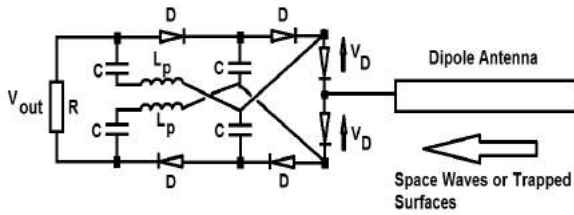


Figure 1: Schematic of the Transducer for Harvesting Electromagnetic Energy.

4. Results and Discussion

The proposed transducer has successfully rectified a 1.6 GHz power at 20 dBm into at least 5.5 V DC on a 500 ohm

load, corresponding to a rectification efficiency slightly above 50%. Fig. 2 shows its performance simulated and measured up to 2 GHz.

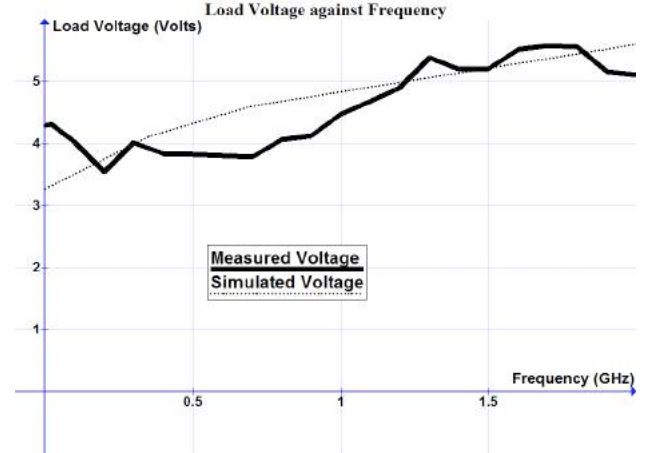


Figure 2: Voltage on a 500 ohm load as function of frequency.

The dipole attached to the proposed voltage multiplier has been used as a built-in antenna to perform direct voltage multiplication on the surface of a suspended layer of high-loss dielectric. Fig. 3 shows the output voltage as a function of the distance between the transmitter and the receiver. By curve-fitting using MathematicaTM, the voltage captured from the surface of suspended wooden plane was found to be proportional to $1/d^{0.5}$, where d is the distance from the transmitter. On the other hand, the measured voltage due to the electromagnetic field in free space was almost zero, with the magnitude proportional to $1/d$. The measured results were highly consistent with the theoretical prediction.

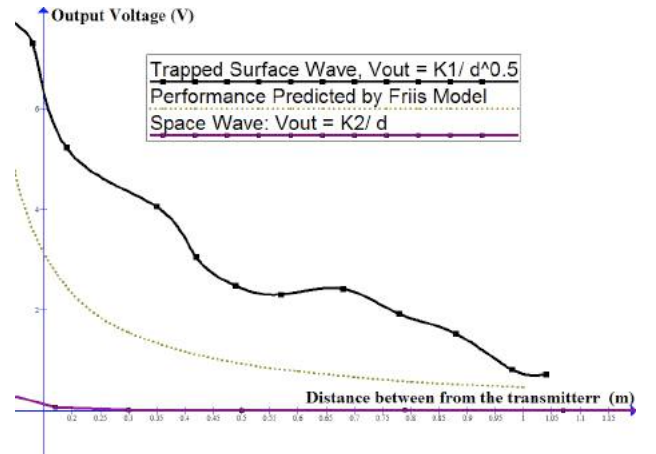


Figure 3: Voltage on a 500 ohm load as function of distance between the transmitter and the receiver.

5. Conclusions

This article has presented a transducer capable of harvesting energy from an ambient time-varying electromagnetic field.

With the fabricated transducer, we have found that the captured voltage from the surface of a suspended dielectric with an elevated loss tangent is inversely proportional to square root of the distance from the transmitter. On the other hand, the captured voltage from free space was found to be inversely proportional to the distance from the transmitter. The experimental results of this work are consistent with the prediction by our complex analysis. The outcome of our investigation reinforces the evidence that a suspended layer of dielectric material with a highly elevated loss tangent supports propagation of trapped surface waves.

Acknowledgements

This work is supported by National Natural Science Foundation of China (61401191), Guangdong Natural Science Funds for Distinguished Young Scholar (2015A030306032, S2013050014223), Shenzhen Science and Technology Innovation Committee funds (KQJSCX20160226193445650, JCYJ20150331101823678, KQCX2015033110182368, JCYJ20160301113918121, JSGG20160427105120572), and Shenzhen Development and Reform Commission Funds (Grant [2015]944).

References

- [1] JR Wait, "Electromagnetic wave theory", Harper & Row New York, 1985
- [2] Collin RE, "Some observations about the near zone electric field of a hertzian dipole above a lossy earth". IEEE Transactions on Antennas and Propagation.
- [3] Collin RE, "Hertzian dipole radiation over a lossy earth or sea: Some early and late 20th century controversies". IEEE Antennas and Propagation Magazine, 46(2): 64–79 (2004b) .
- [4] King, Owens, and Wu, "Lateral Electromagnetic Waves" Springer-Verlag, 1992.
- [5] Kai Li, "Electromagnetic Fields of Stratified Media" , Zhejiang University Press, 2009.
- [6] Louis WY LIU, Qingfeng Zhang & Yifan Chen, " Harvesting Atmospheric Ions Using Surface Electromagnetic Wave Technology " , Journal of Advances in Technology Innovation, Vol 2, No. 4, 2017.
- [7] Louis Liu, Qingfeng Zhang, Yifan Chen, "Capturing Cosmic Rays Using Surface Wave Technologies", International Conference of Power and Renewable Energy, 2016
- [8] N.E.Zaev, S.V.Avramenko & V.N.Lisin, " The measuring of Conduction Current that is stimulated by Polarization current " , Journal of Russian Physical Society, No.2, 1991, in Russian, 1991 .
- [9] Louis WY LIU, Q. Zhang & Yifan Chen, "Capturing Surface Electromagnetic Energy into a DC through Single-Conductor Transmission Line at Microwave Frequencies" , Progress In Electromagnetics Research M, Vol. 54, 29–36, 2017.

Investigation on Various Structural Compositions of Textile-Integrated Antenna

A. A. Sharatol Ahmad Shah¹, N. H. Abd Rahman¹, M. T. Ali¹, M. R. Ahmad² and S. A. Nordin¹

¹Antenna Research Group (ARG), Faculty of Electrical Engineering
Universiti Teknologi MARA Malaysia, 40450 Shah Alam, Selangor, Malaysia

²Faculty of Applied Science
Universiti Teknologi MARA Malaysia, 40450 Shah Alam, Selangor, Malaysia
aidilaidilaidil@gmail.com

Abstract

This paper presents the design of textile-integrated antenna developed for wearable application. In this paper, the results from parametric study, which focused on the thickness of the textile compositions used in the antenna structure is presented. The proposed design structure consists of electro-textile fabric and polyester fabric as the radiating element and substrate respectively. Antennas with three different thicknesses were used, differentiated through the use of single layer, four layers and six layers of polyester substrate respectively. Dielectric permittivity measurement was performed to ensure accurate parameters for the modelling and simulation process. All prototypes of textile-integrated antennas were fabricated and measured for performance validation and the data analysis was conducted to study on the correlation between fabric thickness and the antenna performance. A clear relation between substrate thickness and antenna performance for optimization of textile-integrated antenna has been achieved. By increasing substrate thickness of the fabricated antennas, the return loss improved from -14.96dB for single layer, to -16.5dB for four layers and -18.11dB for six layers. However, as the substrate thickness increases, the frequencies of the respective antenna prototypes are slightly shifted about 5% to the left due to increasing fabrication difficulty that led to higher fabrication error. Furthermore, better performances with thicker substrate are obtained where improvement of bandwidth and signal strength can be seen from the measurement results.

1. Introduction

Flexible wearable antennas are desired in the advancement of wireless sensor development especially for healthcare, biomedical and security applications. Common parameters such as substrate thickness and dielectric permittivity were used in designing a conventional antenna while in this paper, analysis of the effects of the various textile composition on the antenna's performance is performed in detail. The parametric study focused on the thickness of the textile composition used in the antenna structure which are essential for antenna optimization. Polyester is one of the

most common material used in manufacturing of clothing which is suitable for the proposed wearable application [1].

The design of a flexible antenna demands comprehensive knowledge on the electromagnetic properties of the textile composition due to its inconsistent form and exposure to various structural deformation effects. Furthermore, the substrate properties such as its dielectric constant and loss tangent have a pronounced effect on antenna characteristics [2]. Theoretically, bandwidth can be improved by increasing the substrate thickness [3] but are limited due to unwanted surface wave excitation which leads to poor antenna efficiency. However, this condition can be minimized by using a substrate with low dielectric constant to allow the design of antennas with large gain and high efficiency [2]. It is extremely important that sufficient gain is provided by the antennas to improve the signal strength so that the devices can still communicate at a higher range [4]. Friis Transmission equation (1) can be used to investigate the signal strength of the textile-integrated antenna [5].

$$Pr \text{ (dB)} = Pt + Gt + Gr + 20 \log_{10} \left(\frac{\lambda}{4\pi R} \right) \quad (1)$$

where R is the distance between the transmitter and receiver.

Commercially available conductive textiles are commonly used in textile antennas [6]. This commercialized electro-textile provides little information on the electromagnetic properties and structural composition which are crucial in the design of an antenna [7]. This paper presents a study on the optimization of textile-based antenna by varying the thickness of the substrate in order to investigate the effects on bandwidth and signal strength performance.

2. Antenna Design

Figure 1 shows the design of three antenna prototypes which have different substrate thicknesses. The prototypes are designed and developed based on rectangular microstrip patch with resonant frequency of 2.4GHz. The radiating element is an electro-textile fabric which is made from

0.1mm copper wires and polyester yarns. The radiating element performance depends on the structural composition of the electro-textile fabric. The electro-textile used for the fabrication of the antennas consist of 80 ends/inch of non-conductive yarns and 25 ends/inch of conductive yarns in the warp (vertical) and weft (horizontal) direction respectively. Theoretically, the performance of the radiating element could be improved by increasing the numbers of weft. Polyester fabric with different number of layers are used as the antenna's substrate for each of the design. The first antenna design is realized on a single layer polyester, while the second and third antenna design consist of four layers and six layers of polyester substrate respectively.

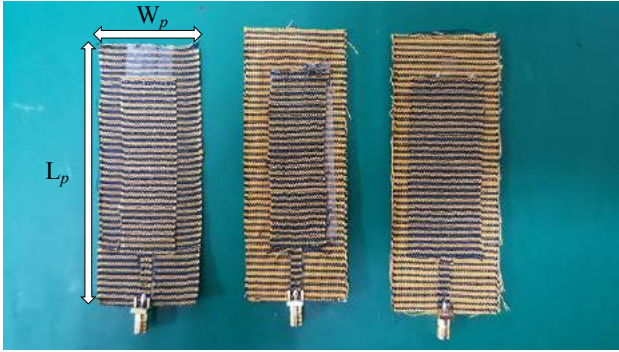


Figure 1: Three antennas design with different substrate thickness.

Table 1 shows the substrate thickness and detail parameter for each of the antennas dimension. A single layer polyester substrate has a thickness of 0.35mm.

Table 1: Substrate thickness

Parameter	Single layer (mm)	Four layers (mm)	Six layers (mm)
Substrate width (W_p)	40	40	40
Substrate length (L_p)	105	110	110
Substrate thickness (h)	0.35	1.4	2.1

The parameter values in Table 1 are used for simulation design in CST Studio. The fabrication of different thicknesses of substrate material is explained in Section 3.

3. Methodology

The first step of this study is to measure the dielectric constant of the substrate material. The actual dielectric constant (ϵ_r) of the polyester substrate was measured using a customized jig that has been developed to ensure consistency in dielectric constant reading. Since the substrate material is flexible and prone to physical deformation, the jig was designed to hold every sides of the substrate material tightly and to minimize fabric movement

when the measurement was taken. The dielectric properties were measured using coaxial probe measurement technique. The jig is shown in Figure 2. This step is crucial in order to get accurate parameters for the simulation.



Figure 2: Customized Jig

Four and six stacks of polyester substrate were glued together using fabric glue in order to prepare the four layers and six layers' antenna substrate. The multiple layered substrates were put in the heat press machine as shown in Figure 3 to achieve uniform fabric compression and temperature distribution.



Figure 3: Heat press machine

Due to compression of substrate during the heat pressing process, the layered substrate thicknesses have been slightly reduced from the initial readings. The compressed substrate thicknesses were measured using a Vernier caliper and is shown in Table 2.

Table 2: Substrate thickness (Initial vs Compressed).

Design	Initial (mm)	Compressed (mm)	Percentage difference (%)
Single layer	0.35	-	-
Four layer	1.4	1.2	14%
Six layer	2.1	1.75	16%

The electro-textile fabric was cut into sizes for each of the antennas design according to the design parameter. It was then attached to the substrate using the double-sided tape and copper tape was used as the ground plane. The

fabricated antennas with different thicknesses are shown in Figure 4, 5 and 6 respectively.



Figure 4: Single layer (0.35mm substrate thickness).



Figure 5: Four layer (1.2mm substrate thickness).



Figure 6: Six layer (1.75mm substrate thickness).

The measurement of reflection coefficient for each of the antennas were performed using Vector Network Analyzer (KEYSIGHT N5234A). Whilst the experimental measurement of signal strength was performed using portable Spectrum Analyzer (KEYSIGHT FIELDFOX N9916A). During the signal strength measurement, the fabricated antennas were connected to a Signal Generator and the signal strength readings from a distance of 1 meter until 5 meters were captured using the portable Spectrum Analyzer. Figure 7 shows the experimental setup for the signal strength measurements.



Figure 7: Signal strength measurement setup.

4. Results and Discussion

4.1. Substrate Dielectric

The dielectric properties obtained from the coaxial probe measurement technique includes dielectric constant, dielectric loss factor and loss tangent. In Table 3, several dielectric properties reading was taken to determine the average and accurate values to be used in the simulation.

Table 3: Single Layer dielectric properties

Parameter	1	2	3	4	5	6
Dielectric constant	2.23	2.28	2.3	2.31	2.35	2.3
Dielectric loss factor	0.27	0.29	0.28	0.28	0.28	0.28
Loss tangent	0.12	0.13	0.12	0.12	0.12	0.12
Parameter	7	8	9	10	11	Avg.
Dielectric constant	2.28	2.32	2.26	2.3	2.34	2.3
Dielectric loss factor	0.29	0.28	0.28	0.28	0.28	0.28
Loss tangent	0.13	0.12	0.12	0.12	0.12	0.12

4.2. Return Loss

The return loss was measured using PNA-L Network Analyzer. As shown in Figure 8, 9 and 10, the fabricated single layer and four layers' antennas managed to produce the most similar reading compared to its simulation results. Whilst there was noticeable variation in terms of resonant frequency and S_{11} magnitude between the simulation and measurement readings for six layer antennas which may be due to increasing fabrication difficulty that led to higher fabrication error. Table 4 shows the summary of return loss readings.

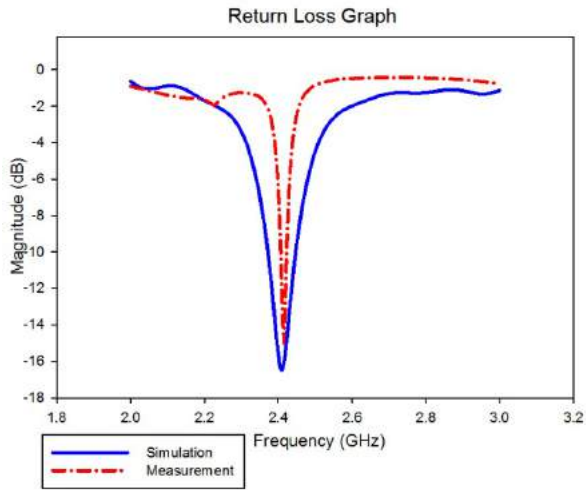


Figure 8: Return loss graph (Single layer).

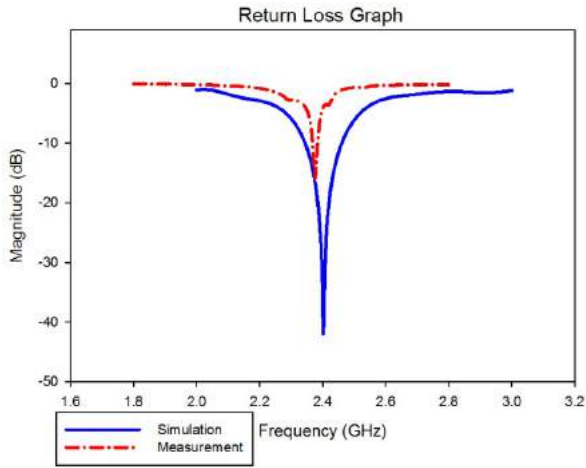


Figure 9: Return loss graph (Four layer).

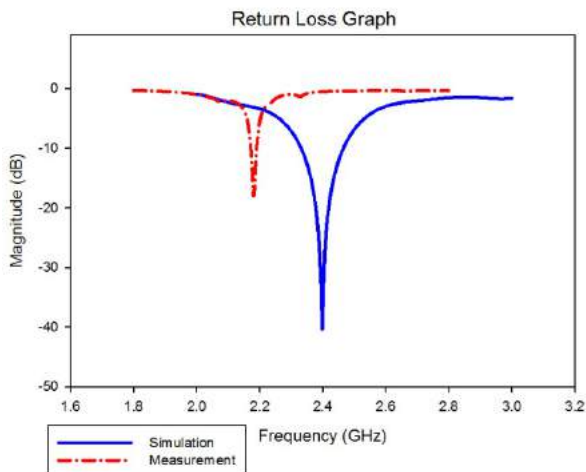


Figure 10: Return loss graph (Six layer).

Table 4: Return Loss (Summary)

Design	Freq. (GHz)		Magnitude (dB)	
	Simulation	Measurement	Simulation	Measurement
Single layer	2.4	2.415	-16.47	-14.96
Four layer	2.4	2.375	-41.93	-16.5
Six layer	2.4	2.18	-40.34	-18.11

4.3. Voltage Standing Wave Ratio, VSWR

Table 5 shows the simulation and measurement result of VSWR. Measurement results indicated that VSWR of the fabricated antennas were still in an acceptable value ($VSWR < 1.5$). The VSWR could be improved during the fabrication process so that very minimal power is reflected which results in maximum available energy being absorbed at the input terminal.

Table 5: Voltage Standing Wave Ratio

Design	Simulation		Measurement	
	VSWR	Freq.	VSWR	Freq.
Single layer	1.35	2.4	1.43	2.415
Four layer	1.02	2.4	1.35	2.375
Six layer	1.02	2.4	1.28	2.18

4.4. Bandwidth

Results in Table 6 indicated that bandwidth improved by increasing the substrate thickness. From the table, minimal bandwidth increment was obtained especially from the measurement readings which may be due to common narrow bandwidth characteristic of a patch antenna.

Table 6: Bandwidth.

Design	Simulation	Measurement
Single layer	75 MHz	16 MHz
Four layer	117 MHz	17 MHz
Six layer	135 MHz	19 MHz

4.5. Signal Strength

In Figure 11, it can be noticed that the signal strength improved as the substrate thickness increases. From this result, it can be said that a suitable antenna thickness must be chosen in order to achieve better signal strength.

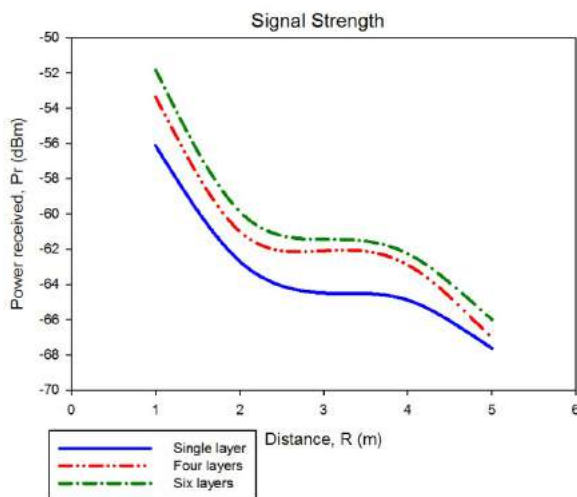


Figure 11: Signal strength graph.

5. Conclusions

Textile-integrated antennas with different composition structure for wearable application have been designed. Parametric observations between simulation and measurement results referring to different substrate thicknesses have been observed. A clear relation between substrate thickness and antenna performance optimization has been achieved. Based on the numerical observation, the increase of substrate thickness managed to increase the bandwidth up to 19% from the initial value. Antenna performance in terms of its signal strength has improved as well due to the effect of higher antenna's gain and efficiency obtained when increasing the substrate thickness. From the study it can be concluded that selection of suitable material thickness to optimize on-body antenna performance is crucial without affecting the comfort level of the user and keeping the undesired surface wave at a minimal level. The simulated and measured results showed that the proposed antenna's composition structure and the electro-textile can perform and radiate well. Although the study found evidence that fabrication error during substrate's compression process affected the antenna performance and measurement results, it was not possible to determine whether other variable such as the electro-textile element might as well cause the error between the simulation and measurement results. Further studies are therefore necessary to determine the effects of electro-textile structural composition on the antenna's performance especially during design process in order to obtain an accurate simulation model.

Acknowledgements

Authors would like to acknowledge Universiti Teknologi MARA (UiTM) and Antenna Research Group members for supporting this research projects.

References

- [1] S. S. Bhatia, and J. S. Sivia, "A Novel Design of Wearable Fractal Antenna for Wideband Applications,"

- International Conference on Advances in Human Machine Interaction (HMI)*, March 2016.
- [2] B. Roy, A. K. Bhatteerchya, and S. K. Choudhury, "Characterization of Textile Substrate to Design a Textile Antenna," *International Conference on Microwave and Photonics (ICMAP)*, December 2013.
- [3] A. A. D. Al-Sajee, and K. A. Hamad, "Improving Bandwidth Rectangular Patch Antenna Using Different Thickness of Dielectric Substrate," *ARPN Journal of Engineering and Applied Sciences*, Vol. 6, April 2011.
- [4] D. Rano, and M. Hashmi, "Design and Analysis of Wearable Patch Antenna Array for MBAN Applications," *22nd National Conference Communication (NCC)*, March 2016.
- [5] T. H. Dao, Q. C. Nguyen, V. D. Ngo, and M. T. Le, "Indoor Localization System Based on Passive RFID Tags," *International Conference on Intelligent System, Modelling and Simulation*, January 2014.
- [6] M. Grilo, and F. S. Correra, "Parametric Study of Rectangular Patch Antenna Using Denim Textile Material," *Microwave & Optoelectronics Conference (IMOC)*, August 2013.
- [7] K. Koski, E. Moradi, A. Vena, and T. Bjorninen, "Characterization of Electro-Textiles Using Wireless Reflectometry for Optimization of Wearable UHF RFID Tags," *PIERS Proceedings, Sweden*, August 2013.

Amalgamation of Rectangular Microstrip Antenna with Light Emitting Diode (LED)

S. Subahir¹, M.T Ali¹, H.Yon¹, N.H Kamarudin¹, A.H Awang¹, W.N.S.Muhamad¹

¹Antenna Research Centre (ARC), Faculty of Electrical Engineering, Universiti Teknologi MARA, Malaysia

*suhailas@salam.uitm.com, mizi732002@yahoo.com, hamizanyon@gmail.com, aaziatihusna@yahoo.com,

Abstract

This paper presents the design of amalgamation of rectangular patch antenna with Surface Mount Device (SMD) LED operating in the S-band region. The Computer Simulation Technology (CST) was used to optimize the position of LED within the radiating patch. The antenna was fabricated on RO6002 substrate with dielectric, $\epsilon_r=2.2$ and thickness $h = 1.57\text{mm}$. The performances of the antenna was compared and analyzed through simulation and measurement. The present results provide an important concept for further investigation of controlling the position and types of LED. Good agreements have been achieved for both the simulation and experimental results.

1. Introduction

As the technology of mobile communication system is increased, there are many research increasingly focus toward future wireless communication system. One of the important components in wireless communication is an antenna. During past several years the development of planar antennas are highly desirable which their characteristic are vital for many commercial applications. Planar antennas can gives many advantages such as compact, light weight construction leading to better portability, ease of conformal and ease of amalgamation with another device leading to extra functionality.

Compact devices has grown tremendously as increasing demand on telecommunication systems. In addition, there is highly desirable for a single device that can operate more than one function [1]-[3]. The existence of a single, rather than two devices which amalgamate of an antenna and Surface Mount Device LED will overcome the limited-space application. This device will have dual functions of wireless and also illumination [4]-[6].

The reason why LED is chosen in this project is because LED offer a number of advantages compared to existing light sources in optoelectronic applications. These include increased lifetime, reduced power consumption, higher brightness and better spectral purity [7]. Besides that LED is a small visible lighting which more practical to be

integrated with the patch antenna that operate at 2.4GHz.

This research highlights about the development on amalgamation LED with rectangular patch antenna where the device can have dual functions. As we identify, lighting source are always placed at the high position in a room to brighten up the surrounding. Besides, most antennas also are always placed at highest position in order to radiate better signals. Therefore, the integration of LED with the patch antenna as one device which has dual functions is beneficial to the users nowadays especially on space-limited application. In [8-10], the papers presented there is an amount of conducting material comes with the LED which has been foreseen to be integrated with the patch antenna. Figure 1 shows the structure of the Surface Mounted Device (SMD) white LED 5050. In simulation, the part which will be integrated with the patch antenna is only the conducting parts which are the anode and cathode of the LED. Figure 2 shows the circuit diagram of the SMD white LED 5050.

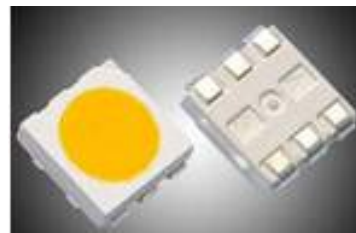


Figure 1 : SMD White LED 5050

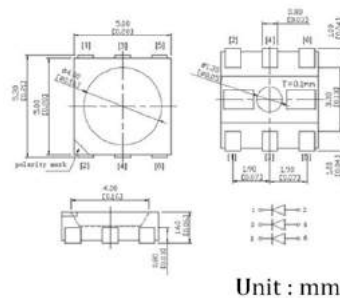


Figure 2: SMD White LED circuit diagram

2. Antenna Design

The basis of the design is the basic rectangular patch operated at frequency of 2.4 GHz with coaxial feeding. The dimensions of the antenna are determined using the equations available in [11]. RT Duroid 6002 was chosen with dielectric permittivity, $\epsilon_r = 2.2$ and the substrate thickness, $h = 1.57\text{mm}$. For an operating frequency of 2.4GHz, the dimensions of width and length of the antenna are 60 mm and 60 mm respectively as shown in Figure 1. A parasitic line was added around the radiating patch considered to place the negative terminal power supply to operate the LED. Table 1 shows the overall antenna parameters. The Computer Simulation Technology (CST) was used in order to optimize the number and position of LED within the radiating patch.

Table 1: Antenna Parameters

Parameters	Value
Patch width, W(mm)	37
Patch length, L(mm)	39.3
Substrate width, w_s (mm)	60
Substrate length, l_s (mm)	60

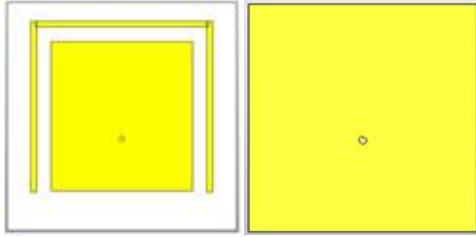


Figure 1: Basic rectangular patch with parasitic line

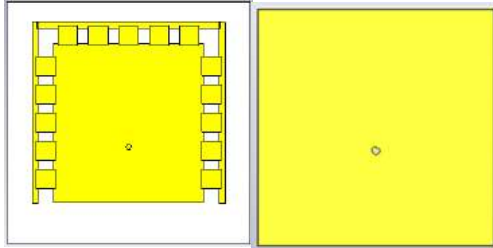


Figure 2: Rectangular patch with SMD LED

Figure 2 shows the rectangular patch antenna integrated with 15 white SMD LED. The LEDs that integrated onto the rectangular patch was conducting part of the LED as the conductor can give effect to antenna performance.

The antennas were implemented on the chosen microwave laminate using LPKF prototyping machine. In order to directly match with the connectors of the measurement set-up, a 50 ohm SMA connectors is soldered at the input of the antenna. Then, the SMD LED was attached with the

radiating patch using copper paste and have to heat in oven in order to make sure all the LEDs are strong enough attached. Figure 3 shows the fabricated antenna integrated with LEDs.

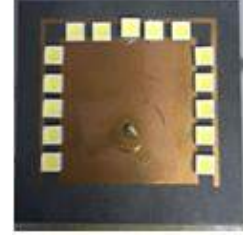


Figure 3: Fabricated rectangular patch integrated with LED

3. Results and discussion

The performances of the antenna were investigated through simulation and measurement. Single and two port measurements were performed using VNA measurement setup in anechoic chamber room. The results for simulation process are shown in section A while measurement in section B.

A. Simulation results

In simulation using CST software, there is several input parameters required which include dielectric constant, loss tangent, height of substrate, conductivity of conductor layer, thickness of conductor and surface roughness. The conducting part of LED will be implemented in the simulation and optimization process. The simulation results obtained are reflection coefficient (S_{11}), input impedance (Z_{in}), voltage standing wave ratio (VSWR), efficiency (η), directivity (D) and radiation pattern.

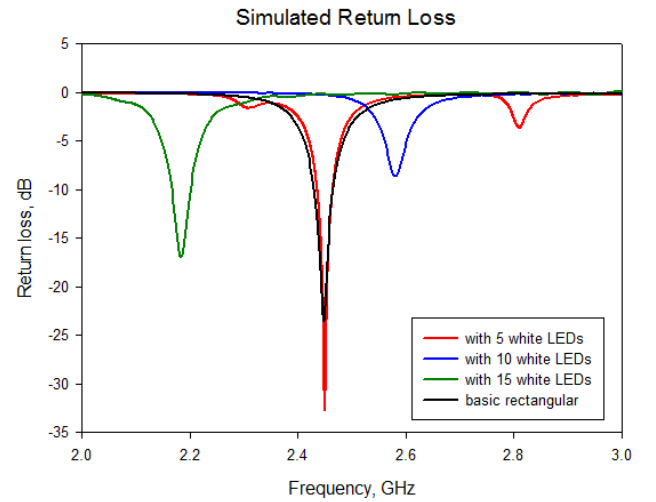


Figure 4: Simulated reflection coefficient

Figure 4 shows the return loss obtained from simulation. It shows the performance of reflection coefficient when the LEDs attached within the radiating patch. Basic rectangular patch showed well matched at their corresponding 2.45GHz, while when 5 LEDs was amalgamate at the radiating edge of the patch, a very low return loss of -33dB at the operating frequency of 2.45 GHz. When 10 LEDs were attached to radiating patch, the frequency shifted to 2.6GHz and the reflection coefficient results show signal reflect at the input. When 5 LEDs were added at non-radiating edge makes total LEDs are 15, the frequency was shifted to 2.18GHz with reflection coefficient -17dB.

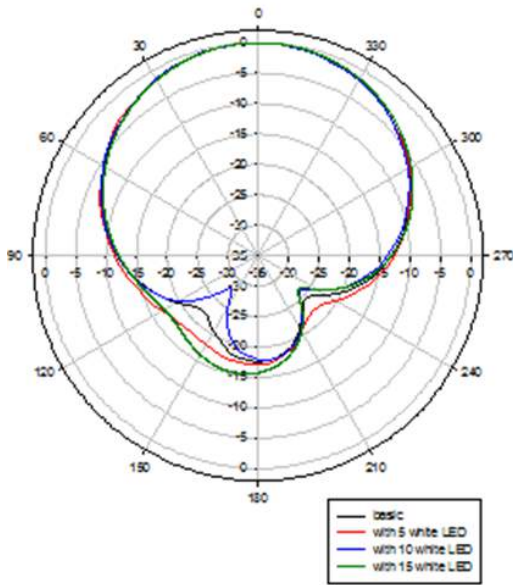


Figure 5: Simulated radiation pattern

Simulated radiation pattern is shown in Figure 5. The pattern shows more directional for all the conditions include basic patch, with 5 LEDs, with 10 LEDs and 15 LEDs. For patch amalgamate with 15 LEDs, there is bigger backlobe compared to others.

B. Measurement results

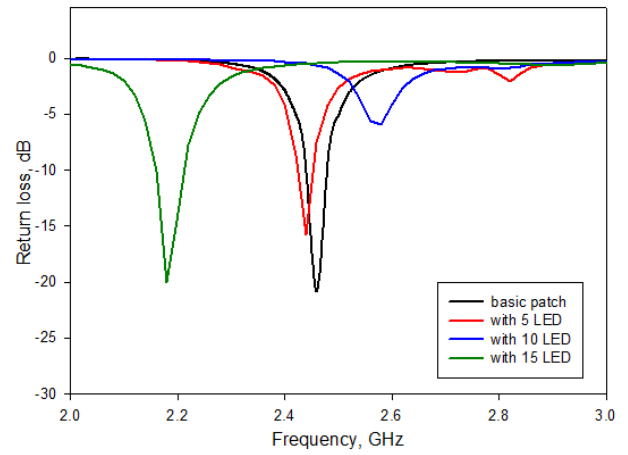


Figure 6: Measured reflection coefficient

Measured reflection coefficient was plotted as shown in Figure 6. The low return loss was obtained shows matching input between patch and feeding. It shows the performance of reflection coefficient when the LEDs attached within the radiating patch. Basic rectangular patch showed well matched at their corresponding 2.45GHz, while when 5 LEDs was amalgamate at the radiating edge of the patch, a low return loss of -15dB at the operating frequency of 2.43 GHz. The frequency shifted to 2.6GHz with reflection coefficient -5.23 dB when 10 LEDs were attached to the other radiating edge. When 15 LEDs attached to non-radiating edge of the patch, the frequency was shifted to the 2.18GHz with reflection coefficient -20dB.

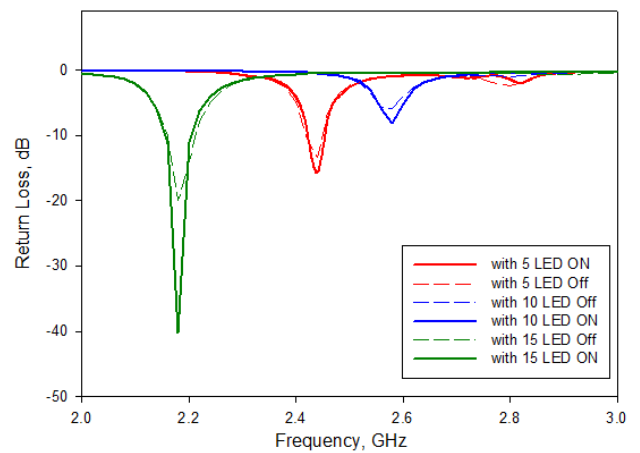


Figure 7 : Measured reflection coefficient for LED On and Off

Figure 7 shows the measurement result of reflection coefficient for LED ON state and OFF state for three situation of amalgamation. It starts with connection for 5 LED, followed by 10 LED at the radiating edge and total 15

LED at both non-radiating edge and radiating edge. The results indicate that low return loss for LED ON state compared to OFF state at the corresponding measured resonant frequency.

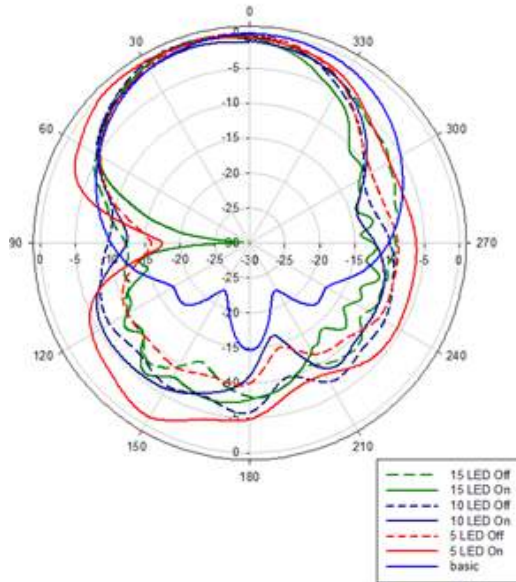


Figure 7 : Measured radiation pattern for LED On and Off

Measured radiation pattern were depicted as shown in Figure 7. There are 6 categories of radiation pattern where the basic rectangular antenna was amalgamate with different numbers of LEDs at radiating edge and non-radiating edge, they are 5 LEDs On and Off state, 10 LEDs On and Off state and also 15 LEDs On and Off state. The amalgamation of microstrip antenna with LEDs was affect the pattern become omnidirectional compared to basic rectangular without LEDs which is more directional. The pattern also shows 15 LEDs On state is more directional compared to 10 LEDs and 5 LEDs.

4. Conclusions

Table 1 shows the comparison results between simulation and measurements of the designed antenna without LED and 15 LEDs.

Table 1: Comparison performances

Parameters	Simulation		Measurement		
	Basic	Antenna with 15 LEDs	Basic	Antenna with 15 LEDs	
				ON	OFF
Frequency Response	2.45	2.185	2.46	2.182	2.182
Return loss, dB	-27.45	-28.48	-27.79	-18.75	-19.43
Bandwidth, MHz	41	42	40	42	41
Directivity, dB	7.19	7.21	8.08	8.68	6.94
Gain, dBi	6.72	6.75	5.46	2.87	1.69

The development of amalgamation rectangular patch antenna with LED was analyzed through simulation and measurement. The size of antenna was rounded of 60mm width and 60 mm length. The SMD LED were used amalgamate with patch antenna, and the performances are obtained through different numbers of LEDs. The amalgamation of LED with radiating patch at the radiating edge will affect the reflection coefficient as it will disrupt the matching system at the input, while LED attached at non radiating edge will reduce the resonant frequency because it has change the length of the radiating patch. The results of measurement verified the results from simulation. The amalgamation of rectangular patch with LED shows inverse proportional between number of LEDs and gain, increase of LEDs integrated with patch antenna the gain will be decreased. However, gain will be increased for LED On state compared to Off state.

Acknowledgements

The authors would like to thank to Universiti Teknologi MARA for sponsoring the work. Express gratitude to the members of Antenna Research Centre (ARC), Faculty of Electrical Engineering for supporting the research work.

References

- [1] M.Hilmi, M.T.Ali, N. Ya'acob, H.M.Zali, H.Ja'afar "Development of Fluorescent Tube Antenna Array for Wi-Fi Application" *2015 IEEE Symposium on Computer Applications & Industrial Electronics*, 12- 14 April 2015.
- [2] A. Valizade, P.Razaei, and A.A Orouji "A new Design of Dual Port Active Integrated Antenna for 2.4/5.2 GHz for Wifi Application", *Progress In Electromagnetics Research B*, Vol. 58, 83-94, 2014.
- [3] Haruyama, S. "Visible light communication", *IDW'10 - Proceedings of the 17th International Display Workshops*, Vol. 3, pp. 2189-2192
- [4] Shi-Wei Dong, Ying Wang, "Spatial Power Combining of Active Integrated Antennas in Microwave Power Transmission," *Microwave, Antenna, Propagation, and EMC Technologies for Wireless Communications (MAPE)*, 2011
- [5] Ja'afar, H. Ali, M.T. ; Halili, N.A. ; Hanisah, M.Z., "Analysis and design between plasma antenna and monopole antenna . International Symposium on Telecommunication Technologies (ISTT), 2012 ,47 – 51
- [6] Anderson, T. Dyer, F."Plasma antenna VSWR and co-site and parasitic interference reduction or elimination" *Antennas and Propagation Society International Symposium (APSURSI)*, 2014 IEEE, 366 – 367

- [7] Alexeff, I., Anderson, T. ; Parameswaran, S. ; Pradeep, E.P."Experimental results of plasma antennas", The 33rd IEEE International Conference Plasma Science, 2006. ICOPS 2006. 351
- [8] S. Subahir, M.T Ali, N.A Ramli, S.N Kamarudin, A.H Awang, M.R Kamarudin "Development of Rectangular Loop Microstrip Antenna with Light Emitting Diode for Wi-fi Application" *Applied Mechanics and Materials*, Vol 781, pp 116-119, 2015
- [9] S.N. Kamarudin, M.T. Ali, S. Subahir, A.A. Azlan, S.Muhamud-Kavat. M. R. Kamarudin. "Design and Investigation of H-Shaped Patch Antenna Integrated with Light Emitting Diodes", *Applied Mechanics and Materials*, Vol. 781, pp. 106-109, 2015
- [10] S. Subahir, M.S Amari, M.T Ali, S.N Kamarudin, M.F Jamlos "Rectangular Spiral Microstrip Patch Antenna Integrated with Light Emitting Diode" *2014 IEEE 2nd International Symposium on Telecommunication Technologies (ISTT)*, Langkawi, Malaysia, pp. 24-26 Nov 2014
- [11] Constantine A. Balanis, "Antenna Theory Analysis and Design". Third Edition John Wiley & Sons, Inc., 2005.

Microwave and Millimeter Circuits and Systems

Substrate Integrated Waveguide Circular Cavity Resonators for Planar Diplexer Design

Noor Hasimah Baba¹, Aziati Husna Awang¹, Mohd Tarmizi Ali¹,
Nurul Huda Abd Rahman¹, and Hizamel Mohd Hizan²

¹Faculty of Electrical Engineering, Universiti Teknologi MARA, Shah Alam, Malaysia

²Advanced Physical Technologies Lab, Telekom Research & Development Sdn Bhd, Cyberjaya, Malaysia

E-mail: nhasimah@salam.uitm.edu.my

Abstract

This paper presents a new design of planar diplexer based on substrate integrated waveguide single mode filters employing circular cavity. The simulation return losses for the lower and upper channels are greater than 20.94 dB and 30.92 dB respectively. The minimum insertion losses obtained are 0.87 dB and 0.74 dB at each band. Equivalent circuit, simulated and experimental results are all provided. The proposed SIW diplexer has a promising application for the uplink/downlink RF front end subsystem that is essential for wireless communications systems.

1. Introduction

Waveguide diplexers or multiplexers are indispensable components in RF/microwave wireless communication systems [1]. They are also widely employed to all types of communication systems such as microwave and millimeter-wave applications. Their applications are used to filter between wanted and unwanted signal frequencies. Diplexers and filters that are manufactured separately in conventional design are bulky in size thus uses more materials and space in fabrication process. In order for them to connect with each other, there is a need of transmission line and other matching circuits which will contribute to losses. This is when they come up with miniaturized filters and diplexers structure that are integrated into substrates resulting in smaller and compact but capable of operating with the same performance [2]. A waveguide or its cavity, when it is synthesized in a planar substrate-based circuit and the propagating waves are constrained by linear arrays of metallic vias, is then referred to as a substrate integrated waveguide (SIW) [3]. Its basic structure is similar to a microstrip structure but it works in TE or TM modes, instead of the quasi-TEM mode of microstrip line.

Many works have been carried out to replace all-metallic waveguide structures to SIW circuits. The SIW offers advantages such as high Q factor, low insertion loss, low cost and high power-handling capacity [5,6]. Apart from the well-known advantages, this technique widely appears in various subsystems such as filters, couplers, power dividers,

and antennas [7-11]. However, the main drawbacks of SIW are when a single row of vias is used, the leakage loss can be substantial. This leakage limits the isolation between adjacent resonators, producing small but non-zero coupling coefficients. In this paper, the performance of the first order diplexer was investigated by simulation. The electrical and physical modelling were attained using ADS software and the full-wave EM simulator CST, respectively. To prove the concept, the diplexer is fabricated using Rogers RO3006 substrate with dielectric constant of 6.15 and thickness of 1.28 mm. Measured results are presented and compared to those simulated.

2. Bandpass Filters Design

The synthesis and design techniques of a 2.2 GHz and 2.4 GHz diplexer is proposed and demonstrated employing SIW technology. The diplexer is synthesized from the generalized low-pass prototypes Chebyshev configurations [12]. The working mode for the diplexer is TM_{010} mode. Firstly, individual bandpass filters using the TM_{010} mode SIW circular resonator were designed at 2.2 GHz and 2.4 GHz. Then, the two filters are combined together to work as diplexer. Normally, the diplexer employs a 3-port device to connect the two filters thus for feeding the two filters, a microstrip T-junction power divider is used. 50-Ohm microstrip lines with inset feed are used to directly excite the filters. Simulated results are presented and compared. A network that meets Table 1 design specification is synthesized using standard filter theory starting with a low-pass filter. Then the lowpass prototype is transformed into bandpass filter at the desired frequencies with -10 dB passband return loss bandwidth of 20 MHz. The equivalent circuit of the first-order diplexer is shown in Fig. 2. In this network, the admittance inverters J01 and J12 are used as the input and output coupling of the filter.

TABLE 1. FIRST-ORDER TM₀₁₀ SIW FILTER SPECIFICATIONS

Filter specifications	
Centre frequency, f_0	2.2 GHz and 2.4 GHz
Passband bandwidth (PBW)	20 MHz
Passband return loss (L_R)	≥ 10 dB
Stopband insertion loss (L_A)	> 10 dB at $f_0 \pm 100$ MHz (SBW)
Order, N	1

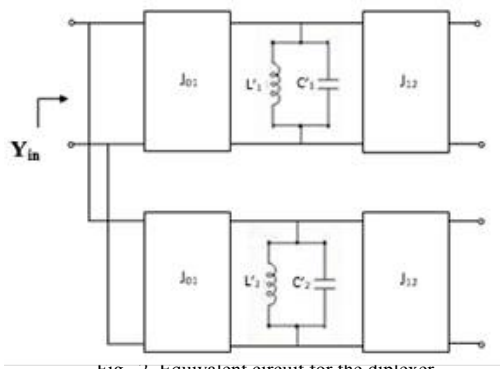


Fig. 2. Equivalent circuit for the diplexer

All the element values for the diplexer are shown in Table 2.

TABLE 2. ELEMENT VALUES FOR SINGLE-MODE DIPLEXER

Element	Value (2.2 GHz)	Value (2.4 GHz)
$L'_1 = L'_2$	0.9865 pH	0.8289 pH
$C'_1 = C'_2$	5.3052 nF	5.3052 nF
$J_{01} = J_{12}$	1	1

The simulated responses of the first order diplexer having center frequencies at 2.2 GHz and 2.4 GHz with 10 dB passband return loss bandwidth of 20 MHz are shown in Fig. 3.

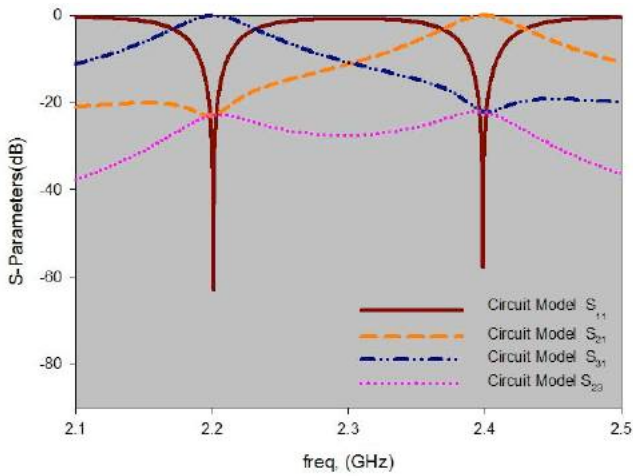


Fig. 3. Equivalent circuit simulation results

3. Diplexer Design

The fundamental parameter in designing the cavity of the SIW filter is the resonant frequency. The radius of the circular SIW cavity is approximated according to the resonant frequency using the formula [13], and then the radius is optimized by electromagnetic software. In this design, the matching from 50-Ohm microstrip line to the SIW cavity resonator section is achieved by the inset excitation structure which converts quasi-TEM mode propagating in microstrip line to the TM₀₁₀ mode of the SIW cavity resonator. The configurations of the proposed filter and diplexer with the transitions are shown in Fig. 4. The optimized geometric parameter of the proposed structure is shown in Table 3. The topology comprises of a metallic top layer and a conductive ground layer (t1), two circular cavity resonators, inset couplings, and linear arrays of via holes to form a circular via wall around the cavity resonators.

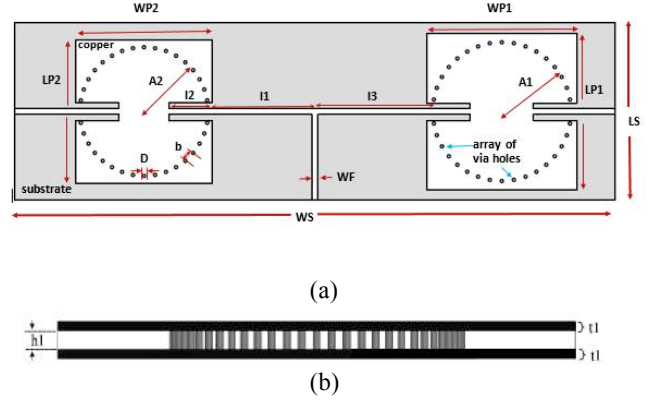


Fig. 4. Configuration of the First-order SIW diplexer (a) top view, (b) side view. The geometrical parameters are:

TABLE 3. GEOMETRIC DIMENSIONS OF DIPLEXER

Symbol	Value (mm)	Symbol	Value (mm)
A1	20.75	Lp1	11
A2	19.05	Lp2	11
b	3.5	Ls	53
D	1	wf	1.76
h1	1.28	w1	1.30
I1	14.4	w2	1.23
I2	11.5	wp1	45
Lf	25.51	wp2	41
Lf1	30	ws	180
Lf2	30.7	t1	0.035

The proposed diplexer was simulated and optimized using the full-wave EM simulator CST. Fig. 5 displays the simulated and measured S parameter response for the

diplexer. It could be observed that there were two resonant points namely 2.2 GHz and 2.4 GHz. From this plot, the simulation return losses for the lower and upper channels are greater than 20.94 dB and 30.92 dB respectively. The minimum insertion losses obtained are 0.87 dB and 0.74 dB at each band. The diplexer provides isolation better than 15 dB at both channels. This moderate performance is caused by the coupling effects that the adjacent resonators introduce. The main limitation of the SIW technology is the maximum isolation that a discontinuous wall made of via holes can provide between adjacent resonators, producing undesirable cross couplings. The S parameter response in Fig. 5 shows a good agreement with the ideal electrical modelling response in Fig. 3. Fig. 6 revealed the corresponding E-field distribution in the cavity resonator at 2.2 GHz. The surface current distribution of the proposed diplexer is shown in Fig. 7. A strong current distribution is contained within the SIW cavity and port 2 at 2.2 GHz. Similarly in Fig. 8, the same observation is seen within the SIW cavity and port 3 at 2.4 GHz.

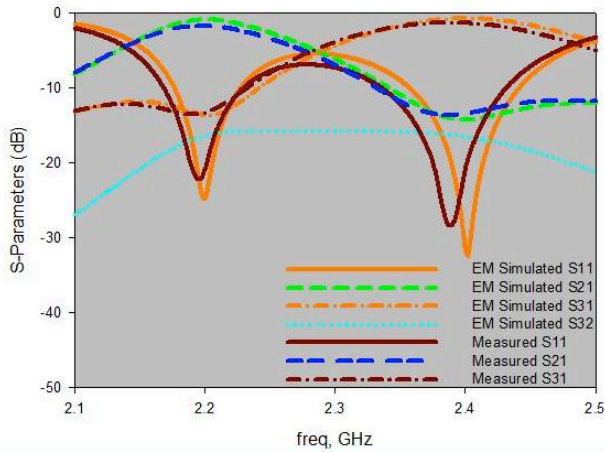


Fig. 5. Simulated and measured S parameters response of SIW diplexer

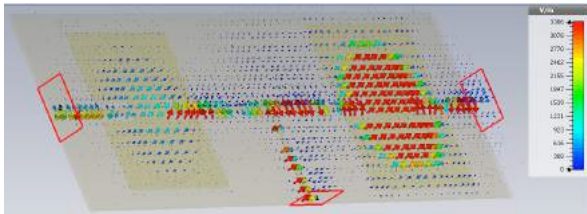


Fig. 6. The diplexer E-field distribution in the cavity at 2.2 GHz.

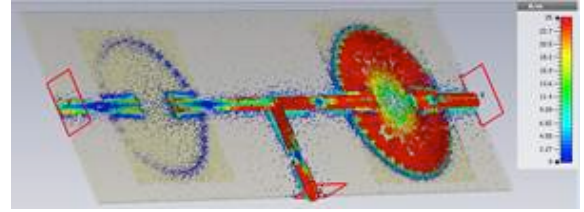


Fig. 7. The diplexer surface current distribution in the cavity at 2.2 GHz.

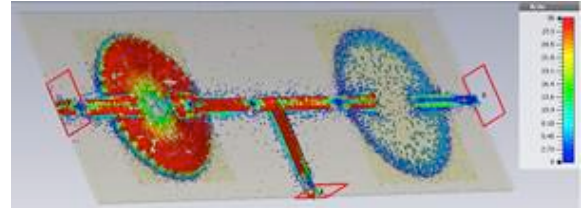


Fig. 8. The diplexer surface current distribution in the cavity at 2.4 GHz.

4. Conclusions

A planar SIW diplexer is proposed employing single-mode circular cavity resonators having centre frequencies at 2.2 GHz and 2.4 GHz, and which is proposed for LTE/WiFi applications. The EM simulated response shows a good agreement with the ideal electrical modelling response. The diplexer features low insertion loss, compact, simple structure and easy to connect to other circuits. This design provides an alternative solution for the uplink/downlink RF front end subsystem that is essential for wireless communications systems. The functionality of the presented results will be validated experimentally in near future.

Acknowledgements

Authors would like to thank the staff of Antenna Research Centre (ARC) off Universiti Teknologi MARA Malaysia (UITM) for the technical support.

References

- [1] Junxia He, Kuandong Gao, Zhenhai Shao "A Novel Compact Ka-Band High-rejection Diplexer Based on Substrate Integrated Waveguide" in *Computational Problem-Solving (ICCP)*, 2012 *International Conference* pp.193-197, 2012
- [2] Zamzam Kordiboroujeni and Jens Bornemann "Mode Matching Design of Substrate Integrated Waveguide Diplexers" *Microwave Symposium Digest (IMS)*, 2013 *IEEE MTT-S International*
- [3] K. Wu, D. Deslandes, and Y. Cassivi, "The Substrate Integrated Circuits- A New concept for high-frequency electronics and optoelectronics," in *6th International*

Conference on Telecommunications in Modern Satellite, Cable and Broadcasting Service. TELSIKS 2003, pp. P-III-P-X.

- [4] Hong Jun Tang, Wei Hong, Member, IEEE, Ji-Xin Chen, Guo Qing Luo, and Ke Wu, Fellow, IEEE "Development of Millimeter-Wave Planar Diplexers Based on Complementary Characters of Dual-Mode Substrate Integrated Waveguide Filters With Circular and Elliptic Cavities" *IEEE Transactions on Microwave Theory and Techniques*, VOL. 55, NO. 4, APRIL 2007
- [5] Nikolaos Athanasopoulos, Dimitrios Makris, and Konstantinos Voudouris "Development of a 60 GHz Substrate Integrated Waveguide Planar Diplexer" 2011 *IEEE MTT-S International Microwave Workshop Series on Millimeter Wave Integration Technologies*.
- [6] D. Zayniyev, H. F. Abu Tarboush, D. Budimir "Microstrip Antenna Diplexers for Wireless Communications" in *the Proceedings of the 39th European Microwave Conference*, pp. 1508-1510 September 2009
- [7] H. J. Tang, W. Hong, Z.C. Hao, J.X. Chen and K. Wu "Optimal design of compact millimeter-wave SIW circular cavity filters" *Electronics Letters* 15th September 2005 Vol. 41 No. 19
- [8] Hamideh Dashti and Mohammad H. Neshati, Senior Member, IEEE "Development of Low-Profile Patch and Semi-Circular SIW Cavity Hybrid Antennas" *IEEE Transactions on Antennas and Propagation*, VOL. 62, NO. 9, September 2014
- [9] Hamideh Dashti, Mahmoud Shahabadi, and Mohammad H. Neshati "SIW Cavity-Backed Slot Antennas with Improved Gain" in *Electrical Engineering (ICEE), 2013 21st Iranian Conference* 2013
- [10] Maurizio Bozzi "Substrate Integrated Waveguide (SIW): an Emerging Technology for Wireless Systems" in *Proceedings of APMC 2012*, Kaohsiung, Taiwan, Dec. 4-7, 2012
- [11] Alejandro Garcia-Lamperez, Magdalena Salazar-Palma, Sai Ho Yeung "SIW Compact Diplexer" in [Microwave Symposium \(IMS\), 2014 IEEE MTT-S International](#) 2014
- [12] I. C Hunter, *Theory and Design of Microwave Filters*. London: Institution of Electrical Engineers, 2001.
- [13] Hizamel M. Hizan, Ian C. Hunter and A. I. Abunjaileh "Integrated SIW Filter and Microstrip Antenna" in *Proceedings of the 40th European Microwave Conference* 28-30 September 2010, Paris, France.

Electromagnetic Compatibility

Electro-Magnetic Effects and Detections on Digital Integrated Circuits

David El-Baze^{1*}, Jean-Baptiste Rigaud¹, Philippe Maurine²

¹Mines Saint-Etienne, Gardanne, France ²LIRMM, Montpellier, France

*corresponding author, E-mail: david.el-baze@emse.fr

Abstract

Radiation and Electro-Magnetic Emissions can cause errors in the operation of digital systems. These kinds of effects must be alleviated as far as possible in critical systems so as nuclear plants, spatial activities and systems dedicated to security purposes. EM perturbations do not always produce a Deny of Service, they can also be used to inject very controlled signals into microprocessors or any integrated circuits to obtain a certain benefit. This paper takes advantage of recent results and analyses to provide a fully digital sensor allowing to detect Electro-Magnetic pulses. Because it is fully digital it is easy to integrate in complex ICs.

1. Introduction

Since [1], it is known that Electro-Magnetic (EM) fields emitted by a digital component can be analyzed to get very accurate information on the data being processed by ICs. Moreover, according to [2] and [3], these fields can not only be used to “listen” to the IC, but also to “talk” to it. It means that EM emissions can change the state of digital systems and so cause soft errors in the operations. This is clearly unwanted as it can have catastrophic consequences when it happens in nuclear plants or security dedicated systems. Indeed in military and smartcard worlds, these effects can be exploited by mathematical means to retrieve secret information, control execution flows or by-pass security protocol [4].

Two models of the effects generated during the injections have been proposed. The first one proved that it changes the propagation time of the information in the combinatorial logic [7]. The second one, which encompasses the first one, that some gates seem to be more affected than others.

The rest of this paper is organized as follows: Section 2 introduces a fault model explaining the observed faulty behaviors. Section 3 details the construction of an embedded sensor able to detect powerful EM fields. Section 4 presents the test protocols and gives experimental results. Before conclusion, section 5 opens a discussion about the interest of such a detector.

2. A recent fault model

However, in 2014, [6] has experimentally demonstrated that it is possible to generate faults within a circuit at rest (clock stopped), using an enhanced EM Pulse Injection (EMPI)

platform. This means that EMPIs are able to induce bitsets and bitresets demonstrating that the delay fault model is not complete. In 2015, Ordas et al., have finally introduced and experimentally demonstrated in [5] the correctness of a new fault model for EMPI. This model is called the sampling fault model. According to this model, EMPIs are able to modify significantly but temporarily the bias of any interconnect within an IC. Considering this, and the fact that the D Flip-Flops (DFF) are the only CMOS gates that must meet some operating constraints (in dynamic mode), they assumed in [5] that DFFs are the main front door to inject faults within IC using EMPI. More precisely, the sampling fault model states that the EM susceptibility of DFFs is higher than any other type of CMOS gates and that its value is:

- really high during their switching, i.e. when a rising edge of the clock occurs. This means that an EMP of moderate amplitude is sufficient to induce a fault in an IC at each rising edge of the clock.
- lower when the clock signal is stable (at 0 or V_{dd}). This does not mean that no fault can be induced but solely that only bitsets or bitresets can be produced using a much more powerful EMP.

As an example, Fig. 1 shows the number of errors produced in a synchronous algorithm, according to the moment of injection. The considered device was running at 50 MHz and gave a reference signal at the start of execution. This signal has been used as a trigger for the EMPI platform. As expected, every 20 ns (the period of a signal at 50 MHz), a peak in the number of faults is observed. It appears to be the time where the clock is rising. Thanks to this better understanding of EM effects on digital ICs, it opens a new way to detect their impacts.

The following section illustrates a way to take advantage of this new model to design an EM detector.

3. A DFF Based Sensor

Embedded sensors are important elements in the set of countermeasures deployed within IC, and especially smartcards, to thwart fault attacks. They allow detecting most but not all fault injection attempts. They are therefore not sufficient to fully stave off fault attacks but remain key elements of a complete defense strategy.

As an application of the experimental model introduced

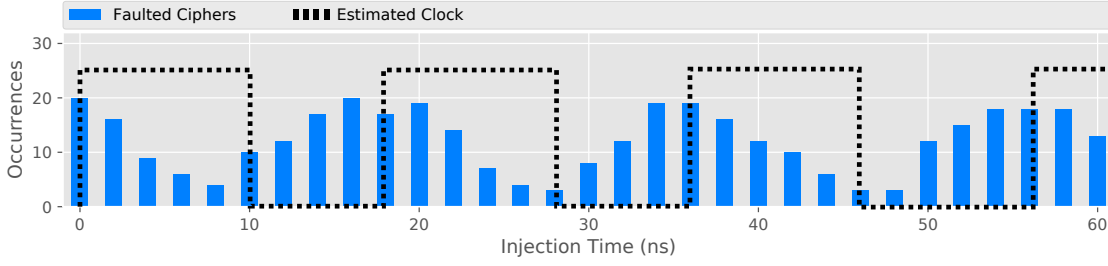


Figure 1: Number of erroneous results of a cryptographic algorithm (blue) according to injection time.

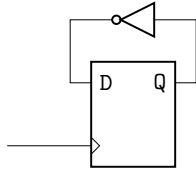


Figure 2: A self looped DFF.

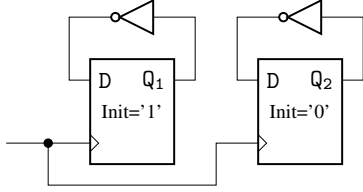


Figure 3: 2 DFFs with different startup values.

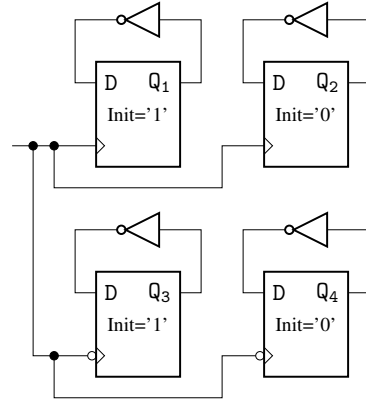


Figure 4: 4 DFFs with different startup values and different sensitivities.

in the previous section, a fully digital sensor has been designed [8]. The sampling fault model puts in evidence that DFF are very susceptible to EM Pulses (EMP), especially during the storage operation. Thereby, the sensor mainly features DFF to increase the probability to catch the effect. To achieve it, the sensor uses oscillating DFF: each latch has an output Q which is inverted, and then connected to its input D as shown in Fig. 2.

The more DFF with different parameters the sensor has, the more chance it has to detect an EMP. Thus, different tweaks are used to multiply the number of DFF and keep in mind that the sensor has to ensure that the global state is correct.

3.1. Initial Value

Each DFF can have a default value at startup, either because the library allows it, or by adding a bit of logic. This value will now be noted in figures as “Init=’1’” when it will start with a high value, and “Init=’0’” when it will be a low one. The sensor can now employ two DFFs (Fig. 3).

3.2. Clock Edge Sensitivity

Another thing that can be done to pluralize the number of DFF, is to have rising clock edge sensitive latches and falling edge sensitive ones. This way, twice more DFFs can be used for the model, half with falling edge sensitivity, and

the other half with rising one (Fig. 4).

3.3. Consistency Checker

The structure obtained permits to check each kind of transition ($0 \rightarrow 1$, $1 \rightarrow 0$) at rising and falling time. Now that the set of flip-flops is defined, the sensor have to check and verify that values are coherent (ie. that none of their values has been impacted by EMI). To do so, by construction, we know that at any time that Q_1 and Q_2 take opposite values. Same reasoning can be applied to Q_3 and Q_4 . By tracing the value of the outputs over time, as shown in Fig. 5, it shows that Q_1 and Q_4 are opposed at every rising clock edge. This is applicable for Q_2 and Q_3 too. As the output of the sensor is one bit long, it does not allow to measure the fields, but it can tell if it is important enough to fault the logic of the IC.

Next section shows some experimental results with IC embedding this new sensor.

4. Applications

4.1. Tests experiments

Experiments were conducted with a ad-hoc probe (Fig. 8), a voltage generator (generating square pulses from 0 V to 400 V) and a motorized stage. The probe scans the Device Under Test (DUT) depicting a regular grid over its surface.

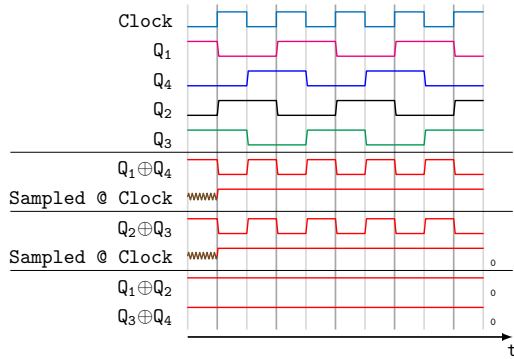


Figure 5: Evolution of signals Q_1, Q_2, Q_3, Q_4 over time.

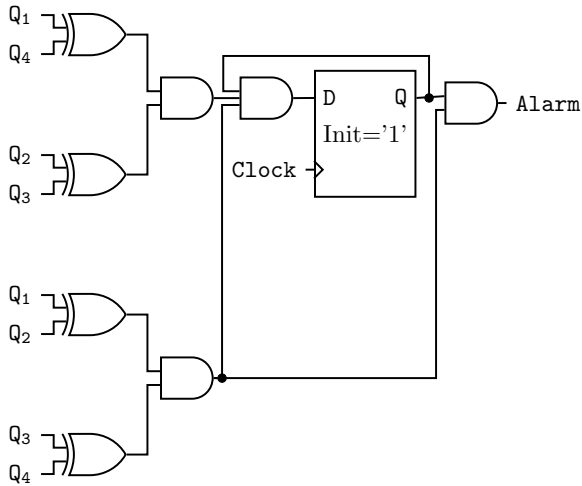


Figure 6: Consistency checker. Verify that values Q_1, Q_2, Q_3, Q_4 are coherent.

This allows to study the effects of the injections according to the firing position. Two indicators have been set up to evaluate the efficiency of the sensor:

- DR : the Detection Rate, which is the ratio between the number detected injections that led to a fault and the number of injections that led to a fault.
- CR : the Coverage Rate, the ratio between the number of position tested where the sensor was efficient and the number tested position where something happened during EMPI.

4.2. Results on FPGA

A FPGA (Field Programmable Gate Array) is an integrated circuit that can be used to prototype a circuit before production on large scale. To test a set of parameters we have taken advantage of such component as the logic it contains can be reprogrammed in a few seconds. Different FPGAs, each with different technological nodes, have been used to

conduct the tests : Virtex II Pro (90 nm, flip-chip with back-side access), Virtex 5 (65 nm, flip-chip with back-side access), Spartan 3E 1600 (90 nm).

Three adapted designs have been made to fit into these FPGAs, one with 34 sensors (Spartan 3), and two with 36 sensors (Virtexs). The cluster of sensors is uniformly distributed over the circuit's floorplan and works as follows : if any triggers an alarm then the global alarm is also triggered. They integrate an AES (a standard cryptographic algorithm) which is acting as a potentially disrupted application. During a test, the number of errors and the number of detections according to the injection time have been pointed out (see Fig. 7). The test was the same as for Fig. 1, but this time, the number of alarms is recorded. As the sensor worked twice as fast than the rest (due to rising/falling sensitivity), its peak of detection is repeated every 10 ns. The results for each tested FPGA are available in Table. 1.

During the tests, ≈ 13.000 injections have been made for each ICs. The summary presented in Table. 1 shows that the sensors are able to efficiently detect EMPs. It is also important to note that the sensor has never been triggered without attack.

Table 1: Results Synthesis.

IC	# of sensors	DR (%)	CR (%)
Spartan 3 1600E	34	87	85
Virtex II Pro	36	89	72
Virtex 5	36	99	99

5. Discussion

These results are encouraging and allow to identify points to be clarified and simulated in order to better understand the coupling phenomena within the IC. Simulations could explain the fault model used and allow the identification of the best areas for implanting a sensor.

Moreover, some technological parameters may be adapted to reduce or increase the latch' EM sensitivity. Design rules could be proposed to do hardening against EMPI.

In addition, these results show that EM susceptibility analysis could gain in being performed synchronously with the clock of integrated circuits.

6. Conclusions

There are multiple advantages of having a digital sensor. First, the overhead: the use of a digital component permits to limit the surface cost of the detector. Thus, in our tests, even with a mesh of 36 sensors, the overhead is under 6% and could certainly be further reduced. Second, the integration with the design workflow is easy as it only uses standard cells available in all standard cell library.

References

- [1] Samyde, David and Skorobogatov, Sergei and Anderson, Ross and Quisquater, Jean-Jacques, "On a new

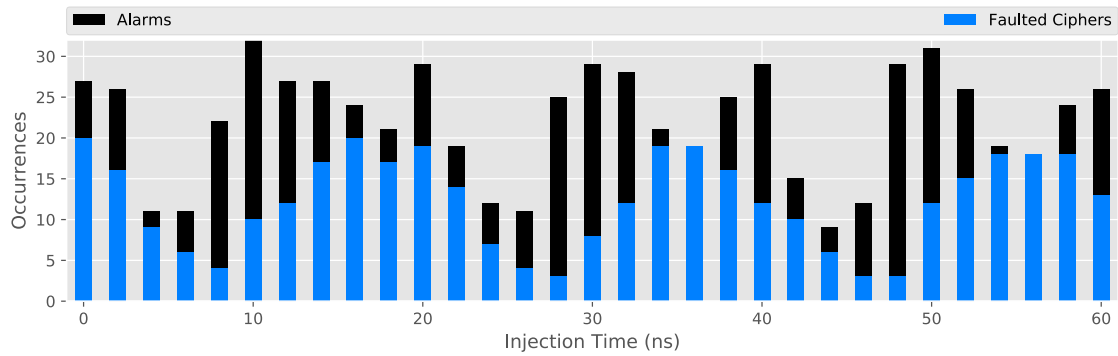


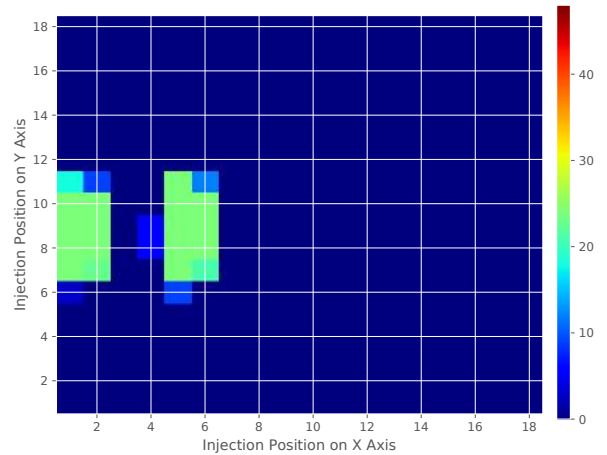
Figure 7: Number of erroneous results of a cryptographic algorithm (blue) and detector activity (black), according to the injection time.



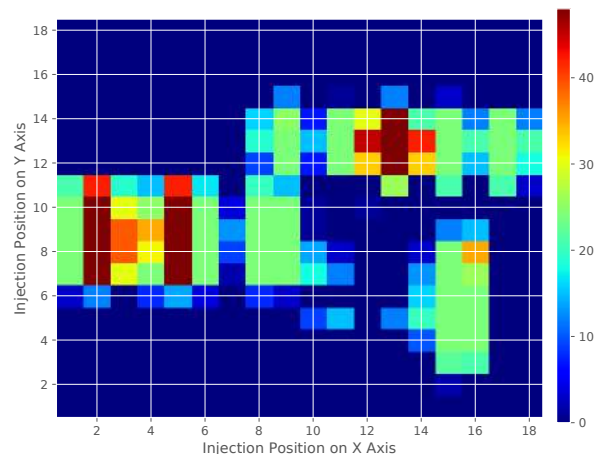
Figure 8: Picture of an EM injection probe.

way to read data from memory”, *Security in Storage Workshop, 2002. Proceedings. First International IEEE*, 65–69, 2002.

- [2] Schmidt, Jörn-Marc and Hutter, Michael, “Optical and EM fault-attacks on crt-based rsa: Concrete results”, 2007.
- [3] Poucheret, François and Tobich, Karim and Lisart, Mathieu and Chusseau, Laurent and Robisson, Bruno and Maurine, Philippe, “Local and direct em injection of power into cmos integrated circuits”, *FDTC 2011* 100–104, 2011.
- [4] Dehbaoui, Amine and Dutertre, J-M and Robisson, Bruno and Tria, Assia, “Electromagnetic transient faults injection on a hardware and a software implementations of AES”, *FDTC 2012*, 7–15, 2012.
- [5] Ordas, Sebastien and Guillaume-Sage, Ludovic and Maurine, Philippe, “EM Injection: Fault Model and Locality”, *FDTC 2015* 2015.
- [6] Ordas, Sbastien and Guillaume-Sage, Ludovic and Tobich, Karim and Dutertre, Jean-Max and Maurine, Philippe, “Evidence of a larger EM-induced fault model”, *CARDIS 2014* 2014.
- [7] Dehbaoui, A. and Dutertre, J. M. and Robisson, B. and Orsatelli, P. and Maurine, P. and Tria, A., “Injection of transient faults using electromagnetic pulses -Practical results on cryptographic system-”, *Cryptology ePrint Archive, Report 2012/123*
- [8] El-Baze, David and Rigaud, Jean-Baptiste and Maurine, Philippe, “A fully digital EM Detector”, *DATE 2016* 2016.



(a) IC's Positions which change the behavior / produce errors in the course of the algorithm.



(b) IC's positions which produce alarm.

Figure 9: EMPs on a Virtex 5 FPGA.

Shielding Effectiveness Measurement for Conductive Textile-based RF-shielded Environment

M. A. Humayun¹, H. A. Rahim¹, M. AbdulMAlek², P. J. Soh³, M.S. Zulkefli⁴, C. M. Nor³, A. A. Al-Hadi³

¹Bioelectromagnetic Research Group, School of Computer and Communication Engineering, Universiti Malaysia Perlis(UniMAP), Kampus Pauh Putra, 02600, Arau, Perlis, Malaysia.

²Faculty of Engineering and Information Sciences, University of Wollongong in Dubai, Dubai, UAE

³School of Computer and Communication Engineering, Universiti Malaysia Perlis, Kampus Pauh Putra, 02600, Arau, Perlis, Malaysia.

⁴Center of Diploma Studies, Universiti Malaysia Perlis

*corresponding author: humayun0403063@gmail.com

Abstract- The electromagnetic noise free environment is important to investigating possible adverse health effect caused by the exposure of the RF-EMF due to its sensitivity to the Electromagnetic Interference (EMI) noise. Thus, an experimental investigation of an EMI shielded, noise free environment has been performed. The shielding effectiveness of the proposed EMI shielded environment was studied in the frequency range of 1800-3200 MHz where it falls under the most widely used frequency by mobile phones, WBAN devices, and wireless communication systems.

Measurement Setup

In order to determine the effectiveness of the shielding in the shielded room, the free space measurement technique (based on Standard No. IEEE 299 (IEEE Standards, 1997) using two horn antennas was applied. The measurement range in this work falls within the high range frequency – from 1.8 to 3.2 GHz in which corresponding to plane wave power (P). The instruments used in the shielding effectiveness measurement were the Rohde & Schwarz Signal Generator (SG) model SMBV100A, the Rohde & Schwarz Handheld Spectrum Analyzer (SA) model FHS4, three horn antennas, two shielded coaxial cables, and connectors. The transmitting antenna was a horn antenna, manufactured by ETS. The receiving antennas were A-Infomw, Standard Gain horn antennas that covered the frequency range of 1.7-2.6 GHz with dimensions of 30.9 x 23.85 x 29.4 cm³ and Xi'an Hengdu Microwave Co. horn antennas that covered the frequency range of 2.2-3.3 GHz.



Fig. 1: Measurement of the shielding effectiveness using two horn antennas: (a) in free space; (b) in an RF-shielded room.

Two Polyvinyl chloride (PVC) antenna stands were used to hold the two horn antennas. The coaxial cables that were used were a 4-m flexible Huber+Suhner cable and a 1-m Agilent cable. The coaxial cable that was connected to SG was calibrated prior to the experiment to exclude cable loss.

RESULTS AND DISCUSSION

The output power was averaged over five measurement readings. To obtain the values of shielding effectiveness, the received signal value measured in RF-shielded room was subtracted from the value of the reference signal, The shielding effectiveness in the RF-shielded room was about and about 50 dB at 2.45 GHz.

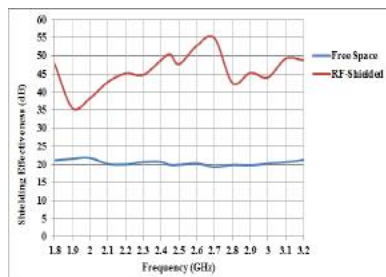


Figure 3: Shielding effectiveness of the enclosure with copper based lightweight textile

The frequency ranges from 1.8GHz to 3.2GHz are found to be consistent for free space, as shown in Fig.3. The average attenuation of shielded enclosure covered with PCPTF conductive textile was about 48 dB within the range 1.8 GHz to 3.2 GHz. The attenuation increases at about 28 dB with the enclosure shielding material. The results show that this type of EMI shielded environment can attenuate the signal noise up to >40 dB, in which provides good shielding effectiveness performance.

CONCLUSION

This paper presents the results of shielding effectiveness of a newly designed cost effective shielded room covered with copper based light weight textile material. The results exhibit that the shielded enclosure with PCPTF textile is able to provide good shielding effectiveness where the unwanted signal noise can be attenuated up to more than 40 dB.

REFERENCES

- [1] A. K. Sharma, K. K. Mishra, M. Raghuramaiah, P. A. Naik, and P. D. Gupta. Design and performance characteristics of an electromagnetic interference shielded enclosure for high voltage Pockels cell switching system, *Sadhana*, vol. 32, part 3, 235-242, June 2007.
- [2] T. W. Wieckowski, and J. M. Janukiewicz. Methods for evaluating the shielding effectiveness of textiles, *Fibers & Textiles in Eastern Europe*, vol. 14, no. 15, 18-22, January 2006.
- [3] J. W. Gooch, J. K. Daher. *Electromagnetic shielding and corrosion protection for aerospace vehicles*, Springer, New York, 2007.

Computational Electromagnetics

Wideband Adjoint Sensitivity of Anisotropic Structures Using the FDTD Method

M. H. Bakr^{1*}, A. Elsherbeni², and V. Demir³

¹ McMaster University, Hamilton, Ontario, Canada

² Colorado School of Mines, Golden, Colorado, USA

³ Northern Illinois University, Dekalb, Illinois, USA

*mbakr@mcmaster.ca

Abstract-We present in this work a novel algorithm for adjoint sensitivity analysis of anisotropic structures using the finite difference time domain (FDTD) method. Using only one extra adjoint simulation, our approach estimates the sensitivities of the desired objective function or response with respect to all components of permittivity, permeability, or conductivity tensors of all anisotropic media using only one extra simulation. Our approach gives good results as compared to the accurate central difference approaches.

Adjoint sensitivity analysis supplies the first-order derivatives of an objective function or responses with respect to all material and shape parameters using at most one extra simulation [1]. For the case of S -parameters and other network parameters, this extra simulation is also eliminated [2]. A simpler implementation of this approach using the FDTD method has been proposed recently [3]. This approach was developed for anisotropic materials using the transmission line matrix (TLM) method [4].

In this paper, we extend this work in [4] to apply to the popular FDTD method. Using the FDTD method, the electromagnetic simulation can be cast in the form:

$$\begin{bmatrix} \boldsymbol{\varepsilon} & \mathbf{0} \\ \mathbf{0} & -\boldsymbol{\mu} \end{bmatrix} \begin{bmatrix} \dot{\mathbf{E}} \\ \dot{\mathbf{H}} \end{bmatrix} + \begin{bmatrix} \boldsymbol{\sigma}^e & \mathbf{0} \\ \mathbf{0} & -\boldsymbol{\sigma}^m \end{bmatrix} \begin{bmatrix} \mathbf{E} \\ \mathbf{H} \end{bmatrix} + \mathbf{K}_c \begin{bmatrix} \mathbf{E} \\ \mathbf{H} \end{bmatrix} = \begin{bmatrix} -\mathbf{J}_i \\ \mathbf{M}_i \end{bmatrix}, \quad (1)$$

where $\boldsymbol{\varepsilon}$, $\boldsymbol{\mu}$, $\boldsymbol{\sigma}^e$, $\boldsymbol{\sigma}^m$ are block diagonal matrices representing the material properties of the computational domain. Each diagonal block represents the material tensor of the respective spatial cell. The vectors \mathbf{E} and \mathbf{H} represent the electric and magnetic fields over all FDTD cells. Together, they form the vector of state variables $\mathbf{V} = [\mathbf{E}^T \ \mathbf{H}^T]^T$. The vectors \mathbf{J}_i and \mathbf{M}_i represent the impressed electric and magnetic current densities. It can be shown that the adjoint simulation corresponding to (1) is given by:

$$\begin{bmatrix} \boldsymbol{\varepsilon}^T & \mathbf{0} \\ \mathbf{0} & -\boldsymbol{\mu}^T \end{bmatrix} \begin{bmatrix} \dot{\boldsymbol{\lambda}}_E \\ \dot{\boldsymbol{\lambda}}_H \end{bmatrix} + \begin{bmatrix} \boldsymbol{\sigma}^{eT} & \mathbf{0} \\ \mathbf{0} & -\boldsymbol{\sigma}^{mT} \end{bmatrix} \begin{bmatrix} \boldsymbol{\lambda}_E \\ \boldsymbol{\lambda}_H \end{bmatrix} + \mathbf{K}_c \begin{bmatrix} \boldsymbol{\lambda}_E \\ \boldsymbol{\lambda}_H \end{bmatrix} = \left(\frac{\partial \psi}{\partial \mathbf{V}} (T_m - \tau) \right), \quad (2)$$

where $\boldsymbol{\lambda}_E$ and $\boldsymbol{\lambda}_H$ are the adjoint electric and magnetic fields and ψ is the kernel of the objective function integral [1]. The excitation in the right hand side of (2) is determined using the considered response or objective function. Using the temporal original and adjoint fields available using (1) and (2), the sensitivities of the response under consideration with respect to all parameters are estimated.

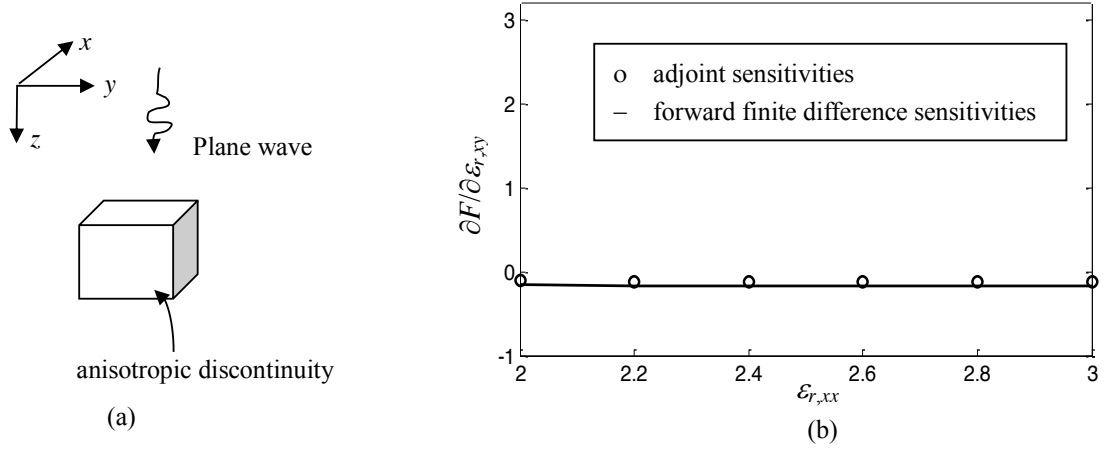


Fig.1. The structure of the example; (a) an anisotropic discontinuity illuminated by an incident plane wave, and (b) the sensitivity of the objective function with respect to the permittivity parameter $\epsilon_{r,xy}$ for a sweep of the parameter $\epsilon_{r,xx}$ as compared with the more expensive finite difference approach

To illustrate the anisotropic adjoint sensitivity algorithm, we consider the structure shown in Fig. 1. The computational domain in this 3D problem has dimensions in the x , y , and z directions of $25\Delta l \times 25\Delta l \times 25\Delta l$ with $\Delta l = 4.0$ mm. An anisotropic discontinuity is at the center of this air-filled computational domain. This discontinuity has dimensions $5\Delta l \times 5\Delta l \times 5\Delta l$. Its permittivity tensor is:

$$\boldsymbol{\epsilon} = \epsilon_0 \begin{bmatrix} 2.0 & 0.2 & 0.4 \\ 0.2 & 2 & 0.5 \\ 0.4 & 0.5 & 3.1 \end{bmatrix}. \quad (3)$$

The domain is terminated by absorbing boundaries in all directions. The excitation is an incident plane wave propagating in the z -direction with its electric field polarized in the x -direction. The objective function is defined by the integral

$$F = 0.5 \int_0^{T_m} E_x^2 dt, \quad (4)$$

where E_x is the x -polarized electric field observed at $(20\Delta l, 20\Delta l, 20\Delta l)$. Fig. 2 shows the sensitivities of the objective function with respect to the permittivity parameter $\epsilon_{r,xy}$ for a sweep of the parameter $\epsilon_{r,xx}$. Good match is achieved as compared with forward finite differences (FFD) for all parameters.

REFERENCES

1. M. H. Bakr and N. K. Nikolova, "An Adjoint variable method for time domain TLM with fixed structured grids," *IEEE Trans. Microwave Theory Tech.*, vol. 52, pp. 554-559, 2004.
2. M. H. Bakr, N. K. Nikolova, and P. A. W. Basl, "Self-Adjoint S-parameter sensitivities for lossless homogeneous TLM problems," *International Journal of Numerical Modelling: Electronic Networks, Devices and Fields*, vol. 18, no. 6, pp. 441-455, 2005.
3. M. H. Bakr, A. Elsherbeini, and V. Demir, "An FDTD-based adjoint sensitivity approach," *Proceedings of the IEEE Antenna and Propagation Symposium (APS 2016)*, Puerto Rico, June 2016.
4. L. S. Kalantari and M. H. Bakr, "Wideband cloaking of objects with arbitrary shape exploiting adjoint sensitivities," *IEEE Trans. Antennas and Propag.*, vol. 64, no. 5, pp. 1963 – 1968, May 2016.

Optimization Techniques

Coupling Matrix Synthesis Method for Microwave Filters using Genetic

Algorithm Optimization

Abdul Rehman¹, M. Salman Khatak², ChangHyeong Lee³, Dajung Han⁴, Heejun Park⁵, M. Kamran Khatak⁶ and Sungtek Kahng*

Incheon National University, South Korea

S-kahng@inu.ac.kr

Abstract

This paper presents the comparison of two different approaches for the synthesis of coupling matrix of cross-coupled microwave filters. A proposed genetic algorithm-based optimization technique for the generation of coupling matrix is compared with the traditional design approach of coupling matrix. The traditional design approach follows the recursive technique procedure, evaluating the reflection and transmission polynomials, given the transmission zeros. After generation of the coupling matrix using the eigenvalues of polynomials, transformation is required to get the practical realizable topology of the coupling matrix. The proposed genetic algorithm-based optimization technique uses efficient cost function that can completely describe the desired filter response. The cost function applies directly on the non-zero elements of the coupling matrix/user defined topology. Both the design methods use the $(N+2)$ -by- $(N+2)$ transversal coupling matrix which requires the input and output couplings as well as the source and load couplings. There is no noticeable difference in the comparison of the results, but the genetic algorithm based optimization takes much fewer computational steps.

1. Introduction

Emerging growth of wireless communication system have led to more demanding requirements for microwave filters. Microwave filters become more important in the design of telecommunication and broadcast system. Synthesis of microwave filters has been the focus of the microwave engineers and one of the most researched topic for several years. There has been an extensive research carried out on both analytical and numerical methods for the synthesis of coupling matrices in the last few years. In the 1970s, Atia

and William first time presented the analytical synthesis technique. It was based upon coupled resonator theory to realize coupling matrix [1] [2]. Secondly, most famous analytical technique based on recursive method to generate polynomials for the transmission and reflection poles and zeros is provided by Cameron. Practical realization of the coupling matrix is not possible at the first stage. A series of similarity matrix transformation is then required to remove the number of non-zero elements to get practical realizable topology [3].

This has open a new window to the development of coupling matrix synthesis methods based on numerical optimization. It avoids the need of matrix transformation and is based on direct optimization. Recently [4] proposed numerical based synthesis approach for microwave filters which applies directly on coupling matrix elements. But it requires initial values of the coupling matrix to be optimized.

In this paper we propose a numerical optimization method using genetic algorithm in the framework of matlab based on user defined matrix topology. This can overcome the problem of complexity in the analytical based approach, where you have to perform a series of matrix transformation to get practical realizable topology. We compare our numerical based approach with the traditional analytical based approach. Fourth order filter having 4 poles and 4 zeros is chosen to test the both methods. Results for both analytical and numerical based approaches has been compared for analysis. In this work the entries of the coupling matrix will be used as an independent variables in the optimization process.

2. Synthesis of $N+2$ Coupling Matrix

Generally transmission and reflection coefficients of a filter

network can be described in the form of

$$S_{21}(s) = \frac{P(s)}{\varepsilon E(s)} \quad (1)$$

$$S_{11}(s) = \frac{F(s)}{\varepsilon_R E(s)} \quad (2)$$

Where $s = j\omega$ is the complex frequency variable. $\varepsilon, \varepsilon_R$ are ripple constant related to the maximum return loss. Polynomial $P(s)$ is determined from finite transmission zeros. $F(s)$ Can be calculated using recursion formula described in [3]. $E(s)$ is determined from the poles.

$$\varepsilon_R = \frac{\varepsilon}{\sqrt{\varepsilon^2 - 1}} \quad (3)$$

$$\varepsilon = \frac{1}{\sqrt{\frac{RL}{10^{10}} - 1}} \quad (4)$$

$E(s)$, $F(s)$ and $P(s)$ have been normalized to their respective higher degree coefficients. S parameters can also be directly related to coupling coefficients as follows.

$$S_{21} = 2 * j * [A]_{N+2,1}^{-1} \quad (5)$$

$$S_{11} = 1 + 2 * j * [A]_{1,1}^{-1} \quad (6)$$

$$A = wU - jR + M \quad (7)$$

Here U is the identity matrix, but for $N+2$ case $U(1,1)$ $U(N+2, N+2)$ is zero. R is the diagonal matrix with all entries is zero except $R(1,1) = R(N+2, N+2) = 1$ and M is the coupling matrix.

2.1 Example

To explain $N+2$ coupling matrix synthesis procedure, fourth order asymmetric filtering function based on fully canonical topology is considered. The filter specifications are:

Order of filter: 4

Return loss: 22dB

Transmission zeros: $-3.7431j$ and $-1.8051j$
(attenuation lobes = 30dB), $1.5699j$ and $6.1910j$ (attenuation lobes = 20dB)

2.1.1 Recursive technique

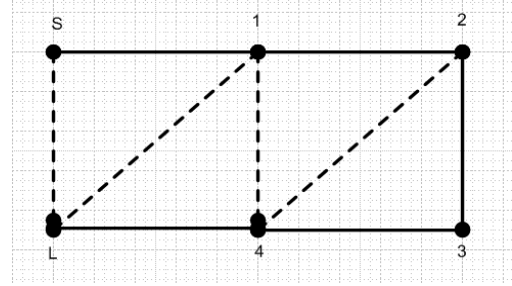


Figure 1: Fourth order Canonical topology

By applying known traditional recursive technique procedure the polynomials $P(s)$, $E(s)$ and $F(s)$ are computed. After a series of similarity transformation explained in the [3] final coupling matrix achieved for $N+2$ 4th order canonical topology shown in Figure 1 is given below.

$$C.M = \begin{pmatrix} C/M & S & 1 & 2 & 3 & 4 & L \\ S & 0 & 1.0603 & 0 & 0 & 0 & 0.0151 \\ 1 & 1.0603 & -0.0023 & 0.8744 & 0 & -0.3251 & 0.0315 \\ 2 & 0 & 0.8744 & 0.0482 & 0.8351 & 0.0340 & 0 \\ 3 & 0 & -0.4033 & 0.8351 & -0.0666 & 0.8727 & 0 \\ 4 & 0 & -0.3251 & 0.0340 & 0.8727 & 0.0170 & 1.0598 \\ L & 0.0151 & 0.0315 & 0 & 0 & 1.0598 & 0 \end{pmatrix}$$

Figure 2 shows the return loss and attenuation level of canonical type 4th order filter. We can get same return loss without applying similarity transformation to the initially generated coupling matrix but in that case we will not have practical realizable topology for the filter. While applying the transformation procedure the symmetry of the coupling matrix must be preserved.

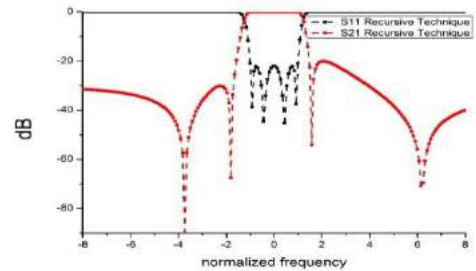


Figure 2: Fourth order Asymmetric Filter response using recursive method

2.1.2 Proposed Optimization Algorithm and Cost Function

Optimization process proposed in this paper directly applies

on the coupling coefficients and desired level of transmission zeros S_{21} and return loss S_{11} . The Genetic algorithm-based optimization technique uses efficient cost function having a minimum set of characteristics that can completely describe the desired filter response. The cost function applies directly on the non-zero elements of the coupling matrix.

$$\text{Cost Function} = \sum_{i=1}^N |S_{11}(\text{specs})_i - S_{11}(\text{tri})_i|^2 + \sum_{i=1}^N |S_{21}(\text{specs})_i - S_{21}(\text{tri})_i|^2$$

Here N is the number of sample frequency points. $S(\text{specs})$ is the required level of S_{21} and S_{11} . $S(\text{tri})$ is the S-parameters comes after evaluation of Cost Function and generation of random values. The algorithm begins by generating random numbers for the entries of coupling matrix. The random number values lies within the specified limits $[-1, 1.5]$. The process will stop after it reaches its termination criteria. S parameters shown in Figure 3 obtained by using proposed algorithm gives good agreement with Figure 2. The final error of the cost function achieved after several iterations was 0.153063. Figure 4 shows error value with number of generations.

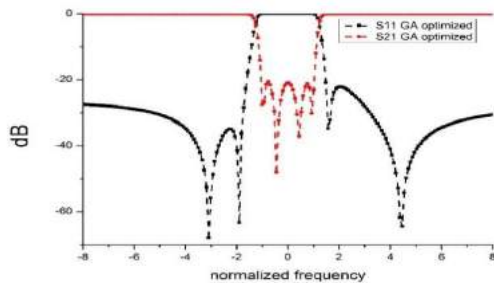


Figure 3: Fourth order Asymmetric Filter response using GA optimization

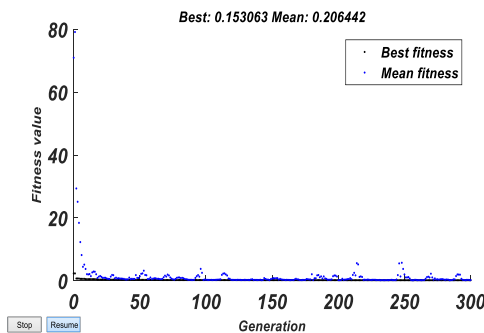


Figure 4: Cost Function error vs number of generations

3. Conclusion

In this paper we proposed a simple and general method for the synthesis of $N+2$ coupling matrix. By strictly enforcing the desired matrix topology, we eliminate the need of similarity transformations. A compact and fast cost function relying only on the determination of S parameter levels has been used as the core of this method. Genetic Algorithm based optimization technique in the framework of matlab is used to evaluate the cost function. Also both symmetric and asymmetric responses with either even or odd degree of filters can be synthesized using proposed method. Results obtained using this approach agree well with the traditional recursive technique method.

Acknowledgment

The authors would like to thank Incheon National University for providing the research grant.

References

1. ATIA A.E., WILLIAMS A.E., NEWCOMB R.W. "Narrow-band multiple-coupled cavity synthesis," *IEEE Trans. Circuits Syst*, 21, (5), pp. 649–655, 1974.
2. Atia, A. E. and A. E. Williams, "New type of waveguide bandpass filters for satellite transponders," *COMSAT Tech. Rev.*, Vol. 1, No. 1, 21–43, Jan. 1971.
3. CAMERON R.J, "General coupling matrix synthesis methods for Chebyshev filtering functions," *IEEE Trans. Microw. Theory Tech*, 47, (4), pp. 433–442, 1999.
4. Guohui Li, "Accurate Coupling Matrix Synthesis for Microwave Filters with Random Initial Value" *Progress In Electromagnetics Research*, Vol. 55, 53–61, 2014

RF and Wireless Communication

Far-Field Measurement of LTE Base Station-like Exposure in RF-shielded Environment

M. A. Humayun¹, H. A. Rahim¹, M. AbdulMAlek², P. J. Soh³, M.S. Zulkefli⁴, C, M, Nor³, A. A. Al-Hadi³

¹Bioelectromagnetic Research Group, School of Computer and Communication Engineering, Universiti Malaysia Perlis(UniMAP),Kampus Pauh Putra, 02600, Arau,Perlis, Malaysia.

²Faculty of Engineering and Information Sciences, University of Wollongong in Dubai,Dubai, United Arab Emirates

³School of Computer and Communication Engineering, Universiti Malaysia Perlis, Kampus Pauh Putra, 02600, Arau, Perlis, Malaysia.

⁴ Center of Diploma Studies, Universiti Malaysia Perlis


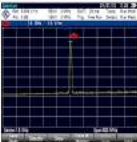
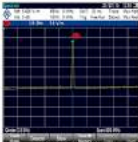
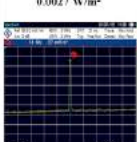
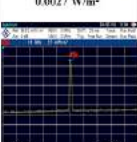
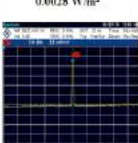
*corresponding author: humayun0403063@gmail.com

Abstract- In this article we demonstrate the far-field measurement with difference values of LTE exposure in RF-shielded environment. We compared the electric-field and power density results from LTE850, LTE1800 and LTE2600 field exposure that adhere to the standard guidelines issued by the ICNIRP. The results for E-field and power density are far below the safety standard value for the public recommended by ICNIRP.

LTE SIGNAL EXPOSURE SETUP

An E-field distribution that emulates the far field of a base station was measured to ensure that power received by each subject is set to 1 V/m, both from LTE850, LTE1800 and LTE2600 field exposure. The SG was connected with the far field EMF probe antenna. Table 3 summarizes the E-field and power density receive outcomes from 850, 1800, and 2600MHz exposure obtained from the spectrum analyzer.

Table 1: Electric field strength of base station signal in far field distance from LTE850, LTE1800, and LTE2600 field exposure

FREQUENCY	LTE850 MHz	LTE1800 MHz	LTE2600 MHz
E-FIELD RECEIVE (V/m)	1 V/m 	1 V/m 	1 V/m 
POWER DENSITY RECEIVE (W/m²)	0.0027 W/m² 	0.0027 W/m² 	0.0028 W/m² 

The results show that the E-field intensity is set at 1V/m for LTE850 signal exposure in the shielded room contributes to the radiation level of only 0.0027 W/m², corresponding to about 0.06% lower than the ICNIRP exposure limit for general public, as shown in Table 8. Meanwhile, the E-field intensity is set at 1 V/m for both LTE1800 and LTE2600 signal exposure leads to the radiation level of 0.0027 W/m² and 0.0028 W/m², respectively. This level corresponds to about 0.03% lower than the ICNIRP exposure limit for general public in both LTE1800 and LTE2600 exposures, as listed in Table 2.

Table 2: Comparison of the measured electric field with the exposure limit recommended by ICNIRP for LTE850, LTE1800, and LTE2600 exposures

	Electric Field (V/m)			Power density (W/m ²)		
	850 MHz	1.8 GHz	2.6G Hz	850 MHz	1.8 GHz	2.6 GHz
Receive value	1	1	1	2.7 10 ⁻³ x	2.7x 10 ⁻³	2.8 x 10 ⁻³
Exposure limit for general public	40.1	58.3	70.1	4.25	9	10
Comparison with exposure limit (%)	0.002	1.71	1.43	0.06	0.03	0.03

ACKNOWLEDGMENTS

This work was supported by the Malaysian Communications and Multimedia Commission (MCMC) under grant No. 900200028, Malaysia. The authors would like to express their gratitude to School of Electrical System Engineering members.

REFERENCES

- [1] Huang, J., Qian, F., Guo, Y., Zhou, Y., Xu, Q., Mao, Z. M., ... & Spatscheck, O. (2013, August). An in-depth study of LTE: Effect of network protocol and application behavior on performance. In *ACM SIGCOMM Computer Communication Review*, vol. 43, no. 4, pp. 363-374. ACM.
- [2] Hsing-Yi Chen and Tsung-Han Lin, "Simulations and Measurements of Electric Fields Emitted from a LTE Base Station in an Urban Area," *International Journal of Antennas and Propagation*, vol. 2014, Article ID 147341, 10 pages, 2014. doi:10.1155/2014/147341.
- [3] Regel, S. J., Negovetic, S., Rösli, M., Berdiñas, V., Schuderer, J., Huss, A., ... Achermann, P. (2006). UMTS base station-like exposure, well-being, and cognitive performance. *Environmental Health Perspectives*, 114(8), 1270–

Adaptive Rate and Power Adaptation for Packet Transmission in IEEE 802.11 Networks.

Wan Norsyafizan W.Muhamad, Darmawaty Mohd Ali, Suzi Seroja Sarnin

Faculty of Electrical Engineering, University Teknologi MARA, 40450 Shah Alam, Selangor, Malaysia.

*corresponding author, E-mail: syafizan@salam.uitm.edu.my

Abstract

In this paper, several energy efficient packet transmission techniques for the IEEE802.11 WLAN have been developed to minimize energy consumption, while meeting the quality of service (QoS) performances of data traffic. The rate and power adaptation algorithms have been developed initially based on a single parameter adaptation technique which adapts the data rate according to the network packet delay. The work further enhanced the rate and power adaptation algorithm by developing a new cost function based approach which is a multi-parameter based optimization technique. Both approaches have been developed to reduce network collision levels by adapting the MAC parameters according to the load conditions. The performance of energy efficient packet transmission techniques proposed in this paper were simulated using discrete event simulation models and analysed for data traffic transmission. Simulation results have shown up to 16% improvement of energy efficiency compared to published works optimal low-energy transmission strategy (Miser) scheme and energy saving of 26.9% compared with the standard IEEE 802.11 MAC protocol. The proposed cost function algorithm introduces significant energy savings of 33% compared to the single parameter approach.

1. Introduction

In today's world, the wireless communication has become an essential part of our daily activities. With the rising demand for wireless services, energy consumption has become a primary concern for the communication industry as it does not only increases the operational energy costs but also contributes to the environmental effects, such as increased greenhouse gas emissions [1]. Due to these reasons, the demand for energy efficient networking is increasing. The link adaptation mechanism offers the ability to adapt the modulation and coding scheme (MCS) and transmit power according to the channel conditions on the radio link. Power adaptation is a method used for selecting appropriate transmission power level to match the channel condition for the correct reception of a packet. Traditionally in WLANs, the link adaptation technique is used to maximize the throughput of a network by taking advantage of good channel conditions. Based on the channel SNR (Signal-to-Noise Ratio) values, the transmitter adapts its

MCS value to maximize the link data rate. Research on a joint rate and power adaptation algorithm that aims at simultaneously improving the energy efficiency and throughput performance of WLAN systems is limited in the literature. How to select the data rate to minimize energy consumption is an important, yet under explored topic. Only a few works [2, 3] apply a rate adaptation with the main goal of reducing energy consumption.

There is always a trade-off between achieving energy efficiency and the QoS performance improvement of a packet radio network [4]. The rate and power adaptation algorithms have been developed initially based on a single parameter adaptation technique, which adapts the data rate according to the network packet delay [5]. At lower traffic loads, the proposed algorithm works well, offering energy saving while sustaining the QoS performances. However, as the load increases, the algorithm cannot sustain the QoS performances. Single parameter approach, which is rate adaptation based on measured delay only cannot control higher collision level when the load starts to increase. Uncontrolled collisions would result in higher energy consumption as well as increase the end to end delay. Therefore, to resolve this problem, the work further enhanced the rate and power adaptation algorithm by developing a new cost function based approach, which is a multi-parameter based optimization technique [6]. It is proved that the proposed cost function algorithm introduces significant energy savings of 33% compared to the single parameter approach.

2. Single parameter approach

Two different energy efficient packet transmission techniques for the IEEE802.11 WLAN are presented with the main objective of minimizing energy consumption, while meeting the quality of service (QoS) requirements of data traffic. The following section discussed both algorithms in details.

2.1. Single Parameter Approach

Fig. 1 illustrates the conceptual model of the proposed algorithm. Initially, each transmitter selects the maximum transmission rate and transmit power for packet

transmission. The receiver measures the end to end delay to adjust the transmission data rate for the subsequent packet transmission. Following that, the receiver sends back the information via feedback packet to the transmitter. A lower delay value indicates a lower traffic load and as the delay increases it can be assumed that the network starts moving to the congested state. For the non-adaptation case, the transmission data rate always remains at the highest rate, which results in high energy consumption due to the higher transmit power required for the higher modulation scheme.

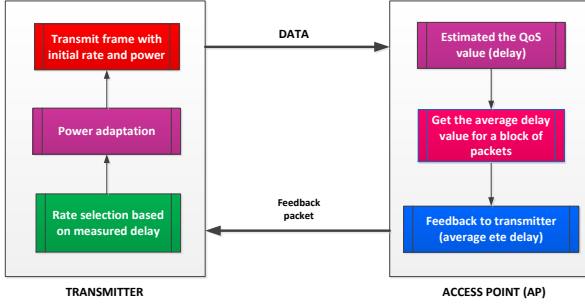


Figure 1: Propose adaptive transmission rate and power adaptation

In this initial algorithm, the transmission channel is assumed to be error free, hence an ACK may be lost due to collision only. The received packet delay is averaged over block of packets. The average delay value is updated for every N packets, based on Equation (1):

$$delay_{avg} = \frac{1}{N} \sum_{i=1}^N T_i \quad (1)$$

The average packet delay is compared with the delay threshold value of the QoS set of the traffic. The receiver uses the average packet delay to decide the new transmission rate. The algorithm for rate selection is divided into two different conditions, when the average end-to-end delay (*ete_delay*) is less than the threshold delay, and when the average *ete_delay* reaches the threshold delay. If the average delay is below 90% of the threshold value, then the transmission data rate is reduced to a lower level. However, a reduced data rate may increase the contention level in the CSMA/CA network. Because the proposed algorithm needs to gain both energy efficiency and control of the delay, the algorithm adaptively adjusts the transmission data rate according to the current contention level. Therefore, as the *ete_delay* increases, the transmission data rate keeps adjusting to higher levels. Minimum level of transmission data rate is selected when the delay value is less than 5% of QoS_{delay} , because lower delay value represents lower contention level, thus with the main aim of reducing energy consumption, the lower data rate is selected. As the delay increased to $0.2 * QoS_{delay}$ and $0.3 * QoS_{delay}$, it is assumed that the network is start moving to medium load condition, thus the transmission data rate is increase by a single step. For the second condition, if the average delay exceeds the threshold value, then the transmission data rate is adjusted to the highest level. After each measurement

period, a feedback packet sent by the receiver informs the transmitters of a suggested transmission rate.

In this paper, the proposed initial rate and power algorithm has limitations in terms of the capacity of the network. At lower traffic loads, the proposed algorithm works well, offering energy saving while sustaining the QoS performances. However, as the load increases the algorithm cannot sustain the QoS performances within the required levels. This is because the rate adaptation based on measured delay only cannot control higher collision level when the load starts to increase. Uncontrolled collisions would result in higher energy consumption as well as increase the ete delay. Therefore, to resolve this problem an enhancement of the rate/power adaptation algorithm with a dual parameter approach is proposed to maximize the capacity of network while maintaining the energy efficiency and QoS performances.

2.2. Dual Parameter Approach

The novelty of this algorithm is that the transmission rate is selected based on average measured delay value and individual queue lengths. The cost function output is calculated by individual transmitters based on its current QoS value. The cost function value $F(t, Q)$ incorporates the measured delay, terminal's current queue length, queue threshold value and a tunable sensitivity parameter. The cost function $F(t, Q)$ is presented in equation (2):

$$F(t, Q) = \begin{cases} C \left(\frac{1}{T_{target} - T_{current}} \times \left(\frac{Q_{current,j}}{Q_{threshold,j}} \right) \right) & \text{for } T_{ert} < T_{target,j} \\ 1 & \text{for } T_{ert} \geq T_{target,j} \end{cases} \quad (2)$$

Where, C denotes rate adaptation sensitivity factor. This parameter can be tuned based on the specific performance objective, either target for improving the energy efficiency or maintaining the QoS performances. Selection for value of rate adaptation sensitivity parameter is done based on the requirement either to maximize the QoS performance or to improve the energy efficiency. T_{target} is the target delay for a specific traffic class; $T_{current}$ is the measured global delay in the network. The global delay value is measured by the Access Point (AP) and this value is send back via feedback packet to the transmitter. $Q_{current,j}$ is the j th terminal transmission queue length. The queue length (unit packet) represents the total number packets inside the transmission queue(s) waiting to be transmitted. The cost function output is an indicator of congestion and current QoS value of each terminal. The queue threshold $Q_{threshold}$ is measured as a short-term average queue length calculated in the past averaging period, for individual terminal. The short-term average queue size is updated for every N packets, based on Equation (3). Q_i is an instantaneous queue length for packet i .

$$Q_{threshold} = \frac{1}{(N-1)} \sum_{i=1}^{N-1} Q_i \quad (3)$$

3. Simulation Results and Analysis

In this work an OPNET based simulation model has been developed to analyse the performance of the proposed algorithm. Several scenarios with different number of user terminals (UE) and one Access Point (AP) are placed randomly in a 200 m x 200 m area, to evaluate the proposed protocol. The user terminals (UE) transmit packets on the uplink using the algorithm described in the previous section. Table 1 lists the main parameter employed for the simulation.

Table 1: Key simulation parameters

Parameter	Value
WLAN Standard	IEEE802.11g
Frequency	2.4 GHz
Transmission range	150 meters
Propagation model	ITU Indoor path loss model
No. of UEs	10
Packet generation	Exponentially distributed
Noise density	8.798×10^{-14} W/Hz
Packet length	1500 bytes
L_{ACK}	14 bytes
T_{target}	0.02 s

Fig. 2 presented the total energy per packet which shows that the energy consumption of the proposed protocol is lower than other protocols. This is because the proposed algorithm uses a much lower transmission data rate than the other techniques. The default MAC protocol always used the highest available data rate, which is 54 Mbps which requires a higher transmit power to decode the packet correctly at the receiver. As for the Miser scheme, the nature of the proposed algorithm with a smaller transmission range, a higher transmission data rate is selected, which results in the selection of a transmission data rate within the 36Mbps/48Mbps/54Mbps ranges that contributes to much higher energy consumption as compared to the proposed algorithm.

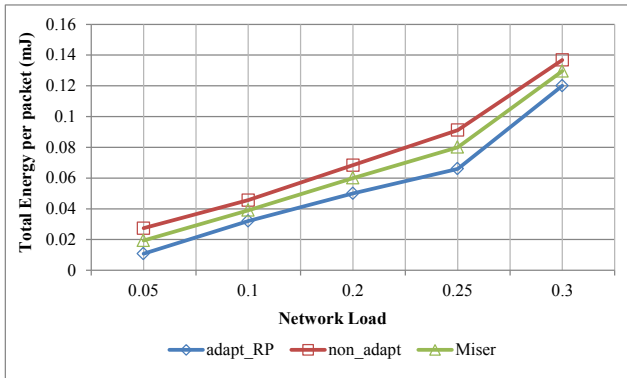


Figure 2: Energy consumption with varying network load.

Table 2 summarized all the components of energy consumption for both techniques at ($p = 0.2$). The proposed algorithm achieves a higher energy efficiency due to the selection of lower data rates which contributes to a lower transmit power value, as in Table 2. Although a higher number of retransmissions of packet is required, due to the longer channel occupancy time, but the lower transmit power overcomes both the lower delay value and the lower number of retransmissions, resulting in a more energy efficient scheme. It can be concluded that the proposed algorithm's selection of lower data rates reduces the transmit power required, which overcomes the higher delay value, subsequently reducing the energy consumption.

Table 2: Breakdown components of energy consumption for both techniques (at $p=0.2$)

Mode	Energy (Idle Mode)	Avg Ptx (Watt)	Energy	Energy	Energy	No of Retx per packet	Tot Energy per pkt (μJ)
	Pidle (Tdif+Tsifs+Tbo)		(Tx mode)	(Rx mode)	per packet		
R/P_adapt	0.003μJ	0.036	8.7μJ	1.26μJ	10μJ	4	50
Miser	0.0025	0.062	13.8	1.09	14.89μJ	3	59.6
Non_adapt	0.00148μJ	0.14	22μJ	0.769μJ	22.8μJ	2	68.4

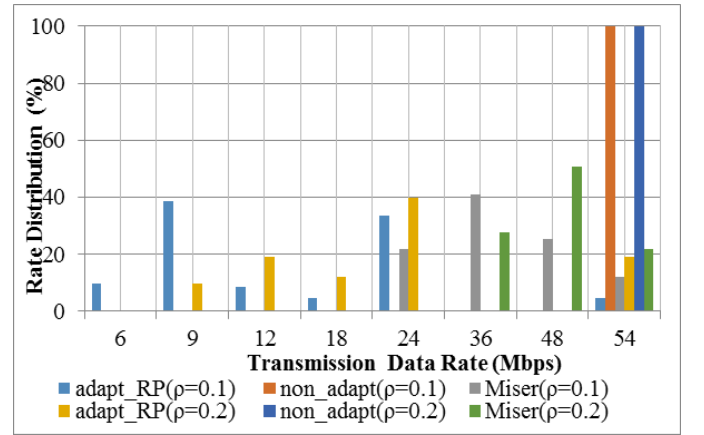


Figure 3: Comparison of the distribution data rate at different load conditions ($p=0.1$ and $p=0.2$)

Fig. 4 shows a comparison of the number retransmission per packet. It can be seen that the proposed protocol experiences a higher number of retransmissions due to the fact that the average channel occupancy time for the proposed protocol is longer than the other techniques because use of a lower selected transmission rate, as detailed in Table 3.5. Hence, for the proposed protocol, with the increase of the network load, the average number of retransmissions is slightly higher. The proposed algorithm achieves a lower energy consumption compared to other protocols due to the selection of a lower data rate, which leads to a lower transmit power being required. Even though it can be seen that the average number of retransmissions for the proposed technique is higher than in the other approaches, the proposed technique still gains better energy efficiency. This can be explained using the analysis of the total energy per packet considering the number of retransmissions per packet as detailed out in Table 2.

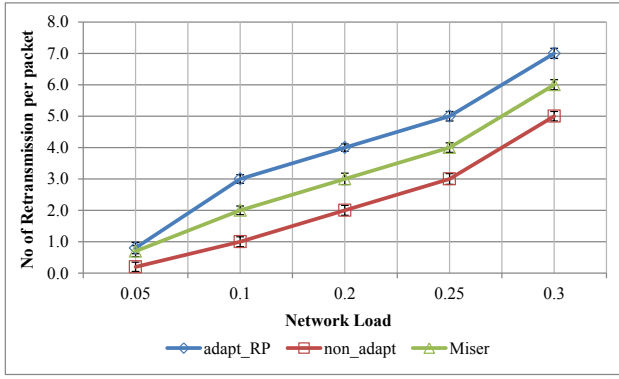


Figure 4: Comparison of the average retransmissions

Dual Parameter

Figure 4.6 compares the total energy per packet for single and dual parameter approaches with varying load conditions. The result of lower energy consumption for the cost function algorithm can be further explained based on Table 3. The table lists the components of energy consumption at ($p = 0.2$). From the table, it can be extracted that the lower energy consumption for the cost function algorithm is gained from the lower transmit power contributed by the selection of a lower data rate, the lower number of retransmission, as well as the lower delay value.

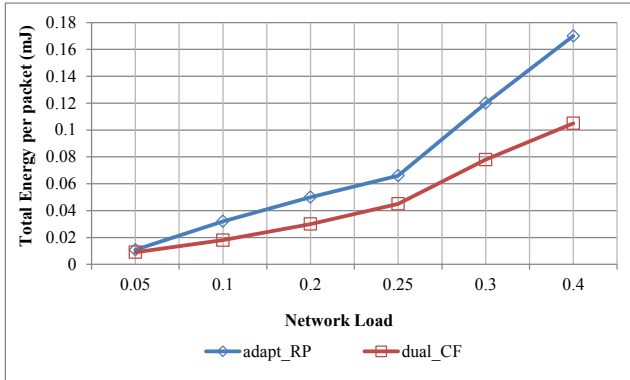


Figure 5: Comparison of total energy per packet for both techniques

Table 3: Breakdown of the components of energy consumption for both techniques at ($p = 0.2$)

Mode	Energy (Idle Mode)	Avg Ptx (Watt)	Energy	Energy	Energy per packet	No of Retx per packet	Tot Energy per pkt (μJ)
	Pidle (Tdifs+Tsifs+Tbo)		(Txmode)	(Rxmode)			
R/P adapt	0.003μJ	0.036	8.7μJ	1.26μJ	10	4	50
Dual CF	0.0015	0.026	6.303	1.258	7.56	3	30.24

The dual cost function gives a faster response in adapting to an appropriate data rate as can be seen from Fig. 3, where the transmission data rate is selected according to the global delay value as well as individual queue length. This gives an advantage in controlling the delay value which leads to a

reduced number of collisions in the network. The advantage of the joint parameters of delay and queue length, as explained above, is that they lead to a lower number of collisions compared to the previous adaptation rate/power, as plotted in Fig. 6.

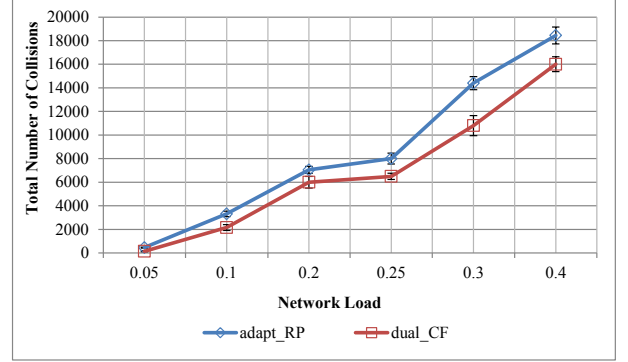


Figure 6: Comparison of the average number of collisions with increasing loads for both techniques

The lower number of collisions can be related to the reduction of energy consumption, as shown in Fig. 5. The dual parameter algorithm results in a less congested network which reduces the percentage of packets loss, thus reducing the number of retransmissions required (presented in Fig. 7) because most of the time packets are successfully transmitted. The lower number of retransmissions also be related to the results of lower energy consumption.

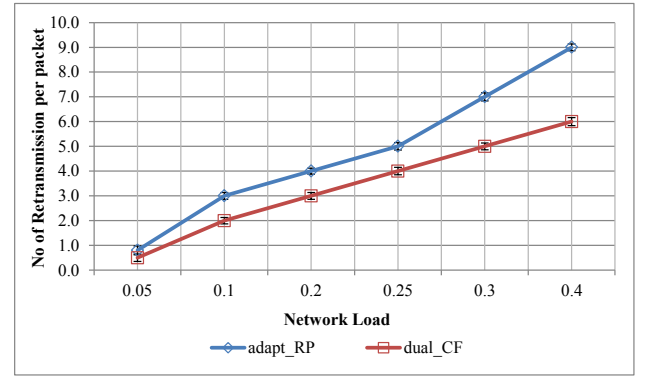


Figure 7: Comparison of the average retransmission per packet with increasing loads for both techniques

Another advantage of low collision levels is reducing the backoff and queuing delays which contribute to a lower ete delay, as shown in Fig. 9. For the proposed cost function algorithm, overall transmission data rate is less than the previous algorithm which contributes to minimizing the energy consumption. The selection of lower transmission data rates leads to a higher channel occupancy time but this is just one component of ete delay. Based on the CSMA/CA delay, there are a few components of delay which need to be considered for the total ete delay which shows that the queuing delay contribute the largest amount of total delay. A

significant reduction in the number of collisions is gained by the proposed cost function algorithm reducing the queue utilization as most of the packets are successfully transmitted, resulting in lower queuing delays.

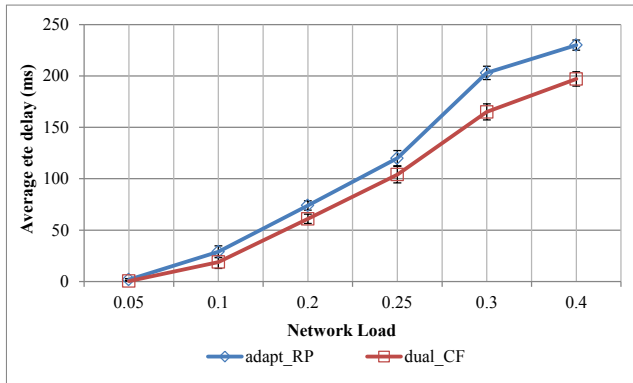


Figure 9: Comparison of the average ete delays with increasing loads for both techniques

4. Conclusions

This paper has presented an energy efficient packet transmission algorithms for the IEEE802.11 standard based on the link adaptation technique. The first single parameter approach using the QoS requirements, specifically referring to the delay for the rate adaptation. The proposed rate adaptation gives priority to the selection of lower transmission data rates as long as the required QoS (delay) is achieved with the main target of reducing the energy consumption. The algorithm only adjusts the data rate to the highest level when the average delay reaches the threshold value in order to control the delay within the required level. Extensive simulation results for the rate and power control algorithm have demonstrated their benefits in reducing energy consumption and maintaining the QoS performances within the required level for background data traffic. At lower traffic loads, the proposed algorithm works well, offering energy saving while sustaining the QoS performances. However, as the load increases the algorithm cannot sustain the QoS performances within the required levels. This is because with single parameter approach which is rate adaptation based on measured delay only cannot control higher collision level when the load starts to increase. The enhanced algorithm which is the cost function algorithm results in improved energy savings and QoS performances due to its collision reduction principles. This is achieved through a combination of the joint parameters of rate adaptation which give a more active response in adapting to optimum transmission data rates, with the main goal of reducing collisions. The reduction of collisions gains both advantages: minimizing energy consumption as well as improving the QoS performances because the lower number of collisions leads to a less congested network where lower contention levels result in a reduction of the overall delay. In addition, energy consumption can also be reduced because a less congested network improves the packet success rate,

which leads to fewer retransmissions of packets being required. As energy consumption is also a function of retransmission, this indirectly gives an advantage of reducing the extra energy required for unsuccessful transmissions.

Acknowledgements

This research was supported by "Dana Pembudayaan Penyelidikan RAGS 2015 (600-RMI/RAGS 5/3 (78/2015))" by Kementerian Pendidikan Malaysia and Universiti Teknologi MARA, Malaysia.

References

- [1] C. Eyupoglu and M. A. Aydin, "Energy Efficiency in Backbone Networks," *Procedia - Social and Behavioral Sciences*, vol. 195, pp. 1966-1970, 2015/07/03 2015.
- [2] Z. F. Li Li "CARLA: Combining Cooperative Relaying and Link Adaptation for IEEE 802.11 Wireless Networks " in *Vehicular Technology Conference (VTC Spring)*, 2012 *IEEE 75th* 2012.
- [3] M. O. Khan, "Model Driven Energy-Aware Rate Adaptation," in *MobiHoc '13 Proceedings of the fourteenth ACM International Symposium on Mobile Ad Hoc Networking and Computing*, Bangalore, India, 2013, pp. 217-226
- [4] A. Helmy, L. Musavian, and L.-N. Tho, "Energy-Efficient Power Adaptation over a Frequency-Selective Fading Channel with Delay and Power Constraints," *Wireless Communications, IEEE Transactions on*, vol. 12, pp. 4529-4541, 2013.
- [5] W. N. W. Muhamad, J. Brown, and J. Y. Khan, "A QoS guaranteed energy optimized packet transmission technique for the IEEE802.11 WLAN," in *Telecommunication Networks and Applications Conference (ATNAC)*, 2013 *Australasian*, 2013, pp. 219-224.
- [6] W. N. W. Muhamad, J. Y. Khan, and J. Brown, "A QoS guaranteed low energy packet transmission technique for the IEEE 802.11 WLAN," in *Communication Systems, Networks & Digital Signal Processing (CSNDSP)*, 2014 *9th International Symposium on*, 2014, pp. 617-622.

Light Harvesting (photovoltaics and solar cells)

Simulation of multilayer waveguide solar cell structure based on nanoparticles

H. J. El-Khozondar^{1*}, R. J. El-Khozondar², M. M. Shabat³, D. M. Schaadt⁴

¹Electrical Engineering Department, Islamic University of Gaza, Gaza, Palestine

²Physics Department, Al-Aqsa University, Gaza, Palestine

³Physics Department, Islamic University of Gaza, Gaza, Palestine

⁴Institute of Energy Research and Physical Technologies, Clausthal University of Technology, Leibnizstr. 4, 38678 Clausthal-Zellerfeld, Germany

*corresponding author: hkhonzondar@iugaza.edu

Abstract-The purpose of this study is to model solar cell waveguide structure based on nanoparticles due to their ability of controlling the light transmission and reflection. Mixture of Ag and Au nanoparticles impeded in a dielectric media are considered in the model. The reflectance is shown to be dependent on the ration of the nanoparticle in the dielectric media.

Recently, solar cell models based on nanoparticles have been extensively investigated in order to enhance solar cell efficiencies. Nanoparticles are considered an alternative materials to conventional materials due to their ability to trap light if they used in right ratios. SiNx is considered as antireflection-coating (ARC) for high refractive index that can be easily varied between 1.9 and 2.3 by varying the deposition parameters. El-Amassi et al. (2015) reported that PV cell efficiency can be improved by using MTM and SiNx layers bounded by glass from bottom and coved by air. El-Khozondar et al. (2016) considered dissipative Metamaterial (MTM) for the same structure to measure the effect of dissipation. In other work, nanoparticles impeded in a dielectric media is used to further control the efficiency of the solar cell. In this study, both nanoparticles impeded in a dielectric media and SiNx are considered in the proposed model.

Figure 1 exhibits the structure of the proposed solar cell. Nanoparticles are taken to be Ag-Au impeded in PAA host media.

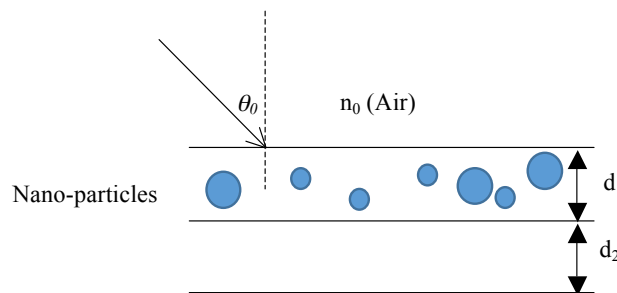


Figure 1 proposed structure

The equation of effective refractive index for the nanoparticles layer is taken from the work presented by Kitsomoboonloha et al. (2011); furthermore, the reflection coefficient is considered as mentioned in the research conducted by El-Khozondar et al. (2016). Then, the relation between reflectance and wavelength is plotted in Figure 2.

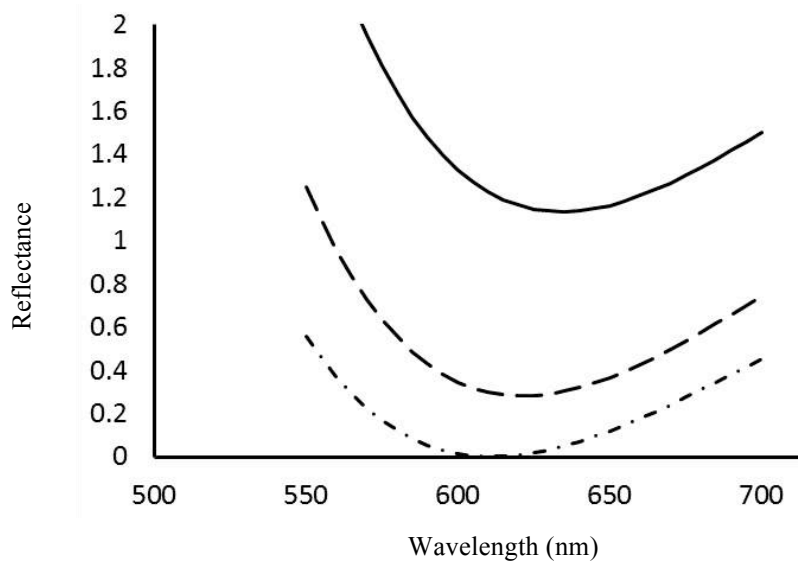


Figure 2 the reflectance as function of wavelength for different values of n_2 . Solid line for $n_2=2$, dash line for $n_2=1.9$, and dash-dot line for $n_2=1.8$.

In all the calculations, the Ag:Au is taken 1:6, $n_s=1.47$, $n_0=1$ and $n_{PPA}=1.527$. Results show that as the refractive index of SiNx layer varies the reflectance changes. The best results obtained at $n_2=1.8$.

REFERENCES

1. Kitsomoboonloha, R., C. Ngambenjwong, W. S. Mohammed, M. B. Chaudhari, G. L. Hornyak, J. Dutta, "Plasmon resonance tuning of gold and silver nanoparticle-insulator multilayered composite structure for optical filters," *Micro & Nano letter*, Vol. 6, No. 6, 342-344, 2011.
2. Beye, M., M. E. Faye, A. Ndiaye, F. Ndiaye, A. S. Maiga, "Optimization of SiNx Single and Double Layer ARC for Silicon Thin Film Solar Cells on Glass," *Research Journal of Applied Sciences, Engineering and Technology*, Vol. 6, 412-416, 2013.
3. Lee, Y., D. Gong, N. Balaji, Y. Lee and J. Yi, "Stability of SiNX/SiNX double stack antireflection coating for single crystalline silicon solar cells," *Nanoscale Res. Lett.*, Vol. 7, No. 1, 50, 2012..
4. El-Amassi, D. M., H. J. El-Khozondar, M. M. Shabat, "Efficiency Enhancement of Solar Cell Using Metamaterials," *International Journal of Nano Studies & Technology (IJNST)*, Vol. 4, 84-87, 2015.
5. El-Khozondar, H. J., D. M. El-Amassi, M. M. Shabat, "Modification of PV behavior using dissipative MTM," in *Proceedings of META16 conference*, Malaga, Spain, July 2016, 1564-1567.
6. Shabat, M. M., D. M. El-Amassi, and D. M. Schaadt, "Design and analysis of multilayer waveguides with different substrate media and nanoparticles for solar cells", *Solar Energy Journal*, V. 137, 409-412, 2016.

Electromagnetic and Nanophotonic Materials (metamaterials, plasmonics, etc)

Lattice vibrations and impurity contribution into terahertz electrodynamic response of semi-insulating InP:Fe.

L. N. Alyabyeva^{1*}, E. S. Zhukova^{1,2}, M. A. Belkin³, and B. P. Gorshunov^{1,2}

¹Laboratory of Terahertz Spectroscopy, Moscow Institute of Physics and Technology (State University), Russia

²A.M. Prokhorov General Physics Institute, Russian Academy of Sciences, Russia

³Department of Electrical and Computer Engineering, The University of Texas at Austin, USA

*corresponding author: aliabeva.ln@mipt.ru

Abstract-Dispersion of complex dielectric permittivity of semi-insulating iron doped InP crystalline wafers was studied in a 2-700 cm⁻¹ (0.06-21 THz) spectral range at room temperature. The results differ from the data for nominally pure InP since incorporation of iron unveils the InP intrinsic dielectric properties such as weak multiphonon vibrations screened by strong free-carrier absorption processes. The spectra of transmission and reflection have complicated structure including one- and two-phonon resonances and impurity-related absorption lines.

High-resistivity semiconductors are highly desired for devices operating in the THz spectral range as the optical losses at THz frequencies are typically dominated by the free-carrier absorption. Semi-insulating (SI) iron-doped indium phosphide (InP:Fe) is widely used in electronic and photonic devices operating in the terahertz spectral range, including Schottky diode detectors, high-electron mobility transistors, photomixers, and quantum cascade lasers [1]. Due to the growth processes, nominally updoped InP crystals always contain different unintentional impurities with the concentrations up to 5·10¹⁵ cm⁻³ that results in shallow donor or acceptor energy levels within the energy gap. Iron doping provides acceptor levels in the mid-gap region of InP that compensate residual shallow donors and produce material with virtually no free carriers [2].

In this study two crystalline wafers of semi-insulating Fe doped InP were investigated. The samples with free-carrier concentration below 10⁹ cm⁻³ have been obtained from two different commercial vendors and had thicknesses of 364 and 991 μm. Spectra of transmission and reflection coefficients in 2-700 cm⁻¹ region were obtained using a set of terahertz and infrared spectrometers: pulsed THz TeraView TPS-Spectra-3000 time-domain spectrometer, a spectrometer based on monochromatic and frequency-tunable continuous-wave (CW) backward-wave oscillators, and standard vacuum Fourier-transform infrared spectrometer (FTIR) (Bruker Optics Vertex 80v). Results obtained were modeled using free Lorentzian function and dielectric parameters such as complex dielectric permittivity, absorption coefficient, complex refractive index, dielectric loss tangent, dynamical conductivity were determined.

Spectra of complex dielectric permittivity contain a number of lines of different nature (fig.1). After profound analysis of the experimental results all lines were associated with one phonon resonance, summation and difference two-phonon absorption processes and with shallow unintentional donor and acceptor impurities.

All spectra for two different samples are in good agreement, the slight difference in real part of dielectric permittivity is caused by small difference in energy gap value due to different growth methods. At low frequencies, we detect excess absorption whose origin is assigned to the hopping conductivity of residual quasi-free charge carriers described by the Mott's dispersion of the ac conductivity $\sigma \sim \nu^s$ [3] $s \approx 0.9$.

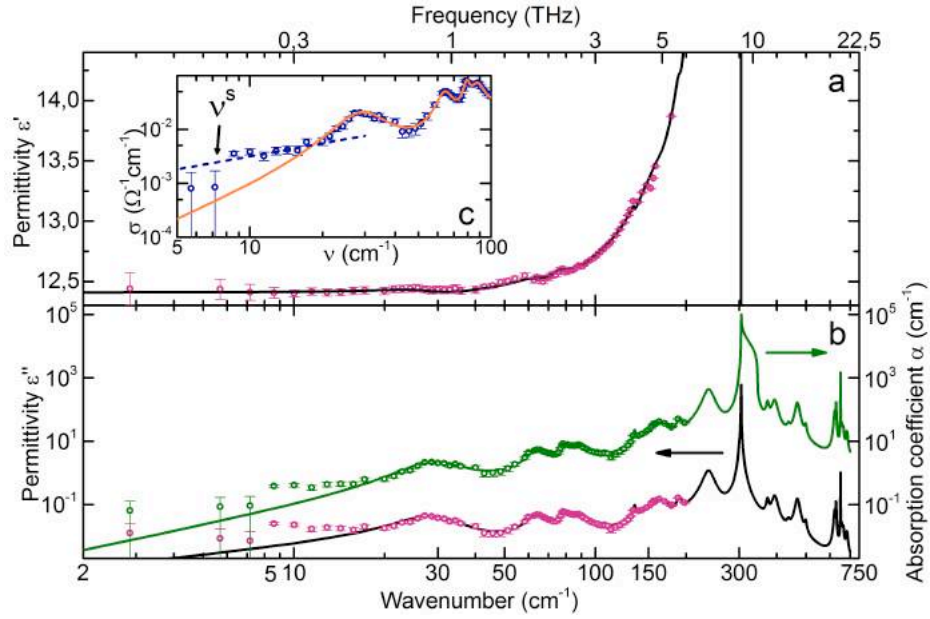


Figure 1. Room temperature spectra of real ϵ' (a) and imaginary ϵ'' (b) parts of the dielectric permittivity, of the absorption coefficient (b) and of dynamical conductivity (c, inset) of 991 μm thick semi-insulating InP:Fe. Dots are experimental data, solid lines are the modeling curves. Dotted line in the inset corresponds to the Mott's expression describing the hopping contribution, $\sigma \sim \nu^s$ with s is about 0.9.

A number of absorption resonances are discovered and their origin is analyzed. The values of the dielectric parameters of SI InP:Fe at frequencies between 2 and 700 cm^{-1} (0.06 and 21 THz) are presented. The data reported here is expected to be useful in designing and improving the performance of numerous microwave and terahertz semiconductor devices based on SI InP:Fe, especially for quantum cascade lasers.

Acknowledgements. The work was supported by the Russian Ministry of Education and Science (Program 'Stop100') and the US National Science Foundation.

REFERENCES

1. Belkin, M.A., and F. Capasso, "New frontiers in quantum cascade lasers: high performance room temperature terahertz sources," *Phys. Scr.* Vol. 90, 118002, 2015.
2. Clerjaud, B. "Transition-metal impurities in III-V compounds," *J. Phys. C* Vol. 18, 3615-3661, 1985.
3. Mott, N.F., and E.A. Davis, *Electronic Processes in Noncrystalline Solids*, Oxford University, London, 1971.

Linking the properties of surface plasmon polaritons and the quality of laser-induced periodic surface structures

T. J.-Y. Derrien^{1*}, Y. Levy¹, J. Bonse², I. Gnilitskyi³, L. Orazi³, T. Mocek¹, N. M. Bulgakova¹

¹HiLASE Centre, Institute of Physics, Academy of Science of the Czech Republic, Za Radnici 828/5,
25241 Dolni Brezany, Czech Republic

²Bundesanstalt für Materialforschung und -prüfung (BAM), Unter den Eichen 44-46,
12203 Berlin, Germany

³ DISMI - University of Modena and Reggio Emilia, Italy

*corresponding author: derrien@fzu.cz

Abstract-Surface plasmon polaritons (SPP) can be triggered by femtosecond-laser pulses on metals and semiconductors leading to formation of sub-wavelength periodic surface structures. In this talk, peculiarities of laser-generated SPP will be analyzed. Plasmonic-based simulations enabled to classify metals in respect of their SPP decay length. Physical insights into SPP propagation indicate that materials with short SPP decay length allow imprinting of highly-regular periodic structures on material surfaces. This result was successfully verified experimentally for several metals.

Irradiation of metals and semiconductors by intense ultrashort laser pulses leads to a transient change of material optical properties, subsequently inducing a strong increase in optical losses [1] and creating favorable conditions for excitation of several types of surface electromagnetic waves (SEW) [2,3], including Surface plasmon polaritons (SPP) [3-5]. The classical SPP theory was developed for noble metals under the assumption of small perturbations of the free-electron gas and weak plasmonic damping [6]. For intense laser irradiation of materials resulting in out-of-equilibrium conditions, the theory is to be revised taking into account high optical losses. Contrarily to traditional plasmonic applications, where losses must be reduced to observe a strong plasmon coupling, upon intense laser irradiation of material surfaces even small coupling efficiencies are sufficient to provide a spatial modulation of the deposited laser energy, yielding in formation surface periodic structures [2-5]. In Ref. [7], it was predicted theoretically that SPP can efficiently be generated on the surfaces of a wide range of irradiated materials, thus broadening the range of plasmonic applications. The SPP properties such as their spatial period and the decay length were calculated for metals where the optical losses are considerable.

In this work, plasmonic-based simulations have enabled to classify plasmonically active metals into several groups in respect of the SPP decay length L_{SPP} (Fig. 1). To check the effects of highly non-equilibrium heating of free electrons at ultrashort laser irradiation, the temporal variations of the dielectric permittivity were modeled numerically for titanium and molybdenum as the examples. For these aims, the two-temperature model was supplemented by the computation of the optical properties in the frame of the Drude model. It has been shown that the SPP decay length is decreasing upon laser-induced excitation of these two metals. Physical insights into SPP propagation indicate that preferred materials with short SPP decay lengths, of the order of 10 μm , allow the imprinting of highly-regular periodic structures on material surfaces. This theoretical result was successfully verified experimentally for several metals when the laser processing parameters are suitably chosen [8].

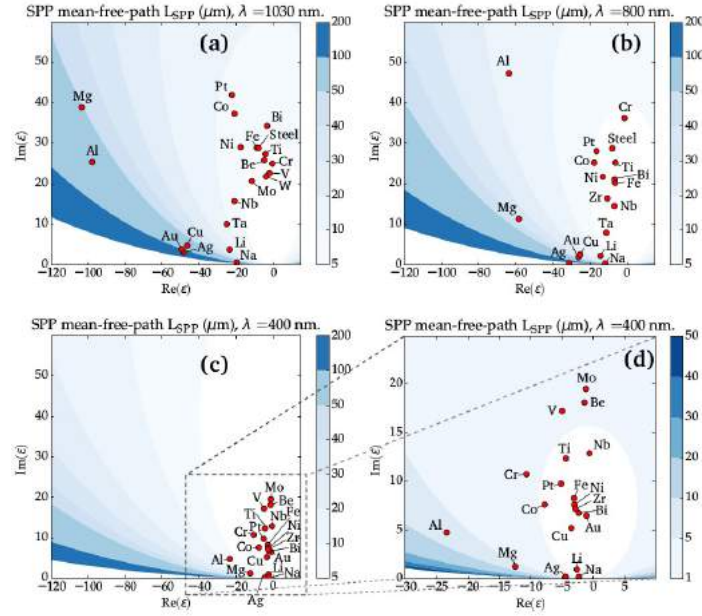


Figure 1: SPP mean free path (i.e. decay length) L_{SPP} for different metals at three laser wavelengths $\lambda = 1030$ nm (a), 800 nm (b) and 400 nm (c, d). According to model-based predictions, metals with small L_{SPP} (located in the bright regions) are more suitable for highly-regular periodic structures (HR-LIPSS) generation at the corresponding laser wavelengths. All color scales are given in micrometers.

REFERENCES

1. Sokolowski-Tinten, K. & von der Linde, D.; Generation of dense electron-hole plasmas in silicon, *Phys. Rev. B*, Vol. 61, 2643-2650 (2000).
2. Sipe, J. E.; Young, J. F.; Preston, J. & Driel, H. V., Laser-induced periodic surface structure. I. Theory, *Phys. Rev. B*, Vol. 27, 1141-1154 (1983).
3. Bonse, J.; Rosenfeld, A. & Krüger, J., On the role of surface plasmon polaritons in the formation of laser-induced periodic surface structures upon irradiation of silicon by femtosecond-laser pulses, *J. Appl. Phys.*, Vol. 106, 104910 (2009).
4. Huang, M.; Cheng, Y.; Zhao, F. & Xu, Z., The significant role of plasmonic effects in femtosecond laser-induced grating fabrication on the nanoscale, *Ann. Phys.-Berlin*, Vol. S25, 74-86 (2013).
5. Derrien, T. J.-Y.; Itina, T. E.; Torres, R.; Sarnet, T. & Sentis, M., Possible surface plasmon polariton excitation under femtosecond laser irradiation of Silicon, *J. Appl. Phys.*, Vol. 114, 083104 (2013).
6. Raether, H., Surface Plasmons on Smooth and Rough Surfaces and on Gratings, *Springer-Verlag*, 1986; Maier, S. A. Science, S. (Ed.), Plasmonics, Fundamentals and Applications, *Springer*, 2007.
7. Derrien, T. J.-Y.; Krüger, J. & Bonse, J., Properties of surface plasmon polaritons on lossy materials: lifetimes, periods and excitation conditions, *Journal of Optics*, Vol. 18, 115007 (2016); the code is available in the website <https://bitbucket.org/tjyderrien/spp-extended-theory>.
8. Gnilitzky, I.; Derrien, T. J.-Y.; Levy, Y.; Bulgakova, N. M.; Mocek, T. & Orazi, L. High-speed, highly regular femtosecond laser printing of laser-induced periodic surface structures on metals: physical origin of the regularity, *submitted*.

Directional thermal infrared absorption and emission of zero refractive index dielectric metamaterials

Byungsoo Kang, Hyeon-Don Kim, Hyun-Sung Park, Kanghee Lee, Sunwoo Han, Jaeman Song, Bong Jae Lee, and Bumki Min*

Department of Mechanical Engineering, Korea Advanced Institute of Science and Technology, South Korea

*corresponding author: bmin@kaist.ac.kr

Abstract- The zero refractive index metamaterial is numerically simulated, proven to exhibit an abrupt change in reflection with respect to the incident angle from the surface normal direction and highly directional infrared absorption, from which directional thermal emission can be inferred.

All objects with non-zero absolute temperature emit infrared waves. A typical material exhibits a spectrum similar to that of a black body, showing a unique asymmetric bell-shaped curve, observed originally by Planck in 1900. On the angular point of view, most surfaces, which can be categorized into the Lambertian surface, obey the cosine law, emitting light strongest towards the surface normal direction and weaker towards direction with an increasing angle with the surface normal.

It was demonstrated that the spectral and angular distribution could deviate from the general trends if the surface has engineered patterns on itself. It was reported that a metamaterial perfect absorber shows an intense thermal emission only at a specific frequency range¹. A highly directional emission of tungsten grating with sharp v-shaped angular distribution was reported².

In this work, a zero-index metamaterial is proposed as a highly directional thermal absorber/emitter. For the verification, FDTD(Finite Difference Time Domain) computer simulation was used. To calculate effective parameters, the Retrieval method was used. Due to the extremely small refractive index, a small deviation of the incident angle from the surface normal direction leads to a large change in the transmission at the surface of the zero index metamaterial, which can be easily understood from the Fresnel's equation. Only light with a very small incident angle from surface normal direction is strongly transmitted at the first surface of the metamaterial while others are mostly reflected. If the metamaterial is semi-infinite in the light propagation direction and has non-zero loss, transmittance becomes zero. According to the energy conservation law, only near-normally incident light is absorbed. Thermally emitted light should follow the same angular absorption behavior according to the Kirchhoff's law. Effective zero refractive index metamaterial with/without an ordinary material substrate was numerically calculated. The effects of a variety of design variables on the spectral and angular distribution of thermal emission were studied. The metamaterial was based on Parikshit Moitra's design³; it consist of a high refractive index dielectric rod array inside a low refractive index dielectric matrix with a pitch shorter than the vacuum wavelength.

A retrieved result confirms both zero effective refractive index, permittivity, and permeability at the given frequency. A computer simulated absorption with respect to the incident angle shows highly angular directional absorption with FWHM of under 10 degrees. As the thickness increased, absorption of normally incident light increased, becoming more similar to the ideal directional emitter.

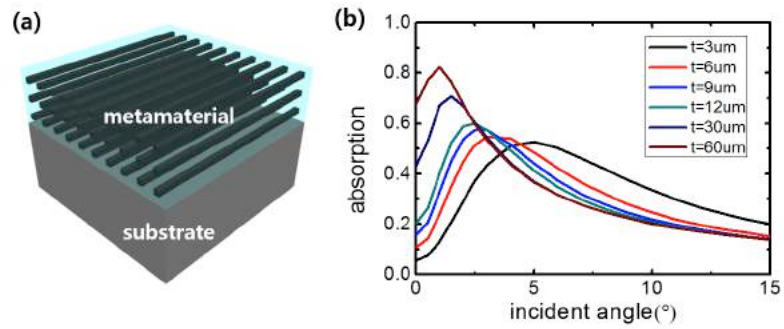


Figure 1. (a) schematic of the metamaterial (b) numerically calculated absorption of ideally homogeneous metamaterial at the zero refractive index frequency with respect to the incident angle

REFERENCES

1. Mason, J. A. "Strong absorption and selective thermal emission from a midinfrared metamaterial," *Applied Physics Letter*, Vol. 98, 241105, 2011.
2. Laroche, M., "Highly directional radiation generated by a tungsten thermal source," *Optics Letters*, Vol. 30, No. 19, 2623-2625, 2005.
3. Moitra, P., "Realization of an all-dielectric zero-index optical metamaterial," *Nature Photonics*, Vol. 7, 791–795, 2013.

Nanocarbon based lossy photonic crystal microwave absorbers.

G. I. Márk^{1*}, K. Kertész¹, G. Piszter¹, I. Biró², A. Paddubskaya³, P. Kuzhir³, and L. P. Biró¹

¹Institute of Technical Physics and Materials Science, (MFA), Centre for Energy Research, Hungarian Academy of Sciences, Budapest, Hungary

²„3D Kívánság”, 2030 Érd, Bíró u. 44/A/2, Hungary

³Research Institute for Nuclear Problems, Belarusian State University, Bobruiskaya Str. 11, 220030 Minsk, Belarus

*corresponding author: mark@mfa.kfki.hu

Abstract- Utilizing a combination of dielectric- and conducting materials it is possible to fabricate devices with predefined BRDF (Bidirectional Reflection Distribution Function) and BTDF (Bidirectional Transmittance Distribution Function). We utilized 3D printing to create a new type of lightweight and environmental friendly lossy photonic crystal structure, composed of plastic and nanocarbon composite materials, which shows excellent electromagnetic shielding properties. The method is capable of producing complex structures with tuneable electromagnetic characteristics, which provides a new route for microwave devices. By the help of the optimization of the layer structure we were able to achieve nearly perfect absorption in a large wavelength and incidence angle range.

Recently we demonstrated [1] that multilayered structures of alternating graphene monolayers and polymer layers can absorb up to 50% of the incident microwave radiation energy. The total thickness of the sandwich structure is less than 1 micrometer. However, in many applications stronger films and more reliable processing conditions are required. 3D printing makes it possible to place different materials with diverse properties at geometrically precisely defined spatial positions – therefore it is an ideal tool to create 3D photonic crystal structures active in the microwave range. In our recent study [2] the source material was a commercial nanocomposite filament, named 3D Black Magic [3], consisting of a nano-carbon filler incorporated in a polylactic acid (PLA) polymer, while the polymer is pure PLA. We studied the electromagnetic wave propagation in those periodic nano-carbon/polymer structures and related this with the texture, structure, and thermal properties [2]. This sandwich structure provides an EMI SE value of 15 dB in the Ka band with only 4 nanocarbon layers and the transmittance can be arbitrarily reduced with increasing the number of layers. Later we were able [4] to shrink the thickness of the material by hot pressing, while preserving its excellent electromagnetic shielding properties.

The attractive EMI SE value, however, comes not only from absorption, but also from reflection. This reflection originates mainly at the first air-nanocarbon interface and is caused by the abrupt change of the dielectric constant at the leading edge. Therefore we planned an optimized layer structure, where the first layer is a nanocarbon-air grating with small aspect ratio in order to prevent reflection. The microwave energy entering into the layer structure is then forced into absorption in the subsequent nanocarbon layers by creating standing waves in the plastic layers separating them. Our 3D Maxwell equation calculations show that this optimized structure has more, than 90% absorption in the whole Ka band and for the 0-60° incidence angle range. The calculations are verified by microwave transmission and reflection measurements.

REFERENCES

1. Batrakov, K., Kuzhir, P., Maksimenko, S., Paddubskaya, A., Voronovich, S., Lambin, Ph., Kaplas, T., and Svirko, Yu., "Flexible transparent graphene/polymer multilayers for efficient electromagnetic field absorption" *Sci. Rep.*, 4, 7191, 2014.
2. Paddubskaya, A., Valynets, N., Kuzhir, P., Batrakov, K., Maksimenko, S., Kotsilkova, R., Velichkova, H., Petrova, I., Biró, I., Kertész, K., Márk, G. I., Horváth, Z. E., and Biró, L. P. "Electromagnetic and thermal properties of three-dimensional printed multilayered nano-carbon/poly(lactic) acid structures" *J. Appl. Phys.*, 119, 135102, 2016.
3. <http://www.blackmagic3d.com>
4. Kotsilkova, R., Ivanov, E., Todorov, P., Petrova, I., Volynets, N., Paddubskaya, A., Kuzhir, P., Uglov, V., Biró, I., Kertész, K., Márk, G. I., and Biró, L. P. "Mechanical and electromagnetic properties of 3D printed hot pressed nanocarbon/poly(lactic) acid thin films" *J. Appl. Phys.* 121, 064105, 2017.

Electroactive and Magnetoactive Materials

Dielectric response of Al substituted $\text{Ba}_{0.8}\text{Pb}_{0.2}\text{Fe}_{(12-x)}\text{Al}_x\text{O}_{19}$ single crystal hexaferrites in terahertz spectral region

L. N. Alyabyeva^{1*}, D. A. Vinnik², V. I. Torgashev³, S. A. Gudkova^{1,2}, E. S. Zhukova¹, A. S. Prokhorov^{1,4},
D. A. Zherebtsov², B. P. Gorshunov^{1,4}

¹Moscow Institute of Physics and Technology (State University), Russia

²South Ural State University, Russia

³Faculty of Physics, Southern State University, Russia

⁴A.M. Prokhorov General Physics Institute, Russian Academy of Sciences, Russia

*corresponding author: aliabeva.ln@mipt.ru

Abstract. The phonon spectra of Al substituted M-type $\text{Ba}_{0.8}\text{Pb}_{0.2}\text{Fe}_{(12-x)}\text{Al}_x\text{O}_{19}$ hexaferrites ($x=0, 1, 3.3$) are studied in the region $5\text{-}1000\text{ cm}^{-1}$. An intensive line with complicated structure and dielectric contribution of about 10-20 into real part of dielectric permittivity is observed in the low-frequency region. Temperature change of dielectric parameters of this line is studied in 6-300 K temperature range. The presence of phase transition in $\text{Ba}_{0.8}\text{Pb}_{0.2}\text{Fe}_{12}\text{O}_{19}$ around 100 K is suggested.

The M-type hexaferrites with general formula $\text{MFe}_{12}\text{O}_{19}$ ($\text{M} = \text{Ba}, \text{Pb}, \text{Sr}$), possess ferroelectric and ferromagnetic properties. These materials are prospective for application in microwave electronics, magnetic memory devices, permanent magnets, etc. [1]. M-type hexaferrites have complex crystal structure (space group $\text{P6}_3/\text{mmc}$) with Fe ions occupying five different site-positions: three octahedral (2a, 4f₁, 12k), one tetrahedral (4f₂) and trigonal bipyramidal (2b). The last one is unstable and could be presented as a superposition of three different positions: a trigonal bipyramid itself and “quasi-bipyramid”, constructed of two tetrahedral; the Fe^{3+} ion dynamically oscillates between these three positions [2].

Substitution with paramagnetic Al ions increases anisotropy of the solid solution and thus, shifts the phonon modes to higher frequencies. In this study, we investigated $\sim 180\text{ mkm}$ thick z-cuts of bulk single crystalline $\text{Ba}_{0.8}\text{Pb}_{0.2}\text{Fe}_{(12-x)}\text{Al}_x\text{O}_{19}$ ($x=0, 1, 3.3$) hexaferrites grown by the flux technique [3]. Spectroscopic measurements were performed using terahertz frequency-domain backward-wave oscillator and time-domain TeraView TPS-Spectra-3000 spectrometers; for the infrared measurements, standard infrared Fourier-transform spectrometer Bruker Optics Vertex 80v was used. The far-infrared and terahertz reflectivity spectra (fig.1) reveal complex structure due to presence of intensive phonon modes. The spectra were modeled with a number of Lorentzian functions:

$$\varepsilon^*(\nu) = \varepsilon_1(\nu) + i\varepsilon_2(\nu) = \sum_j \frac{f_j}{(\nu_j^2 - \nu^2) + i\nu_j\gamma_j} \quad (1),$$

where $f_j = \Delta\varepsilon\nu_j^2$ is the oscillator strength of the j -th resonance, $\Delta\varepsilon_j$ is its dielectric contribution, ν_j represents the resonance frequency and γ_j is the damping. Parameters of ε_∞ required for the modeling were obtained from mid-infrared frequency-independent room-temperature “tails” of bulk reflectivity spectra of the $\text{Ba}_{0.8}\text{Pb}_{0.2}\text{Fe}_{(12-x)}\text{Al}_x\text{O}_{19}$ samples and had values of 6.2 for $x=0$, 6.95 for $x=1$ and 5.3 for $x=3.3$, respectively. Spectra of complex dielectric permittivity are presented in fig.1.

Analysis of the temperature dependence of terahertz dielectric response of $\text{Ba}_{0.8}\text{Pb}_{0.2}\text{Fe}_{12}\text{O}_{19}$ has showed that the low frequency absorption band consists of at least four lines. Each of them revealing temperature shift of resonance frequency and dielectric permittivity values (fig.2).

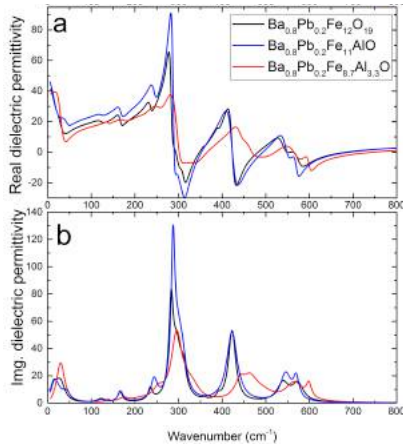


Figure 1. Spectra of real (a) and imaginary (b) parts of dielectric permittivity of $\text{Ba}_{0.8}\text{Pb}_{0.2}\text{Fe}_{(12-x)}\text{Al}_x\text{O}_{19}$ ($x=0, 1, 3.3$) at 300 K.

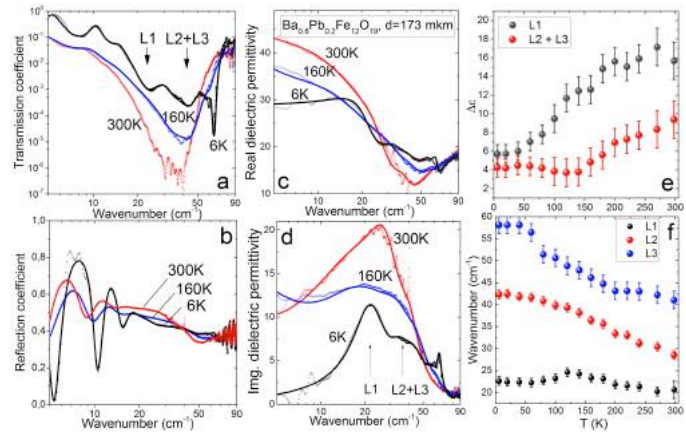


Figure 2. Experimental data (dots) and model fits (lines) of transmission (a), reflection (b), real (c) and imaginary (d) permittivity of $\text{Ba}_{0.8}\text{Pb}_{0.2}\text{Fe}_{12}\text{O}_{19}$ at 6 (black), 160 (blue) and 300 (red) K. Temperature dependences of dielectric contribution (e) and frequency positions (f) of low-frequency modes.

The experimental results show strong deviations from the data obtained for pure $\text{BaFe}_{12}\text{O}_{19}$ (Ba ions are in ordered positions [2]) and pure $\text{PbFe}_{12}\text{O}_{19}$ (Pb ion are reported to occupy site-position disordered over 12 subpositions [4]). Crystal field disorder induced by presence of both Ba and Pb affects the phonon modes spectra and dielectric response. Incorporation of Al ions contribute additional disorder of crystal field and also affects dielectric properties of the compound. Low-frequency mode is probably a manifestation of an anharmonic oscillation of Fe ion in splitted bipyramidal 2b site-position.

Acknowledgements. The research was supported by the Russian Ministry of education and science (Program “5Top100”, and partially 4.1346.2017/PP) and Russian Foundation for Basic Research (Grant 15-02-03021). Additionally the single crystal growth was supported by the Act 211 Government of the Russian Federation (02.A03.21.0011).

REFERENCES

1. Kumar, P., A. Gaur and R.K. Kotnala. “Magneto-electric response in Pb substituted M-type barium-hexaferrite,” *Ceram. Int.*, Vol. 43, 1180-1185, 2017.
2. Mikheykin, A.S. et al. “Lattice anharmonicity and polar soft mode in ferromagnetic M-type hexaferrite $\text{BaFe}_{12}\text{O}_{19}$ single crystal,” *Eur. Phys. J. B*, Vol. 87, No. 10, 232, 2014.
3. Vinnik, D.A. et al. “Structural and millimeter-wave characterization of flux grown Al substituted barium hexaferrite single crystals,” *Ceram. Int.*, Vol. 41, 12728-12733, 2015.
4. Zhukova, E.S. et al. “Crucial influence of crystal site disorder on dynamical spectral response in artificial magnetoplumbites,” *Solid State Sci.*, Vol. 62, 13-21, 2016.

Bioeffects of EM fields, Biological Media, Medical electromagnetics

PLANAR MICROWAVE RESONATOR FOR BIO-SENSING AND MATERIAL CHARACTERISATION

Ayodunni Oloyo, Zhirun Hu
*School of Electrical & Electronic Engineering, The University of Manchester
Manchester, M13 9PL, United Kingdom*

ayodunni.oloyo@postgrad.manchester.ac.uk, Z.Hu@manchester.ac.uk

Abstract – The use of planar microwave resonator for bio-sensing and material characterization of biological materials in a non-invasive method is presented. The resonator was used to measure the scattering parameter values of biological phantom of human tissues including blood, skin, fat, muscle, and bone. Relative permittivity of the test materials was estimated through conversion of the s-parameter values by the method of Classical Nicolson-Ross-Weir. The results obtained indicated that planar microwave resonator could replace the conventional method of relative permittivity measurements in human tissues and subsequently useful in human healthcare management in the near future.

Introduction

There are several ways to measure the permittivity of a material; this project employs microwave resonator. The microwave resonator is used for radiating and for receiving signal; it's a structure between a guiding device (transmission line) and free space [1]. The resonator is used to measure the permittivity of the material under test (MUT). The principle is based on the fact that the properties of liquid can be determined when the electromagnetic wave interacts with the biological tissue; this theory is governed by complex permittivity [2]. The complex permittivity is defined in terms of angular frequency ω and the concentration χ of the electrical properties.

$$\epsilon_r(\omega, \chi) = \epsilon_r'(\omega, \chi) - j\epsilon_r''(\omega, \chi) \quad (1)$$

Simulation Test

The antenna was loaded with five different dielectric materials namely skin, bone, fat, blood and muscle one at a time. These tissues were chosen to prove that the microwave resonator can differentiate between biological materials and can be used for bio-sensing and material characterization.

Table 1: Tissues versus Frequency Shift

Material	S-parameter[Magnitude] in dB	Frequency
Without	-23.801	0.8946

MUT		
Blood	-30.434	0.8009
Bone	-14.96	0.5396
Fat	-26.917	0.6658
Skin	-22.874	0.9667
Muscle	-28.275	0.8009

The result above certifies the principle that the properties of liquid can be determined when the electromagnetic wave interacts with the biological tissue; the responses of the materials are determined by the placement of their atomic moments. The result shows that resonance frequency is dependent on the water content in each biological material i.e. the less the water content the lower the conductivity. The resonator sensor gave an excellent response in regards to load permittivity. The increase in water content caused an increase in the frequency value; the decrease in water content causes a decrease in permittivity. This is probable as the permittivity decreased when the glucose concentration increased as reported by [3] and [4].

Conclusion

A microwave resonator was introduced to differentiate between biological tissue. The sensor was simulated and tested; the effect of dielectric properties was characterized by placing different materials [muscle, bone, blood, skin and fat] on the most sensitive part of the device. The simulation results have shown that the new approach to investigate material properties is valid. This shows that there is an opportunity that the microwave resonator can be used for medical diagnostics in a non-invasive way.

References

- [1] D. M. Pozar, *Microwave Engineering*, 4th ed., Chicago: John Wiley & Sons, 2012.
- [2] R. N. K. R. C. A. Mahesh P Abegaonkar, "A microwave microstrip ring resonator as a moisture sensor for biomaterials: application to wheat grains," Pune, 1998.
- [3] G. Yoon, A. Amerov, K. J. Jeon, J. B. Kim and Y.-J. Kim, "Optical measurement of glucose levels in scattering media," *IEEE*, vol. 20, no. 4, pp. 1897-1899, 1998.
- [4] V. Turgul and I. Kale, "Characterization of the Complex Permittivity of Glucose/Water Solutions for Noninvasive RF/Microwave Blood Glucose Sensing," in *2016 IEEE International Instrumentation and Measurement Technology Conference Proceedings*, 2016.

Influence of the Metallic Loop-like Accessory on the SAR of Broadband Wearable Planar Monopole Textile Antenna

H. H. Zainal^{1*}, H. A. Rahim¹, P.J.Soh², K.N.Abdul Rani³, H. Lago², M.S.Zulkefli⁴,
and N.F.N.Yah¹

¹Bioelectromagnetics Research Group (BioEM),

²Advanced Communication Engineering (ACE),

School of Computer and Communication Engineering, Universiti Malaysia Perlis (UniMAP), Kampus
Pauh Putra, Perlis, Malaysia

³Faculty of Technology Engineering Universiti Malaysia Perlis (UniMAP), Padang Besar
Perlis, Malaysia

⁴Centre of Diploma Studies (CDS), Universiti Malaysia Perlis (UniMAP), Campus UniCITI Alam Sg.
Chuchuh, Perlis, Malaysia

*corresponding author: hayatibuan@yahoo.com

Abstract

This paper presents the investigation of influence of the common metallic loop-like accessory on the Specific Absorption Rate (SAR) averaged over 10g of body tissue. Numerical analysis conducted using a broadband textile monopole antenna (TM) with variations of orientation and distance showed that peak SAR values increased when the TM is horizontally polarized. This is up to 70% more than vertically polarized TM placed closest to the metallic item at 2 mm.

1. Introduction

The growing usage of mobile phones and gadgets has raised public concerns about the possible health effects of electromagnetic (EM) radiation of these devices on user [1]. The effects of radio frequency (RF) includes the rise of the body temperature and, which potentially affects the eyes, brain and other sensitive areas [2]. This project aims to investigate the value effect of metallic loop-like accessory items on antenna radiation and consequently the human body via SAR value. Many studies have been conducted to examine the effects of metallic objects on SAR distribution, metallic objects on the resulting SAR values [3]. A more recent study [4], found that the values of the SAR on the existence of antenna ground plane besides antenna-to-phantom. However, to the best of authors' knowledge, a thorough experimental investigation of the influence of metallic body accessory on the SAR of on-body wearable antenna has yet to be reported in the open literature. It was hypothesized that the presence of metallic body accessories may affect the

SAR values when the on-body wearable antenna was mounted in close proximity to the human body.

2. Antenna Mounted on Human Body

The design of monopole antenna is presented in [5]. This wearable textile monopole operates at 2.45 GHz where ShieldIt Super as conducting element and felt fabric as substrate element are used. In order to investigate the interaction between the antenna and the human body, a cylindrical phantom model is used in the simulation to human body structure. Numerical simulations are conducted using CST Microwave Studio based on the Finite Integral Technique (FIT). The generic human body consists of three cylindrical bricks, representing the upper human body torso and two arms. The parameters (ϵ_r , σ) of the human body tissues are defined according to the standard tissue equivalent liquids recommended by the Electrical and Electronics Engineers (IEEE) and Federal Communications Commission FCC [3]. As the transmitting antenna, a $\pi/4$ planar monopole textile antenna (TM) is used which was based on the work in [5]. Such type of antenna is chosen due to its partial ground plane, which allow radiation towards the human body. The TM is positioned against the metallic loop-like accessory, place on the left wrist of the generic arm at a distance of between 2 mm until 20 mm away from the phantom. Metallic loop-like accessory made of silver with a conductivity, $\sigma = 6.30 \times (10^7)$ and sized at outer radius 68 mm and inner radius 64mm. The energy absorption when antenna is placed in varied distances from metallic item in two different orientations (vertical and horizontal polarizations with respect to the human body model) are calculated. The SAR results are averaged over 10g of tissue.

Figure 1 illustrates that S_{11} variation depends on the distance from the metallic loop like accessory. The worst case of S_{11} is observed when the TM is horizontal polarization, which is parallel to the human body model with the closest distance to the metallic item, i.e., 8mm.

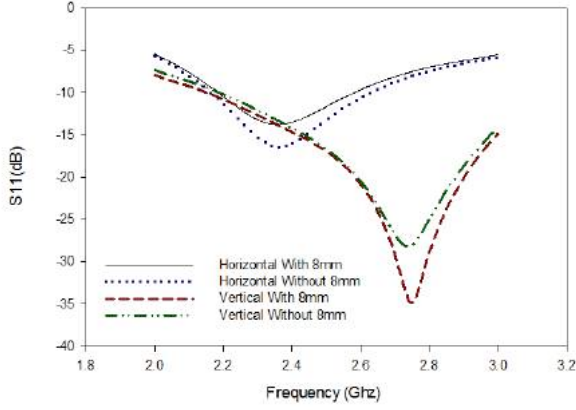


Figure 1: S_{11} of the antenna for different position from metallic loop like accessory

Figure 2 shows the maximum 10g SAR value inside the human body for different antenna orientations and distances antenna from metallic item. The highest value of peak 10g SAR (30.0 W/Kg) occurs when antenna is horizontally polarized and placed 2 mm from the metallic item. It shows that the antenna orientation is one of the contributing factors which could increase the averaged SAR in human body by up to 70% compared to vertical polarization case in the closest distance of TM to the metallic item. The lowest SAR value is observed when the antenna is placed far from the metallic loop like accessory for both cases. Moreover, the SAR resulting from placing the TM in vertical polarization is lower than antenna in horizontal polarization. In addition, the graph also shows that the SAR decreases when the distance between the antenna and metallic loop like accessory was increased, as was also found in [1], [4]. However, the SAR values remain unchanged in the case of a vertically polarized TM, suggesting that such orientation is robust against excessive EM absorption. This concludes that the metallic loop-like accessory affects the SAR and the reflection coefficient of the planar wearable textile monopole.

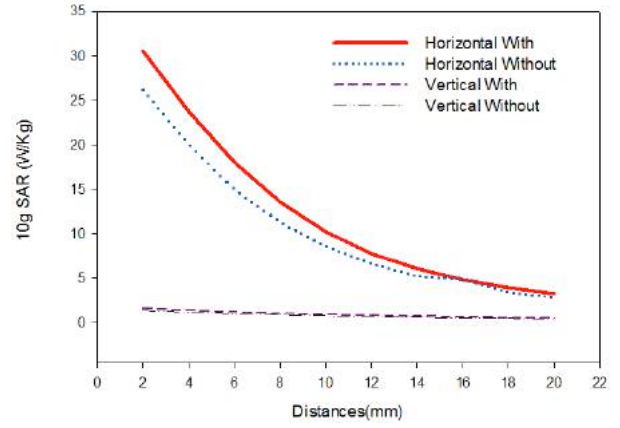


Figure 2: Result of SAR averaged over 10g

3. Conclusions

The results presented in this paper are solely based on computer simulation using commercially software CST Microwave Studio. In this paper, a monopole antenna has been used as the radiating sources. This study has indicated the additional metallic loop like accessory worn on human body has an additional effect. Results show that the SAR inside the human body increased due to the presence of metallic loop like accessory. Nevertheless, the SAR values are varying depending on the distance between the antenna and metallic loop like accessory as well as the orientation of the antenna. This concludes that the metallic loop-like accessory affects the SAR and the reflection coefficient of the planar wearable textile monopole.

Acknowledgements

No potential conflict of interest was reported by the authors.

References

- [1] M. Safari and A. Abdolali, "Dental Implants and Mobile-Phone Use," no. August 2016, pp. 43–51.
- [2] C. Zhu, D. Wu, L. Ping, and W. Liang, "The Effects of Head Parameters on the Specific Absorption Rate in the Human Head," no. Bmei, pp. 423–427, 2015.
- [3] S. H. Ronald, M. F. A. Malek, S. I. S. Hassan, C. E. Meng, M. H. Mat, M. S. Zulkefli, and S. F. Maharimi, "Designing Asian-Sized Hand Model for SAR Determination at GSM900/1800: Simulation Part," *Prog. Electromagn. Res.*, vol. 129, no. May, pp. 439–467, 2012.
- [4] P. J. Soh, G. A. E. Vandenbosch, F. H. Wee, A. Van Den Bosch, M. Martínez-vázquez, and D. Schreurs, "Specific Absorption Rate (SAR) Evaluation of

Textile Antennas,” vol. 57, no. 2, pp. 229–240, 2015.

- [5] H. A. Rahim, M. Abdulmalek, P. J. Soh, and G. A. E. Vandenbosch, “Evaluation of a broadband textile monopole antenna performance for subject-specific on-body applications,” *Appl. Phys. A*, vol. 123, no. 1, p. 97, 2017.

Measurement Techniques

RCS Evaluation from Small Scatters in Automotive Collision

Avoidance Rader Band

H.-J. Hsieh^{1*}, T.-H. Hsieh¹, S.-K. Tuan¹, and W.-J. Liao¹

¹National Taiwan University of Science and Technology, Taiwan

*Email: m10407602@mail.ntust.edu.tw

Abstract- An effective and accurate RCS evaluation procedure is developed for small-sized scatters in the 24 GHz band using an antenna measurement range. Simple targets of known RCS values are measured. Results indicate that the proposed method can yield relatively accurate results. This technique can be applied to the evaluation of RCS properties from small scatters on the road, such as pedestrians and bicycles. The results can be forwarded to the development of corresponding detection algorithms.

I. INTRODUCTION

The radar cross section (RCS) is a convenient indicator about the ability of an object reflecting incident electromagnetic waves [1]. Specifications of a radar can only be determined by knowing the typical RCS range of its intended targets. RCS values of real-world scatters are complicated functions of frequency, polarization, scatter geometry, surface roughness and material properties, and is usually sensitive toward the angle of incidence. RCS measurements is therefore a direct and effective measure to assess the scatter properties. The automotive collision avoidance radar is going to be a critical safety measure on cars because it can detect object direction and distance in front of or surrounding the car. Active and passive measures can be taken to ensure passenger safety. There are large clutters on the road, such as cars and trucks, which are considered with large RCS values. On the other hand, there are also small targets on the road, such as pedestrians, bicycles and motorcycles. Their RCS values are substantially smaller. Miss detections may put people in danger.

II. METHOD

In this paper, RCS values of small targets, which may be found on pedestrians and bicycles, are evaluated in an antenna range. A metal disk of 5 cm diameter and a metal sphere of a 6 cm diameter are measured. The tested band includes 24 GHz, which is one of the popular frequency for automotive radar. RCS values are extracted from reflection coefficient spectra measured in the frequency domain. Fig. 1 shows the RCS measurement setup in the anechoic chamber and targets to be measured. A standard gain horn of 13.5 dBi is employed to provide incidence. The distance between the turn table and transmitting horn is about 0.8 m. The number of samples is 16001 points. The IF Bandwidth and the output power of the network analyzer are set as 1 KHz and 0 dBm respectively. The frequency sweep is from 18 to 27 GHz, which is broad enough to perform Fourier transform. Time gating is applied near the target reflection time and the result is transformed back to the frequency domain. Using the radar equation, RCS σ can be derived as

$$\sigma = 33 + 40 \log R - 20 \log \lambda_0 - 2G + S_{11,NA} \quad (1)$$

where R is the standard horn to DUT distance, G is the standard horn gain and $S_{11,NA}$ is the time gated reflection coefficient. This method is employed in [2], which detail the range calibration and RCS estimation procedure.

III. RESULTS

Fig. 2 shows measured RCS value of the metal sphere at 24 GHz with different incident angles. The values are not the same at all angles. This may be due to miss alignment metal on the turn table. At $\theta = 0^\circ$, the metal sphere

RCS value is about -25.23 dBsm. Since the sphere size approaches to the geometric optic region [3], the value is nearly the same as its physical aperture, which is -25.48 dBsm, as suggested in (2).

$$\sigma = \pi a^2 \quad (2)$$

Fig. 3 shows measurement RCS values of the metal disc at 24 GHz. Measurements are conducted with two orthogonal incidence polarizations. For normal incidence, the RCS value is about -6.5 dBsm. This number is close to the RCS value estimated using (3), which is applicable for flat square plates at normal incidence [4].

$$\sigma = \frac{4\pi A^2}{\lambda^2} \quad (3)$$

where A is area of metal disc. The calculated RCS number is -5.08 dBsm.

When the transmitting horn rotates from $\theta = 0^\circ$ to 90° , the RCS value drops rapidly due to lack of specular reflection. At the grating region, the RCS value rises due to edge diffraction. Note the angular profile of the perpendicular polarization is somewhat different to the parallel polarization one because of unlike edge diffraction mechanism and possible fabrication errors.

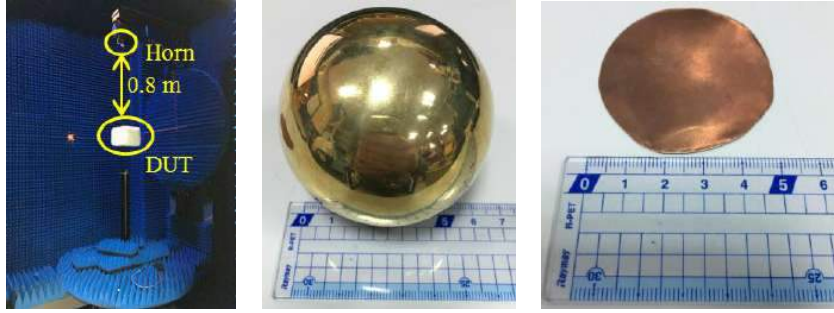


Fig. 1. RCS measurement system structure in anechoic chamber and target to be measured

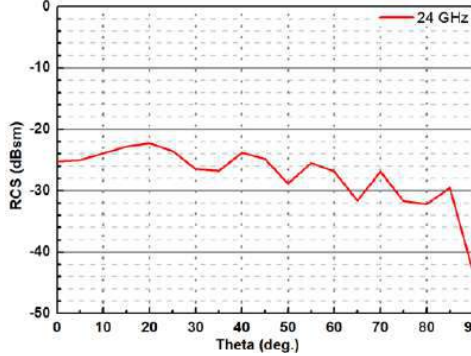


Fig. 2. Metal ball RCS value

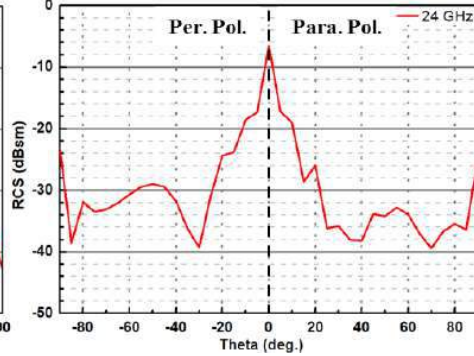


Fig. 3. Metal disc RCS value

IV. CONCLUSION

This work demonstrates that monostatic RCS assessment of small targets is feasible using existing antenna range. The resulting RCS numbers is very close to theoretical one. Variations in angular profiles also comply with known scattering mechanisms.

REFERENCES

1. Knott, E. F., J. F. Schaeffer and M. T. Tuley, *Radar Cross Section*, SciTech, Netherland, 2004.
2. Tsai, C.-C., C.-T. Chiang and W.-J. Liao, "Radar cross section measurement of unmanned aerial vehicles," in *iWEM*, Nanjing, China, July, 2016.
3. Balanis, C. A., *Advanced Engineering Electromagnetics*, 2nd ed., Wiley, 2011.
4. Hou, Y.-C., Tsai, C.-C., W.-J. Liao and S.-H. Chen, "Planar multi-layer structure for broadband broad-angle RCS reduction," *IEEE Trans. Antenna Propag.*, Vol. 64, No. 5, 1859–1867, 2016